Thermoresponsive Microgels for Multicellular Spheroids Formation

Xiaolin Cui

This thesis is submitted for the degree of Doctor of Philosophy
in
School of Chemical Engineering
Faculty of Engineering, Computer and Mathematical Sciences
at
The University of Adelaide

September 2016

"Dubito ergo cogito, cogito ergo sum"

René Descartes

To my family

Yi Cui, Aili Zheng

PENEL OF SUPERVISORS

Principal Supervisor

Dr. Hu Zhang (PhD)
School of Chemical Engineering
The University of Adelaide
Email: hu.zhang@adelaide.edu.au
Phone: +61 8 831 33810

Co-supervisors

A/Prof. Jingxiu Bi (PhD)
School of Chemical Engineering
The University of Adelaide
Email: jingxiu.bi@adelaide.edu.au
Phone: +61 8 831 31015

A/Prof. Sheng Dai (PhD)
School of Chemical Engineering
The University of Adelaide
Email: s.dai@adelaide.edu.au
Phone: +61 8 831 34118

Declaration for a thesis that contains publications

I certify that this work contains no material which has been accepted for the award of any other degree or diploma in my name, in any university or other tertiary institution and, to the best of my knowledge and belief, contains no material previously published or written by another person, except where due reference has been made in the text. In addition, I certify that no part of this work will, in the future, be used in a submission in my name, for any other degree or diploma in any university or other tertiary institution without the prior approval of the University of Adelaide and where applicable, any partner institution responsible for the joint-award of this degree.

I give consent to this copy of my thesis when deposited in the University Library, being made available for loan and photocopying, subject to the provisions of the Copyright Act 1968.

I acknowledge that copyright of published works contained within this thesis resides with the copyright holders of those works.

I also give permission for the digital version of my thesis to be made available on the web, via the University's digital research repository, the Library Search and also through web search engines, unless permission has been granted by the University to restrict access for a period of time.

I acknowledge the support I have received for my research through the provision of an Australian Government Research Training Program Scholarship.

Name: Xiaolin Cui

Signature:.. Date:..

Preface

This doctoral thesis is prepared in “Publication” format according to the “Specifications for Thesis (2016)” of the University of Adelaide. It includes publications that have been published, submitted for publication, or prepared in publication format:

1. X. Cui, Y. Hartanto and H. Zhang, Advances in multicellular spheroids formation", Journal of Royal Society Interface, accepted.
2. X. Cui, S. Dini, S. Dai, J. Bi, B. J. Binder, J. E. F. Green and H. Zhang, A mechanistic study on tumour spheroids formation in thermosensitive hydrogels: experiments and mathematical modelling. RSC Advances, 2016, 6, 73282-73291. DOI: 10.1039/C6RA11699J.
3. X. Cui, Y. Liu, Y. Hartanto, J. Bi, S. Dai and H. Zhang, Multicellular spheroids formation and recovery in microfluidics-generated thermoresponsive microgel droplets. Colloid and interface science communication, 2016, 14, 4-7, DOI: 10.1016/j.colcom.2016.09.001.
4. X. Cui, Y. Hartanto, J. Bi, S. Dai and H. Zhang, Tuning the microenvironment for tumour spheroids formation. (Prepared in publication style).
5. X. Cui, Junnan Tang, J. Bi, S. Dai, K. Cheng and H. Zhang, Exploring thermal reversible hydrogels for cardiac stem cell expansion and function in three-dimensions. (Prepared in publication style).

During the PhD candidature, some relevant researches were conducted in collaboration with other researchers which lead to a publication. The finalized works are:

1. H. Zhang, X. Cui, J. Bi, S. Dai and H. Ye, Single-cell analysis for bioprocessing, Engineering in Life Sciences, 2015, 15, 582-592. DOI: 10.1002/elsc.201400155.
2. Y. Hartanto, M. Zargar, X. Cui, Y. Shen, B. Jin and S. Dai, Thermoresponsive cationic copolymer microgels as high performance draw agents in forward osmosis

desalination, Journal of Membrane Science, 2016, 518, 273-281. DOI: 10.1016/j.memsci.2016.07.018.

3. Y. Liu, Z. Wang, L. Lia, X. Cui, J. Chua, S. Zhang and Y. Zhuang, On-line monitoring the aggregate size distribution of Carthamustinctorius L. cells with multi-frequency capacitance measurements, RSC Advances, 2016, 6, 89764 – 89769, DOI: 10.1039/C6RA13527G.
4. L. Yan; X. Cui; T. Harada, S. Lincoln, S. Dai and T, Kee, Generation of Fluorescent and Stable Conjugated Polymer Nanoparticles with Hydrophobically Modified Poly(acrylate)s, Macromolecules, 2016, 49, 8530-8539, DOI: 0.1021/acs.macromol.6b02002.
5. J. Tang, X. Cui, M. Hensley, A. Vandergriff, J. Cores, T. Allen, P. Dinh, Y. Hartanto, T. Caranasos, J. Zhang, H. Zhang and K. Cheng, Heart repair using thermosensitive microgel –encapsulated human cardiac stem cells in immunocompetent mice, Advanced functional material, submitted (co-first author).

In addition, some awards were achieved during the PhD work:

1. Faculty of Engineering, Computer and Mathematical Sciences Divisional Scholarship.

Acknowledgement

Here I would like to acknowledge all the people who have helped me through the whole journey as without them I would not have achieved what I have achieved.

I would like to thank my supervisor Dr Hu Zhang for his continuous guidance, enthusiasm and tremendous support during my candidature. I have learned so much during this three and a half years study under his supervision. His encouragement, great attitude towards research and life in general, as well as constructive advices helped me develop my skills and enrich my knowledge to be an independent research which is crucial for my future. I also would like to thank my co-supervisor A/Prof. Sheng Dai. He is like the captain who guided me the research direction. His support and advices helped me get through this roller coaster journey. I would like to thank my co-supervisor A/Prof Jingxiu Bi. Her help and care have helped me go through those tough times. What I have learned from all my supervisors is beyond the science itself. Their wisdom and their positive attitude will always inspire me.

Many thanks to A/Prof. Ke Cheng from North Carolina State University. The short period visiting in his lab has been one of the highlights during my journey. His inspiration and knowledge have broadened my horizon, and spark my interest to continue working in biomedical research. I would like to thank Junnan Tang. Without her help, I would not finish all the experiment. I remembered all the long hours we had spent in the lab. It may be felt miserable at time, but every time when I look back, it is full of joys. I also would like to thank other members from Dr Cheng's group: Michael, Adam, Jhon, Tyler and Phuong-Uyen. You guys made me feel home at Raleigh.

Many thanks to my group members in Adelaide, Yusak, Jiabin, Amir, Eric, Wanxia, David, Seonho, Qi. Thanks your guys for your support and friendship. Many thanks to Jason and Jeff from the workshop for their kind help for the past couple of years.

I would like to thank university of Adelaide, faculty of engineering, computer and mathematic science, school of chemical engineering to provide me with the divisional scholarship. Because of their generous financial support, I have this precious opportunity to pursue my dream.

I would like to thank my mates: Sammy, Xiu, Yuzhe, Mengjue, Clinton, David, Michael, Yu, Yinlu, Jie etc. You guys have shared all the highs and lows with me during my journey. Without your encouragement I couldn't get to the finish line.

Lastly, I would like to give my gratefully thank to my family. Thanks to my grandparents for their endless support. Thanks to my parents who have been the rock for my whole life. Their unconditional love and support are the main reason making me keep going no matter how tough it can be.

Abstract

Multicellular spheroids (MCS) are considered as the most promising three dimensional (3D) *in-vitro* model which will narrow down the gap between *in-vitro* two-dimensional culture and *in-vivo* animal models. They exhibit physiologically relevant cell-cell and cell-matrix interactions, and present similar gene expression, heterogeneity and structural complexity as *in-vivo* tissues. Multicellular spheroids have been attempted for drug screening and evaluation, mechanical studies on cancer cell invasion and migration, and regeneration medicine. However, fabrication of uniform-sized MCSs at a high throughput platform, and evaluation of MCSs for clinical relevance are two main challenges. In this thesis, thermally responsive microgels were employed as physical supports to culture multicellular spheroids from both tumor cells and stem cells, which are potentially applied in anti-cancer drug evaluation, tissue engineering and regeneration medicine.

The thermally reversible poly (*N*-isopropylacrylamide-co-acrylic acid) (P(NIPAM-AA)) microgels were first employed to fabricate HeLa MCSs. This microgel approach restricted cell mobility at a lower initial cell density due to a large volume in the microgel networks, which resulted in uniform-sized spheroids formation compared to non-adhesive culture. Moreover, because of thermal reversibility of this microgel, spheroids were released from the physical supports via cooling down the system to room temperature.

After demonstrating the formation of tumor spheroids in the microgel, HeLa cells were further encapsulated inside microgel-droplets generated from flow focusing microfluidics to obtain controllable uniform-sized spheroids. This approach combined the benefit of using thermal sensitive microgels as physical supports for MCS formation and droplet generation at a high throughput platform. Highly uniform-sized MCSs were obtained through this method. Importantly, the MCSs were easily released from the droplets by reducing the culture temperature to room temperature without using strong chemical or enzyme reagents. This approach may be used for generation of uniform-sized MCSs for drug screening and evaluation.

The microenvironment generated from the microgel plays an important role in MCS formation. The key characteristics of the microenvironment, such as surface charge density, hydrophobicity, mechanical strength, and the microstructure of the microgels, were investigated by synthesizing a range of poly(*N*-isopropylacrylamide) (P(NIPAM)) based microgels, including P(NIPAM), P(NIPAM-co-methacrylic acid) (P(NIPAM-MAA)), P(NIPMAM-co-acrylic acid) (P(NIPAM-AA)), P(NIPAM-co-malic acid) (P(NIPAM-MA)) and P(NIPAM-co-itaconic acid)(P(NIPAM-IA)). It was found that the moderate negatively charged surface with high hydrophilicity P(NIPAM-IA) microgels was beneficial for cellular growth. The high or low charge density resulted in slow cell proliferation. The hydrophobicity of microgels had a negative impact on cell growth. The large pore size of the P(NIPAM-IA) networks also allowed cell migration which promoted MCSs formation. Different cell types (HEK 293, U87, HeLa and mesenchymal stem cells) have been demonstrated to successfully form MCSs within the P(NIPAM-IA) microgel.

The thermal sensitive microgels were further applied to form stem cell MCSs. Human cardiac stem cells (hCSCs) were cultured in the P(NIPAM)) based microgel networks including P(NIPAM-co-dimethyl amino ethyl methacrylate) (P(NIPAM-DMAEMA)), P(NIPAM-IA), (P(NIPAM-co-2-hydroxyethyl methacrylate) (P(NIPAM-HEMA)), P(NIPAM-co-poly(ethylene glycol) methyl ether acrylate) (P(NIPAM-PEGA)). These microgels displayed different charges (cationic, anionic, and neutral) and different degrees of hydrophobicity. Through evaluation of hCSCs viability, proliferation and release of regenerative factors, P(NIPAM-IA) was identified as one of the best candidates for forming hCSCs spheroids because of its negatively charged surface with high hydrophilicity. The thermal reversibility of P(NIPAM-IA) renders it as injectable hydrogels. Initial results showed that injection of this microgel into mice did not elicit immune system responses, reduced myocardial apoptosis and promoted angiogenesis in the mice.

In summary, we have fabricated MCSs in different types of thermal responsive microgels through either physical control of the uniform size by confining cells in the microgel-droplets generated from microfluidics or fine tune of the microenvironment for MCS formation. The P(NIPAM-IA) microgel with moderated anionic charge and high hydrophilicity was found to promote MCSs formation. This microgel did not elicit any immune response, which indicates the potential of using this microgel for future clinical studies.

Table of Contents

Table of Figures

Table of tables

CHAPTER ONE

1. Introduction

Chapter 1: Introduction

1.1 Background

Cell behaviors in three-dimensional (3D) culture have gained increasing attention in the past decades because lack of cell-to-cell and cell-to-matrix interactions on two-dimensional (2D) culture plastic dishes makes it impossible for cells in 2D to replicate their biological functions *in-vivo* [1].

Multicellular spheroids (MCSs) are one typical product produced from the 3D culture and MCSs are widely considered to be an advanced tool for biomedical research due to its capability in mimicking the characteristics of real tissues. MCSs have a similar structure with the spatial and temporal complexities to one in the *in-vivo* environment. Therefore, MCSs have been utilized for drug screening and evaluation, tissue engineering and regeneration medicine [2].

There have been many approaches developed for fabricating MCSs, such as liquid overlay based culture[3-5], non-adhesive surfaces[6-8], suspension culture in mechanically stirred spinner flasks [9]and hanging drops[10-12]. However, the intensive skilled labor requirement and limited capacity for large-scale production of uniform-sized tumour spheroids hamper commercialization of these methods [8]. The Aeronautics and Space Administration invented a rotary cell culture bioreactor that can be used for scalable production of produce MCSs[13, 14]. However, due to lack of matrix support during MCSs formation in this bioreactor, cells experience different microenvironments compared to the *in-vivo* condition, which results in cellular agglomerate growth without reaction with extracellular milieu.

3D scaffold based cell culture emerges as a promising approach to culture MCSs. The scaffold provide matrices to MCSs to induce cell-matrix interactions which are vital for cell functions[15]. Natural polymeric scaffolds, one type of common scaffolds used to culture MCSs, such as collagen[16], hyaluronic acid-based hydrogel[17], chitosan[18] and matrigels[19], can promote cell proliferation and maintain high cell viability due to their enriched proteins/carbohydrates and high biocompatibility. However, these natural polymeric scaffolds lack design flexibility in manipulation of individual matrix properties and have poor handling characteristics as well as poor reproducibility[20]. Hence, the synthetic scaffold is considered as a replacement for the natural polymers. Synthetic scaffolds can be copolymerized from monomers which have the desired ECM characteristics such as encouraging cell attachment and growth[21]. Poly(ethylene glycol) (PEG)[22], poly(ε-carpolacton)[23], and poly(latic-co-glycolic acid) (PLGA)[24] have been employed as a scaffold for MCSs formation. The challenge of using synthetic polymer scaffolds is how to harvest the MCSs after their maturity without the introduction of toxic chemicals.

The thermally sensitive poly (*N*-isopoylacrylamide) (PNIPAM) based scaffold is a most promising material since the MCSs can be easily released from the scaffold by simply cooling down the scaffold into room temperature. P(NIPAM) based microgels have been used for stem cell culture, and it can maintain cells in a 3D network as well as promote cell growth in comparison with conventional 2D culture[25, 26]. In this thesis, we proposed to use P(NIPMA) based microgels as the scaffold to culture uniform-sized tumour spheroids that have the potential for drug screening. We also cultured cardiac stem cell spheroids with enhanced biological/physiological functions and applied stem cells/microgel mixture for heart regeneration. We hypothesized the microenvironment created from the microgels for cells have a great influence on the spheroid formation. Therefore, we co-polymerized different co-monomers with NIPAM to generate the microenvironment with different chemical functional groups, surface charge, and degrees of hydrophobicity/hydrophilicity.

1.2 **Aim and objectives**

This thesis explores the applications of p(NIPAM) based microgels for producing multicellular spheroids in a 3D microenvironment. The overall aim of this thesis is to develop a technique for forming and culturing multicellular spheroids from either tumor or normal cells) in the three-dimension thermally sensitive matrices. Several objectives are formulated basing on the overall aim:

1. To obtain uniform-sized tumour spheroids for future drug screening by using thermal sensitive microgels as the scaffold.

2. To achieve high-throughput production of spheroids by encapsulating cells in the microgel-based droplets for a controllable size.

3. To investigate the impact of the microenvironment on the spheroids formation by co-polymerizing NIPAM with different monomers to produce different surface charges, and degrees of hydrophobicity/hydrophilicity.

4. To explore the use of the thermally sensitive microgels to culture cardiac stem cell spheroids and the potential for treatment of myocardial infarction (MI) in the immune-competent mice.

1.3 The thesis outline

The thesis was prepared in a publication-based format. The thesis outline is summarized below:

Chapter 1 (Introduction) introduces the multicellular spheroids (MCSs) concept as a new advanced 3D tool for bio-applications, current research gaps on the MCSs formation approach, and the objectives and outline for this thesis.

Chapter 2 presents a comprehensive literature review on the recent development of MCSs for biomedical research. The detailed analyses of different approaches for fabricating MCSs are discussed.

In Chapter 3, we applied thermal sensitive microgels poly(N-Isopopylacrylami (NIPAM)-co-acrylic acid (AA)) (P(NIPAM-AA) as a 3D scaffold to culture HeLa cell spheroids. The tumour spheroids were analyzed via fluorescent and SEM images to display the spheroid morphology and structure, and the MTT assay was employed to investigate Hela cell proliferation in the microgel. The size distribution and morphology of spheroids were discussed in comparison with conventional suspension culture. In addition, a cellular automata (CA) model was developed to understand the mechanism of tumour spheroids formation within the scaffold.

In Chapter 4, to further produce Hela cell spheroids with a uniform size, water-in-oil (w/o) droplets were made by pumping the cell-laden P(NIPAM-AA) microgel solution in the central microfluidic channel and the continuous oil phase in the side channels. The droplets were heated to gel and then incubated in the culture medium to form HeLa spheroids. The Lattice Boltzmann immiscible two-phase model was used to simulate droplet formation. Optical and fluorescent images were used to examine HeLa spheroids formation evolution within the microgels-based droplets.

In Chapter 5, the impact of the microenvironment of HeLa cells on the spheroids formation was investigated. The microenvironment was created by copolymerizing different co-monomers with NIPAM to obtain thermally sensitive microgels with different surface charges and different degrees of hydrophobicity. The microgels were characterized using dynamic light scattering, titration, rheometer and SEM. The spheroids formation within different microgels were analyzed through optical and fluorescent images. Cell proliferation was evaluated by the MTT assay.

In Chapter 6, we further studied the impact of the microenvironment of human cardiac stem cells (hCSCs) on their spheroid formation, viability and biological functions. The microenvironment was tuned with the surface charge, chemical functional groups and hydrophobicity/hydrophilicity by co-polymerizing NIPAM with different co-monomers to synthesize thermo-sensitive microgels. The microgels were characterized by dynamic light scattering, Fourier transform infrared spectroscopy, rheometer and SEM. The spheroid morphology and cellular viability were characterized by fluorescent images. hCSCs proliferation within the microgels network was analyzed via the MTT assay. The biological functions of hCSCs in the microgel-based microenvironment were evaluated by *in-vitro* cytokine factor release. The conditional medium collected from the hCSC culture in the microgels was applied to culture myocytes. The best microgel, p(NIPAM-IA) was further injected into mice to evaluate its biocompatibility and therapeutic efficacy of treating MI.

Chapter 7 is the conclusion of this thesis where key outcomes are summarized and future development derived from this thesis is recommended.

1.4 **Key contributions of this thesis**

This thesis initiates the development of thermosensitive microgel based 3D culture to fabricate MCSs for different biomedical applications and to advance our understanding of the influence of the microenvironment on multicellular spheroids formation. The research outcomes have direct impact on the 3D scaffold cell cultures for drug screening and regeneration medicine. The following summaries key contributions of this thesis:

1. The development of thermo-responsive microgels as a novel scaffold to culture uniform-sized tumour spheroids for drug screening. This study demonstrated that the utilization of the microgels scaffold resulted in spherical cell clusters with a narrow size distribution that may be used for drug screening. The study also explored the mechanism of spheroids formation within the microgel scaffold.

2. The uniform-sized MCSs achieved by droplet-based 3D culture. This study first time showed the use of thermally sensitive microgels to encapsulate Hela cells into droplets for 3D culture via micro-channels. The size was controlled by the channel width with a narrow

size distribution. This approach allows long-term culture spheroids and minimal damage during the spheroid harvest process.

3. The microenvironment with moderate negative charges and hydrophilicity from the microgel promoting cell proliferation and spheroids formation. This result demonstrated that the surface characteristics of the microgels had a great impact on cell behaviors, such as cell attachment, migration, growth and spheroids formation.

4. The anionic and hydrophilic microenvironment stimulating cardiac stem cell spheroid formation and enhancing biological functions in comparison with a cationic and neutral microenvironment. The study demonstrated cardiac stem cells within the negative charged and hydrophilic microenvironment proliferated better and released more growth factor than cells in the positive charged, neutral charged and hydrophobic microenvironment. In addition, the anionic and hydrophilic microgel p(NIPAM-IA) did not elicit immune responses, which paves a way for the microgel to use as an injectable hydrogel to encapsulate and deliver stem cells for *in-vivo* studies. Furthermore, the p(NIPAM-IA) microgel helped MI repair after injection into the injured heart area in the immune-competent mice.

1.5 **Reference**

1. Nath, S. and G.R. Devi, Three-Dimensional Culture Systems in Cancer Research: Focus on Tumor Spheroid Model. Pharmacology & Therapeutics, 2016.

2. Ravi, M., et al., 3D cell culture systems: advantages and applications. J Cell Physiol, 2015. **230**(1): p. 16-26.

3. Landry, J., et al., Spheroidal aggregate culture of rat liver cells: histotypic reorganization, biomatrix deposition, and maintenance of functional activities. The Journal of cell biology, 1985. **101**(3): p. 914-923.

4. Yuhas, J.M., et al., A simplified method for production and growth of multicellular tumor spheroids. Cancer Research, 1977. **37**(10): p. 3639-3643.

5. Hamilton, G.A., C. Westmoreland, and E. George, Effects of medium composition on the morphology and function of rat hepatocytes cultured as spheroids and monolayers. In Vitro Cellular & Developmental Biology-Animal, 2001. **37**(10): p. 656-667.

6. Nyberg, S.L., et al., Rapid, large-scale formation of porcine hepatocyte spheroids in a novel spheroid reservoir bioartificial liver. Liver transplantation, 2005. **11**(8): p. 901-910.

7. Lazar, A., et al., Extended liver-specific functions of porcine hepatocyte spheroids entrapped in collagen gel. In Vitro Cellular & Developmental Biology-Animal, 1995. **31**(5): p. 340-346.

8. Wang, C., et al., Three-dimensional in vitro cancer models: a short review. Biofabrication, 2014. **6**(2): p. 022001.

9. Song, H., et al., Spatial composition of prostate cancer spheroids in mixed and static cultures. Tissue engineering, 2004. **10**(7-8): p. 1266-1276.

10. Lin, R.-Z., et al., Dynamic analysis of hepatoma spheroid formation: roles of E-cadherin and β1-integrin. Cell and Tissue Research, 2006. **324**(3): p. 411-422.

11. Kelm, J.M., et al., Method for generation of homogeneous multicellular tumor spheroids applicable to a wide variety of cell types. Biotechnol Bioeng, 2003. **83**(2): p. 173-80.

12. Kelm, J.M. and M. Fussenegger, Microscale tissue engineering using gravity-enforced cell assembly. Trends in biotechnology, 2004. **22**(4): p. 195-202.

13. Ingram, M., et al., Three-dimensional growth patterns of various human tumor cell lines in simulated microgravity of a NASA bioreactor. In Vitro Cellular & Developmental Biology-Animal, 1997. **33**(6): p. 459-466.

14. Khaoustov, V.I., et al., Induction of three-dimensional assembly of human liver cells by simulated microgravity. In Vitro Cellular & Developmental Biology-Animal, 1999. **35**(9): p. 501-509.

15. Gurski, L.A., et al., Hyaluronic acid-based hydrogels as 3D matrices for in vitro evaluation of chemotherapeutic drugs using poorly adherent prostate cancer cells. Biomaterials, 2009. **30**(30): p. 6076-6085.

16. Goodman, T.T., P.L. Olive, and S.H. Pun, Increased nanoparticle penetration in collagenase-treated multicellular spheroids. International journal of nanomedicine, 2007. **2**(2): p. 265.

17. Ananthanarayanan, B., Y. Kim, and S. Kumar, Elucidating the mechanobiology of malignant brain tumors using a brain matrix-mimetic hyaluronic acid hydrogel platform. Biomaterials, 2011. **32**(31): p. 7913-7923.

18. Chung, T.W., et al., Preparation of alginate/galactosylated chitosan scaffold for hepatocyte attachment. Biomaterials, 2002. **23**(14): p. 2827-2834.

19. Sonoda, T., et al., Expression of angiogenesis factors in monolayer culture, multicellular spheroid and in vivo transplanted tumor by human ovarian cancer cell lines. Cancer letters, 2003. **196**(2): p. 229-237.

20. Weigelt, B. and M.J. Bissell. Unraveling the microenvironmental influences on the normal mammary gland and breast cancer. in Seminars in cancer biology. 2008. Elsevier.

21. Langer, R. and D.A. Tirrell, Designing materials for biology and medicine. Nature, 2004. **428**(6982): p. 487-492.

22. Nyga, A., U. Cheema, and M. Loizidou, 3D tumour models: novel in vitro approaches to cancer studies. Journal of cell communication and signaling, 2011. **5**(3): p. 239-248.

23. Wenger, A., et al., Modulation of in vitro angiogenesis in a three-dimensional spheroidal coculture model for bone tissue engineering. Tissue engineering, 2004. **10**(9-10): p. 1536-1547.

24. Kang, S.-W. and Y.H. Bae, Cryopreservable and tumorigenic three-dimensional tumor culture in porous poly (lactic-co-glycolic acid) microsphere. Biomaterials, 2009. **30**(25): p. 4227-4232.

25. Shen, Z., et al., Exploring thermal reversible hydrogels for stem cell expansion in three-dimensions. Soft Matter, 2012. **8**(27): p. 7250-7257.

26. Shen, Z., et al., A thermally responsive cationic nanogel-based platform for three-dimensional cell culture and recovery. RSC Advances, 2014. **4**(55): p. 29146-29156.

CHAPTER TWO

2 .Literature Review

Chapter 2: Recent development for multicellular spheroids culture for bioapplications

X. Cui, Y. Hartanto, J. Bi, S. Dai and H. Zhang

School of Chemical Engineering, The University of Adelaide, SA 5005, Australia

Graphical Abstract

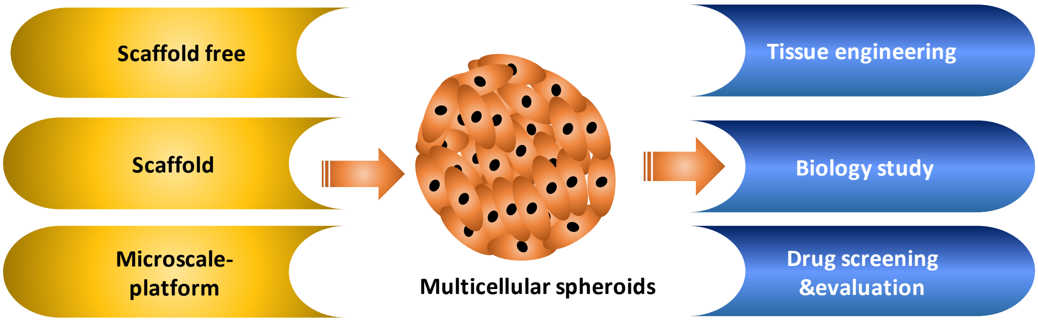

*Corresponding author

Email: hu.zhang@adelaide.edu.au

2.1 **Abstract**

Three dimensional multicellular spheroids have a complex architectural structure, dynamic cell-cell/cell-matrix interactions and bio-mimicking *in-vivo* microenvironment. As a fundamental building block for tissue reconstruction, multicellular spheroids have emerged as a powerful tool to narrow down the gap between the *in-vitro* and *in-vitro* model. In this review paper, we discussed the structure and biology of multicellular spheroids, and detailed fabricating methods. Among these methods, the approach in the microfluidics with the hydrogel support for MCSs formation is promising since it allows essential cell-cell/cell-matrix interactions in a confined space.

Key words: Multicellular spheroids, Tissue engineering, Three-dimensional culture, Microfluidics, Hydrogel.

2.2 Introduction

Traditionally cell culture on the two-dimensional (2D) tissue plastics has been employed for studying cell biology, disease models and drug screening with the assumption that monolayer cells reflect the physiology of real tissues. However, in such a 2D platform, cells are typically exposed to a rigid solid surface on the basal side and to a liquid at the apical surface. Inhabiting such a 2D rigid substrate requires cytoskeletal adjustments by the surviving cells because they lack exposure to the extracellular matrix (ECM) that is unique to each cell type, which may produce counterfeit polarity and cause abnormal cell metabolism and protein expression [1]. Furthermore, 2D systems cannot provide a complex and dynamic microenvironment for cells, and thus lead to spurious findings to some extent by forcing cells to adjust to an artificial and rigid surface. Studies have shown that 2D cell culture cannot replicate real microenvironment and cell behaviours *in vivo* because of lack of cell-cell and cell-matrix interactions and loss of tissue-specific architecture, mechanical and chemical cues, which are essential for unique functions of real tissues in the human body. For instance, a decrease in β1-integrin hindered multicellular spheroid (MCS) formation of PC3 prostate adenocarcinoma cells, while the decrease was not found in the 2D culture[2]. Therefore, a new platform for *in-vitro* cell culture has been pursued and 3D cell culture has been demonstrated to recreate the *in-vivo* microenvironment and physiological relevance[3].

A number of 3D culture models have been explored. 3D multicellular spheroid (MCS) is an excellent *in-vitro* 3D model, mimicking the *in-vivo* processes, such as embryogenesis, morphogenesis, and organogenesis [4]. Multicellular spheroids are cell aggregates that have complex cell-to-cell adhesion and cell-to-matrix interaction, which result in gradient generation for nutrients, gases, growth factors and signal factors. This structure recapitulates the microenvironment of cells that has been observed in the real tissues.

MCSs were first fabricated by Moscona and Moscona through self-assembling of cell suspensions and they found out these tissue-like aggregates were able to restore characteristics in the original tissue [5]. Since then, methods have been developed to form MCSs. Furthermore, a range of cells have been explored to form MCSs, including cancer cells [6], mesenchymal stem cells, and human pluripotent stem cells [7]. MCSs exhibit similar features in the *in-vivo* physiological conditions [8], for example, cardiomyocyte spheroids beat with heart-like rhythms [9], hepatocyte spheroids perform liver-like functions

[9], and human endothelial cells vascularize fibroblast microtissues [10]. Therefore, MCSs are considered as a bridge to bring in vitro and in vivo together, and they are becoming an emerging biomedical tool in many areas.

This paper give a comprehensive review on MCSs from its biology to its applications as well as the method of MCSs fabrication. Special foci are devoted to recent progress in MCSs in the last five years. It covers the progress in the understanding of MCSs and fabrication approaches which are missing from other review articles.

2.3 **Formation Mechanism and Structure of Multicellular Spheroids**

MCS formation may be due to cell adhesion and/or cell differentiation. It has been reported MCSs formation involves three critical steps[11]: (1) Dispersed cells initially are drawn closer to form loose aggregates due to their long-chain ECM fibres with multiple RGD motifs that can bind tightly to the integrin on the cell membrane surface. Direct cell-cell contact due to initial aggregation results in upregulated cadherin expression; (2) Cadherin is accumulated at the membrane surface; (3) Cells are compacted into solid aggregates to form MCSs due to the homophilic cadherin-cadherin binding [12] (Fig. 2-1). The ECM fibres and cadherin type and concentration may vary for different type of cells [13-15]. For example, E-cadherin is responsible for tight packing of MCF7, BT-474, T-47D and MDA-MB-361 cells[14]. It was reported that β-catenin sequestrated by E-cadherin can initiate transcriptional activation of proteins such as cyclin D1 and c-Myc, which control the G1 to S phase transition in the cell cycle to help cell proliferation which also result in cell differentiation within MCSs [16]. Meanwhile N-cadherin medicates the spontaneous formation of spheroids in MDA-MB-435S [14]. MDA-MB-231 and SK-BR-3 cells form a spheroid structure due to collagen I/integrin β interaction without cadherin involvement [17].

Intercellular adhesion proteins such as connexion and pannexins that influence cell-cell contacts contribute to the formation of MCSs. As a class of gap junction proteins [18], pannexins were introduced into the C6 glioma cells in order to accelerate the MCS formation process and obtain a more mature F-actin cytoskeleton. The result showed pannexin 1 as the conduits for ATP release initiated a signalling that dramatically accelerated the assembly of large MCSs [19].

The cytoskeleton also plays an important role in MCS formation. The actin filaments undergo significant changes during MCS formation. The expanded microfilaments as stress fibres become localized along the cell periphery. The cytoskeleton as a force generation structure performs as a continuous pre-stressed lattice that keeps cellular structural stability. Morphogenetic phenomena promote the emergence of ordered structures, result in the MCSs formation[20].

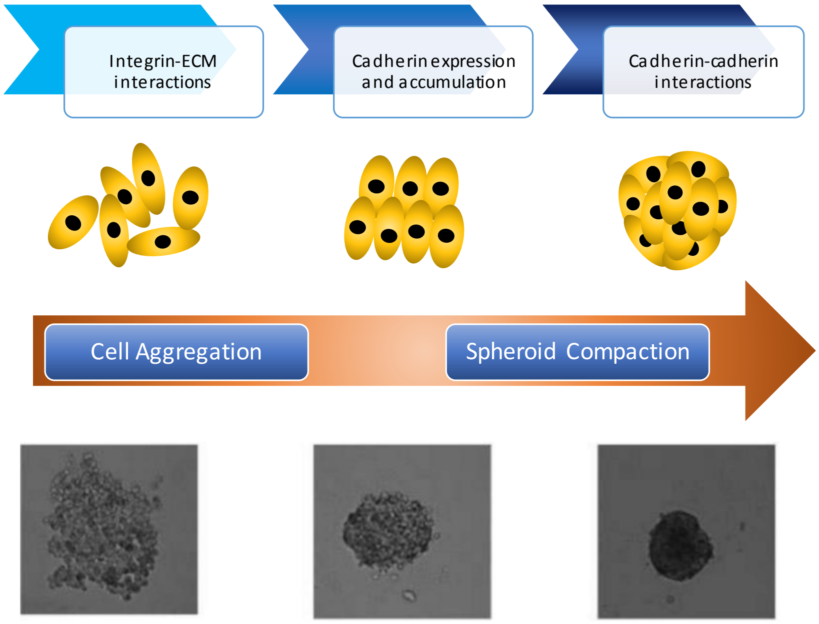

Figure 2-1 Multicellular spheroids formation process. Cells establish loose bonds through integrin-ECM. A delay stage is followed for cadherin expression and accumulation on the extracellular surface. A compact MCS form due to homophilic cadherin-cadherin interactions. The optical spheroid images are extracted from Lin's work[12].

Tumor MCSs *in-vivo* have two major components: one is proliferating neoplastic parenchymal cells, and the other is supportive stroma, constituting half mass of most malignant tumours and including fibroblasts, dendritic cells, lymphocytes, blood vessels, macrophages as well as other myeloid cells [21].The parenchymal cells determine growth and differentiation of tumour spheroids, while stroma contributes to tumor progression. Normal stroma delays or prevents MCS formation but the abnormal one promotes tumourgenesis [22]. Hence, stroma plays a crucial role in the MCS morphology and the evolution of tumour spheroids. Additional stroma elements promotes tumour spread and invasion [23] and stroma composition or structure may be altered when the function of vascular cells or fibroblasts changes, or the influx of inflammatory cells increases [24]. The interaction between endothelial and tumour cells in fabricated MCSs offers information on blood capillaries in tumours.

In-vitro MCSs have been fabricated with different structures. The most common one is a three-layered structure with cells in asynchronous proliferative, quiescent and necrotic states respectively (Fig. 2-2). The proliferative rim contains cells with intact nuclei and abundant microvilli and these cells are active in proliferation and metabolism. Cells with shrunk nuclei and sunken-in membranes are distributed in the quiescent stage and these cells have minimum metabolic activities but become active after exposure to nutrients. Cells in the necrotic core have disintegrated nuclei and membranes and they lose their activities because of starvation of nutrients and accumulation of toxic wastes. The layer thickness is dependent on the size of the spheroids. The diffusion limitation of most small molecules like oxygen in MCSs is around 150-200 µm, which is similar to that in the avascular tissue and tumour mass in vivo. Beyond the diffusive limit, metabolic wastes are accumulated in the inner layer of MCSs [25-27], leading to a necrotic core. Proton magnetic resonance with pH-sensitive indicators [27] as well as microelectrodes [26, 28] have been used to study the transportation of nutrients, wastes and oxygen transportation and confirm the concentration gradients inside the MCS.

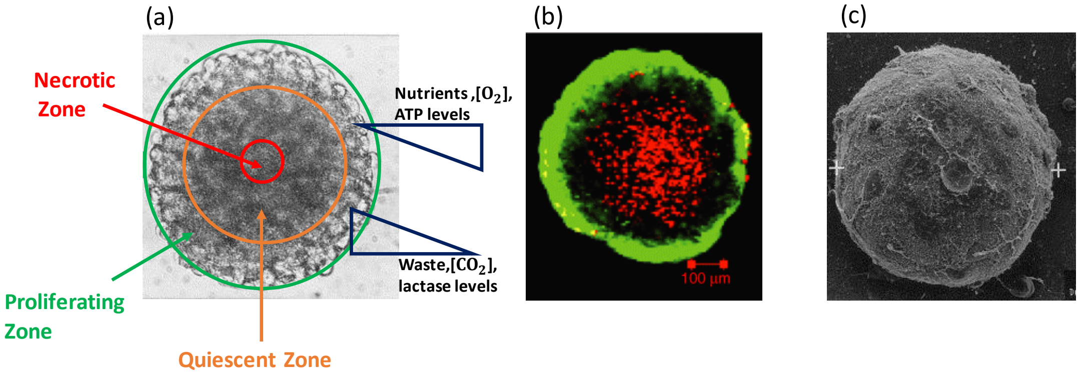

Figure 2-2 Microenvironment and structure of a MCS. (a) MCS has a spherical geometry with different regions occupied by proliferating, quiescent and dead cells respetcily. Different mass transport rates for nutrient, O_2, ATP, waste, CO_2 and lactase are presented in the multilayer structure.[29] (b) The Live/Dead image indicates the morphology of a MCS, green representing live/proliferating cells(proliferating zone), while red representing dead cells(quiescent and necrotic zone)[30]. (c) The scanning electron image of a human epithelial carcinoma A431 MCS grown for 3 days[29]. The smooth profile shows the final stage of spheroids formation. Cadherin-cadherin interactions lead to the deposition of ECM. As a result the compact, a smooth profile of spheroid can be observed without distinguishable individual cell morphology.

A vascular lumen-like hollow structure has also been observed for endothelial MCSs due to the apoptosis caused by central cell polarization [31]. A unique phenotype of MCSs formed when Bovine aortic EC(BAEC)cells grew within a matrix that was full of basal membrane constituents. A polarized epithelium was established in the outermost layer with an apical surface pointing inside and a lumen was formed due to gradual loss of cells in the sphere interior. The spheroid structure obtained from human mammary epithelia cells [32, 33] have been used for studying apoptosis and tissue morphogenesis. This model is also employed for investigating the oncogenic pathway to affect cellular cycles and biochemical pathways to transmit signals from the cell-matrix contact in order to increase the cell survival rate.

Heterotypic cell-to-cell interactions play an important role in maintaining the hierarchy architecture and physiological functions of tissues and heterotypic MCSs are generated for mimicking the architecture and functions of real tissues. The heterotypic MCSs have been generated from co-culturing fibroblasts (parenchymal hepatocytes with human drmal fibroblasts, rat hepatocytes with NIH/3T3 fibroblasts) [34, 35], pancreatic islet cells with hepatocytes [36], or bone marrow stoma cells with hepatocytes [37]. Different architectures for normal and malignant breast epithelial cells have been fabricated to simulate the tumour micro-environment [38]. Co-culture of tumor cells with endothelial cells allows building small capillaries within the MCS structure to avoid a necrotic or quiescent core in the center. Transportation of nutrients and oxygen from the outer layer to the center by the endothelial cells is realized, which mimics the transportation in the *in-vivo* tumours. MCSs were co-cultured with macrophages or lymphokine-actived killer cells in order to measure the cytotoxic and cytostatic activity and examine the immigration of the immune cells [39]. It was found that lactic acid generated from MCSs disturbed the migration of monocytes into MCSs, working as a potent immune suppressor for monocytes/dendritic in the tumour milieu. Tumor cell invasion and metastasis have been also investigated through interactions between tumour cells and fibroblasts [40, 41]. Furthermore Epithelia cells in a heterotypic spheroid has been used to investigate cell-cell interaction between epithelia cells and different type of cells [42]. A spheroid formed by co-culturing mesenchymal stem cells and primary liver cells behaved like hepatocyte cells, and it was explored for the heterotypic cell co-culture for cell proliferation and differentiation with the potential for regeneration medicine since the co-culture system was more efficient in inducing differentiation of mesenchymal stem cells into hepatocyte-like cells [43].

The microenvironment of MCSs is crucial for cell behaviors and functions. The MSCs model has been used to investigate the impact of the architectural, physical and physiological microenvironment on the tumorigenic phenotypes. Intracellular gene expression is influenced by altering the chemical composition of the extracellular microenvironment [22]. Abnormal cell behaviors such as tumour progression are caused by inappropriate cell-microenvironment interactions [44]. Martin et al. [45] reported that cells performed normal emryogenesis if they were located in the uterus, while they were differentiated into malignant tissue cells when they were co-cultured with ectopic embryonic cells. Oral squamous cell carcinoma (OSCC) cells had similar behaviors in the synthetic poly lactide-co-glycide (PLG) scaffold *in vitro* and *in-vivo* condition compared to 2D culture as evidenced by an increase in secretion of vascular endothelial growth factor (VEGF), interleukin 8 (IL-8). An overall increase in the VEGF and FGF expression were able to mimic that in the in vivo tumours. The results also highlight that some factors were found in the 3D culture but not in the 2D culture, such as IL-8. Through analysis of the cumulative percentage of these factors, IL-8, instead of VEGF, were proven to play the most important role in angiogenesis, while the role of IL-8 was unable to examined in the 2D study [46].

2.4 **The application of MCSs**

Multicellular spheroids can replicate structure and functional properties of real tissues. Thus MCSs are important for biomedical research in many different aspects [47] (Fig. 2-3). The MCS model has been used for examining genes for cell apoptosis, migration, and invasion through specific blocking antibodies, short-interference RNA and signalling inhibitors [47], such as caspase [48], intereukin-6 [49], urokinase-type plasminogen activator (uPa) and its receptor [50], as well as E-cadherin [51].

Cells in a complex spheroid structure are surrounded by various other cells as well as a wall structured matrix [52] and the spheroid structure can mimic a natural cellular niche. Therefore, MCSs are considered an important tool to study tissue-based mechanistic assays, cell to cell contacts as well as cell-matrix interactions [53]. Tumor MCSs have been widely used for metastasis and invasion research on tumour progression as well as drugs screening. Primary or progenitor cells MCSs show improved viability and functional performance compared with monolayer cells, which can be beneficial for some applications such as implantation [47].

MCSs show different expressions in intercellular and extracellular adhesion, immune response and tissue development compared with the monolayer culture [52]. Normally, drug evaluation in 2D reveals limited and misleading information on the drug efficacy and functions. The MCSs on the other hand provide a more complex structure that narrows down the gap between *in-vitro* 2D culture and the animal models for drug screening and evaluation [52]. MCSs recreate the mass transport resistance for active pharmaceutical ingredients (API) which is widely seen in the in vivo models [3]. Spheroids exhibit gradients in oxygen, metabolic wastes and nutrients [47]. The combination of the pathophysiological gradients and cell-cell/cell-matrix interactions induce specific RNA and protein expression in spheroids, which has impact on the drug treatment on cancer spheroids [3]. As a result, MCSs have been proposed as a great model for drug discovery, development and evaluation.

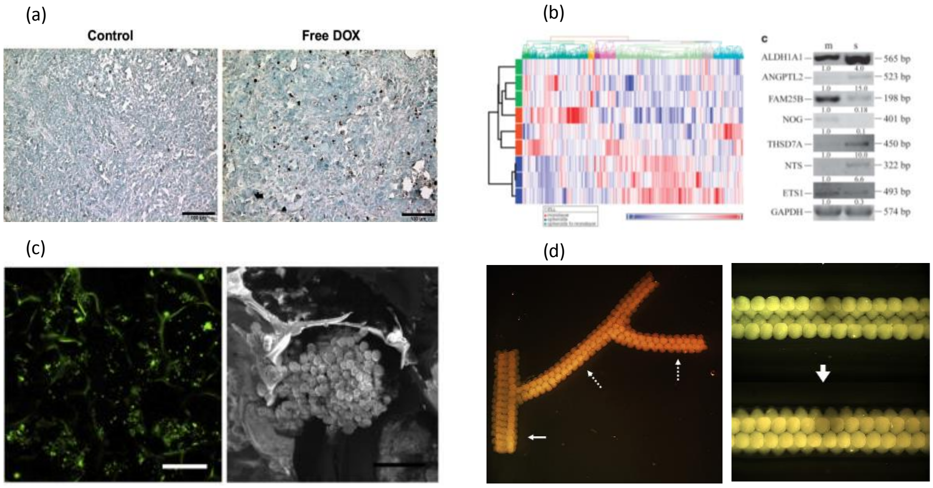

Figure 2-3 MCSs for bio-applications. (a) Drug delivery in MCSs to discover Dox efficacy [54]. (b) Gene express in MCSs [55]. (c) Cell-matrix interactions in a poly(l-glutamic acid)/chitosan scaffold [56]. (d) Tissue engineering, by using MCSs to build a vascular tissue via bioprinting [57].

Niemalanandhan et al. [58] has compared cellular responses to the drugs in regarding to drug potency and efficacy: Paclitaxel, KU174, Alimta, Zactima, and doxorubicine in a 3D MCS model and a 2D model based on H358 and A549 lung cancer cells. Paclitaxel and KU174 were less potent in 3D and the cytotoxicity of paclitaxel, KU174, Alimta, Zactima and Doxrubicin was significantly decrease in the 3D model. Another study demonstrated hepatocyte spheroids had higher sensitivity to drug hepatotoxicity than the 2D hepatocyte monolayer [59]. Shih-Feng et al. [60] employed HepG2 MCSs encapsulated in a gel to metabolize the pro-drug EFC (7- ethoxy-4-trifluromethyl) for optimising the pharmacokinetic responses from the *in-vitro* model and the study showed HepG2 MCSs were less affected by methotrexate compared with the 2D culture, which was confirmed by an increase in drug resistance to methotrexate in 3D cultured rat hepatocytes [61]. The efficacy of anticancer drugs (doxorubicin and paclitaxel) was significantly different in the 2D and the 3D human epithelial ovarian cancer (EOC) MCSs and HT1080 MCSs. [62, 63]. Cells in MCSs exhibit higher drug resistance to anticancer drugs, which results in a lower efficacy of drugs.

The MCS model has been used to study the signaling pathway and alternative survival mechanisms of tumours when exposing to cytotoxic drugs [64, 65]. Overexpression of epidermal growth factor receptor type 2(HER2) in breast cancers were found in the MCS model that can induce cell transformation. In the 3D model, HER2 homodimers accumulate at the membrane raft, which can improve inhibition of the cancer cells growth with trastuzumab (Herceptin) that targets HER2 as a monoclonal antibody. Because of resistance of tumours to the HER2 targeting drugs, current treatment is not effective. The MCS model that replicates the molecular mechanism in the *in-vivo* tumour is a useful tool of investigating drug resistance.

The MCS model is advantageous in studying long-term drug effect because of their low proliferation rate, while confluency of the 2D culture in a very short frame hampers its long-term study. Fong et al. [66] exposed 3D PCL engineered Ewing sarcoma tumor (EWS) cells to various concentrations of doxorubicin for different time frames. The antineoplastic responses of drugs at different exposure time were clarified and this will provide essential information for drug administration.

2.5 Scaffold Free MCS Formation

Many approaches have been developed to fabricate MCSs. Efficiency is one of the most important criteria for choosing an approach for MCS formation. The ability of producing uniform-sized MCSs is also crucial. Damages of MCSs and its impact on the physiology should also be considered.

Forced-floating or cell culture on a non-adhesive surface is one of the most common methods that have been widely used in the laboratory (Fig. 2-4a). Through coating cell culture surfaces to prevent cell attachment, cells are forced to float in the cell culture medium, and cell-cell contacts are established through connections between their ECM fibers or coalescence due to cell motion in the cell culture medium, which result in spheroid structure formation. The cell culture surface is often coated with agarose, or hydrophobic polymers. Ivascu et al. [17] coated a 96 well plate with 0.5 % poly-2-hydroxyethyl methacrylate(poly-HEMA), and the coated surface was dried for 3 days before seeding cells inside the wells. They succeeded in forming MCSs from breast cancer cell lines such as MCF7-ADR, T47D, and MCF7. 1 wt % agarose coating was used to culture HeLa MCSs, and the size of MCSs depended on the initial cell density in each well [67]. Poly-N-p-vinylbenzyl-D-lactonamide was coated on the cell culture surface. Several cell lines including 3T3 clone A31 and Type II lung alveolar cell were able to form MCSs [68]. In general, this approach is simple and reproducible. By adjusting the initial cell seeding density and the size of culture wells, the size of MCSs can be manipulated [69]. This approach allows high throughput production of MCSs and rapid evaluation of drug-MCS interactions, which makes this approach appealing for drug screening[17]. However, large variations in MCS size and shape as well as drug-MCS interactions prevent it from large scale and using for high-through drug screening.

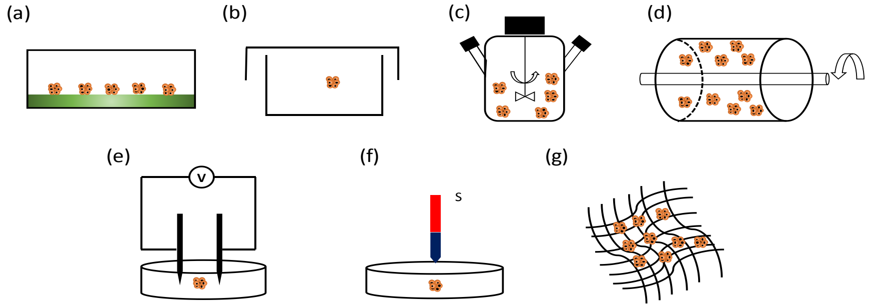

Figure 2-4 Methods for MCSs formation. (a) Forced floating; (b) Hanging drop; (c) Spinning flask; (d) Rotating vessel; (e) Electrical-force assisted; (f) Magnetic-force assisted; (g) Scaffold-based.

Another popular conventional approach is the hanging drop method (Fig. 2-4b). After cells are seeded in the cell culture medium in a microwell, the microwell is placed upside down to form cell suspension hanging drops. The drops maintain their shape due to the surface tension. Cells cluster at the tip of each drop because of the gravity. Oxygen and carbon dioxide diffused through the liquid-air interface and nutrients supplied from the cell culture medium inside each drop allow cells to proliferate and further compact into MCSs. Numerous cell lines have been reported to form MCSs. For instance, HepG2 liver cancer cells and MCF-7 breast cancer cells formed tightly packed MCSs and produced their own "tissue like" ECM [70]. Based on the hanging drop principle, a super hydrophobic chip was developed to fabricate MCSs [71]. The polystyrene and poly (lactic acid) super hydrophobic surface was produced through UV/ozone and plasma gas treatment. Cell suspension drops were distributed at the wettable region. Hanging drops were formed through inverting the chip. L929 and Sarcoma osteogenic cells (SaOs-2 cells) were demonstrated inside the drops on the chip to formed spheroids. The hanging drop approach has almost 100% reproducibility and produces relatively uniform-sized MCSs. However, the maximum volume of a drop is 50 μL and beyond the maximum volume the surface tension cannot maintain the drop shape [72]. Therefore, the size of MCSs is relatively small in such a small volume of drops. Another disadvantage of this approach is unable to change the culture medium without disturbing drops. Nevertheless, this approach has been adapted for commercialization. Two companies, 3D Biomatrix and InSphero, have fabricated 384-wells for hanging-drop production of MCSs [73].

Spinner flask (Fig. 2-4c) and rotational culture bioreactors (Fig. 2-4d) are also widely used for producing MCSs. The bioreactor allows scalable production, long-term culture, and controlled cell culture environment, making it popular in industry. Both bioreactors use continuous stirring or rotating to achieve good mixing for better cell growth, to increase the cell-cell interactions for promoting MCS formation, and to prevent cell attachment to walls [74]. However, the shear stress generated from fluid motion may have an impact on cellular physiology, which is one of the biggest drawbacks of this approach [47]. Rotating cell culture bioreactors developed by NASA is believed to perform better in reducing the impact on the cell physiology from the shear force than the spinner flask bioreactors. A lower speed is used at the single cell phase to maximally reduce the impact of shear force on cells. The rotation speed is increased once the cell aggregates appear and a high rotation speed allows squeezing cell aggregates into a compact MCS structure. The requirement of a large amount of cell culture medium also restrains the bioreactors as a mainstream method for MCS production. Normally spinner flasks need 10-15 times more medium than stationary methods such as forced-floating [75]. In addition, MCSs with a wide range of sizes are obtained from this approach, which need intensive downstream processing to screen the desirable size of MCSs for drug screening test. The combination of forced-floating cell culture and spinner flask bioreactors has been proposed to reduce the size variations [76]. Small MCSs were formed at 96 wells using the force-floated approach, which narrowed down the size of the MCSs. The resultant MCSs werethen transferred into a spinner flask for long-term culture with continuous supply of nutrients and oxygen [76]. Spheroids with relatively narrow size distribution were generated from this approach.

Cells can be brought together to form aggregates by external forces such as magnetic force [77, 78] (Fig. 2-4e) and electric force [79] (Fig. 2-4f). NIH/3T3 cells were mixed with magnetic nanoparticles (Fe_3O_4, an average size of 10 nm) and cultured for 24 hours to allow cellular uptake of the magnetic nanoparticles. By exposing to a magnet field, cells with magnetic particles self-assembled into MCSs due to the magnetic force [77] . The magnetic force-driven MCS formation in a hanging drop was demonstrated by using monosized magnetic microspheres-labelled human umbilical vein endothelial cells. In addition the MCSs can be transferred and patterned by manipulating the magnet field [80]. A high throughput MCS fabrication platform driven by magnetic force was developed by Kim et al. [81]. Bone marrow-derived human mesenchymal stem cells with magnetic nanoparticles (40-50 nm) were seeded in the 96 well plate. On the top of the wells was a magnetic pinpoint that drove cell-cell interactions to form MCSs. Dielectrophoresis is also applied for fast formation of MCSs. Jurkat cells were placed into a chamber, and an electrical field was exerted in the chamber[82, 83]. The electric force dragged cells together to generate the MCSs and the size of the MCSs increases with the upsurge of the applied voltage. The aggregate shape and size can be manipulated by adjusting the dielectrophoresis setup. This external force-driven approach allows fabrication of MCSs in a very short period time (less than 5 minutes) compared with days of culture by other methods. In addition, this approach holds the feature of high reproducibility and well-controlled MCS size and shape. Furthermore different types of cells can be manipulated by placing them into different magnetic fields to generate aligned structures such as core-shell or a random mixed structure. However, magnetic nanoparticles may have a negative impact on cell functions and MCS physiology. Without proper ECM and cadherin production, the structure may become loose once the external magnetic or electric field is removed. The produced MCSs may also not function properly.

2.6 Physical supported MCS Formation

Hydrogel networks as scaffolds provide bio-mimicking matricies to MCSs to induce cell-matrix interactions for fabrication of MCSs (Fig. 2-4g). The scaffold structure, morphology and component can be adjusted for tuning the microenvironment so that the cellular responses to the microenvironment can be monitored during the MCSs formation[84].

Table 2-1 Comparison of Approaches for Fabrication of MCSs

Fabrication Approaches	Advantages	Disadvantages
Forced-floating or Non- adhesive	• Inexpensive cost • Simple procedure • Easy accessibility • Reproducibility • Large-scale production	• Variations in MCS size and shape • Intensive labour requirement • Lack of cell-matrix interactions
Hanging Drops	• Uniform-sized MCSs • Easy operation • High reproducibility • Long-term culture • Controlled environment	• Intensive labour requirement • Small-sized MCSs • Incompetency for mass production • Short-term culture
Spinning or rotating bioreactors	• Simple culture method • Mass production • Long-term culture • Dynamic controlled environment • Excellent mixing for nutrient and oxygen delivery, and waste removal	• Variations in MCS size and shape • High shear force in the spinning bioreactor • Lack of cell-matrix interactions
Magnetic force-driven MCS formation	• Short time for MCS formation • Controllable MCS shapes • Easy to transport MCSs	• Toxic magnetic materials • Lack of cell-matrix interactions • Incompetency for mass production • Damage of cell morphologies due to extra forces
Electrical force-driven MCS Formation	• Rapid cell aggregation • Controllable MCS sizes and shapes • Applicability to a variety of cell types for forming MCSs • Co-culture of two or more different types of cells for MCS formation	• Loss of aggregate integrity after removal of the electrical field • Damage of cell morphologies due to extra forces • Lack of cell-matrix interactions

Natural polymer supports for MCS Formation	• Promotion in cell proliferation • High cell survival rate • Strong cell-matrix interactions • 3D extracellular supports for ECM synthesis and development • Biodegradability • Simple procedure	• Lack of design flexibility • Variations of polymer supports from batch to batch
Synthesized polymer supports for MCS formation	• Flexible polymer design to meet the requirements for MCS formation • Tuneable microenvironment from supports for MCS formation • Strong cell-matrix interactions • 3D extracellular supports for ECM synthesis and development	• Issues of biocompatibility and biodegradability
Micro-moulding	• Uniform-sized MCSs • Strong cell-matrix interactions • 3D extracellular supports for ECM synthesis and development	• Multiple-step operations for fabrication of MCSs • Challenging in recovery of MCSs • Incompetency for mass production • Special fabrication of micro-molding
Micro-well technology for MCS formation	• Uniform-sized MCSs • Controllable cell culture environment • High-throughput for mass production	• Lack of cell-matrix interactions • Sophisticated micro-fabrication technology for micro-wells • Expensive robot-assisted liquid handling system, otherwise intensive labour operations
Droplet encapsulation	• Controllable MCS sizes • High throughput for mass production • Strong cell-matrix interactions • 3D extracellular supports for ECM synthesis and development	• Special control of droplet generation • Incompetency in releasing embedded MCSs from the cross-linked droplets

2.6.1 Natural polymers

Natural scaffolds from natural hydrogels, such as collagen, matrigel, and chitosan, have been used to culture MCSs. Other natural polymers, such as agar for ovarian cancer cellular MCSs [1], fibrin [85] and silk fibroin protein [86] for B16-F1 cell and breast cancer cell line MDA-MB-231 cells respectively, have also been explored. Natural hydrogels are favorable for cell proliferation due to its enriched ECM proteins or mimicking ECM components. They are also highly biocompatible [87].

Collagen is a main structural protein in human tissues. Collagen is often used as an excellent matrix for cell attachment due to its integrin-binding sites [88]. The 3D porous structure of collagen hydrogels allows sufficient exchange of oxygen, wastes and nutrients inside the scaffold [89] for short-term or long-term MCS culture [90]. The biodegradability due to enzymatic reactions offers a simple method harvesting MCSs from the scaffold. Human embryonic stem cells (hESC) were introduced into the collagen scaffold, and after 5 days culture hESC were differentiated into hepatocytes. The hepatocytes formed MCSs which possessed all characteristics and functions of *in-vivo* human in hepatocytes [91]. Luminal cells were co-cultured with myoepithelial cells and fibroblasts in the collagen type I matrix, and after 7 day culture heterotypic MCSs were formed inside the matrix [92]. Fang et al [93]. crossed linked collagen with matrigel to create a hydrogel scaffold to culture human breast carcinoma cells (MDA-MA-231) and colorectal carcinoma cells (HCTT116) for forming MCSs. The new hydrogel had better biocompatibility and reproduced the *in-vivo* solid tumour microenvironment.

Hyaluronic acid (HA)-based hydrogels are also applied in MCS culture. Natural HA is found in the ECM of malignant tumours and it promotes cancer cell proliferation and spheroid formation [94] because the excellent viscoelasticity of the HA hydrogel is able to mimic the stiffness of the natural environment. Prostate cancer cells (LNCaP PCa) were seeded into the HA hydrogel system, and after 7 day culture MCSs were harvested with a size of 100 μm, and showed a significant upregulation of $VEGF_{165}$ and Interleukin 8 (IL-8) expression. LNCap had a lower proliferation rate in the HA scaffold than 2D culture, which was similar to the LNCaP growth *in-vivo*. Human glioblastoma U373-MG and U87-MG cells were found to form heterotypic MCSs after culturing them inside the HA scaffold for 24 hours [95]. MDA-MB-231 and MDA-MB-468 cells mixed with the HA hydrogel were injected into mice to mimic the *in-vivo* environment for tumour spheroid formation and HA were found to stimulate cell proliferation and reduce the variability in the tumour size. This hydrogel was also found to facilitate tumour-tissue integration. Necrosis inside the formed MCSs was reduced, and vascularization in the structure was improved [96].

Chitosan is the second most abundant material that can be produced from crustacean, mollusks, squid, and insects. The biodegradability by lysozyme on the β-1, 4 glyosidic linkages enables mature MCS release from the chitosan-based scaffold [97]. A porous chitosan scaffold was attempted to culture MCF-7 cells for producing MCSs and the scaffold with a high degree of deacetylation was found to improve cancer cells attachment and proliferation [98]. However, very low solubility of chitosan in water due to its strong hydrogen bonding hampers its wide applications in MCS formation. Chitosan co-polymers have been synthesized to improve the solubility. Chitosan-alginate was synthesized as a hydrogel scaffold for culturing prostate cancer cell MCSs [99]. This co-polymer was more biocompatible, biodegradable, and less immunogenic [100]. In addition its chemical structure is similar to glycosaminoglycans (GAGs), a vital part of MCS ECMs. Instead of a hydrogel scaffold, chitosan-alginate was also fabricated as a fibrous scaffold coated with collagen to culture MCF-7 cells. Its porous structure optimally replicated the *in-vivo* environment [101]. Small aggregates were observed after two days culture. The size of spheroids was up to more than 100 μm after six days. Cell growth within this scaffold presented a spatial growth pattern with an improved growth rate and drug-resistance. Apart from co-polymerization with nature polymers, chitosan is also combined with synthesized polymers for MCS formation. For instance, the poly(l-glutamic acid) (PLGA) and chitosan(CS) scaffold was developed to culture MCSs from adipose derived stem cells (ADSCs) for cartilage regeneration. This scaffold was repulsive to protein adsorption and facilitated ADSC MCSs formation by minimizing cell-matrix attachment to promote cell-cell contacts. The MCSs with size of 100 μm were observed after 2 day culture [56]. ADSCs spheroids grown in this scaffold improved chondrogenic differentiation and dramatically decreased the deposition of collagen type I.

Matrigel is derived from the basement membrane of Engelbreth-Holm-Swarm(EHS) mouse tumor cells. Some key components for cell growth and attachment such as collagen and laminin are found in matrigel[102]. As one of popular ECM protein enriched hydrogels, matrigel has been widely used for MCS formation from PC-3M, PrCa, and NCI-H600 cells [103]. The comparison of HepG2 MCS culture in collagen, gelatin and matrigel hydrogels revealed cells proliferated rapidly in matrigel, and MCSs with a large size were harvested from matrigel [104]. Moreover, a matrigel with lung cancer cell mixture injected into an animal model resulted in rapid formation of tumour MCS formation in animals compared with cell injections without matrigel. The similar results were also obtained from cancer cells of A253 and B16F10 [105]. However, 3D tumor models grown on the matrigel exhibited less similarity to the *in-vivo* tumor compared with 3D PLG engineered tumours because of a decreased level of IL-8 expression in the matrigel [46]. Therefore, it is important to choose appropriate 3D physical supports for fabricating MCSs.

The natural polymers share the structural or composition similarity with normal tissue ECM, have rich components, meet the amplified extracellular signalling needs, and support cell behaviours. The impediments for using natural polymers for MCSs are the accessibility of the materials for the tissues of interest, dreary methodology, and undesirable remnant proteins and confounding signalling proceeding [106]. In the case of multiple-component scaffolds, additional composition may be required for optimal support of cell growth.

2.6.2 Synthesized polymers

Synthesized polymers have better structural complexity and design flexibility that are tuned to mimic the *in-vivo* environment for MCS culture and formation. In contrast to natural polymers, synthesized polymers are able to be modified to have desired ECM characteristics for the cell type of interest to promote cell aggregation and maintain tissue functionality [107].

Poly(ethylene glycol) (PEG) is one of the most popular polymers for 3D cell culture due to its nontoxicity and non-immunogenicity. PEG is crosslinked via various means such as photo-polymerization and emulsion polymerization. PEG was crosslinked with other polymers such as poly(ethylene oxide) (PEO) to enhance polymer network performance for MCS fabrication. Through adjusting PEG amount in the co-polymer, PEG based hydrogels with different mechanical properties were used to culture Huh7.5 cells for formation of MCSs to explore the impact of microenvironmental stiffness on cell aggregations [11]. Larger spheroids formed within the hydrogel network with better compliance or lower stiffness. Furthermore, cell proliferation, albumin secretion and CY450 expression in spheroids were found to perform better within compliant hydrogels, which may be due to better diffusion of oxygen and nutrients within the more compliant matrix. PEG based hydrogels via two different polymerization approaches, chain addition methacrylate-based and step-growth thiolene polymerization, were used for submandibular glands (SMG) MCS growth and formation. Step-growth thiolene polymerization had better performance for cell viability, proliferation and cell aggregation due to the reduced membrane peroxidation and intracellular reactive oxygen species formation [108].

Poly (lactide-co-glycolide) (PLG) due to its biodegradability has been widely investigated for 3D cell culture. The key component of this synthesised polymer is extracted from natural metabolites and it has great biocompatibility. PLG has been used in different forms such as foams, fibres and sponges [109]. A porous PLG microsphere scaffold was developed to culture hepatocytes spheroids [110]. This approach accelerated MCS formation and the porous scaffold structure maximized cell attachment and transportation of nutrients, oxygen and wastes. MCF-7 and U87 cell lines were cultured in the PLG scaffold to form MCSs, and the PLG scaffold exhibited good performance in recreating the microenvironment for tumour engineering [111]. The tumour model obtained from the PLG scaffold possesses similar microenvironmental characteristics of *in-vivo* tumours. The expression of IL-8, an angiogenetic factor, was found to be upregulated in cells cultured in the PLG scaffold [107]. The angiogenic feature was mapped with that in the *in-vivo* tumours, and cells in this model were less sensitive to chemotherapy, which demonstrated the yielded tumours had the improved malignant potential. PLG was also mixed with hydroxyapatite (HA) to replicate a bone-like environment to culture breast cancer spheroids [112]. This scaffold promoted breast cancer cell proliferation and aggregation because HA encouraged the neoplastic and metastatic growth of breast carcinoma cells and promoted IL-8 secretions.

The poly(N-isopropylacrylamide) (PNIPAM) hydrogel is another popular polymer network due to its thermal-reversibility which allows to harvest MCSs without toxic or potent chemicals. Through co-polymerization with other monomers, the resultant copolymers can accommodate different types of cells, promote cell proliferation and aggregation, and maintain tissue functionality. This PNIPAM network was used for culture HepG2 MCSs and the particle size of microgels around 300 nm was found to have better cell proliferation and MCS formation [113]. The PNIPAM polymer was modified by acrylic acid (AA) for culturing HepG2 MCSs. PNIPAM-AA exhibited less shrinkage for long-term culture and maximally maintained the scaffold structure, and HepG2 cells proliferated best in the hydrogel with 1% AA[114]. PNIPAM-AA microgels was further galactosylated to culture HepG3 MCSs. The galactose ligands helped HepG3 MCSs in performing liver-specific functions [6]. PEG was also introduced to PNIPAM hydrogel for better cell attachment. Human pluripotent stem cells (hPSCs) were cultured in the hydrogels to form spheroids. hPSCs derived spheroids showed high proliferation, and maintained the pluripotency in the suboptimal culture condition and a high survival rate [7].

Others polymers have also been reported for MCS formation. Ploy(ε-carpolacton) (PCL) was used to culture TC-71 Ewing's sarcoma cells to form MCSs and the MCSs exhibited greater chemo-resistance and different gene expressions from the 2D culture [66]. MCSs from breast, prostate and Lewis lung cancer cells were successfully demonstrated in the poly(lactic-co-glycolic acid)(PLGA) scaffold [107].

Overall, synthesize polymers show great design flexibility through co-polymerizing with other functionalized monomers. The physical and chemical properties are tuned to mimic the microenvironment for MCS formation. In addition, different from natural polymers with variations from batch to batch, synthesized polymers have high reproducibility and improved handling characters. However, their toxicity and degradability are two major concerns for their applications in MCS formation.

2.7 **MCSs formation on the microfluidic platform**

The microenvironment that comprises complex chemical and mechanical cues is one of the most crucial factors for forming MCSs. Specific physicochemical properties, such as oxygen tension, temperature, pH, osmolality, and local concentration of soluble factors, can significantly influence cell-cell and cell-matrix interactions [115]. Conventional approaches for forming MCSs are less flexible in tuning the microenvironment and performing temporal and spatial stimuli on cells. Microfluidics, as an emerging tool to control the flow within micrometre-scale channels, is capable of manipulating the parameters dynamically and spatially, thus to create unique environments to meet the requirements for MCS formation. In addition, microfluidics can reduce the shear stress in order to minimize cell damage, and micrometre scale chambers inside the microfluidics can be manipulated to control the size of MCS [116]. Furthermore integration of analytical tools with microfluidics, such as Raman, fluorescence spectrometry, and UV-Vis spectrometry, enables rapid, *in-situ*, and dynamical analyses during the MCS formation process. During screening for optimized culture conditions for forming MCS from rare cells or primary cells in the microfluidics, consumption of chemical or biochemical reagents is reduced since the microfluidics often requires a very small amount of liquid [117].

Table 2-2 Typical Polymers used as matrix supports for MCS fabrication

Polymer type		Features for MSC formation	Cell type
Natural Polymers	Collagen	• Protein-based hydrogels for better cell attachment • Weak mechanical strength	Human embryonic stem cells, Hepatocytes[91], Luminal cells[92], MDA-MA-231, HCTT116[93]
	Hyaluronic acid (HA)-	• Excellent viscoelasticity • Cell proliferation promotion	LNCap[94], U373-MG, U87-MG[95], MDA-MB231, MDA-MB-468[96]
	Chitosan	• Carbohydrate structure similar to ECM component glycosaminoglycans for better cell attachment • Insoluble in aqueous solution at physiological conditions.	MCF-7[98], Adipose derived stem cells[56]
	Matrigel	• Rich in growth factor, signal factors for cell proliferation • Expensive • Batch to batch variations	PC-3M, PrCa, NCI-H600[103], HepG2[104],A235, B16F10[105]
	Agar	• Forces from gel formation may damage cells inside the agar. • Excellent mechanical properties	Human foreskin dermal fibroblasts [118], Cortical cell[119]
	Alginate	• Rapid formation of hydrogel scaffolds • Strong chemicals required for breaking the hydrogel network to harvest MCSs	Human fat–derived stromal vascular fraction cells[120], Human colon cancer cells (HCT116)[121]
	Fibrin	• Promoting cell attachment • High cell viability	Human mesenchymal stem cell[122], B16-F1 cell[123]
Synthesized polymers	PEG	• Good biocompatibility • Unable to release MCSs due to irreversible gelation	Huh7.5 cells[11], Submadibular glands[108]
	PLG/PLGA	• Biodegradable and Biocompatible	Hepatocytes[110], MCF-7, U87[46]
	P(NIPAM)	• Thermal reversible to release MSCs during harvest • Low viscoelasticity • Porous structure with great nutrient, oxygen and waste transport	HepG2[114], HeLa[124], Human pluripotent stem cells[7]
	Poly(ε-carpolacton)	• high porosity • a large surface area-to-volume ratio for cellular attachment • tunable fiber diameter • low cost • high reproducibility	TC-71 Ewing's sarcoma cells[66]

2.7.1 Micro moulding

The micro moulding method has been explored to generate MSCs by fabricating complex structures using lithography techniques [125] [126]. It has been documented that this micro moulding method can significantly reduce consumption of reagents, create desired concentration and gradient of growth/signal factors and nutrients, allow high-density culture at a high cell-to-fluid volume ratio, and decrease shear stress under the laminar condition in micro-scale structures. [127].

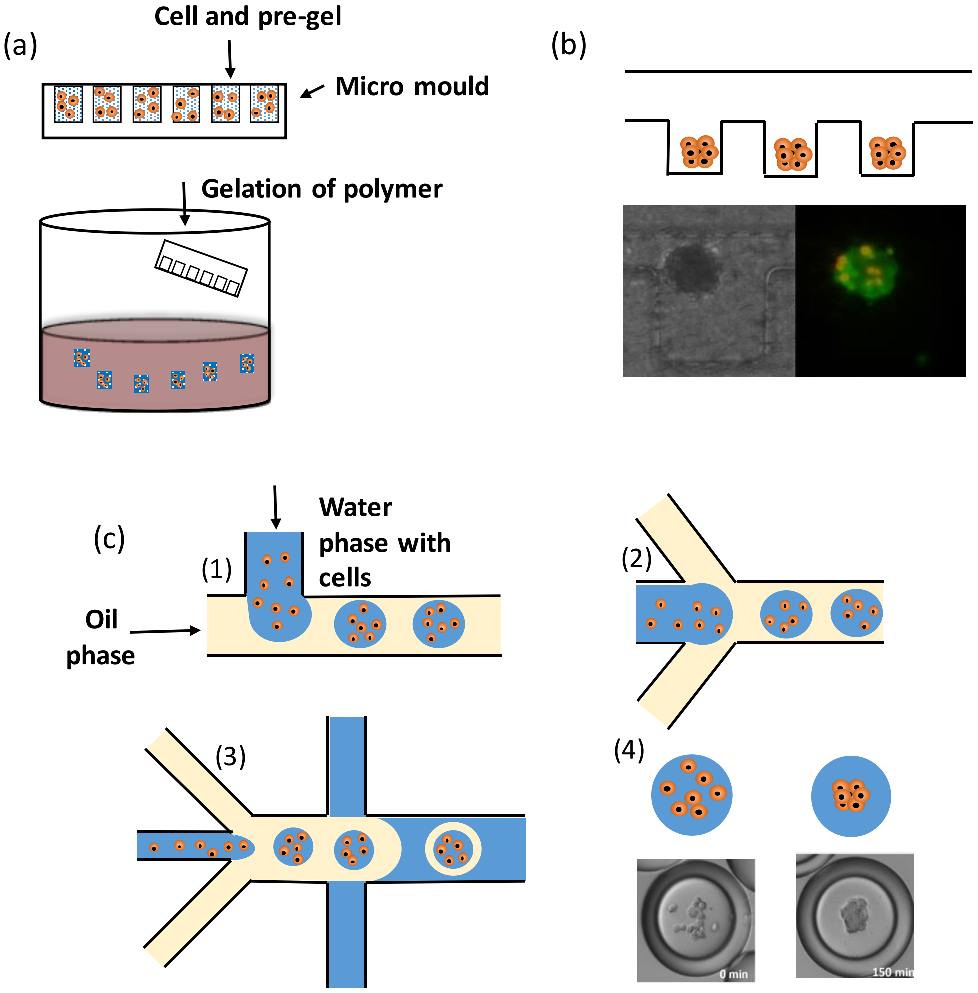

Figure 2-5 Microfluidic methods for MCSs fabrication. (a) MCSs formation in micro mould. (b) PC-3 prostate cancer MCSs formation in microwells [129]. (a) MCS formation in droplets generated from microfluidic channels: (1) T-junction cell encapsulation; (2) Flow-focusing cell encapsulation; (3) Double emulsion cell encapsulation; (4) human mesenchymal stem cells MCSs formation inside droplets[128].

Du et al. [130] proposed a method to fabricate different micro-scale structures with PEG-based cell laden hydrogels to form MCSs from NIH 3T3 mouse fibroblasts. The hydrophobic effects drove the “lock and key” assembly of microgels to form cross- or rod-shaped structures. 3D tissue constructs containing MCSs were generated from these structures. Micro-patterned methacrylated hyaluronic acid (HA) hydrogels were applied to fabricate similar MCSs from NIH 3T3 mouse fibroblasts [131] (Fig. 2-5a). A patterned PDMS stamp was used to hold the HA precursor solution mixed with cells and the photo-initiator. After exposure to UV light, the HA solution solidified and the PDMS mould was removed. The size and shape of MCSs were manipulated by the geometry of the PDMS mould. In addition, HA was bio-gradable by enzyme and MCSs were released from the block during the harvest process. The PDMS membrane templates to encapsulate cells for forming MCSs have been developed [132] [133]. Collagen hydrogel mixed with NIH 3T3 cells and collagen/matrigel mixture contained HepG2 were loaded into a mould from the PDMS membrane. After gelation, gel blocks were transferred into the culture medium for further forming MCSs. The MCS size was controlled by the size of the gel blocks.

A ‘bottom-up” fabrication approach was developed for macroscale 3D structures [134]. Collagen beads containing HepG2 cells were generated from an axisymmetric flow focusing device in a PDMS mould. The cell-laden beads were stacked to form a complex millimetre-thick tissue. After couple of hours, the beads contacted with each other and compacted into a designed shape. This approach can re-create the *in-vivo* tissue environment to mimic the *in-vivo* cell-matrix interactions.

Hardelauf et al. [135] designed an array of PDMS microwells to produce uniform tumour spheroids. Human colon carcinoma cells (HT29), BT474 breast carcinoma cells and NCI-H1792 lung carcinoma cells were pumped into the PDMS microwells and MCSs were observed after 3-4 days. The microwells were further modified to be concave in the bottom to culture hepatoshpere and hepG2 spheroids for drug screening [136]. Gong et al. [137] used the same concave microwell approach but replaced PDMS with agarose microplates to culture MCF-7 spheroids to test cancer drugs. Instead of a concave well at the bottom, side-chambers were designed was used to culture MCSs [129] (Fig. 2-5b). In this device two-layer PDMS microchannels were separated by a semi-permeable polycarbonate membrane. 28 dead-end side-chambers in the upper channel were designed to capture and stabilize PC-3 prostate cancer cells, meanwhile the lower channel allowed continuous medium flow for nutrient and waste diffusion. This design kept the spheroids stationary during media exchange and MCSs were monitored *in-situ* during long-term cultures. Beside concave microwells, other similar designs for MCS culture have been proposed. Jin et al. [138]

proposed a design to remove cell trapping barriers to facilitate MCS harvest. Cell suspension was supplied via the cell inlet port and distributed into four culture wells. Pressure from the membrane pressure port deformed the membrane at the bottom of the culture wells to form a horseshoe shape for trapping cells inside the wells. After spheroids formation, the membrane was deflated by reducing the pressure. Cell trapping barriers were removed and spheroids were harvested at the spheroid collection port. Kim et al. [139] developed a 3D tumour spheroid chip with balanced droplet dispensing . The hydraulic-head difference between the nutrient stream inlet and the waste outlet triggered the removal of waste droplets at the outlet. A fresh medium droplet was supplied by the dispensing layer due to the decreased pressure caused by volume expansion. This design allowed automatic supply of fresh medium and removal of waste droplets. Lee et al. [140] proposed an approach for *in-situ* multicellular spheroids formation and encapsulation. They used a PDMS mould to form uniform-sized HepG2 MCSs within the alginate hydrogel scaffold in the concave wells, and the nano-porous membrane to control the diffusion of crosslinker calcium ions for alginate gelation.

A portable bioreactor was developed to maintain a sterile microenvironment and sustain cell growth, maturation and organ formation [127]. MCF-AT1 cells were encapsulated into the matrigel that was placed at the bottom part of the PDMS bioreactor. Nutrients were perfused through the top section of the bioreactor. MCF-AT1 MCSs were harvested after couple of days. This bioreactor maintained cell viability during long-term culture, and also allowed visualization of the tumour spheroid formation progress through the transparent PDMS.

2.7.2 Micro-droplets based MCS formation

Uniform sized droplets generated from microfluidic devices provide a confined environment for cells and hydrogels inside the droplets offer a 3D physical support for formation of functional MCSs. Two configurations of microfluidic devices: flow focusing and T-junction are often employed to generate uniform-sized droplets. In the flow focusing device shown in Fig.2-5c, the aqueous phase with cells flows through the middle inlet as a dispersed fluid, and the immiscible organic solvent flows flow through both side inlets as a continuous fluid. The shear force from the continuous fluid squeezes the dispersed fluid to generate spherical individual droplets. On the other hand, in the T-junction device, the dispersed fluid penetrates into the continuous fluid to form droplets and the newly formed droplets are swept by the continuous fluid. The hydrogels inside the droplets are often gelled due to external stimuli, such as temperature, light or ions. Thermal responsive hydrogels, such as agarose, NIPAM based hydrogels or gelatin, solidify due to a temperature shift of the hydrogel system. Photoresistive hydrogels, such as poly(ethylene glycol)(PEG), form the physical gel by crosslinking triggered by exposure to UV light. Alginate is solidified by the introduction of divalent cations into the system (e.g. Ca^{2+}). Normally UV exposure or dramatic temperature change has negative impact on cell viability as wells as its physiology. Hence, the ion-based crosslinking gelation method is considered as a safer alternative for cell encapsulation.

This droplet-based method is rapid and has the capacity of high throughput. Velasco et al. [141] demonstrated that the approach based on cell-loaded hydrogel droplets significantly reduced the dependence on skilled labours requested in the conventional methods of fabricating MCSs. In the porous micro droplets, oxygen and nutrients were diffused in and metabolic wastes out to maximize the cell viability [142]. In addition when the formed MCSs encapsulated inside the hydrogel droplets were injected into the patients' body, they were protected from host immune responses, which minimizes administration of immunosuppressive drugs and increaseed the successful transplantation rate [143]. This approach also has a high degree of control over the morphological and physical properties [125].

Sakai et al. [144] used flow focusing microdevices to generate droplets for encapsulating HepG2 cells (Fig.2-5c1). Gelatin hydrogel with cells flew through from the top inlet, and paraffin oil flew through the left inlet. The hydrogel-containing droplets were heated to the melt point and the gelation was realized by cooling down to the gelation point when collecting the droplets. The size of the droplets from 300 μm to 100 μm was controlled by varying the paraffin flow rate. The HepG2 cells were cultured inside the droplets and they were aggregated to form MCSs in 24 hours. This approach generated a desired size of MCSs since the size of droplet was controllable. Yoon et al. [145] proposed a similar approach, but they used alginate instead of gelatin to minimize the damage in the gelation process on the cell viability. Magnetic iron oxide nanoparticles were uptaken with the spheroids to achieve easy collection and separation of the spheroids during the harvest process. Instead of using alginate or gelatin, a mixture of alginate and matrigel was introduced for MCS culture by Wang et al. [116]. This mixture gels performed better in the formation of HeLa spheroids compared with pure alginate beads. Tsuda et al. [146] used self-assembling peptides (SAP, Purmatrix RADA 16) to encapsulate bovine carotid artery endothelial cells [147, 148]. This synthetic peptide was functionalized with other monomers to enhance cell attachment, increase cell proliferation and promote cell differentiation. The peptide hydrogels inside the droplets were solidified by exposure to the crosslinking agent in the continuous phase. After culturing the cells inside the droplets for 3 days, endothelial cells inside droplets migrated to form loose aggregates due to initial cell-to-cell contacts, and then spheroids were formed in long-term culture. The PuraMatrix hydrogels were solidified in the presence of certain ions. This hydrogel was attempted to encapsulate HepG2 cells in a double T-junction and the gelation was achieved by crosslinking with the ions in the cell medium [149].

Chan et al. [150] developed a double emulsion system to fabricate MCSs from bone marrow derived human mesenchymal stem cells (hMSCs). The double emulsion was performed in two flow focusing devices (Fig. 2-5c3). The water/oil emulsion was generated in the first device, which had an inner core containing a mixture of the hMSCs and the culture medium and an out layer of oil. The water/oil droplets went through the second device to generate the water/oil/water emulsion. The middle oil layer served as a barrier to prevent the inner core from mixing with the culture medium at the outer layer. The selective permeability of the oil layer allowed nutrient diffusion from the outer aqueous phase into the inner core and waste removal in the opposite direction.

2.8 **P(NIPAM) for bioapplications**

2.8.1 Chemical and Physical Properties

Poly(N-isopropylacrylamide), ($H_2C{=}CHCONHCH(CH_3)_2$), as the most studied thermally responsive material, Poly(N-isopropylacrylamide) undergoes a sol-gel transition once it reaches its lower critical solution temperature (LCST) of 32ºC. The water molecules rearrange around the isopropyl group within the polymer over LCST, which results in an aqueous phase separation [151]. Thus, intra- and inter molecular hydrophobic interactions between the isopropyl groups are increasing which and ultimately it presents a gel state. Due to the existence of C=C double bond, NIPAM can be modified with other functional monomer with C=C double bond through co-polymerization. For instance, one of most common monomer incorporated to NIPAM is acrylic acid. C=C double bond from NIPAM and AA can be both broke during reaction resulting in –C-C-from NIPAM and AA and a new co-copolymer with a COOH functional group.

2.8.2 P(NIPAM) for bio applications

Due to its thermally responsive ability, P(NIPAM) has been widely used for different applications such as drug delivery, tissue engineering and so forth.

2.8.2.1 Drug delivery

Microgels of P(NIPAM) are tiny hydrogels whose size ranging is from tens of nanometers to several microns[152, 153]. PNIPAM microgels have the benefits of both hydrogels and nanoparticles. For example, same as hydrogels, P(NIPAM) microgels are hydrophilic, flexible, highly biocompatible. P(NIPAM) microgels also have long life span during circulation, and they can actively or passively target to desired location (such as tumour inner core) to achieve effective target delivery as nanoparticles [154]. In order to prevent the removal of colloidal drug carrier from the blood compartment, based on recognition by the reticuloendothelial [155], the size of nanoparticle drug carriers cannot be over be below 200 nm to increase their blood circulation time, which can be easily achieved for the PNIPAM microgels. The PNIPAM microgels have been employed to tested anticancer drugs for controlled release [156, 157]. Due to their small size (below 200 nm), P(NIPAM) microgels can be optimally delivered into tumour. Through physical methods or chemical bonding, the drug can be incorporated with microgels. The controlled release mechanism is based on biological stimuli such as a shift in pH/temperature or reactions interactions with enzymes, ions, or proteins. And via modifying with different surface functional groups, microgels can conjugate with target biophase to achieve target drug delivery[158, 159].

2.8.2.2 Biosensor

Due to their limited size distribution, flexibility of surface functional group as well as large surface area, PNIPAM microgel particles were considered as one of best candidates for biosensing. For example, Ali et al[160] successfully manipulate DNA on a PNIPAM microgel surface. Via EDC chemistry, a 50 -amine modified DNA oligonucleotide (DNA1) was onto the microgel surface. Then due to the existence of T4 DNA ligase and a template oligonucleotide, the coupled DNA1 was coupled with a second DNA oligonucleotide (DNA2). Rolling circle amplification (RCA) was employed to amplify signal. Finally, in order to detect signal, a fluorescent DNA probe was incorporated. Paper strips fixed with DNA oligonucleotide modified microgels were further developed, which can be employed to detect DNA through perform ligation/RCA-mediated amplification [161]. These DNA sensors have great ability to identify a biological sources, such as a specific pathogens.

2.8.2.3 Tissue engineering

The porous structure of P(NIPAM) hydrogels not only allows sufficient mass transportation (oxygen, nutrient and waste) which is beneficial for cells growth, but also provides necessary physical support for cells. In addition, the high biocompatibility of P(NIPAM) makes it a popular material for tissue engineering.

A poly(N-isopropylacrylamide-co-propylacrylic acid-co-butyl acrylate) hydrogel was developed by Garbern and co-workers which was used in the ischemic tissue[162]. This hydrogel was used as a topical controlled release tool for bFGF that can promote the revascularisation of ischemic myocardium. The result indicates that P(NIPAAm-co-PAA-co-BA) is able to provide spatio-temporal control of bFGF delivery. After 28-day post treatment, microvessel density was increase, regional blood flow was improved and cardiovascular function was recovered.

Through coupling P(NIPAM)-COOH with aminated hyaluronic acid via amide bond pair, a series of thermosensitive copolymer hydrogels, HA-g-PNIPAMaminated hyaluronic acid-g-poly(N-isopropylacrylamide) (HA-PNIPAM), were synthesized [163]. Human adipose-derived stem cells was encapsulated within the hydrogel. The result indicates that the gel system can increase cell survival rate and kept human adipose-derived stem cells spherical morphology. In order to investigate *in-vivo* biocompatibity, hydrogels were injected into the dorsal subcutaneous region of athymic nude mice for 5 days. The retention of the hydrogel in the tissue was high. Also no excessive infection was observed in the skin and subcutaneous tissues, which showed the potential of the AHA-g-PNIPAAm copolymer as an injectable hydrogel for adipose tissue engineering.

Fibroblasts and PNIPAM-gelatin mixture in DMEM was injected into the subcutaneous tissue of Wistar rats. White, opaque gel and cell mixture was formed immediately [164]. The shape of fibroblasts was spherical inside gel matrix and cells were homogeneously distributed. After two days' post-injection, fibroblasts had spread and grew. Therefore, PNIPAM-gelatin can be served as an injectable, in situ-formed scaffold on and in which fibroblasts can grow, spread and proliferate. In addition, PNIPAM-gelatin was high biocompatible without any further inflammatory reactions with great biodegradability.

2.9 Discussion and the future

With the advancement in MCSs culture, the *in-vitro* model is able to mimic the *in-vivo* animal in many aspects. The MCSs complex structure allows a better understanding of cell-

cell interactions. In addition, recapitulation of the *in-vivo* microenvironment by MCSs enable fundamental research on cancers and tissue development and provides an opportunity for culturing functional tissues *in-vitro*. However, many challenges for current fabricating methods. Firstly, a high initial cell density is required to form spheroids and cells in the MCSs structure are not required for further expansion while *in-vivo* tumour spheroids form from a relatively low cell density and the size of the tumour spheroids increases due to cell expansion inside the structure. Secondly, the reproductive and quality assurance of conventional means are low. Thirdly, the microenvironment and marcoenvironment for MCSs formation from current methods are still different from *in-vivo*, which results in different cellular behaviors. For instance, cell migration from MCSs is not realized from current methods. There is a gap to produce functional tissues cell through the multicellular *in-vitro* culture due to heterogeneous cell-cell interactions, cell and ECM organization and cell signaling pathway within the tissue. Hence, the correlation between real tissue and MCSs should be thoroughly documented through gene expression profiling analysis. Moreover, cells behaviors may alter to the microenvironment/marcoenvironment and cells are adapted to different type of MCSs formation in real tissue, which are still missing in the *in-vitro* MCSs model. Furthermore, the heterogeneous metabolism and gene expression in MCSs can be influenced by the MCSs size. Thus, uniform size in the approximate range of MCSs should be determined for different applications.

The method for fabrication of MCSs *in-vitro* has been developed significantly in the past decade. The integration of microfluidics with scaffolds can be considered as a new promising approach since it can not only produce controlled uniform-sized MCSs but also restore the complex cell-matrix/cell-cell interaction which are vital for MCSs morphology and functionality. The physical matrix support provided by the scaffold can facilitate in MCSs developing their extracellular matrices that are crucial for cell functions. Scaffold from the microfluidics allows fabrication of MCSs in a confined space to develop controllable uniform-sized MCSs. This approach is also able to tune the microenvironment for MCSs formation and growth to mimic the *in-vivo* conditions. In addition, the potential of commercialization makes the approach even more attractive. More elegant designs for microfluidics and scaffold approaches for MCSs formation are needed to create physiological relevant microenvironment and marcoenvironment to address the above challenges for MCSs formation.

2.10 Reference

1. Nath, S. and G.R. Devi, Three-Dimensional Culture Systems in Cancer Research: Focus on Tumor Spheroid Model. Pharmacology & Therapeutics, 2016.

2. Mahmood, T.A., et al., Adhesion-mediated signal transduction in human articular chondrocytes: the influence of biomaterial chemistry and tenascin-C. Experimental cell research, 2004. **301**(2): p. 179-188.

3. Mehta, G., et al., Opportunities and challenges for use of tumor spheroids as models to test drug delivery and efficacy. J Control Release, 2012. **164**(2): p. 192-204.

4. Achilli, T.-M., J. Meyer, and J.R. Morgan, Advances in the formation, use and understanding of multi-cellular spheroids. Expert opinion on biological therapy, 2012. **12**(10): p. 1347-1360.

5. Moscona, A. and H. Moscona, The dissociation and aggregation of cells from organ rudiments of the early chick embryo. Journal of Anatomy, 1952. **86**(Pt 3): p. 287-301.

6. Wu, Y., et al., Galactosylated reversible hydrogels as scaffold for HepG2 spheroid generation. Acta Biomaterialia, 2014. **10**(5): p. 1965-1974.

7. Lei, Y. and D.V. Schaffer, A fully defined and scalable 3D culture system for human pluripotent stem cell expansion and differentiation, in Proceedings of the National Academy of Sciences. 2013. p. E5039-E5048.

8. Vinci, M., et al., Advances in establishment and analysis of three-dimensional tumor spheroid-based functional assays for target validation and drug evaluation. BMC Biology, 2012. **10**(1): p. 1-21.

9. Abu-Absi, S.F., et al., Structural Polarity and Functional Bile Canaliculi in Rat Hepatocyte Spheroids. Experimental Cell Research, 2002. **274**(1): p. 56-67.

10. Kelm, J.M., et al., Design of custom-shaped vascularized tissues using microtissue spheroids as minimal building units. Tissue engineering, 2006. **12**(8): p. 2151-2160.

11. Lee, B.H., et al., Modulation of Huh7.5 Spheroid Formation and Functionality Using Modified PEG-Based Hydrogels of Different Stiffness. PLoS ONE, 2015. **10**(2): p. e0118123.

12. Lin, R.-Z., et al., Dynamic analysis of hepatoma spheroid formation: roles of E-cadherin and β1-integrin. Cell and Tissue Research, 2006. **324**(3): p. 411-422.

13. Robinson, E.E., R.A. Foty, and S.A. Corbett, Fibronectin Matrix Assembly Regulates α5β1-mediated Cell Cohesion. Molecular Biology of the Cell, 2004. **15**(3): p. 973-981.

14. Ivascu, A. and M. Kubbies, Diversity of cell-mediated adhesions in breast cancer spheroids. Int J Oncol, 2007. **31**(6): p. 1403-13.

15. Shimazui, T., et al., Role of complex cadherins in cell-cell adhesion evaluated by spheroid formation in renal cell carcinoma cell lines. Oncol Rep, 2004. **11**(2): p. 357-60.

16. Cavallaro, U. and G. Christofori, Cell adhesion and signalling by cadherins and Ig-CAMs in cancer. Nat Rev Cancer, 2004. **4**(2): p. 118-132.

17. Ivascu, A. and M. Kubbies, Rapid generation of single-tumor spheroids for high-throughput cell function and toxicity analysis. Journal of biomolecular screening, 2006. **11**(8): p. 922-932.

18. Panchina, Y., et al., A ubiquitous family of putative gap junction molecules. Current Biology, 2000. **10**(13): p. R473-R474.

19. Bao, B.A., et al., Pannexin1 drives multicellular aggregate compaction via a signaling cascade that remodels the actin cytoskeleton. J Biol Chem, 2012. **287**(11): p. 8407-16.

20. Tzanakakis, E.S., L.K. Hansen, and W.-S. Hu, The role of actin filaments and microtubules in hepatocyte spheroid self-assembly. Cell motility and the cytoskeleton, 2001. **48**(3): p. 175-189.

21. Kimlin, L.C., G. Casagrande, and V.M. Virador, In vitro three-dimensional (3D) models in cancer research: An update. Molecular Carcinogenesis, 2013. **52**(3): p. 167-182.

22. Kim, J.B., R. Stein, and M.J. O'Hare, Three-dimensional in vitro tissue culture models of breast cancer-- a review. Breast Cancer Res Treat, 2004. **85**(3): p. 281-91.

23. Ronnov-Jessen, L., et al., The origin of the myofibroblasts in breast cancer. Recapitulation of tumor environment in culture unravels diversity and implicates converted fibroblasts and recruited smooth muscle cells. J Clin Invest, 1995. **95**(2): p. 859-73.

24. Chen, Y., et al., Wnt signaling is required for organization of the lens fiber cell cytoskeleton and development of lens three-dimensional architecture. Dev Biol, 2008. **324**(1): p. 161-76.

25. Curcio, E., et al., Mass transfer and metabolic reactions in hepatocyte spheroids cultured in rotating wall gas-permeable membrane system. Biomaterials, 2007. **28**(36): p. 5487-5497.

26. Mueller-Klieser, W., Method for the determination of oxygen consumption rates and diffusion coefficients in multicellular spheroids. Biophysical Journal, 1984. **46**(3): p. 343-348.

27. Alvarez-Pérez, J., P. Ballesteros, and S. Cerdán, Microscopic images of intraspheroidal pH by 1H magnetic resonance chemical shift imaging of pH sensitive indicators. Magnetic Resonance Materials in Physics, Biology and Medicine, 2005. **18**(6): p. 293-301.

28. Carlsson, J. and H. Acker, Relations between pH, oxygen partial pressure and growth in cultured cell spheroids. International journal of cancer, 1988. **42**(5): p. 715-720.

29. Santini, M.T., G. Rainaldi, and P.L. Indovina, Apoptosis, cell adhesion and the extracellular matrix in the three-dimensional growth of multicellular tumor spheroids. Critical Reviews in Oncology/Hematology, 2000. **36**(2–3): p. 75-87.

30. Han, M., et al., Enhanced Percolation and Gene Expression in Tumor Hypoxia by PEGylated Polyplex Micelles. Mol Ther, 2009. **17**(8): p. 1404-1410.

31. Korff, T. and H.G. Augustin, Integration of Endothelial Cells in Multicellular Spheroids Prevents Apoptosis and Induces Differentiation. The Journal of Cell Biology, 1998. **143**(5): p. 1341-1352.

32. Debnath, J., et al., The Role of Apoptosis in Creating and Maintaining Luminal Space within Normal and Oncogene-Expressing Mammary Acini. Cell 2002. **111**: p. 29-40.

33. Weaver, V., M., et al., β4 integrin-dependent formation of polarized three-dimensional architecture confers resistance to apoptosis in normal and malignant mammary epithelium. Cancer cell, 2002. **2**: p. 205-216.

34. Takezawa, T., et al., Morphological and immuno-cytochemical characterization of a hetero-spheroid composed of fibroblasts and hepatocytes. J Cell Sci, 1992. **101 (Pt 3)**: p. 495-501.

35. Lu, H.-F., et al., Three-dimensional co-culture of rat hepatocyte spheroids and NIH/3T3 fibroblasts enhances hepatocyte functional maintenance. Acta Biomaterialia, 2005. **1**(4): p. 399-410.

36. Lee, K.W., et al., Influence of pancreatic islets on spheroid formation and functions of hepatocytes in hepatocyte-pancreatic islet spheroid culture. Tissue Eng, 2004. **10**(7-8): p. 965-77.

37. Murakami, S., et al., Development of co-culture system of hepatocytes with bone marrow cells for expression and maintenance of hepatic functions. Int J Artif Organs, 2004. **27**(2): p. 118-26.

38. Lee, G.Y., et al., Three-dimensional culture models of normal and malignant breast epithelial cells. Nat Methods, 2007. **4**(4): p. 359-65.

39. Gottfried, E., et al., Brave Little World: Spheroids as an in vitro Model to Study Tumor-Immune-Cell Interactions. Cell Cycle, 2006. **5**(7): p. 691-695.

40. Seidl, P., et al., Three-dimensional fibroblast–tumor cell interaction causes downregulation of RACK1 mRNA expression in breast cancer cells in vitro. International Journal of Cancer, 2002. **102**(2): p. 129-136.

41. Kunz-Schughart, L.A., et al., A Heterologous 3-D Coculture Model of Breast Tumor Cells and Fibroblasts to Study Tumor-Associated Fibroblast Differentiation. Experimental Cell Research, 2001. **266**(1): p. 74-86.

42. Kim, J.B., Three-dimensional tissue culture models in cancer biology. Seminars in Cancer Biology, 2005. **15**(5): p. 365-377.

43. Qihao, Z., et al., Spheroid Formation and Differentiation into Hepatocyte-Like Cells of Rat Mesenchymal Stem Cell Induced by Co-Culture with Liver Cells. DNA and Cell Biology, 2007. **26**(7): p. 497-503.

44. Ronnov-Jessen, L., O.W. Petersen, and M.J. Bissell, Cellular changes involved in conversion of normal to malignant breast: importance of the stromal reaction. Physiological reviews, 1996. **76**(1): p. 69-125.

45. Martin, G.R., Teratocarcinomas and mammalian embryogenesis. Science, 1980. **209**(4458): p. 768-776.

46. Fischbach, C., et al., Engineering tumors with 3D scaffolds. Nature methods, 2007. **4**(10): p. 855-860.

47. Lin, R.Z. and H.Y. Chang, Recent advances in three-dimensional multicellular spheroid culture for biomedical research. Biotechnol J, 2008. **3**(9-10): p. 1172-84.

48. Gdynia, G., et al., Basal caspase activity promotes migration and invasiveness in glioblastoma cells. Mol Cancer Res, 2007. **5**(12): p. 1232-40.

49. Sansone, P., et al., IL-6 triggers malignant features in mammospheres from human ductal breast carcinoma and normal mammary gland. J Clin Invest, 2007. **117**(12): p. 3988-4002.

50. Gondi, C.S., et al., Intraperitoneal injection of a hairpin RNA-expressing plasmid targeting urokinase-type plasminogen activator (uPA) receptor and uPA retards angiogenesis and inhibits intracranial tumor growth in nude mice. Clin Cancer Res, 2007. **13**(14): p. 4051-60.

51. Haga, T., et al., Role of E-cadherin in the induction of apoptosis of HPV16-positive CaSki cervical cancer cells during multicellular tumor spheroid formation. Apoptosis, 2008. **13**(1): p. 97-108.

52. Ravi, M., et al., 3D cell culture systems: advantages and applications. J Cell Physiol, 2015. **230**(1): p. 16-26.

53. Fennema, E., et al., Spheroid culture as a tool for creating 3D complex tissues. Trends Biotechnol, 2013. **31**(2): p. 108-15.

54. Kim, T.-H., et al., The delivery of doxorubicin to 3-D multicellular spheroids and tumors in a murine xenograft model using tumor-penetrating triblock polymeric micelles. Biomaterials, 2010. **31**(28): p. 7386-7397.

55. Condello, S., et al., [beta]-Catenin-regulated ALDH1A1 is a target in ovarian cancer spheroids. Oncogene, 2015. **34**(18): p. 2297-2308.

56. Zhang, K., et al., In-situ birth of MSCs multicellular spheroids in poly(l-glutamic acid)/chitosan scaffold for hyaline-like cartilage regeneration. Biomaterials, 2015. **71**: p. 24-34.

57. Norotte, C., et al., Scaffold-free vascular tissue engineering using bioprinting. Biomaterials, 2009. **30**(30): p. 5910-5917.

58. Nirmalanandhan, V.S., et al., Activity of anticancer agents in a three-dimensional cell culture model. Assay Drug Dev Technol, 2010. **8**(5): p. 581-90.

59. Meng, Q., Three-dimensional culture of hepatocytes for prediction of drug-induced hepatotoxicity. Expert Opin Drug Metab Toxicol, 2010. **6**(6): p. 733-46.

60. Lan, S.F., B. Safiejko-Mroczka, and B. Starly, Long-term cultivation of HepG2 liver cells encapsulated in alginate hydrogels: a study of cell viability, morphology and drug metabolism. Toxicol In Vitro, 2010. **24**(4): p. 1314-23.

61. Yin, J., et al., Differential methotrexate hepatotoxicity on rat hepatocytes in 2-D monolayer culture and 3-D gel entrapment culture. Chem Biol Interact, 2009. **180**(3): p. 368-75.

62. Loessner, D., et al., Bioengineered 3D platform to explore cell-ECM interactions and drug resistance of epithelial ovarian cancer cells. Biomaterials, 2010. **31**(32): p. 8494-506.

63. Millerot-Serrurot, E., et al., 3D collagen type I matrix inhibits the antimigratory effect of doxorubicin. Cancer Cell International, 2010. **10**: p. 26.

64. Pickl, M. and C. Ries, Comparison of 3D and 2D tumor models reveals enhanced HER2 activation in 3D associated with an increased response to trastuzumab. Oncogene, 2009. **28**(3): p. 461-468.

65. Weigelt, B., et al., HER2 signaling pathway activation and response of breast cancer cells to HER2-targeting agents is dependent strongly on the 3D microenvironment. Breast cancer research and treatment, 2010. **122**(1): p. 35-43.

66. Fong, E.L.S., et al., Modeling Ewing sarcoma tumors in vitro with 3D scaffolds. Proceedings of the National Academy of Sciences, 2013. **110**(16): p. 6500-6505.

67. Ma, H.-l., et al., Multicellular tumor spheroids as an in vivo-like tumor model for three-dimensional imaging of chemotherapeutic and nano material cellular penetration. Molecular imaging, 2012. **11**(6): p. 487.

68. Yuhas, J.M., et al., A Simplified Method for Production and Growth of Multicellular Tumor Spheroids. Cancer Research, 1977. **37**(10): p. 3639-3643.

69. Breslin, S. and L. O'Driscoll, Three-dimensional cell culture: the missing link in drug discovery. Drug Discov Today, 2013. **18**(5-6): p. 240-9.

70. Kelm, J.M., et al., Method for generation of homogeneous multicellular tumor spheroids applicable to a wide variety of cell types. Biotechnol Bioeng, 2003. **83**(2): p. 173-80.

71. Oliveira, M.B., et al., Superhydrophobic Chips for Cell Spheroids High-Throughput Generation and Drug Screening. ACS Applied Materials & Interfaces, 2014. **6**(12): p. 9488-9495.

72. Kurosawa, H., Methods for inducing embryoid body formation: in vitro differentiation system of embryonic stem cells. Journal of bioscience and bioengineering, 2007. **103**(5): p. 389-398.

73. Tung, Y.-C., et al., High-throughput 3D spheroid culture and drug testing using a 384 hanging drop array. Analyst, 2011. **136**(3): p. 473-478.

74. Kim, J.B. Three-dimensional tissue culture models in cancer biology. in Seminars in cancer biology. 2005. Elsevier.

75. Rodday, B., et al., Semiautomatic growth analysis of multicellular tumor spheroids. Journal of Biomolecular screening, 2011. **16**(9): p. 1119-1124.

76. Hirschhaeuser, F., et al., Test system for trifunctional antibodies in 3D MCTS culture. Journal of biomolecular screening, 2009.

77. Ino, K., A. Ito, and H. Honda, Cell patterning using magnetite nanoparticles and magnetic force. Biotechnology and bioengineering, 2007. **97**(5): p. 1309-1317.

78. Bae, J.-E., et al., The effect of static magnetic fields on the aggregation and cytotoxicity of magnetic nanoparticles. Biomaterials, 2011. **32**(35): p. 9401-9414.

79. Ye, T., H. Li, and K.Y. Lam, Motion, deformation and aggregation of two cells in a microchannel by dielectrophoresis. ELECTROPHORESIS, 2011. **32**(22): p. 3147-3156.

80. Lin, R.-Z., et al., Magnetic Reconstruction of Three-Dimensional Tissues from Multicellular Spheroids. Tissue Engineering Part C: Methods, 2008. **14**(3): p. 197-205.

81. Kim, J.A., et al., High-throughput generation of spheroids using magnetic nanoparticles for three-dimensional cell culture. Biomaterials, 2013. **34**(34): p. 8555-8563.

82. Sebastian, A., A.-M. Buckle, and G.H. Markx, Formation of multilayer aggregates of mammalian cells by dielectrophoresis. Journal of Micromechanics and Microengineering, 2006. **16**(9): p. 1769.

83. Sebastian, A., A.M. Buckle, and G.H. Markx, Tissue engineering with electric fields: Immobilization of mammalian cells in multilayer aggregates using dielectrophoresis. Biotechnology and bioengineering, 2007. **98**(3): p. 694-700.

84. Ruedinger, F., et al., Hydrogels for 3D mammalian cell culture: a starting guide for laboratory practice. Applied microbiology and biotechnology, 2015. **99**(2): p. 623-636.

85. Liu, J., et al., Soft fibrin gels promote selection and growth of tumourigenic cells. Nature materials, 2012. **11**(8): p. 734-741.

86. Talukdar, S. and S.C. Kundu, A Non-Mulberry Silk Fibroin Protein Based 3D In Vitro Tumor Model for Evaluation of Anticancer Drug Activity. Advanced Functional Materials, 2012. **22**(22): p. 4778-4788.

87. Nyga, A., U. Cheema, and M. Loizidou, 3D tumour models: novel in vitro approaches to cancer studies. Journal of cell communication and signaling, 2011. **5**(3): p. 239-248.

88. Walters, B.D. and J.P. Stegemann, Strategies for directing the structure and function of three-dimensional collagen biomaterials across length scales. Acta biomaterialia, 2014. **10**(4): p. 1488-1501.

89. Dagalakis, N., et al., Design of an artificial skin. Part III. Control of pore structure. Journal of biomedical materials research, 1980. **14**(4): p. 511-528.

90. Themistocleous, G., et al., Three-dimensional type I collagen cell culture systems for the study of bone pathophysiology. in vivo, 2004. **18**(6): p. 687-696.

91. Baharvand, H., et al., Differentiation of human embryonic stem cells into hepatocytes in 2D and 3D culture systems in vitro. International Journal of Developmental Biology, 2006. **50**(7): p. 645.

92. Holliday, D.L., et al., Novel multicellular organotypic models of normal and malignant breast: tools for dissecting the role of the microenvironment in breast cancer progression. Breast Cancer Research, 2009. **11**(1): p. 1-11.

93. Fang, J.Y., et al., Tumor bioengineering using a transglutaminase crosslinked hydrogel. PloS one, 2014. **9**(8): p. e105616.

94. Gurski, L.A., et al., Hyaluronic acid-based hydrogels as 3D matrices for in vitro evaluation of chemotherapeutic drugs using poorly adherent prostate cancer cells. Biomaterials, 2009. **30**(30): p. 6076-6085.

95. Ananthanarayanan, B., Y. Kim, and S. Kumar, Elucidating the mechanobiology of malignant brain tumors using a brain matrix-mimetic hyaluronic acid hydrogel platform. Biomaterials, 2011. **32**(31): p. 7913-7923.

96. Liu, Y., X.Z. Shu, and G.D. Prestwich, Tumor engineering: orthotopic cancer models in mice using cell-loaded, injectable, cross-linked hyaluronan-derived hydrogels. Tissue engineering, 2007. **13**(5): p. 1091-1101.

97. Xu, F. and K.J. Burg, Three-dimensional polymeric systems for cancer cell studies. Cytotechnology, 2007. **54**(3): p. 135-143.

98. Burdett, E., et al., Engineering Tumors: A Tissue Engineering Perspective in Cancer Biology. Tissue Engineering Part B: Reviews, 2010. **16**(3): p. 351-359.

99. Wang, K., et al., 3D Porous Chitosan–Alginate Scaffolds as an In Vitro Model for Evaluating Nanoparticle-Mediated Tumor Targeting and Gene Delivery to Prostate Cancer. Biomacromolecules, 2015. **16**(10): p. 3362-3372.

100. Muzzarelli, R.A., Chitosan composites with inorganics, morphogenetic proteins and stem cells, for bone regeneration. Carbohydrate Polymers, 2011. **83**(4): p. 1433-1445.

101. Wang, J.-Z., et al., Developing multi-cellular tumor spheroid model (MCTS) in the chitosan/collagen/alginate (CCA) fibrous scaffold for anticancer drug screening. Materials Science and Engineering: C, 2016. **62**: p. 215-225.

102. Caliari, S.R. and J.A. Burdick, A practical guide to hydrogels for cell culture. Nature methods, 2016. **13**(5): p. 405-414.

103. Härmä, V., et al., A Comprehensive Panel of Three-Dimensional Models for Studies of Prostate Cancer Growth, Invasion and Drug Responses. PLoS ONE, 2010. **5**(5): p. e10431.

104. Dubiak-Szepietowska, M., et al., Development of complex-shaped liver multicellular spheroids as a human-based model for nanoparticle toxicity assessment in vitro. Toxicology and Applied Pharmacology, 2016. **294**: p. 78-85.

105. Asghar, W., et al., Engineering cancer microenvironments for in vitro 3-D tumor models. Materials Today, 2015. **18**(10): p. 539-553.

106. Rijal, G. and W. Li, 3D scaffolds in breast cancer research. Biomaterials, 2016. **81**: p. 135-156.

107. Liu, Z. and G. Vunjak-Novakovic, Modeling tumor microenvironments using custom-designed biomaterial scaffolds. Current Opinion in Chemical Engineering, 2016. **11**: p. 94-105.

108. Shubin, A.D., et al., Development of Poly(Ethylene Glycol) Hydrogels for Salivary Gland Tissue Engineering Applications. Tissue Engineering Part A, 2015. **21**(11-12): p. 1733-1751.

109. Kasuya, J., et al., Reconstruction of 3D stacked hepatocyte tissues using degradable, microporous poly(d,l-lactide-co-glycolide) membranes. Biomaterials, 2012. **33**(9): p. 2693-2700.

110. Chou, M.-J., et al., Application of open porous poly(D,L-lactide-co-glycolide) microspheres and the strategy of hydrophobic seeding in hepatic tissue cultivation. Journal of Biomedical Materials Research Part A, 2013. **101**(10): p. 2862-2869.

111. Fischbach, C., et al., Engineering tumors with 3D scaffolds. Nat Meth, 2007. **4**(10): p. 855-860.

112. Pathi, S.P., et al., A novel 3-D mineralized tumor model to study breast cancer bone metastasis. PLoS One, 2010. **5**(1): p. e8849.

113. Gu, J., et al., Effect of particle size in a colloidal hydrogel scaffold for 3D cell culture. Colloids and Surfaces B: Biointerfaces, 2015. **136**: p. 1139-1147.

114. Wang, D., et al., Thermoreversible Hydrogel for In Situ Generation and Release of HepG2 Spheroids. Biomacromolecules, 2011. **12**(3): p. 578-584.

115. Gao, D., et al., Recent developments in microfluidic devices for in vitro cell culture for cell-biology research. TrAC Trends in Analytical Chemistry, 2012. **35**: p. 150-164.

116. Wang, Y. and J. Wang, Mixed hydrogel bead-based tumor spheroid formation and anticancer drug testing. Analyst, 2014. **139**(10): p. 2449-58.

117. Montanez-Sauri, S.I., D.J. Beebe, and K.E. Sung, Microscale screening systems for 3D cellular microenvironments: platforms, advances, and challenges. Cell Mol Life Sci, 2015. **72**(2): p. 237-49.

118. Salmenperä, P., et al., Fibroblast spheroids as a model to study sustained fibroblast quiescence and their crosstalk with tumor cells. Experimental Cell Research, 2016. **345**(1): p. 17-24.

119. Dingle, Y.-T.L., et al., Three-Dimensional Neural Spheroid Culture: An In Vitro Model for Cortical Studies. Tissue Engineering Part C: Methods, 2015. **21**(12): p. 1274-1283.

120. Williams, S.K., et al., Encapsulation of Adipose Stromal Vascular Fraction Cells in Alginate Hydrogel Spheroids Using a Direct-Write Three-Dimensional Printing System. BioResearch Open Access, 2013. **2**(6): p. 448-454.

121. Shakibaei, M., et al., Curcumin potentiates antitumor activity of 5-fluorouracil in a 3D alginate tumor microenvironment of colorectal cancer. BMC Cancer, 2015. **15**(1): p. 1-15.

122. Murphy, K.C., S.Y. Fang, and J.K. Leach, Human mesenchymal stem cell spheroids in fibrin hydrogels exhibit improved cell survival and potential for bone healing. Cell and Tissue Research, 2014. **357**(1): p. 91-99.

123. Liu, J., et al., Soft fibrin gels promote selection and growth of tumorigenic cells. Nat Mater, 2012. **11**(8): p. 734-741.

124. Cui, X., et al., A mechanistic study on tumour spheroid formation in thermosensitive hydrogels: experiments and mathematical modelling. RSC Advances, 2016. **6**(77): p. 73282-73291.

125. Kang, A., et al., Cell encapsulation via microtechnologies. Biomaterials, 2014. **35**(9): p. 2651-63.

126. Kwapiszewska, K., et al., A microfluidic-based platform for tumour spheroid culture, monitoring and drug screening. Lab Chip, 2014. **14**(12): p. 2096-104.

127. Markov, D.A., et al., Thick-tissue bioreactor as a platform for long-term organotypic culture and drug delivery. Lab Chip, 2012. **12**(21): p. 4560-8.

128. Chan, H.F., et al., Rapid formation of multicellular spheroids in double-emulsion droplets with controllable microenvironment. Scientific reports, 2013. **3**.

129. Hsiao, A.Y., et al., Microfluidic system for formation of PC-3 prostate cancer co-culture spheroids. Biomaterials, 2009. **30**(16): p. 3020-3027.

130. Du, Y., et al., Directed assembly of cell-laden microgels for fabrication of 3D tissue constructs. Proc Natl Acad Sci U S A, 2008. **105**(28): p. 9522-7.

131. Khademhosseini, A., et al., Micromolding of photocrosslinkable hyaluronic acid for cell encapsulation and entrapment. J Biomed Mater Res A, 2006. **79**(3): p. 522-32.

132. McGuigan, A.P., et al., Cell encapsulation in sub-mm sized gel modules using replica molding. PLoS One, 2008. **3**(5): p. e2258.

133. Bruzewicz, D.A., A.P. McGuigan, and G.M. Whitesides, Fabrication of a modular tissue construct in a microfluidic chip. Lab Chip, 2008. **8**(5): p. 663-71.

134. Matsunaga, Y.T., Y. Morimoto, and S. Takeuchi, Molding cell beads for rapid construction of macroscopic 3D tissue architecture. Adv Mater, 2011. **23**(12): p. H90-4.

135. Hardelauf, H., et al., Microarrays for the scalable production of metabolically relevant tumour spheroids: a tool for modulating chemosensitivity traits. Lab Chip, 2011. **11**(3): p. 419-28.

136. Wong, S.F., et al., Concave microwell based size-controllable hepatosphere as a three-dimensional liver tissue model. Biomaterials, 2011. **32**(32): p. 8087-96.

137. Gong, X., et al., Generation of Multicellular Tumor Spheroids with Microwell-Based Agarose Scaffolds for Drug Testing. PLoS One, 2015. **10**(6): p. e0130348.

138. Jin, H.J., et al., A multicellular spheroid formation and extraction chip using removable cell trapping barriers. Lab Chip, 2011. **11**(1): p. 115-9.

139. Kim, T., I. Doh, and Y.-H. Cho, A 3D tumor spheroid chip with the pharmacokinetic drug elimination model developed by balanced droplet dispensing. Sensors and Actuators B: Chemical, 2012. **174**: p. 436-440.

140. Lee, K.H., et al., Diffusion-mediated in situ alginate encapsulation of cell spheroids using microscale concave well and nanoporous membrane. Lab Chip, 2011. **11**(6): p. 1168-73.

141. Velasco, D., E. Tumarkin, and E. Kumacheva, Microfluidic encapsulation of cells in polymer microgels. Small, 2012. **8**(11): p. 1633-42.

142. Serra, M., et al., Microencapsulation technology: a powerful tool for integrating expansion and cryopreservation of human embryonic stem cells. PLoS One, 2011. **6**(8): p. e23212.

143. Zhang, W., et al., A Novel Core-Shell Microcapsule for Encapsulation and 3D Culture of Embryonic Stem Cells. J Mater Chem B Mater Biol Med, 2013. **2013**(7): p. 1002-1009.

144. Sakai, S., et al., Cell-enclosing gelatin-based microcapsule production for tissue engineering using a microfluidic flow-focusing system. Biomicrofluidics, 2011. **5**(1): p. 13402.

145. Yoon, S., et al., Droplet-based microfluidic system to form and separate multicellular spheroids using magnetic nanoparticles. Lab Chip, 2013. **13**(8): p. 1522-8.

146. Tsuda, Y., Y. Morimoto, and S. Takeuchi, Monodisperse cell-encapsulating peptide microgel beads for 3D cell culture. Langmuir, 2010. **26**(4): p. 2645-9.

147. Morimoto, Y., et al., Monodisperse semi-permeable microcapsules for continuous observation of cells. Lab Chip, 2009. **9**(15): p. 2217-23.

148. Morimoto, Y., W.H. Tan, and S. Takeuchi, Three-dimensional axisymmetric flow-focusing device using stereolithography. Biomed Microdevices, 2009. **11**(2): p. 369-77.

149. Um, E., et al., Continuous generation of hydrogel beads and encapsulation of biological materials using a microfluidic droplet-merging channel. Microfluidics and Nanofluidics, 2008. **5**(4): p. 541-549.

150. Chan, H.F., et al., Rapid formation of multicellular spheroids in double-emulsion droplets with controllable microenvironment. Sci Rep, 2013. **3**: p. 3462.

151. Kaneko, Y., et al., Rapid Deswelling Response of Poly(N-isopropylacrylamide) Hydrogels by the Formation of Water Release Channels Using Poly(ethylene oxide) Graft Chains. Macromolecules, 1998. 31(18): p. 6099-6105.

152. Saunders, B.R. and B. Vincent, Microgel particles as model colloids: theory, properties and applications. Advances in colloid and interface science, 1999. 80(1): p. 1-25.

153. Karg, M. and T. Hellweg, New "smart" poly (NIPAM) microgels and nanoparticle microgel hybrids: properties and advances in characterisation. Current Opinion in Colloid & Interface Science, 2009. 14(6): p. 438-450.

154. Guan, Y. and Y. Zhang, PNIPAM microgels for biomedical applications: from dispersed particles to 3D assemblies. Soft Matter, 2011. 7(14): p. 6375-6384.

155. Alexis, F., et al., Factors affecting the clearance and biodistribution of polymeric nanoparticles. Molecular pharmaceutics, 2008. 5(4): p. 505-515.

156. Das, M., et al., Biofunctionalized pH-Responsive Microgels for Cancer Cell Targeting: Rational Design. Advanced Materials, 2006. 18(1): p. 80-83.

157. Zhang, J., Z. Qian, and Y. Gu, In vivo anti-tumor efficacy of docetaxel-loaded thermally responsive nanohydrogel. Nanotechnology, 2009. 20(32): p. 325102.

158. Blackburn, W.H., et al., Peptide-Functionalized Nanogels for Targeted siRNA Delivery. Bioconjugate Chemistry, 2009. 20(5): p. 960-968.

159. Hoare, T.R. and D.S. Kohane, Hydrogels in drug delivery: progress and challenges. Polymer, 2008. 49(8): p. 1993-2007.

160. Ali, M.M., et al., Enzymatic manipulations of DNA oligonucleotides on microgel: towards development of DNA-microgel bioassays. Chemical Communications, 2007(43): p. 4459-4461.

161. Ali, M.M., et al., Detection of DNA using bioactive paper strips. Chemical Communications, 2009(43): p. 6640-6642.

162. Garbern, J.C., et al., Delivery of basic fibroblast growth factor with a pH-responsive, injectable hydrogel to improve angiogenesis in infarcted myocardium. Biomaterials, 2011. 32(9): p. 2407-2416.

163. Tan, H., et al., Thermosensitive injectable hyaluronic acid hydrogel for adipose tissue engineering. Biomaterials, 2009. 30(36): p. 6844-6853.

164. Ohya, S., Y. Nakayama, and T. Matsuda, In vivo evaluation of poly(N-isopropylacrylamide) (PNIPAM)-grafted gelatin as an in situ-formable scaffold. J Artif Organs, 2004. 7(4): p. 181-6.

CHAPTER THREE

3 .A Mechanistic Study on Tumour Spheroids Formation in Thermosensitive Hydrogels: Experiments and Mathematical Modelling

Chapter 3: A Mechanistic study on tumour spheroids formation in thermosensitive hydrogels: experiments and mathematical modelling

X Cui[a], S Dini[b], S Dai[a], J Bi[a], B J Binder[b], J E F Green[b] and H Zhang[a]

a. School of Chemical Engineering, The University of Adelaide, SA 5005, Australia

b. School of Mathematical Sciences, The University of Adelaide, Adelaide, SA 5005, Australia

Graphical Abstract

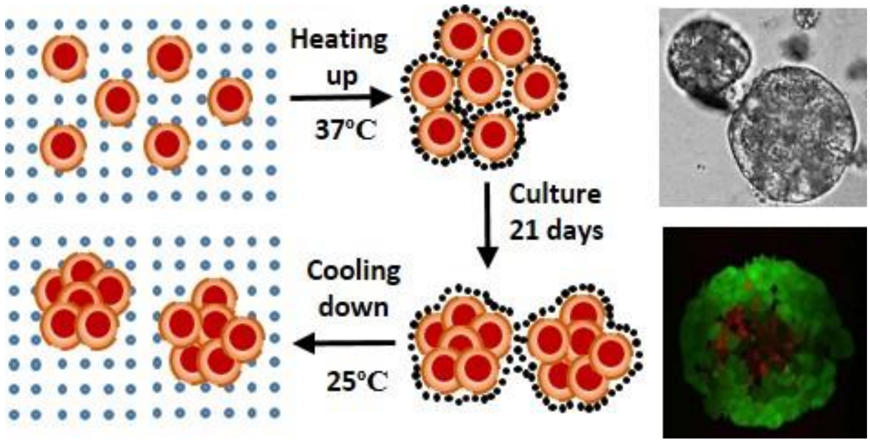

*Corresponding author

Email: hu.zhang@adelaide.edu.au

Published: RSC Advances, 2016, 6, 73282-73291 DOI: 10.1039/C6RA11699J

3.1 **Abstract**

A tumour is a complex, growing tissue with a dynamic microenvironment. Its shape and size affect mass transport and thus the ability of drugs to penetrate into the tumour. Three-dimensional (3D) tumour spheroid culture has thus been recognised as an advanced tool for anti-cancer drug screening. However, the use of tumour spheroids has been hampered by the large variation in the spheroid size distribution, their irregular shape and the labour-intensive culture process. We explore thermosensitive hydrogels, pNIPAM-AA, for culturing tumor spheroids and compare our approach with a traditional suspension culture method (non-adhesive surface) in terms of cell proliferation, tumour spheroid size distribution and spheroid morphology. Spheroids cultured in the microgel network show a narrower size distribution and a more spherical shape. We hypothesised that these observations could be explained by that cells are homogeneously retained inside the hydrogels, cell aggregate formation is much slower due to network resistance and the cell death rate is smaller in comparison with suspension culture. We developed a cellular automata (CA) model to validate these hypotheses. Spheroid formation with different parameter values representing culture in suspension and in microgels is simulated. Our results are consistent with the hypothesis that microgel culture produces a more uniform size distribution of spheroids as a result of reduced cell death and the gel network resistance.

Key words: Biomaterial, Thermal sensitive microgels, Tumour spheroids, Cellular automata

3.2 **Introduction**

Cancer is a leading cause for human death. 7.9 million people died of the disease in 2007 and the number is estimated to reach 12 million per year by 2030 [1]. This has motivated intense research efforts to develop new drugs over several decades [2]. As part of these efforts, two dimensional cancer cell culture has been widely used to screen cancer therapeutic drugs. However, these culture methods have limitations when it comes to replicating the cell-cell and cell-extracellular matrix (ECM) interactions which are important regulators of cell behaviour in physiological tissues. Three-dimensional (3D) cell culture methods which mimic, to some extent, the complex spatial and temporal structure of tissues observed in *in-vivo* models, are increasingly being used to help us understand cancer biology and screen potential treatments. In addition, the *in-vitro* 3D culture system can restore functional, environmental, and histomorphological features of human tissues [3].

Numerous 3D culture models currently exist for cancer-related research, such as liquid overlay based culture on non-adhesive surfaces [4-6], suspension culture in mechanically stirred spinner flasks [7-9], and hanging drops [10-14]. However, these conventional means either have a high labour cost or limited capacity for generating large-scale uniform-sized tumour spheroids. The National Aeronautics and Space Administration developed a rotary cell culture system that can achieve a large scalable production of tumour spheroids. However the micro-environment experienced by cells during spheroid formation is very different to that *in-vivo* [15, 16], as without the physical resistance given by ECM, multicellular spheroids grow as individual cell agglomerates and do not interact with their extracellular milieu. Naturally derived hydrogels [17-19] have been employed as scaffolds in tissue engineering to mimic the *in-vivo* microenvironments due to their rich networks of ECM proteins and cellular support matrices [20-22]. Cells grown in hydrogels not only interact with each other but also exhibit matrix attachment. The scaffold provides physical and structural support for the formation of tumour spheroids [23]. However, these naturally derived hydrogels lack design flexibility in manipulating individual matrix properties, have poor handling characteristics and display poor reproducibility due to different compositions from batch to batch [24]. Synthetic hydrogels have emerged as a replacement for naturally derived hydrogels for 3D cell culture since they are not only able to mimic the key features of the natural extracellular microenvironment [25-28], but also can be modified with specific functional groups to modulate cell behaviour [29-33]. However, harvesting tumour spheroids from hydrogels for subsequent use in screening potential therapeutic drugs remains a significant challenge.

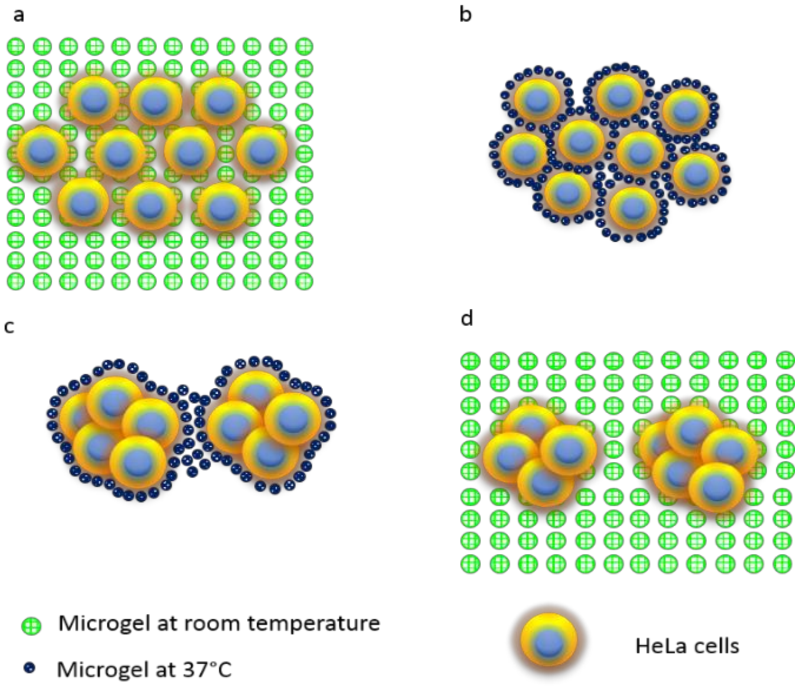

Figure 3-1 Thermal sensitive microgels for culturing tumour spheroids: (a) HeLa cells are homogenously mixed with microgels at room temperature; (b) At 37 ºC, P(NIPAM-AA) microgels constrain single cells in a three-dimensional network as the microgels are solidified due to the hydrophobic attraction; (c) After incubating HeLa-laden microgels in cell culture medium for a pre-determined period, HeLa multicellular spheroids are generated in P(NIPAM-AA) microgels; (d) By cooling down the temperature to 25ºC, the 3D microgel turns into solution as microgels become hydrophilic again and are re-dispersed into medium, and HeLa spheroids are released from the liquefied solution.

We have previously developed a range of thermo-reversible hydrogels or microgels, and used them to mimic the extracellular microenvironment for mesenchyme stem cells [34-36]. In this study we employ these thermo-reversible microgels to culture and harvest tumour spheroids. In our method, as shown in Scheme 1, single cells are homogeneously embedded inside the microgel network that have been heated to 37 ˚C. Cells proliferate in the cell culture medium, and multiple cells interact to form clusters. After the clusters reach the desired size, the spheroids are easily released and collected by cooling the system down to room temperature. In this confined environment, we expect to obtain uniform-sized spheroids with a narrow size-distribution. We characterize the spheroid size, size distribution and shape, and examine the detailed structure of spheroids through fluorescent images and SEM analysis for the tumour spheroid biology that is missing from the previous study [37].

This approach can be easily adapted for producing large quantities of tumor spheroids for high throughput screening potential drugs. We put forward possible mechanisms for spheroid formation, which we then investigate using an agent-based or cellular automata (CA) model. CA models have previously been widely used to investigate various biological phenomena [38, 39], including tumour growth [40-42]. However the study of tumour spheroid formation progression within the hydrogel scaffold has not been conducted yet. By changing some of the parameters in our model, we are able to take into account the different environments experienced by cells in hydrogel and suspension cultures, and investigate their effects on spheroid formation. Of particular interest was to determine the factors affecting the uniformity of the spheroid size distribution. Combined the CA model and experimental results, we explored the mechanism for tumour spheroid formation between microgel scaffold culture and suspension culture.

3.3 Experimental

3.3.1 Materials

N-Isopopylacrylamide (NIPAM), acrylic acid (AA), N,N'-methylenebis(acrylamide) (MBA), potassium persulphate(KPS) were purchased from Sigma-Aldrich, sodium dodecyl sulphate (SDS) was purchased from VWR. NIPAM was recrystallized in n- hexane and dried in vacuum at room temperature. AA was purified by vacuum distillation. Dulbecco's Modified Eagle's Medium (DMEM), trypsin-EDTA, pencillin-streptomycin PS) and fetal bovine serum (FBS) were ordered from Gibco. 3-(4,5-Dimethlthiazol-2-yl)-2,5-diphenyltetrazolium bromide (MTT) was purchased from Merck. The LIVE/DEAD® Viability/Cytotoxicity Kit was purchased from Life Technologies.

3.3.2 Microgels synthesis

The P(NIPAM-AA) microgels were synthesized by free radical emulsion polymerization based on the method reported previously [34]. Based on table 1, 9.9 mmol NIPAM, 0.1 mmol AA, 0.2 mmol MBA and 0.12 mmol of SDS were dissolved in 97 mL of water. After thoroughly mixing, the solution was transferred to a 250 mL three-necked flask fitted with a condenser and a mechanical stirrer. Before the polymerization, the solution was under nitrogen atmosphere for degassing 30 min. After degassing, the flask was placed into a pre-heated oil batch (70 ˚C). 3.0 mL of KPS aqueous solution (0.1 mmol) was injected into the mixture solution to initiate the polymerization. The polymerization was carried out for 5 h under the protection of nitrogen atmosphere with continuous stirring. After reducing the temperature to the ambient temperature, the microgels were purified by membrane dialysis with a cut-off molecular weight of 12-14 kDa against Milli-Q water for one week with a daily water change. The purified microgels were concentrated at 70°C with continuous stirring. The success of copolymerization was confirmed by FTIR (Fig. 3-11) and titration (Fig. 3-12 document) in supporting document.

3.3.3 Tumor spheroid formation from three dimensional cell culture

HeLa cells were cultured in a growth medium (DMEM with 10% FBS and 1% PS) in a T-75 flask. The flask was incubated at 37 °C in a humidified atmosphere with 5 % CO_2 until it was confluent. Trypsin was added into the flask to harvest cells. Cells were resuspended in a complete growth medium at a cell concentration of 1.4×10^6 cells/mL.

To prevent Hela cells attached to the bottom of the 24 well plates, all wells were pre-coated with 400 μL 5% agarose. After coating, HeLa cell dispersion was mixed with 50 mg/mL microgels (in phosphate buffered saline (PBS), pH≈7.2) at a volumetric ratio of 2: 3. Therefore, the initial concentration of cells was 5.6×10^5 cells/mL, and the concentration of microgels was 30 mg/mL. 0.5 mL of mixture was seeded to each well of a 24-well plate. The cell-microgel mixture was incubated at 37°C for 2 h until the mixture becomes soft gel. 1 mL growth medium was added on the top of the soft gel in each well. Cells were incubated at 37 °C in a humidified atmosphere with 5 % CO_2 and the growth medium was changed daily. Cells were harvested for further analysis at day 7, 14, and 21. For comparison of cell culture in the absence of microgels, 0.5 mL of the HeLa cell dispersion in the complete growth medium with a concentration of 5.6×10^5 was seeded to each coated well of a 24-well plate, and then another 1 mL culture medium was added to each well. Other experimental conditions were identical to 3D cell culture in the microgels.

3.3.4 Cell proliferation assay

Cell proliferation was determined by the standard MTT assay. After culturing for a predetermined period, 100 μL MTT solution (5.0 mg/mL) was added into each well with microgels or without microgels. After further incubating for 4 h, the medium was completely removed. 1 mL DMSO was added to dissolve the formazan crystals. All solutions from each well were transferred to a 96 well plate and the absorbance of the solubilized formazan crystals was recorded using an ELx808 Absorbance Microplate Reader (BioTek Instruments In., USA) at a wavelength of 490 nm.

3.3.5 Spheroid release and collection

After the culture period has elapsed, the scaffold and cells structure are left at room temperature for 1 h. The microgels liquefy when the temperature is below LCST, and the released spheroids can be easily collected through centrifuge.

3.3.6 Spheroid morphology and structure analysis

After the Hela cells were cultured in the microgels for a fixed time point, the cell-microgel mixture was cooled down to the room temperature. The microgels turned into solution and spheroids were released. The morphology of the HeLa cell spheroids in the microgel solution was observed under an Olympus IX50 inverted microspore (USA). The optical images were analysed by a software package Analysis LSR (USA) to quantify the cell size distribution and sphericity. The spheroids size was analysed through 12 pictures that were taken from 3 wells (3 pictures per well) for each day and the total number of spheroids analysed was at least 100.

The Live/Dead cell viability/cytotoxicity kit was used to assess live and dead cells in the spheroid structure. The dye solution was prepared according to protocol. 3μL Ethidium homodimer-1 (red) and 0.75μL calcein AM (green) was added 1.5 mL PBS buffer. Before staining, the gel and cells mixture was washed with pre-warmed PBS buffer 2 times. Then 200 μL dye solution was added to each well. After another 30 minutes incubation at 37°C, gel and cells mixture was washed with pre-warmed PBS buffer for two more times. A fresh 300μL PBS buffer was added after rinse process. The stained mixture was observed under confocal microscopy for spheroid morphology examination. The excitation wavelength for calcein Am was selected to be 504 nm-553 nm, and for Ethidium homodimer-1 was 569 nm-619 nm. The Leica TCS SP5 confocal microscope was used to record fluorescent images.

The scanning electron microscopy (SEM) was also further employed for spheroid structure analysis. The cellular spheroid was fixed for 30 min in the EM fixative (4% paraformaldehyde / 1.25% glutaraldehyde in PBS, and 4% sucrose, pH7.2). The sample was rinsed in a washing buffer (PBS + 4% sucrose) for 5 min. The spheroid was post-fixed in a 2% OsO_4 aqueous solution for 30 min. After fixing the sample, the sample was dehydrated by rinsing it by 70%, 90% and 100% ethanol thrice and 10 min for each step. The sample was submerged into a mixture of HMDS (hexamethyldisilazane) and 100% ethanol at a volumetric ratio of 1:1 for 10 min. The sample was further placed into 100% HMDS for 10 min. HMDS was removed and the sample was dried. The dried sample was coated with platinum and observed under a Philips XL30 Field Emission Scanning Electron Microscope at an accelerating voltage of 10 kV.

3.3.7 Development of CA model

The CA model consists of a lattice, where each site on the lattice can either be empty or occupied by a cell. At the beginning of a simulation, a specified number of cells are placed at random on the lattice. The number and position of the cells are updated at discrete intervals of time, Dt. During each timestep, cells are selected in random order, and act according to rules for cell behaviour (including cell movement, proliferation and death) that are described in detail below. Our model uses a two-dimensional lattice, as the experimental data derives from two-dimensional images. This has the further advantage of reducing the computational cost compared to a three-dimensional model. The method by which we take into account the three-dimensional nature of the experiments is explained in detail below.

3.3.7.1 Cell movement

We let the probability that a cell will attempt to move during a time step be $P_{m.}$ We assume this probability will depend upon the cell's environment. We take a higher value of P_m to represent cells in suspension, and a lower value of P_m for cells in microgels, representing some resistance to movement (such as cell-ECM adhesion). Cell movement is assumed to involve two component behaviours: unbiased random motion (in which a cell will attempt to move to one of the four neighbouring lattice sites with equal probability) and biased motion (where cells will preferentially move towards other cells). In our model, cells attempt to move according to the biased motion rule with probability P_b (hence the probability of moving according to the unbiased random motion rule is 1- P_b). Thus the tendency of cells to aggregation is represented by the probability of biased motion, P_b: for cell types that are strongly inclined to create clusters after seeding, P_b will be close to one, whilst for those that do not tend to aggregate, P_b is close to zero [38]. P_b and P_m are chosen based on the hypothesised characteristics of the cells in the medium before the start of each simulation.

When a cell attempts to move using the biased motion rule, the direction in which it moves is determined as follows. For each of the four directions, we calculate the following probability: This can be implemented by the following probability

$$P_v(\mathrm{k}) = \frac{v(k)}{\sum_{i=1}^{4} v(i)} \quad \text{for k= 1, 2, 3, 4} \tag{3.1}$$

where $v(k)$ is the number of cells at the right (k = 1), left (k = 2), up (k = 3) and down (k = 4) direction of a cell within its range of attraction (l) (see Figure 3-2). Note that the $P_v(k)$ sum to unity. We then subdivide the interval [0,1] into four sub-intervals: [0, $P_v(1)$], ($P_v(1)$, $P_v(1) + P_v(2)$], ($P_v(1) + P_v(2)$, 1- $P_v(4)$), (1-$P_v(4)$, 1], and draw a random number uniformly distributed on [0,1]. If the number chosen lies in the first interval, the cell attempts to move right, if in the second, it attempts to move left, etc.

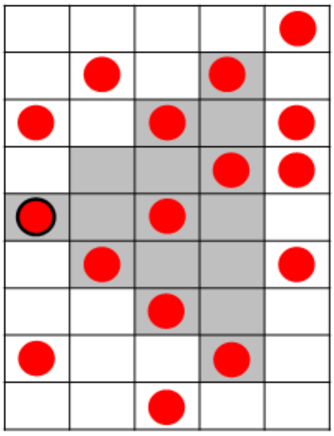

Figure 3-2 A sample distribution of cells is depicted. For example, the red cell marked out with the black border senses 7 cells at its right side, v(k = 1) = 7, where l = 3 is the radius of the attraction range, illustrated by the shaded sites.

Area exclusion is accounted for in the cell movement rules [39]: two or more cells cannot occupy a site at a time. Therefore, at any point a cell attempts to move to an already occupied site, the movement is aborted.

Mombach and Glazier [40] suggest that in Brownian motion a cell moves 1/6 of its size in 30 minutes. Therefore, in 3 hours each cell moves one site in the lattice when Pm = 1.

The probability of biased motion is set to Pb = 0.9 with the range of attraction, l = 3 for both types of culture. Thus, it is very likely that the cells move towards each other when they are very close to each other (e.g. close enough that some parts of the cell may make physical contact). Long range attractions are not considered here as the chemotactic signals are assumed to be negligible.

3.3.7.2 Cell proliferation

The probability of proliferation, Pp, determines the rate of proliferation at each timestep. When proliferation occurs for a cell, the parent cell keeps its position and the daughter cell occupies one of the four adjacent sites. Area exclusion is accounted for in the proliferation rules as well, i.e. if a cell already occupies the chosen site for the daughter, the proliferation event is aborted.

We follow the model of Qi et al. [41]who take into account the effects of nutrient depletion as cancer cells proliferate by making the probability of proliferation dependent upon the total number of cells. We define the two-dimensional cell density, ρ, as the area fraction occupied by the cells, given by

$$\rho = \frac{N(t)B}{A}$$

where $N(t)$ is the number of cells at time t, B is the cell area (15^2 μm^2) and A is the area of the lattice in μm^2. The area of a well in the experiments is around 20 mm^2. Thus, the length of each side of the well is $a = \sqrt{A} \approx 4.5$mm. Therefore, a lattice representing the wells has a length of $L = a/0.015 = 300$ sites. As the proliferation rate is assumed to decrease when cell density increases, due to lack of nutrients, we define the probability of proliferation as

$$P = k(1 - \frac{\rho(t)}{C})$$

where C is carrying capacity and k is growth rate. Qi et al. [41] suggest $0.26\ d^{-1} < k < 0.48\ d^{-1}$. From the experimental data shown in Figure 2, cells have approximately the same rate of proliferation in suspension and microgel: we hence use the same probability of proliferation for both types of culture with $k = 0.48\ d^{-1} = 0.06\ (3h)^{-1}$. C is estimated to be 0.6 by processed the images of the experiments to obtain the maximum area fraction that may occur.

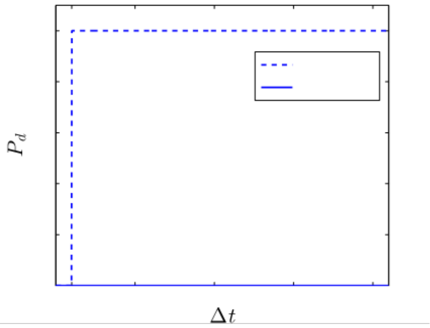

Figure 3-3 The probability of death (Pd) applied in the CA model, described in Eqn. (1.2). Δt is the number of timesteps (each of 3h) where a cell is not adhered to another cell

3.3.7.3 Cell death

Cells need to adhere to another cell or a surface to survive and proliferate [42]. As the cells in suspension culture are prevented from adhering to the substrate, based on our experimental observations, we assume that they are likely to die after one day if they do not adhere to other cells [42].(In the model, we assume a cell is adhered to another cell if there is a least one cell in the four squares adjacent to it.) However, in microgel culture, the cells can survive and proliferate by adhering to the microgel. We thus considered two different death probabilities, P_d, in simulations of suspension and microgel experiments. In suspension simulations, P_d for an isolated cell is low during the first day of culture, increasing rapidly to unity thereafter. For microgel simulations, for the sake of simplicity, P_d is taken to be zero.

Thus, the probability of death for isolated cells in suspension and microgel culture respectively can be defined as follows

$$P_d == \begin{cases} \frac{1}{1+e^{-100(\Delta t-8)}}, & \text{suspension} \\ 0, & \text{microgel} \end{cases} \tag{3.2}$$

where Δt is the number of timesteps (each timestep represents 3h) where a cell is not adhered to another cell. This equation

gives a rapid increase in the death probability after $\Delta t = 8$ (1 day) for suspension culture, whilst $P_d = 0$ for microgel cultures for $0 \leq \Delta t \leq 168$ timesteps, see Figure2. Note that the functional form of P_d in Eqn. (1.2) is simply chosen to reproduce the assumed qualitative behaviour of the cells in the two different culture environments described above. In the case of suspension culture, other functions that increase rapidly to unity after a period of 1 day would be expected to produce similar results.

The CA model was run at a timestep of Ts of 3 hours. The initial population was set to $\rho_0 = \rho(0) = 0.05$ in suspension and $\rho_0 = 0.005$ in microgel to have the best fit to the experiments. The reason for this difference is that in suspension most cells settle down and interact in a layer close to the substrate, whereas the cells in microgels lie in multiple layers. Note that ρ_0 represents the effective initial population of cells in our 2D CA model, i.e. the cells that interact with each other within a layer, not the total population of cells in a well. This leads to a considerably higher effective ρ_0 for the suspension culture case where the cells are mainly within one layer, compared to the microgel, where they are distributed more evenly throughout the gel.

The length of the lattice side was scaled down to half: 150 sites, similar to the size of the images of the experiments. Moreover, a periodic boundary condition was applied in the simulations. This means that when a cell moves out of the domain at one side, it will re-enter from the opposite side. Applying periodic boundary conditions mitigates the effect of boundaries on the distribution of cells [38], since there is no physical boundary present at the edge of the experimental images with which we aim to compare our results.

The size of the clusters (cluster diameter) was calculated as follows. Firstly, the areas of the clusters were computed, using the function #bwarea in MATLAB. This function gives an estimate of the area, n, created from adjacent connected pixels, using the algorithm explained in [43]. Multiplying the area by 15^2 (area of a cell), gave the area of a cluster in μm^2. The cluster diameter, D, was then calculated as the diameter of a circular cluster of equivalent area – i.e.:

$$D = 30\sqrt{\frac{N}{\pi}}$$

3.3.8 Data analysis

All experimental data were expressed with mean ± standard deviation. Student's t test was used to for statistical analysis. Data were considered to be significantly different at $p < 0.05$.

3.4 Results and discussion

3.4.1 Cell proliferation

We have previously used synthesized microgels to culture mesenchymal stem cells and cell proliferation in the microgels was found to be better than that by the conventional two-dimensional cell culture [34-36]. We again employed this novel three-dimensional cell culture platform in this study to form HeLa tumor spheroids and compare them with suspension culture controls. When HeLa cells are cultured in the microgels, the cells display rapid proliferation in the first 7 days, maintain a dynamically balanced cell growth from day 7 to 14, and start to decrease in cell number from day 14 to 21 as shown in Fig. 3-4. A similar trend of cell proliferation was also observed for the cells in suspension culture. Interestingly, the growth kinetics for HeLa cells in microgels are quite similar to those of tumour *in vivo* [44].

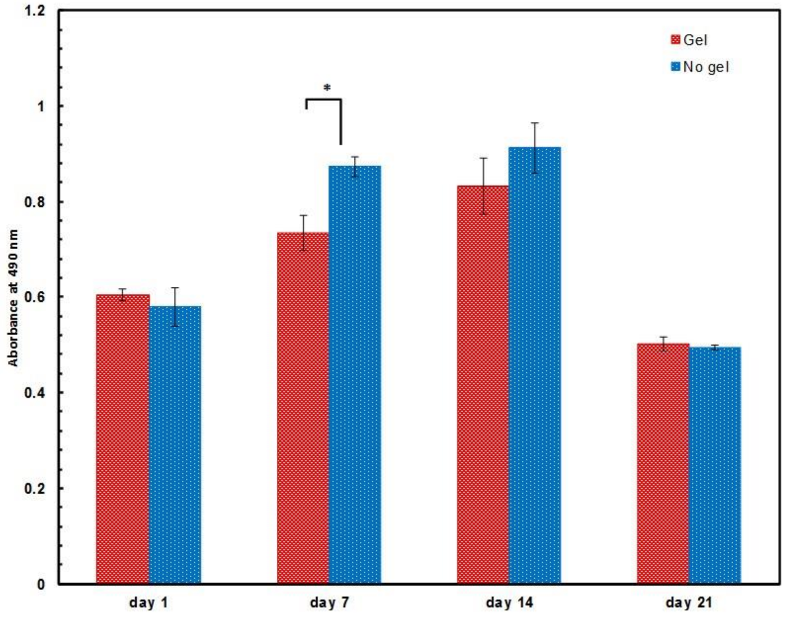

Figure 3-4 HeLa cell proliferation inside microgel network

At day 1 the MTT result shows cells growing within microgels or in suspension have a very similar absorbance rates which indicates good biocompatibility of the P(NIPAM-AA) microgels with HeLa cells. At day 7, cells in suspension proliferate relatively faster than those within the microgels. However, the number of viable cells increases significantly in microgels, which means oxygen and nutrients can diffuse through the microgel pore networks to support cell growth. As cell growth progresses, the number of proliferating cells starts to decrease and the proportion of non-proliferating (quiescent) cells starts to increase [44]. This may be due to the maximum cell density being achieved in each well [37]. However, the lower growth rate in the microgels in the previous 7 days results in more rapid growth from day 7 to day 14 in comparison with suspension culture. At day 21, the viable cell number with and without gels shows a dramatic drop. This may be due to formation of large clusters in which the inner cells are dead because of limited oxygen and nutrients. At this stage, the maximum size of clusters is reached, and there are many more inner dead cells. Cell death may also due to toxic products discharged by the cells [37].

3.4.2 Spheroid structure analysis

The Live/Dead viability and cytotoxicity kit was further employed to examine the structure of individual tumour spheroids. Live cells are coloured green, whilst dead cells are red. The fluorescent images clearly show the inner structure of the spheroids. Fig. 3-5(a-d) illustrates the progression of spheroid development. At day 1, the single cells are dispersed in the microgel network. At day 7, as shown in Fig. 3-5 (b), small clusters are able to be seen and the inner cells become dead due to starvation of oxygen, glucose and other nutrients as well as accumulation of toxic metabolites secreted by cells [44]. A solid and compact spheroid structure appears at day 14, and dead cells in the central core are distinguishable from those in the outer layers. At day 21, the compact structure becomes loose and some cells detach from it and start to migrate. High-resolution SEM images in Figure 4 clearly reveal the spheroid structure. Cells are tightly bound to each other to form a nearly spherical structure (Fig. 3-5(e)). The strong interactions between cells are due to the extracellular matrix (ECM) derived from cells (Fig. 3-5(f) and Fig. 3-13, supporting document). This confirms that the ECM is one of the key driving forces which maintains the structure.

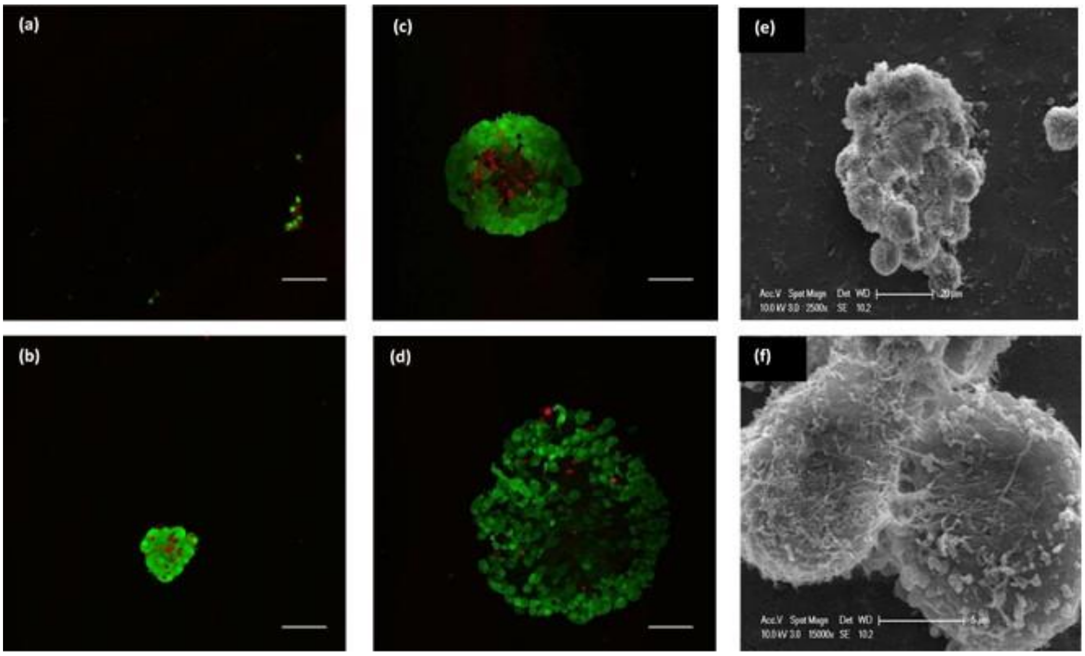

Figure 3-5 HeLa cell Live/Dead and SEM images. (a-e) HeLa cells fluorescent images within microgels network at day 1, day 7, day14, day 21 respectively. Scale bar is 100µm. (e,f) SEM of a HeLa cell spheroid at day 7.

3.4.3 Spheroid size analysis

The physiological state of spheroids is dependent on their size, and the cell density within them. Three dimensional cell-cell and cell-matrix interactions are established when the spheroid size reaches 150 µm and gene expression profiles are significantly altered, compared to 2D culture. Chemical gradients, such as oxygen, nutrients and catabolizes, are developed at diameters between 200 and 500 µm, and a central secondary necrosis is established for a diameter greater than 500 µm. Thus, spheroid size has a great impact on drug screening. Optical images were used to study the morphology of the spheroids, and the images are presented in Figure 4. 4x magnification images reveal the evolution of cluster sizes at each time stage. It can be seen that cells remaining inside microgels tend to form a cluster structure at a slower rate than those in suspension. At day 7, without the control of microgels, cells cultured in the suspension medium have been packed a cluster structure (Fig. 3-6a), while cells grown in the microgels form a much smaller cluster containing two or three cells (Fig. 3-6b). At day 14, a clear spheroid structure can be observed both within and without microgels. However, the size of the cluster in microgels (Fig. 3-6c) is considerably less than those in suspension medium (Fig. 3-6d). A number of single cells are seen in the microgel system. After culturing for 21 days, the number of clusters within microgels increases although some single cells can still be observed (Fig. 3-6e). In suspension culture, the number of clusters begins to drop but the size of the clusters continues to increase (Fig. 3-6f).

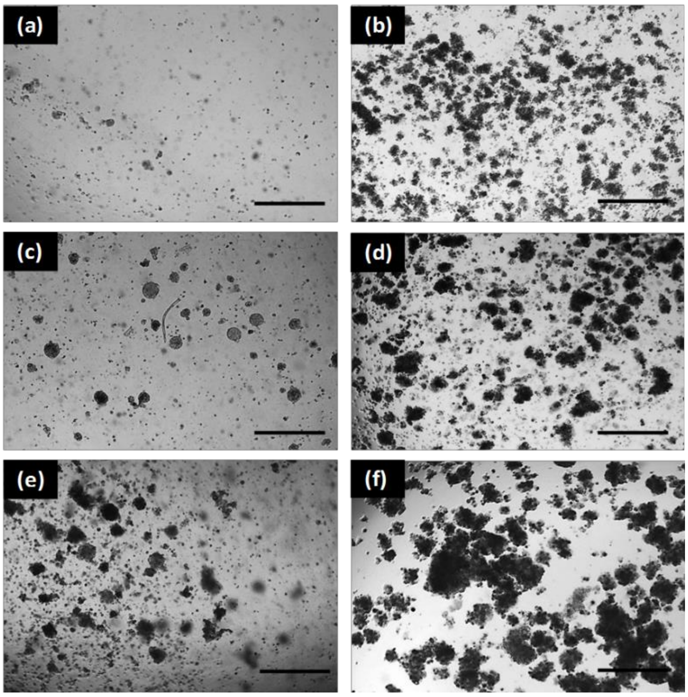

Figure 3-6 HeLa cells within and without microgel at different culture days released from microgel at room temperature. Scale bar is 500µm. (a),(c),(e) is HeLa cells within microgels culture after 7 days, 14 days, 21 days respectively. (b), (d), (f) is HeLa cells in suspension culture after 7 days, 14 days and 21 days respectively.

Clusters may be formed due to interactions between two neighboring cells or between parent and the daughter cells, depending on their physical locations and the secretory molecules surrounding them [31]. Clusters in the suspension medium may be formed due to interactions between parent and daughter cells as well as neighboring cells. Further increases in cluster size may be due to cluster-cluster, cluster-cell and cell-cell interactions. However, inside the microgels, the restraint provided by the microgel networks slows down the formation of cell clusters. Neighboring cells inside the scaffold are separated by the physical barriers formed by the microgel network and they cannot migrate freely to form clusters. Most likely, clusters are formed by parent cells and their adjacent daughters. In the first day, the initial cell density is low, and cells are scattered inside the microgel network. Gradually cells start to proliferate and two-cell clusters are formed. As the culture time extends, multicellular spheroid structure are generated.

3.4.4 Cluster size distribution

The optical images were further analyzed using an imaging software package to obtain the size distribution of the clusters which is shown in Fig. 3-7. At the first 7 days, cells grown in microgels form clusters with a size range of 20 µm to 70 µm (Fig. 3-7a). By contrast, cells grown in suspension form larger clusters more rapidly. More than 60% of the clusters are bigger than 70 µm. Most clusters are around 70 µm to 120 µm (Fig. 3-7b). At day 14, a shift in spheroid size towards larger sizes becomes more evident in both types of culture. The majority of clusters in microgels are around 70 µm to 120 µm with a narrow size distribution, while the cluster size in the suspension medium shows a much wider distribution. Equal numbers of spheroids are found in the range of 70 µm to 120 µm and 120 µm to 170 µm. Bigger-sized clusters can be observed in the suspension medium than in microgels. At day 21, the cluster size increases again. The incremental rate of cluster size growth in the suspension medium is much faster than that in the microgels. In microgel scaffold culture, the majority of the cluster size is at a range of 70 µm to 120 µm, with a relevantly narrower size distribution than that without microgels.

The stiff microenvironment formed by the microgels has a significant impact on the size distribution of spheroids. It has been reported that a higher stiffness surrounding cells results in much smaller spheroids [45]. The microgels generated in the study are relatively soft, with an elastic modulus (G’) of around 1 Pa, far less than the values reported ranging from 241 to 1201 Pa G’ of other hydrogels[45]. It would be expected that a higher stiffness may also lead to a very narrow size distribution. However, spheroids with a size below 150 µm generated in the *in vitro* environment may not be able to represent the tumors in the human body. It is clearly shown that the soft microgels in our study can significantly reduce variability in spheroid size and also produce spheroids with a size range similar to the in vivo environment.

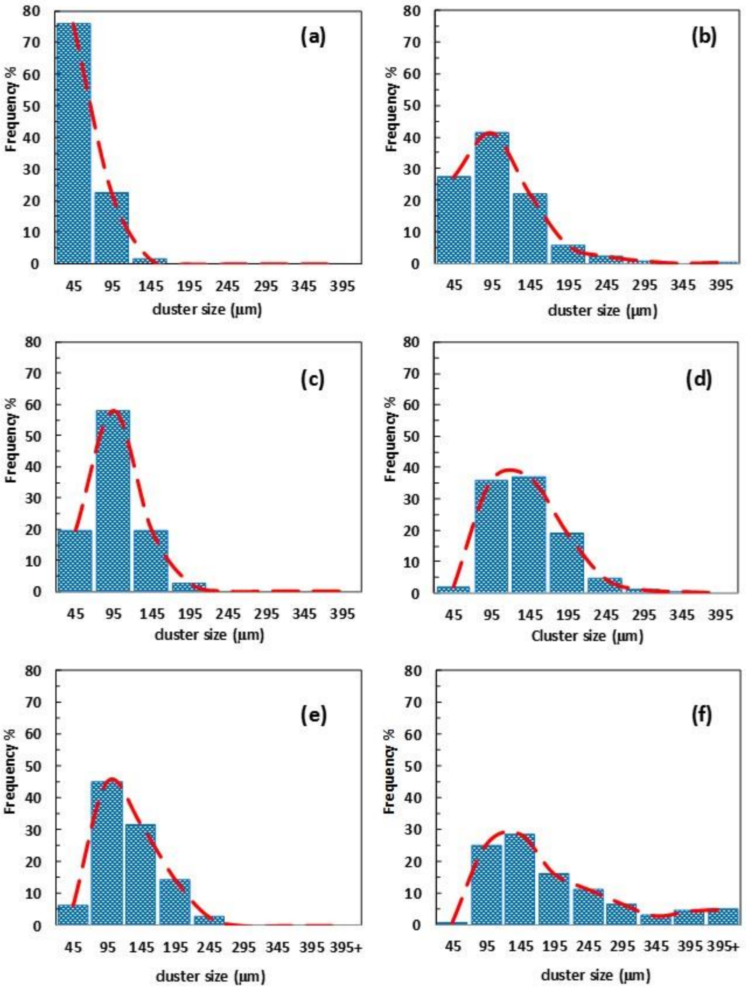

Figure 3-7 HeLa cells spheroids size distribution. (a),(c),(e) is HeLa cells within microgels culture after 7 days, 14 days, 21 days respectively. (b), (d), (f) is HeLa cells in suspension culture after 7 days, 14 days and 21 days respectively.

3.4.5 Sphericity

The measurement of sphericity was based on the central moment, and the sphericity was defined as the ratio of perimeter of the object (P) to that of a circle with the same projected area as the object (πd_{eq}) [46]. The calculated sphericities for spheroids with and without microgels are shown in Fig. 3-8.

$$s = P/\pi d_{eq}$$

It can be seen from Figure 7 that the sphericity in the suspension does not vary with the culture time. Above 70% of clusters have sphericity of 0.4 to 0.6, which means the shape of the clusters is far from spherical. In the microgel culture, at day 7, the sphericity seems similar to that in the suspension medium. However, over 70% of clusters present sphericity of 0.8-1.0, showing that the most of clusters exhibit a spherical shape. As the culture time extends to 21 days, the sphericity shifts from 0.8-1.0 to 0.6-0.8, with the frequency of eccentric shapes increasing after 14 days in culture. The results demonstrate the stiffness of the microenvironment formed by microgels also plays a role in maintaining the spherical shape of spheroids.

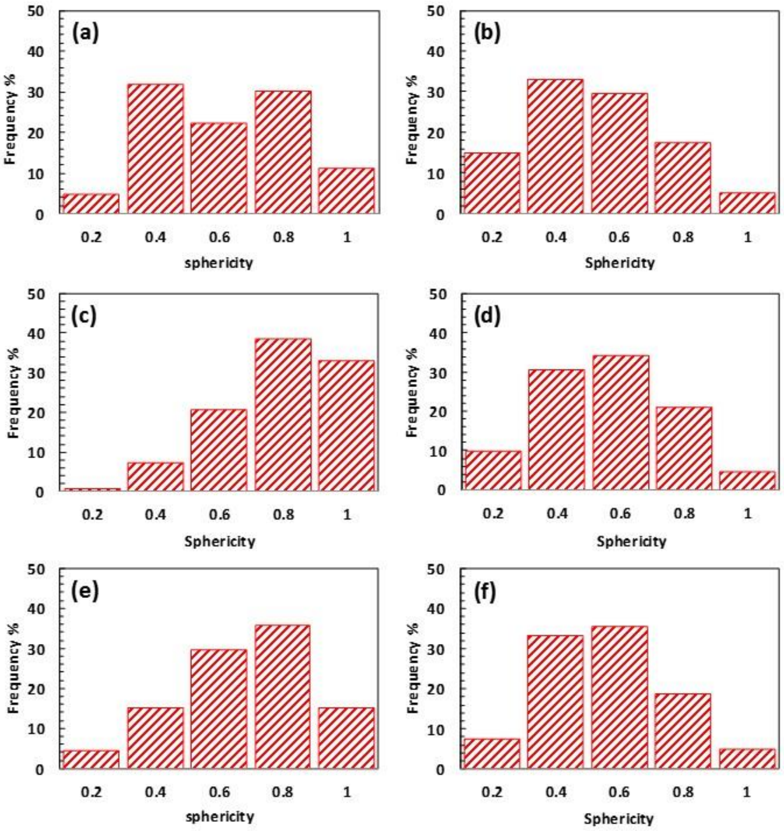

Figure 3-8 Shpericity of HeLa clusters within and without microgels. (a),(c),(e) is HeLa cells within microgels culture after 7 days, 14 days, 21 days respectively. (b), (d), (f) is HeLa cells in suspension culture after 7 days, 14 days and 21 days respectively.

3.4.6 CA model

Fig. 3-9 shows the pattern and distribution of clusters in suspension and microgel simulations. Here, we consider extreme cases for P_m of is 1 for suspension and 0 for microgels respectively. Thus, the cells are very motile in suspension and the cells in microgel do not move at all. Note that in the histograms clusters with $n < 7$ are not included, since they are too small to be considered as spheroids.

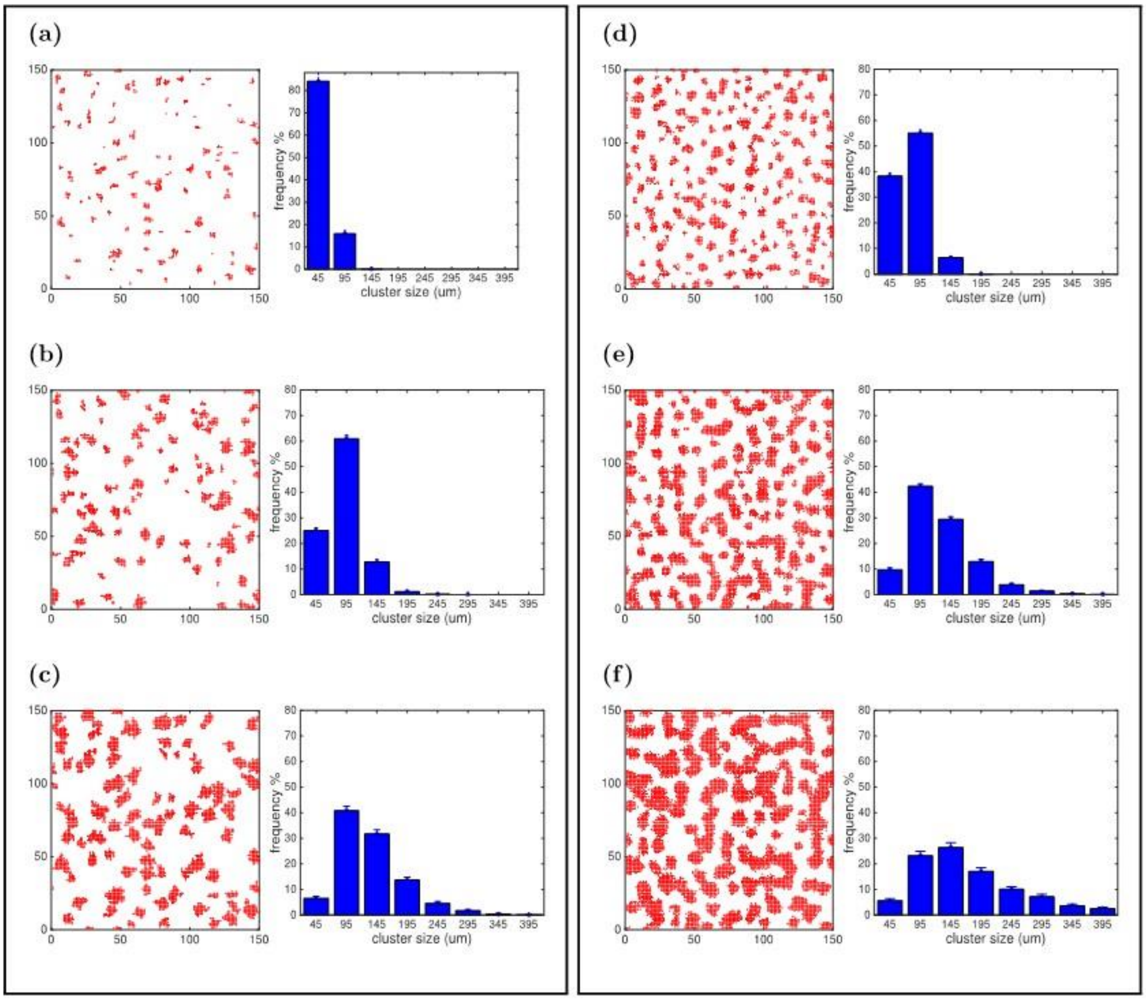

Figure 3-9 Patterns of spheroid formation and distribution of cluster size in microgel (left box) and suspension (right box) simulations. (a,d) day 7, (b,e) day 14 and (c,f) day 21. The average with the %95 confidence intervals of t-distribution are depicted for 50 simulations. In suspension: $P_m = 1$ and $\rho_0 = 0.05$. In microgel: $P_m = 0$ and $\rho_0 = 0.005$. The lattice has side of $L = 150$ sites, the range of attraction is $l = 3$, the probability of biased movement is $P_b = 0.9$, the proliferation constant is $k = 0.06$, the carrying capacity is $C = 0.6$ and the death probability is defined in Eqn. (1.1). The dead cells are not shown in the images.

Comparing Fig. 3-9 with Fig. 3-6 shows that the simulation results are in good agreement with the experimental results. At day 21, the average cluster size is $\overline{D} \approx 160$ μm and the standard deviation of the cluster size is $\delta \approx 220$ μm for simulated suspension cultures, while $\overline{D} \approx 72$ μm and $\delta \approx 67$ μm for simulated microgel cultures. Hence, the distribution of clusters is more uniform in the microgel with a lower standard deviation and the average cluster size is smaller as well.

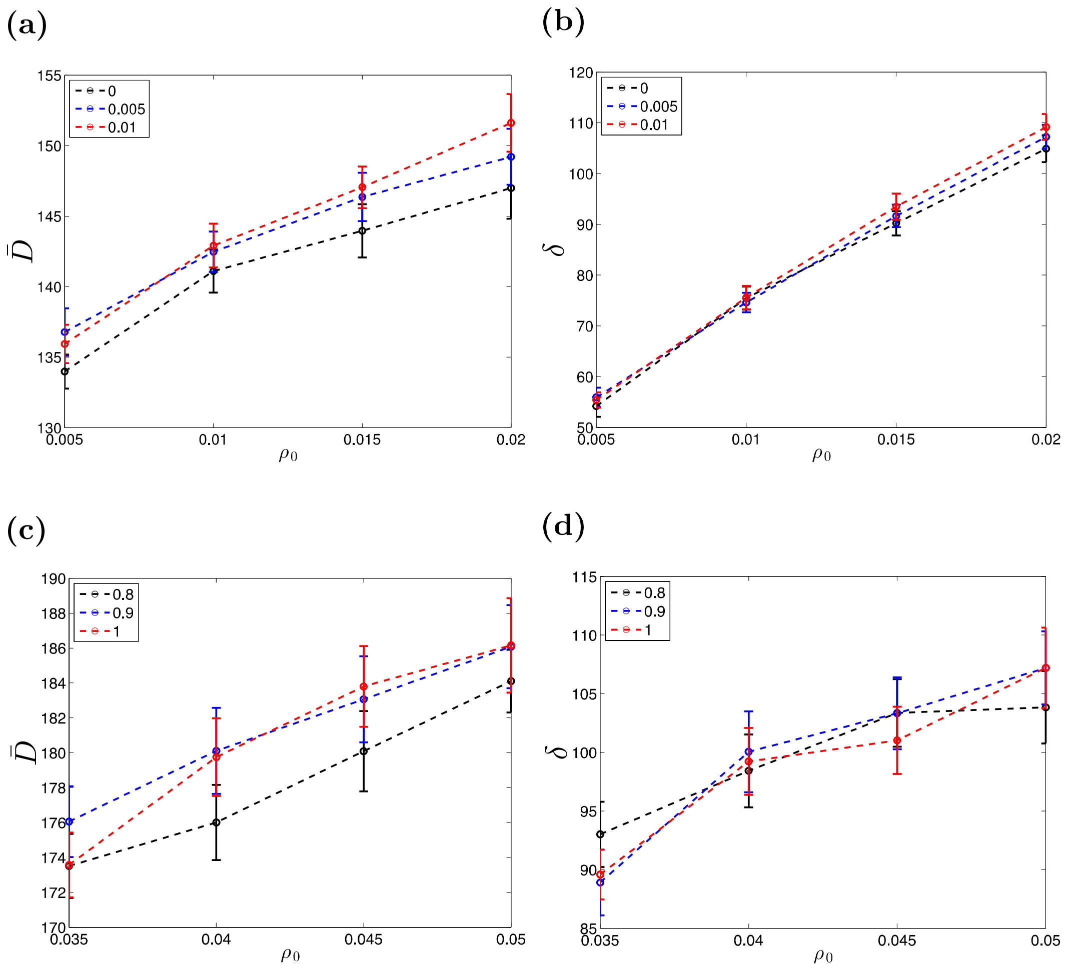

Figure 3-10 Parameter sweeping test. Standard deviation, δ, and average, $\overline{D}$, of cluster size are depicted. (a,b) microgel: ρ0 = {0.005, 0.01, 0.015, 0.02}. Pm = 0 black, Pm = 0.005 blue and Pm = 0.01 red. (c,d) suspension: ρ0 = {0.035, 0.04, 0.045, 0.05}. Pm = 0.8 black, Pm = 0.9 blue, Pm = 1 red. The points in the graphs are computed average over 50 simulations and the error bars are %95 confidence intervals of t-distribution. The values of the other parameters are the same as in Fig. 3-9.

The main differences between the simulated suspension and microgel experiments are in the motion of cells and the initial cell density. We aim to understand how each of them affects the distribution of cluster size, and so, parameter-sweeping tests were carried out in which one of the parameters is varied while the others are kept constant. We swept the parameters in a physically plausible region, i.e. where their values are within a range that is consistent with the physical properties of the medium. Small variations about the previous values of P_m and ρ_0 (see the caption of Fig. 3-10) are analyzed.

We have also examined general cases where the parameter ranges are not necessarily in the plausible region, see supporting document Fig. 3-14and Fig. 3-15. This allows us to analyses other different media that might be used for spheroid formation in future work.

The parameter sweeping was done for 150×150 lattice with ρ0 = {0.005, 0.01, 0.015, 0.02} and Pm = {0, 0.005, 0.01} in the microgel and ρ0 = {0.035, 0.04, 0.045, 0.05} and Pm = {0.8, 0.9, 1} in suspension. Fig. 3-10 shows that $\overline{D}$ and δ increase with ρ0. Thus our model suggests that using a higher initial cell density, ρ0, leads to formation of bigger clusters, which is desirable, but this has the unwanted effect of reducing the uniformity of cluster size. Hence the choice of ρ0 would involve a trade-off between cluster size and size-variability.

As illustrated in Fig. 3-10b and 3-10d, our model predicts that the rate of increase of δ with ρ0 for microgel culture is greater than for suspension culture. Thus, increasing the initial population would have a more deleterious effect on the uniformity of the clusters in microgels compared to suspension culture.

Sweeping the values of Pm in a wider range, we determined that motility of cells can strongly affect $\overline{D}$ and δ. Figure S4 in supporting document shows that increasing Pm leads to the formation of bigger clusters. The reason is that, when Pm is high enough, randomly moving cells can find bigger clusters nearby and attach to them. In addition, the highly motile cells in small clusters are more likely to find bigger clusters and attach to them. Therefore, increasing Pm can reduce the number of small clusters and increase the number of larger ones. Further details can be found in the supporting document.

3.5 **Conclusion**

In summary, we conducted a serial of experiment to demonstrate the advantages of using microgel scaffolds to culture tumour spheroids instead of conventional suspension culture methods. Microgel culture produces more uniformly-sized spheroids, with a more spherical shape. Also it could be used for saleable production of multicellular spheroids. The introduction of the microgel network can be helpful to mimic the stiff environment of tumour growth in vivo. Spheroids produced by our technique can be easy released and collected. Further study on the mechanism of cells' behavior in microgels can be conducted, and it will be meaningful to understand the spheroid formation progress in real tissue. This material, with some modifications, could be used to re-create a controlled microenvironment for other scaffold applications such as regeneration medicine, tissue engineering and so forth.

We developed a CA model to explore the reasons for the different size distributions observed in spheroids grown in microgels and suspension culture. In the model, the cells behave according to rules for movement, proliferation and death. We tried to keep the model as simple as possible in order to focus on the effect of the major parameters on the spheroid formation. The CA model was developed in two-dimensions, since this facilitates comparison with the two-dimensional experimental images, and also reduces the computation time required.

Our CA model was successfully able to reproduce the experimental results for spheroid formation rate and size distribution, for both microgel and suspension cultures. Our results are thus consistent with the main differences between cells in the two different cultures being in their proliferation and death rates, and their initial effective density. Hence, the more uniform size distribution of spheroids produced by microgel culture could be due to its ability to separate the cells in multiple layers, reducing the effective initial density. However, even when the number of cells is low, the microgel provides a substrate for cells to survive and proliferate, so spheroids can still be produced. By contrast it is not possible to reduce the initial population of cells significantly in suspension cultures, since the cells would die out and spheroid formation would not occur.

The model predicts that the initial cell density plays a crucial role in determining the features of the formed spheroids. For the parameter ranges we considered, higher initial densities led to larger spheroids, but at the cost of introducing greater variability in spheroid size. This effect was predicted to be more pronounced for microgel cultures than suspension cultures. Further experiments will be required to test these predictions.

3.6 **Acknowledgements**

XC acknowledges financial support from a University of Adelaide scholarship. HZ would like to acknowledge the financial support from ARC Discovery Project (DP160104632) and The Medical Advancement Without Animal (MAWA) Trust. The work of SD and JEFG was supported by an ARC Discovery Early Career Researcher Award (DE130100031) to JEFG. SD also acknowledges a University of Adelaide Full Fees Scholarship. BJB was supported by an ARC Discovery Project Grant (DP160102644). HZ and JEFG thank the Faculty of Engineering, Computer & Mathematical Sciences of the University of Adelaide for multidisciplinary research collaboration funding.

3.7 **Reference**

1. Nyga, A., U. Cheema, and M. Loizidou, 3D tumour models: novel in vitro approaches to cancer studies. J Cell Commun Signal, 2011. 5(3): p. 239-48.

2. Wang, C., et al., Three-dimensional in vitro cancer models: a short review. Biofabrication, 2014. 6(2): p. 022001.

3. Hirschhaeuser, F., et al., Multicellular tumor spheroids: an underestimated tool is catching up again. Journal of biotechnology, 2010. 148(1): p. 3-15.

4. Landry, J., et al., Spheroidal aggregate culture of rat liver cells: histotypic reorganization, biomatrix deposition, and maintenance of functional activities. The Journal of cell biology, 1985. 101(3): p. 914-923.

5. Yuhas, J.M., et al., A simplified method for production and growth of multicellular tumor spheroids. Cancer Research, 1977. 37(10): p. 3639-3643.

6. Hamilton, G.A., C. Westmoreland, and E. George, Effects of medium composition on the morphology and function of rat hepatocytes cultured as spheroids and monolayers. In Vitro Cellular & Developmental Biology-Animal, 2001. 37(10): p. 656-667.

7. Nyberg, S.L., et al., Rapid, large-scale formation of porcine hepatocyte spheroids in a novel spheroid reservoir bioartificial liver. Liver transplantation, 2005. 11(8): p. 901-910.

8. Lazar, A., et al., Extended liver-specific functions of porcine hepatocyte spheroids entrapped in collagen gel. In Vitro Cellular & Developmental Biology-Animal, 1995. 31(5): p. 340-346.

9. Song, H., et al., Spatial composition of prostate cancer spheroids in mixed and static cultures. Tissue engineering, 2004. 10(7-8): p. 1266-1276.

10. Lin, R.-Z., et al., Dynamic analysis of hepatoma spheroid formation: roles of E-cadherin and β1-integrin. Cell and Tissue Research, 2006. 324(3): p. 411-422.

11. Kelm, J.M., et al., Method for generation of homogeneous multicellular tumor spheroids applicable to a wide variety of cell types. Biotechnology and bioengineering, 2003. 83(2): p. 173-180.

12. Kelm, J.M. and M. Fussenegger, Microscale tissue engineering using gravity-enforced cell assembly. Trends in biotechnology, 2004. 22(4): p. 195-202.

13. WARTENBERG, M., et al., Tumor-induced angiogenesis studied in confrontation cultures of multicellular tumor spheroids and embryoid bodies grown from pluripotent embryonic stem cells. The FASEB Journal, 2001. 15(6): p. 995-1005.

14. Kelm, J.M., et al., Design of custom-shaped vascularized tissues using microtissue spheroids as minimal building units. Tissue engineering, 2006. 12(8): p. 2151-2160.

15. Ingram, M., et al., Three-dimensional growth patterns of various human tumor cell lines in simulated microgravity of a NASA bioreactor. In Vitro Cellular & Developmental Biology-Animal, 1997. 33(6): p. 459-466.

16. Khaoustov, V.I., et al., Induction of three-dimensional assembly of human liver cells by simulated microgravity. In Vitro Cellular & Developmental Biology-Animal, 1999. 35(9): p. 501-509.

17. Kleinman, H.K. and G.R. Martin. Matrigel: basement membrane matrix with biological activity. in Seminars in cancer biology. 2005. Elsevier.

18. Kramer, R.H., K.G. Bensch, and J. Wong, Invasion of reconstituted basement membrane matrix by metastatic human tumor cells. Cancer research, 1986. 46(4 Part 2): p. 1980-1989.

19. Castelló-Cros, R., et al., Staged stromal extracellular 3D matrices differentially regulate breast cancer cell responses through PI3K and beta1-integrins. BMC cancer, 2009. 9(1): p. 94.

20. Holliday, D.L., et al., Novel multicellular organotypic models of normal and malignant breast: tools for dissecting the role of the microenvironment in breast cancer progression. Breast Cancer Research, 2009. 11(1): p. R3.

21. Gurski, L.A., et al., Hyaluronic acid-based hydrogels as 3D matrices for in vitro evaluation of chemotherapeutic drugs using poorly adherent prostate cancer cells. Biomaterials, 2009. 30(30): p. 6076-6085.

22. Talukdar, S., et al., Engineered silk fibroin protein 3D matrices for in vitro tumor model. Biomaterials, 2011. 32(8): p. 2149-2159.

23. Paszek, M.J., et al., Tensional homeostasis and the malignant phenotype. Cancer cell, 2005. 8(3): p. 241-254.

24. Weigelt, B. and M.J. Bissell. Unraveling the microenvironmental influences on the normal mammary gland and breast cancer. in Seminars in cancer biology. 2008. Elsevier.

25. Langer, R. and D.A. Tirrell, Designing materials for biology and medicine. Nature, 2004. 428(6982): p. 487-492.

26. Lutolf, M. and J. Hubbell, Synthetic biomaterials as instructive extracellular microenvironments for morphogenesis in tissue engineering. Nature biotechnology, 2005. 23(1): p. 47-55.

27. Griffith, L.G. and M.A. Swartz, Capturing complex 3D tissue physiology in vitro. Nature reviews Molecular cell biology, 2006. 7(3): p. 211-224.

28. Lutolf, M.P., Integration column: artificial ECM: expanding the cell biology toolbox in 3D. Integrative Biology, 2009. 1(3): p. 235-241.

29. Loessner, D., et al., Bioengineered 3D platform to explore cell–ECM interactions and drug resistance of epithelial ovarian cancer cells. Biomaterials, 2010. 31(32): p. 8494-8506.

30. Lei, Y. and D.V. Schaffer, A fully defined and scalable 3D culture system for human pluripotent stem cell expansion and differentiation. Proceedings of the National Academy of Sciences, 2013. 110(52): p. E5039-E5048.

31. Wu, Y., et al., Galactosylated reversible hydrogels as scaffold for HepG2 spheroid generation. Acta Biomaterialia, 2014. 10(5): p. 1965-1974.

32. Ehrbar, M., et al., Enzymatic formation of modular cell-instructive fibrin analogs for tissue engineering. Biomaterials, 2007. 28(26): p. 3856-3866.

33. Ehrbar, M., et al., Biomolecular hydrogels formed and degraded via site-specific enzymatic reactions. Biomacromolecules, 2007. 8(10): p. 3000-3007.

34. Shen, Z., et al., Exploring thermal reversible hydrogels for stem cell expansion in three-dimensions. Soft Matter, 2012. 8(27): p. 7250-7257.

35. Shen, Z., et al., A thermally responsive cationic nanogel-based platform for three-dimensional cell culture and recovery. RSC Advances, 2014. 4(55): p. 29146-29156.

36. Mellati, A., et al., A biodegradable thermosensitive hydrogel with tuneable properties for mimicking three-dimensional microenvironments of stem cells. RSC Advances, 2014. 4(109): p. 63951-63961.

37. Wang, D., et al., Thermoreversible Hydrogel for In Situ Generation and Release of HepG2 Spheroids. Biomacromolecules, 2011. 12(3): p. 578-584.

38. Agnew, D., et al., Distinguishing between mechanisms of cell aggregation using pair-correlation functions. Journal of theoretical biology, 2014. 352: p. 16-23.

39. Binder, B.J. and K.A. Landman, Exclusion processes on a growing domain. Journal of theoretical biology, 2009. 259(3): p. 541-551.

40. Mombach, J.C. and J.A. Glazier, Single cell motion in aggregates of embryonic cells. Physical review letters, 1996. 76(16): p. 3032.

41. Qi, A.-S., et al., A cellular automaton model of cancerous growth. Journal of theoretical biology, 1993. 161(1): p. 1-12.

42. Alberts, B., et al., Extracellular control of cell division, cell growth, and apoptosis. 2002.

43. Pratt, W.K., Image segmentation. Digital Image Processing: PIKS Inside, Third Edition, 1991: p. 551-587.

44. Sutherland, R.M., Cell and environment interactions in tumor microregions: the multicell spheroid model. Science, 1988. 240(4849): p. 177-184.

45. Loessner, D., et al., Growth of confined cancer spheroids: a combined experimental and mathematical modelling approach. Integrative Biology, 2013. 5(3): p. 597-605.

46. Asundi, A., Digital holography for MEMS and microsystem metrology. Vol. 7. 2011: John Wiley & Sons.

3.8 Supporting Document

Chapter 3: A Mechanistic study on tumour spheroids formation in thermosensitive hydrogels: experiments and mathematical modelling

X Cui[a], S Dini[b], S Dai[a], J Bi[a], B J Binder[b], J E F Green[b] and H Zhang[a]

[a] School of Chemical Engineering , University of Adelaide, Adelaide, SA, Australia 5005

[b] School of Mathematical Sciences, University of Adelaide, Adelaide, SA, Australia 5005

Corresponding :Dr. Hu Zhang

Hu.zhang@adelaide.edu.au

1.

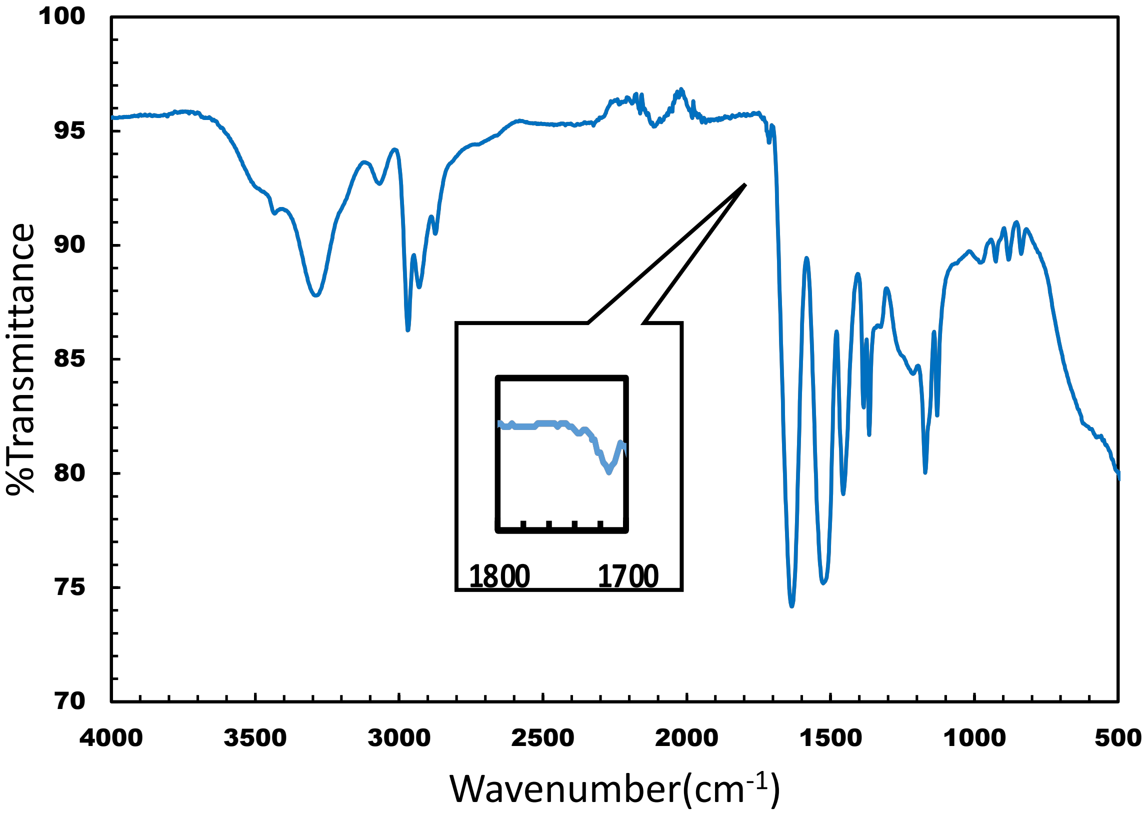

Figure 3-11 FTIR for P(NIPAM-AA)

2.

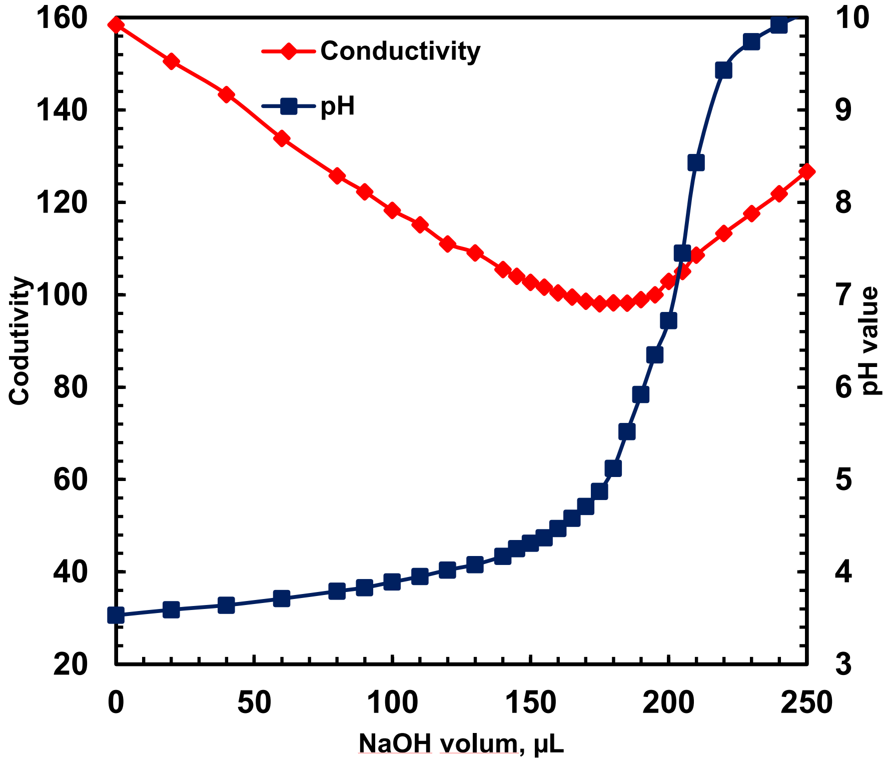

Figure 3-12 pH and conductive Titration of P(NIPAM-AA) microgel

3.

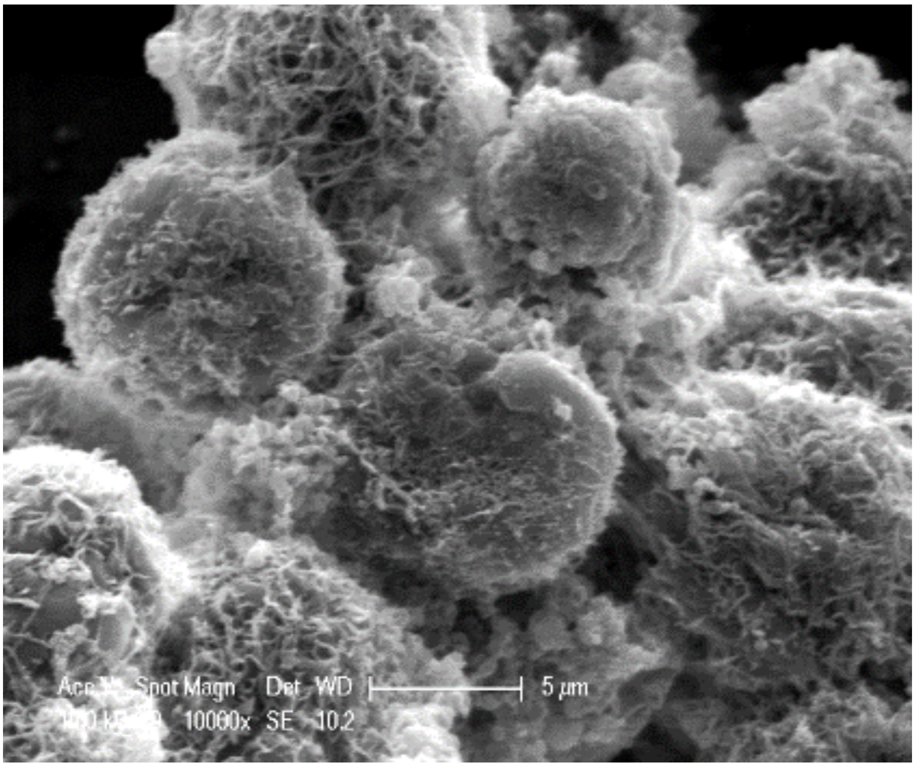

Figure 3-13 SEM of a HeLa spheroid showing cell to cell interaction

4.

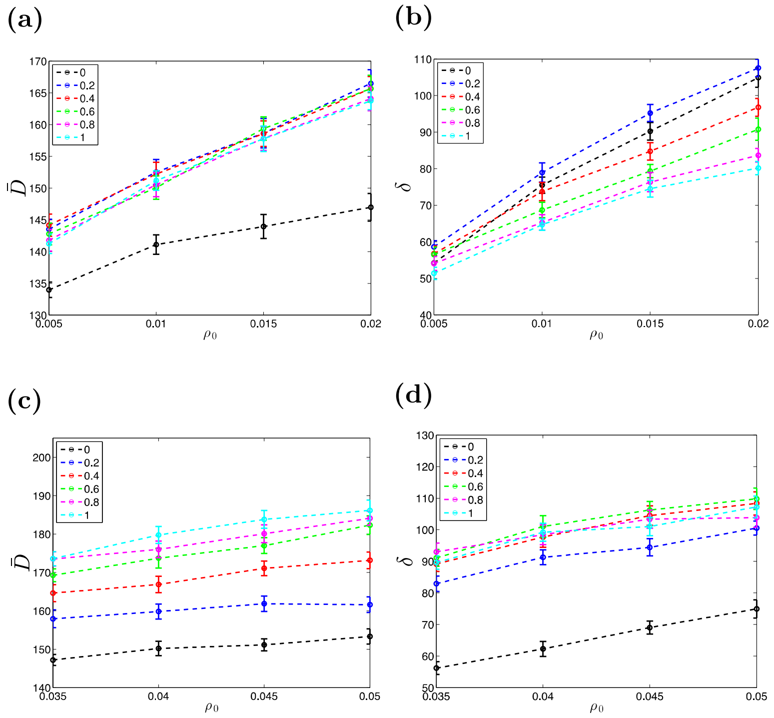

Figure 3-14 Parameter sweeping with a same range of Pm for the culture media. Standard deviation, δ, and average, $\bar{D}$, of cluster size are depicted for (a,b) microgel and (c,d) suspension. The curves are for Pm = {0, 0.2, 0.4, 0.6, 0.8, 0.1} with the colours as indicated in the legends of the graphs. Other parameters are the same as for the simulations of Figure 3-9

Here, we assess spheroid formation for a wider range of Pm values. This allows to analyse this process for culture methods with different characteristics than those of the experiments reported in this paper.

Fig. 3-14(a) and 3-14(c) show that $\bar{D}$ increases with Pm (see also Figure 3-15(a) for further simulations of microgel). This is because when the cells are able to move freely, random movements help them to find clusters in their surrounding area and adhere to them. The simulations show that even cells in small clusters may find larger ones in their neighbourhood and attach to them. This leads to removal of some of small clusters and formation of bigger ones.

Fig. 3-14(d) illustrates a big gap between δ for Pm=0 and δ for other values of Pm in suspension. This occurs due to the fact that cells die when they cannot move towards the other cells and adhere to them. Hence, few clusters remain after 21 days and this results in a lower standard deviation of cluster size. However, we note that this is not practically desirable. This figure indicates that there is no significant difference between the curves of δ for higher values of Pm.

The standard deviation of cluster size for microgels is quite different: δ reduces with Pm, see Fig. 3-14(b). This means that a hypothetical medium allowing higher cell motility (whilst retaining the other features of microgels) might improve the uniformity of size of the clusters. However, this is not applicable to the experiments undertaken here as the parameter regime for those cases is quite different. However, these results give insights into how different culture methods might affect spheroid formation.

5.

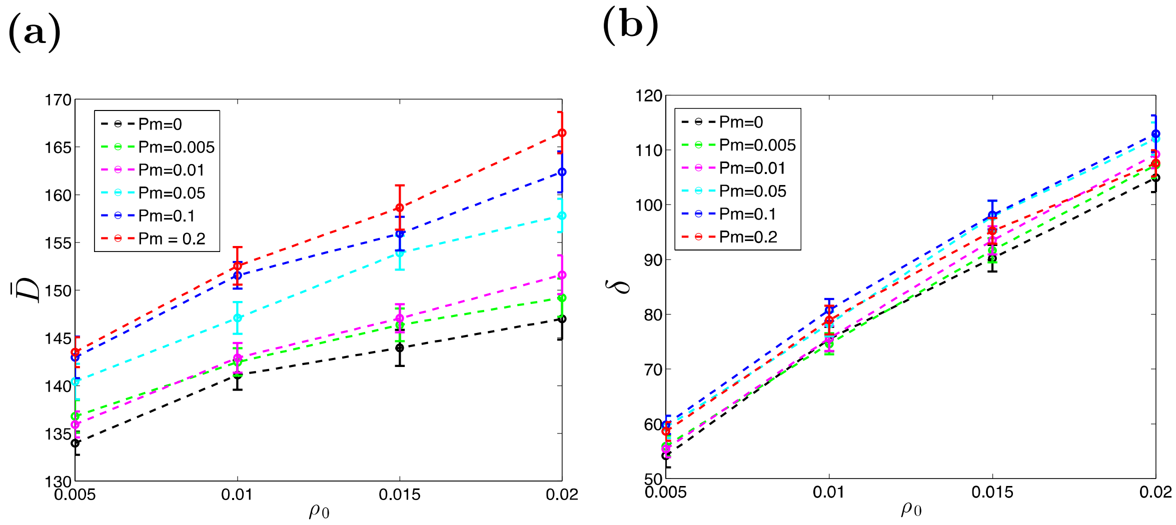

Figure 3-15 Microgel simulations with low values of Pm = {0, 0.005, 0.01, 0.05, 0.1, 0.2}. (a) standard deviation, δ, and (b) average, $\overline{D}$, of cluster size are depicted. The value of Pm for each curve is indicated in the legends. Other parameters are the same as for the simulations of Figure 3-10.

Table 3-1 Preparation of P(NIPAM-AA) microgels

NIPAM	AA	MBA	SDS	KPS
9.9 mmol	0.1 mmol	0.2 mmol	0.12 mmol	0.1 mmol
1.12g	6.86 µL	31 mg	35 mg	27 mg

CHAPTER FOUR

4. Multicellular spheroids formation and recovery in microfluidics-generated thermoresponsive microgel droplets

Chapter 4: Multicellular spheroids formation and recovery in microfluidics-generated thermoresponsive microgel droplets

X. Cui[a], Y. Liu[b], Y. Hartanto[a], J. Bi[a], S. Dai[a] and H. Zhang[a]

a School of Chemical Engineering, The University of Adelaide, Adelaide SA 5005, Australia

b School of Biochemical Engineering, East China University of Science and Technology, Shanghai, China

Graphical Abstract

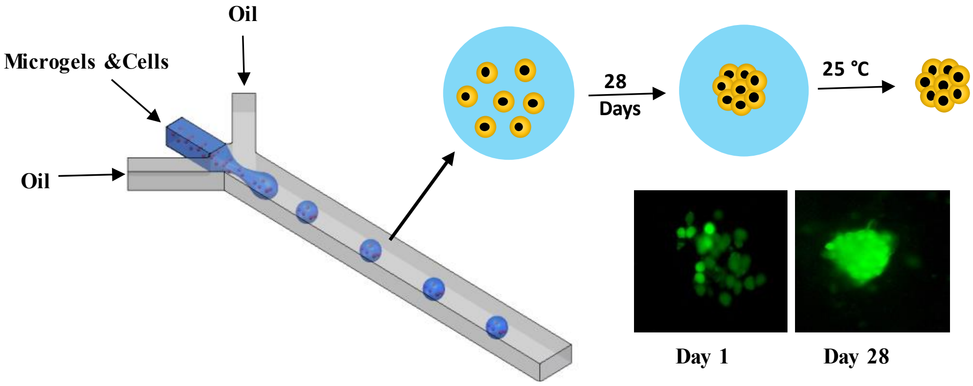

*Corresponding author: Dr Hu Zhang

Email: hu.zhang@adelaide.edu.au

Colloid and Interface Science Communication, 2016, 14, 4-7, DOI: 10.1016/j.colcom.2016.09.001

4.1 Abstract

Multicellular spheroids (MCSs) have a unique structure to represent the *in vivo* complex tissues and they have many potential applications, such as drug screening and evaluation. Traditional methods of fabricating MCSs have a low throughput and are incapable of controlling the MCS size and recovering MCSs during the harvest process. We developed a microfluidic approach to encapsulate Hela cells in thermoresponsive microgel-based droplet. After the microgels were turned into gel by raising the temperature to 37 °C, the oil residues were removed and the droplets were suspended in the cell culture medium to culture cells into spheroids. The microgel network provided a physical scaffold for cells so that cell aggregates formed in a mimicking *in vivo* condition. Due to the thermal reversibility of microgels, MCSs were released and harvested from the microgels droplets by simply cooling the droplets down to room temperature. This approach may open a new door for generating and harvesting uniform-sized MCSs

Key words: Biomaterial, Droplet, Thermal sensitive microgels, Tumour spheroids

4.2 **Introduction**

Most cells in the human body are living in a three-dimensional (3D) environment through interactions with neighboring cells and extracellular matrices (ECM) which are missing in traditional two dimensional monolayer culture [1]. Cell-cell and cell-ECM interactions have great impact on many biological activities such as homeostasis and cell signaling through functional junctions between cells [2]. The 3D cell culture model based on multicellular spheroids (MCSs) is a powerful tool to recapitulate the cell-cell and cell-matrix interactions that have been found in vivo [3] to preserve cellular viability, functionality and phenotype [4, 5] as well as a building bridge to connect cell-based and animal-based study [6]. Hence, a myriad of methods have been developed for fabrication of MCSs.

Conventional methods such as the hanging drop [7-9], the gyratory method [10, 11], non-adhesive culture [12], micro-fabricated confined culture [13, 14], accelerated aggregate-forming method [15] as well as liquid overlay culture [16] has been explored. Among them, micro-fabrication technology have been recently pursued due to the manipulatable sizes and shapes of MCSs in the confined environment. Microarrays [17], microwells [18] and microfluidic devices [19] are fabricated to generate small cavities and a high cell density is seeded in these cavities so that cells aggregate rapidly in such a confined environment to form MCSs. However, in this method, cells tend to settle in the bottom of the cavity due to gravity and the formed MCSs are unable to easily recover from the microfabrication devices.

Cell encapsulated in microfluidic channels is achieved by mixing the cell-laden hydrogels in one channel with crosslinking agents from another channel(s). This approach allows rapid formation of high-throughput [20] and miniaturized bioreactors for cell culture [21]. To date, hydrogels like alginate, agarose, gelatin and poly (ethylene glycol) [22-25], as well as double emulsion [26] have been attempted to encapsulate cells inside of droplets. Very few attempts are reported to culture cells in the crosslinked gel for a long term. Since the polymers are chemical crosslinked, potent or toxic chemicals may be required to break the shell to release MCSs [27]. For the double emulsion encapsulation since the middle layer between cells and the culture medium is an oil phase, the oxygen and nutrient diffusion rate is low, and this becomes the constraints for MCS growth.

In this study, we proposed a droplet-based microfluidics system to form and release spheroids as described in Fig. 4-1. HeLa cells were encapsulated inside the Poly (N-Isopropylacrylamide-co-acrylic acid) (P(NIAM-AA)) microgel based droplets. P(NIPAM-

AA) has a unique amphiphilic structure so the microgel network is thermal reversible. Its porous structure not only provides the physical support to embed cells in a 3D microenvironment but also allows sufficient oxygen and nutrient transportation. Our group has succeeded in using P(NIPAM-AA) microgels for culture of stem cells and HeLa tumor spheroids [28]. The cell-laden P(NIPAM-AA) microgel aqueous solution was squeezed into individual droplets by the oil phase from two side channels. The droplets were collected, heated and re-suspended in the cell culture medium for long-term culture for MCS formation after removal of oil residues. MCSs were harvested by cooling the gel to room temperature. The Lattice Boltzmann model (LBM) was employed to simulate the droplet formation process to optimize the control parameters. We are the first group to propose a droplet-based microfluidics system to form and release spheroids using thermal-responsive synthetic polymers. Different from natural polymers, this unique thermoresponsive material can release MCSs easily after long-term culture without introduction of toxic chemicals. In addition, through copolymerizing different co-monomers, the properties of the synthesized polymers can be tuned for different types of cells.

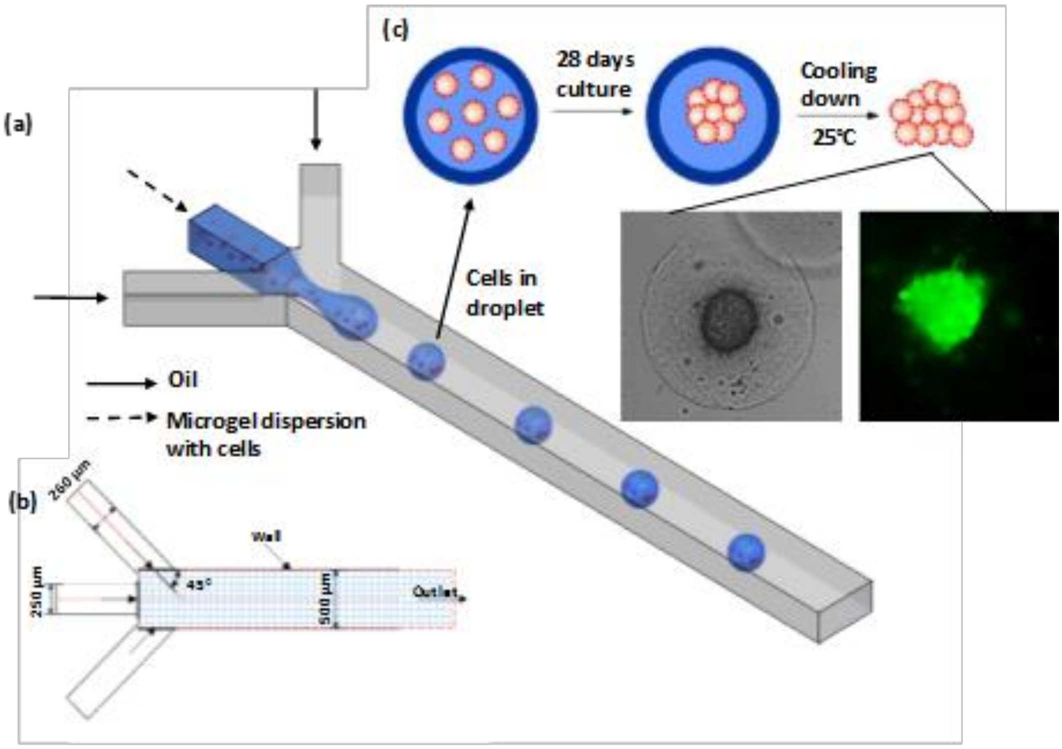

Figure 4-1 Droplet generation and cell encapsulation through microfluidics. (a) Droplet generation process inside a micro-channel; (b) Dimension and geometry of the micro-channel; (c) Multicellular spheroid formation inside the droplets and release from the droplets.

4.3 Materials and methods

4.3.1 Materials

N-Isopropylacrylamide(NIPAM, 99%+), acrylic acid (AA), *N,N*-methylenebisacrylamide(MBA, 98%+), potassium persulfate (KPS,99%+), and sodium dodecyl sulphate (SDS, 98.5%+) were purchased from Sigma-Aldrich. NIPAM was recrystallized in n-hexane for purification and dried in vacuum at room temperature. Dulbecco's Modified Eagle's Medium (DMEM), penicillin-streptomycin, phosphate-buffered saline (PBS), fetal bovine serum (FBS) as well as the Live/Dead viability/cytotoxicity kit (L3224) were purchase from Life Technologies.

4.3.2 Microchip fabrication

The geometry of the microchannel with its dimensions is shown in Fig.1. SU-8 50 photoresist (MicroChem, USA) was used to prepare the photolithography on silicon wafers. The soft-lithography technology was used to fabricate the PDMS-based micro-channels. PDMS was mixed with the curing agent at a ratio of 10:1 before pouring onto the silicon wafer. After placing it in the oven at 80 °C for 2 hr, PDMS was peeled off from the wafer. The inlet and outlet holes were punched. A cover slide was coupled with the micro-channel side after oxygen plasma treatment for 40 s at 20 W.

4.3.3 Microgel synthesis

Free radical emulsion polymerization was carried out for P(NIPAM-AA) microgels based on the formula provided in Table 1. For a standard procedure, 9.9 mmol NIPAM and 0.1 mmol AA, 0.2 mmol MBA (31 mg) along with 0.2 mmol SDS (57.5 mg) were dissolved in 97 mL Milli-Q water. After mixing thoroughly, the solution was transferred into a 250 ml three-necked flask. The flask was fitted with a condenser and a mechanical stirrer. The solution was degassed under a nitrogen atmosphere for 30 min before moving to a pre-heated 70 °C bath. 3.0 mL KPS aqueous solution (0.1 mmol, 27 mg) was injected into the solution to trigger the polymerization. The synthesis lasted 5 hr under continuous stirring and nitrogen atmosphere. After the polymerization, the microgels were purified by membrane dialysis (the cut-off M_w of 12-14 kDa) against Milli-Q water for a week and Milli-Q water was changed daily. The purified microgels were concentrated by heating up to 70 °C with continuous stirring. 200 μL microgel dispersion was dried at 70 °C in order to calculate the concentration of microgels.

4.3.4 Cell culture

The HeLa cells were incubated in a pre-mixed culture medium (DMEM with 10 % FBS, 100 units per mL penicillin) in a humidified environment with 5 % CO_2 supply at 37 °C until confluence and they were harvested for droplet encapsulation.

4.3.5 Droplet generation and cell encapsulation

The microgel dispersion was mixed with cells at a cell density of 2.5×10^5 /mL at a ratio of 3:2 to obtain a final concentration of 1.0×10^5 cells/mL. The mixed solution was pumped through a syringe pump at a flow rate 20 µL/hr into the middle inlet. Cooking oil was pumped into both side inlets at a flow rate of 100 µL/hr. The droplets were collected from the outlet of the microchannel, and stored in the oil in a 24 well-plate.

4.3.6 Three-dimensional cell culture in the droplet

After collecting all droplets, the cooking oil was heated up to 37 °C and the temperature maintained at 37 °C until all the droplets turned into white. The droplets were washed with pre-warmed PBS buffer 3 times to remove any oil residues. The droplets were dispersed in the pre-warmed culture medium. Cells were cultured for a predefined period and the culture medium was changed every two days.

4.3.7 Spheroid morphologies

The Live/Dead cytotoxicity/viability kit was applied to stain live and dead cells so that the cell cluster morphologies were observed. Typically, 1 µM calcein AM and 2.5 µM ethidium homodimer-1 (EthD-1) solutions was prepared based on the protocol provided from the supplier. Before staining the cells, the culture medium was removed first. The droplets were washed with warmed PBS buffer two times then the stain solution was added into the droplets. After 30 min incubation, the droplets were washed with warm PBS buffer again to remove the dye residue. The droplets were picked up by pipettes, and placed on a glass slide. The droplets were observed under a fluorescent microscopy.

4.3.8 LBM modelling: Lattice Boltzmann immiscible two-phase model

The Reis and Phillips model [29], which belongs to the RothmanKeller(RK) family and is based on the colour gradients to maintain a sharp interface, was used in this study. The advantage of this approach is its flexibility with the model parameters to be chosen, such as surface tension, density ratio and viscosity ratio between fluids on either side of an interface.

In this model, The Lattice Boltzmann equation with a single relaxation parameter for each fluid was applied with a D2Q9 lattice.

The distribution function for a fluid of colour k (with k = r for red and k = b for blue) was noted as $N_i^k = (\vec{x}, t)$, and $N_i = (\vec{x}, t)$ was the sum of $N_i^r = (\vec{x}, t)$ and $N_i^b = (\vec{x}, t)$. If the time step was set as $\triangle$t = 1, the algorithm was based on the following evolution equation:

$$N_i^k(\vec{x} + \vec{c}_i, t + 1) = N_i^k(\vec{x}_i, t) + \Omega_i^k(N_i^k(\vec{x}_i, t)) \qquad (1)$$

Where $\vec{c}_i$ was the velocity vectors[30], and Ω_i^k was the collision operator, which was the combination of two sub-operators[30]

$$\Omega_i^k = (\Omega_i^k)^{(1)} + (\Omega_i^k)^{(2)} \quad i = 0 \ldots .8 \qquad (2)$$

The first sub-operator $(\Omega_i^k)^{(1)}$ was the standard BGK operator for the single-phase LBM, and $(\Omega_i^k)^{(2)}$ was the two-phase collision operator[29]. The distribution functions were relaxed towards a local equilibrium and ω_k was the relaxation factor:

$$\left(\Omega_i^k\right)^{(1)}\left(N_i^k\right) = N_i^k - \omega_k(N_i^k - N_i^{k(e)}) \qquad (3)$$

The density of the fluid k was given by:

$$\rho_k = \sum_i N_i^k = \sum_i N_i^{k(e)} \qquad (4)$$

The total fluid density was the summation of the density of two phases $\rho = \rho_r + \rho_b$, and the total momentum was defined as:

$$\rho\vec{u} = \sum_i \sum_k N_i^k \vec{c}_i = \sum_i \sum_k N_i^{k(e)} \vec{c}_i \qquad (5)$$

in which $\vec{u}$ was the local velocity of the fluid. The equilibrium functions were formulated by [29]:

$$N_i^{k(e)} = \rho_k(\emptyset_i^k + W_i\left[3\vec{c}_i \times \vec{u} + \tfrac{9}{2}(3\vec{c}_i \times \vec{u})^2 - \tfrac{3}{2}(\vec{u})^2\right]) \qquad (6)$$

These equilibrium distribution functions, $N_i^{k(e)}$, were chosen for the conservation of mass and momentum [29]. The weight, W_i, was assigned for a standard D2Q9 lattice:

$$W_i = \begin{cases} 4/9\,, i = 1 \\ 1/9\,, i = 2,4,6,8 \\ 1/36, i = 3,5,7,9 \end{cases} \qquad (7)$$

Moreover, $\emptyset_i^k$ as

$$\emptyset_i^k = \begin{cases} \alpha_k, & i = 1 \\ (1-\alpha_k)/5, & i = 2,4,6,8 \\ (1-\alpha_k)/20, & i = 3,5,7,9 \end{cases} \tag{8}$$

Where α_k was a free parameter[29].

Further, the color field ψ was a function with its value between -1 and 1. The value of -1 and 1 represented only red fluid or only blue fluid in the calculated grid, respectively. In an interface, the color field was between -1 and 1.

$$\Psi = \frac{\rho_r - \rho_b}{\rho_r + \rho_b} \tag{9}$$

The LBM method was implemented in the Matlab code, which was modified from Leclaire et al. [30]

4.4 Result and discussion

4.4.1 Droplet formation

A polydimethylsiloxane (PDMS) microfluidic microchannel was fabricated using the soft-lithography technique. The PDMS microchannel was designed as a flow focusing device, which was composed of one water channel in the middle and two oil channels at both sides to produce the immiscible interfaces when the two flows focused at the intersection. Two streams of continuous oil phase flowed through two sides and squeezed the forefront stream of the dispersed fluid into droplets. One of the important control parameters in the droplet generation was the flow ratio between the dispersed and continuous phase. When the flow ratio was beyond a certain point, the shear force generated from continuous flow streams was no longer strong enough to cut off the dispersed phase to form individual droplets, and a jetting flow pattern was produced [31]. We first used LBM simulations to map the flow patterns inside the microchannel by varying the flow ratios and then to determine the optimized flow ratio for droplet generation.

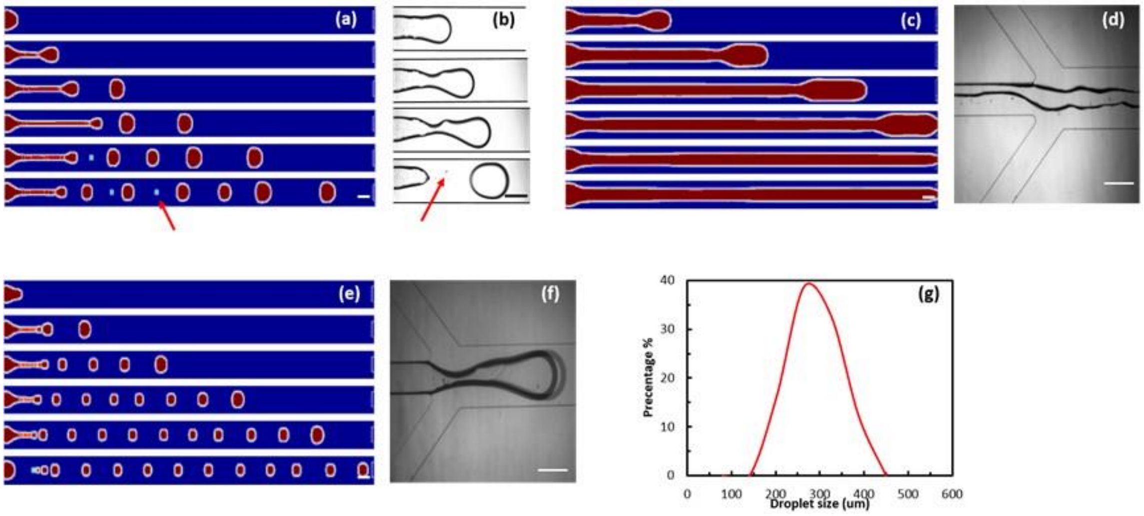

Figure 4-2 LBM simulation results at different flow ratios and comparison between simulation and experimental results. The dispersed aqueous solution entered the middle inlet at a fixed flow rate at 5 µL/h, and the continuous oil phase flew from the side inlets at different flow rates. Red represents water and blue represents oil. (a) LBM temporal results at a flow ratio of 1:4 of microgel dispersion phase to the oil phase. (b) Experiment results for temporal droplet formation in the same microchannel and at the same flow conditions as (a). The red arrow indicates the satellite droplet occurring during the experiment. (c) LBM results at a flow ratio of 1:1. (d) Experimental results in the same microchannel and at the same flow conditions as (c). (e) LBM results at a flow ratio of 1:6. (f) Experiment result in the same microchannel and at the same flow conditions as (e). (g) Droplet size distribution at a flow ratio of 1:4 between the dispersed and the continuous phase. Scale bar is 200µm.

The LBM approach has been widely applied to predict and simulate the fluid flow in the microchannel due to its well-defined boundary conditions [32]. Fig. 4-2a,c,e show temporal development of droplet generation at different flow ratios and the simulation results are also compared with experimental results shown in Fig. 4-2b,d,f. At a flow ratio of 1:4 between the dispersed and continuous fluid as shown in Fig. 4-2a, the flow of the central fluid was disturbed by two flows from the side inlets and a spherical shape was formed at the forefront of the flow. The central stream was attenuated at the merging position by side streams. The attenuated part was further stretched and a single droplet was produced because the surface tension force was not able to maintain the neck of the spherical part at the forefront. Due to disparity of the capillary force during the droplet formation, satellite droplets were observed as indicated by the red arrow in Fig. 4-2a and Fig. 4-2b [33]. The droplet evolution as the flow development inside the channel from LBM was further compared with that from experimental observations shown in Fig. 4-2b. The predictions were able to map the fluid flow from the experimental observations. To further increasing the fluid flowrate at the side inlets to keep a flow ratio of 1:6, individual single droplets were generated as shown in Fig.

4-2e. As the force generated from the side streams was larger than that at a flow ratio of 1:4, the attenuated part was less stretched. The size of droplets was around 100 µm, smaller than that for the flow ratio of 1:4 (around 200 - 300 µm). At a flow ratio of 1:1, a jetting flow pattern [31] was observed inside the microchannel (Fig. 4-2c). A stable immiscible oil/water interface was developed as the central fluid traveled along with the continuous phase. The force from the side flows was not strong enough to squeeze the central fluid into droplets, and the spherical shape at the forefront was elongated as the fluid further developed inside the channel. The predictions were in agreement with the experimental image as shown in Fig. 4-2d. Fig. 4-2g shows the size distribution of the droplet at a flow ratio of 1:4. The majority (more than 40%) of the droplets have the size around 260 µm. More than 80% of the droplets are in the range between 250 - 350 µm. The distribution may reflect the nature of droplet coalescence within the microchannel in the absence of surfactants [34]. Based on the LBM simulations, the optimal flow ratio was chosen to be 1:4 for the following experiments.

4.4.2 Droplet collection and thermal –reversibility

P(NIPAM-AA) has a unique amphiphilic structure so the microgel network is thermally reversible, which was confirmed from the temperature dependence of its hydrodynamic size (Fig. 4-6) and elastic/viscous modulus (Fig. 4-7). The SEM image (Fig. 4-8) in supporting document shows a porous structure which not only provides the physical support for embedding cells in a 3D microenvironment but also allows sufficient oxygen and nutrient transportation. After collecting the droplets at the exit of the microchannel, the droplets were heated up to 37 °C, and their colour changed from transparent (Fig. 4-3a) into white which is shown at Fig. 4-3b. When the temperature of the microgels within the droplets was above the volume phase transition temperature of the microgels (VPTT, around 32ºC from our previous report [28]), the microgels became hydrophobic from hydrophilic due to the presence of N-isopropylacrylamide. In additional, due to hydrophobic attractions and electrostatic repulsions, physical gel was formed [28]. The physical gel presented a white cloudy colour, which is shown darkness under an optical microscope. The size of the droplet slightly decreased during the heating up process since the microgels shrank due to loss of surrounding water molecules.

After washing the microgels with pre-warmed PBS buffer (37 °C) to remove the oil residue, the droplets were transferred into a pre-warmed culture medium. The physical gel was able to maintain its spherical shape as shown in Fig.4-3c since at 37 °C, the hydrophobic nature of the microgel prevented water from entering into its inner structure. Fig. 4-3d-h demonstrate the collapse process of the microgel structure every two minutes when the temperature reduced to the room temperature. During the first 6 min, the colour of the droplet gradually changed into transparent and the droplets were able to maintain their size and shape. After 6 min, the droplets started to lose their shape, and the size of the droplets expanded, which indicated microgels were dispersed into water.

We hypothesized that cells are encapsulated into the uniform-sized droplets generated from the microchannel, and then the droplets gel at 37 °C and disperse in the cell culture medium for cell growth and cellular spheroid formation, finally the cellular spheroids are released from the droplets after the temperature reduces to the room temperature for harvest, as shown in Fig. 4-1. Comparing with other previous reports using droplet encapsulation of cells [25, 27], in which cells are unable to release from droplets without strong or toxic chemicals.

4.4.3 Three dimensional culture inside droplets

We encapsulated HeLa cells inside the microgel-containing droplets. After suspending droplets in the cell culture medium for the pre-set days, we collected the droplets and cooled down to the room temperature to harvest the MCSs. We found out that it took 20 minutes to dissolve the droplets and release the MCSs. Fig. 4-4 shows the HeLa MCS formation process inside the droplets for up to 28 days. The microgels inside the droplet provided a 3D structure to support cell growth from our previous study [28]. The porous structure inside the droplet provided a 3D structure to support growth due to sufficient nutrient, oxygen and bio-waste transportation (Figure 4-8, supporting document). At day 7, cells proliferated and aggregated to form a few cell clusters in each droplet, and the cell cluster size varied depending on the initial cell distribution within the droplets in comparison with single individual cells at day 1 as shown in Fig. 4-9 (supporting document), which was similar to cluster formation in the 3D scaffold [35]. After continuing cell culture for another 7 days (Fig. 4-4b), the size of the big cluster increased to 40 - 50 μm while a few small clusters scattered around the big clusters. The loose structure indicates the first step of multicellular spheroid formation where cells are drawn together due to the combination of ECM fibers with multiple RGD motifs. At day 21 (Fig. 4-4c), smaller clusters aggregated into the big cluster to have a size of 50 μm and a few smaller clusters were observed within the droplet. At day 28, the edge of the big cluster became smoother which indicated the spheroid compaction stage was reached [36] where the hemophilic cadherin-cadherin binding and microfilaments of cells become localized along the cell. Due to the controlled microenvironment provided from the droplet, the spheroid size can be manipulated by adjusting the droplet size, initial cell density and cell culture duration. Compared with the normal HeLa cluster size around 250 µm with a size variation of 50 µm in the conventional culture condition [21], this approach can provide more uniform-sized multicellular spheroids.

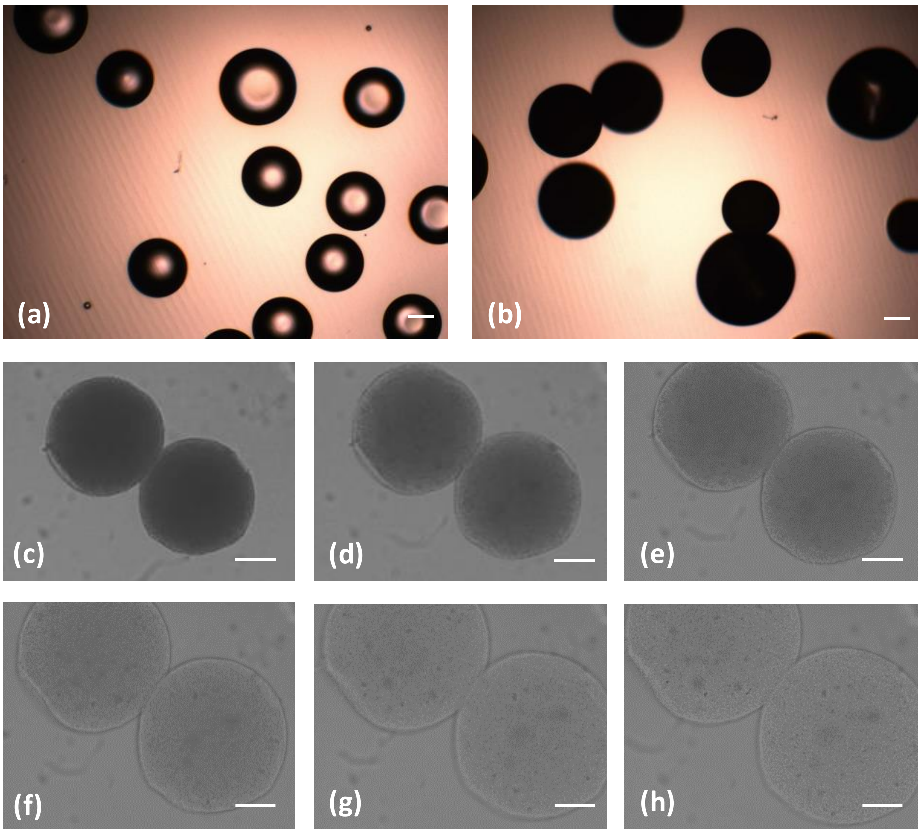

Figure 4-3 Droplet collection and thermal response at different temperatures. (a) Microgel-containing droplet collection at room temperature in the oil. The dark edge of droplets is seen due to light reflection between oil and water. (b) The hydrophilicity of droplets turns into hydrophobicity at 37 °C in oil. Opaque hydrophobic droplets show complete darkness. (e) to (h) Snapshot of reversible changes of droplets in the cell culture medium when cooling down to room temperature every 2 minutes. Scale bar is 100 µm.

To further investigate the cluster morphology, live/dead cells images were taken by staining cells with Live/Dead cell kit. Fig. 4-5 shows cluster formation process from variable cells within a droplet. This approach was less toxic to cells and most cells were still green up to 28 day culture, which means cells had a high viability. At day 7, within the droplet, smaller clusters started to form (Fig. 4-5a), and these clusters were drawn closely as cells synthesized their extracellular matrices. After another 7-day culture (Fig. 4-5b), small clusters aggregated to form a loose structure, and a few single cells or small clusters were observed around the loose structure. At day 21 (Fig. 4-5c) the loose structure started the compaction process, but the cavities were seen inside the structure. After 28 day culture (Fig. 4-5d), mature spheroids were obtained with a spherical shape and a very compact structure was observed.

In this microgel-containing droplet microenvironment, cells are confined in the given space and aggregated to form the spheroids. Meanwhile the nutrients and wastes are transferred to the cell clusters to maintain cellular activities. Importantly, the spheroids are harvested simply by reversing the temperature to the room temperature without physical or chemical damage. Therefore, this technique can be used to generate size-controllable spheroids for further drug screening or biological investigations.

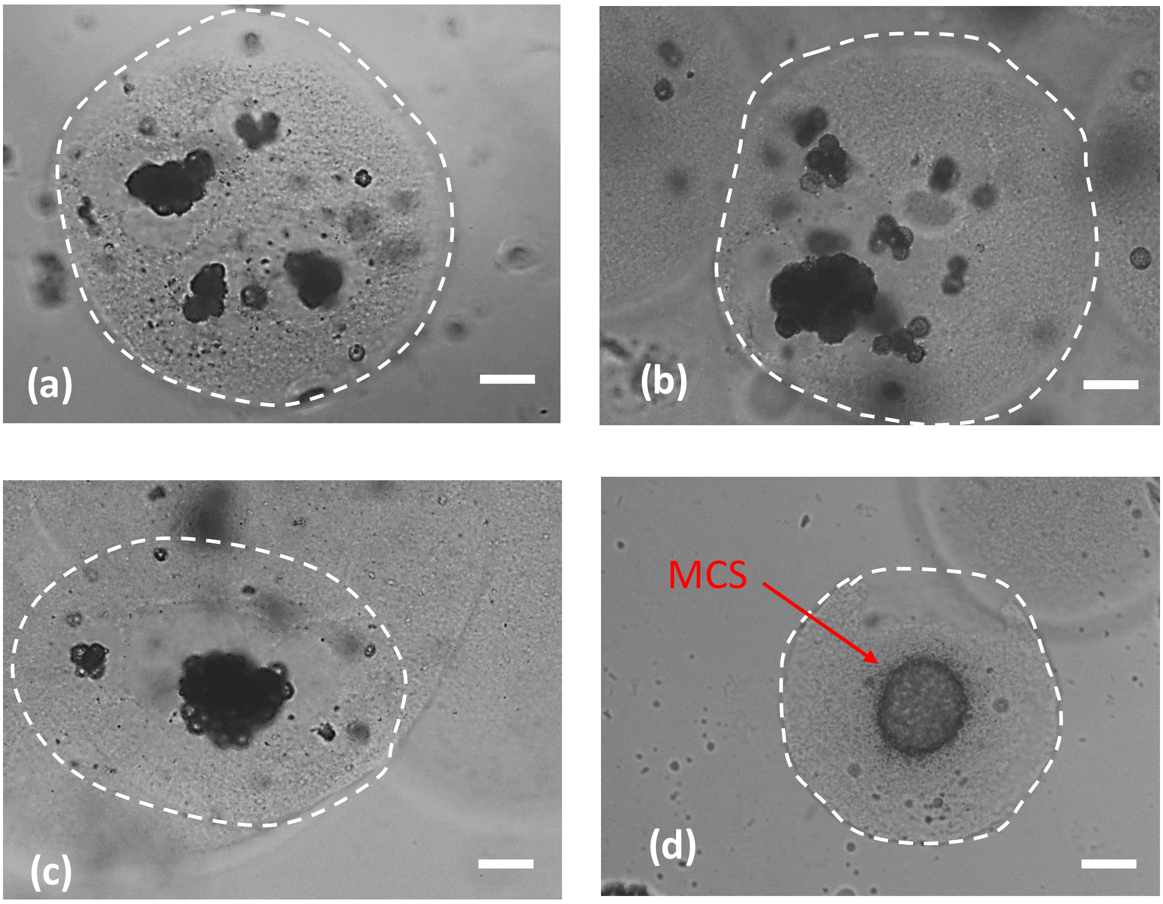

Figure 4-4 MCSs formation inside the droplets at (a) day 7, (b) day 14, (c) day 21, (d) day 28. Scale bar is 50 µm. Dash line is droplet boundary

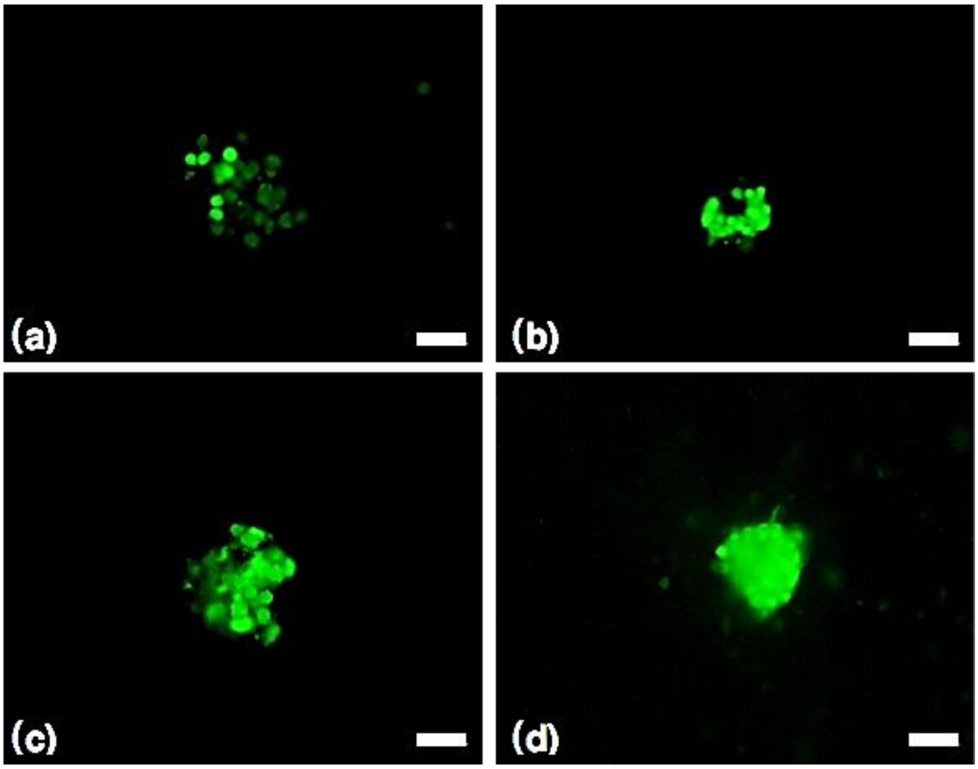

Figure 4-5 Live/Dead images of the MCSs inside the droplets at (a) day 7, (b) day 14, (c) day 21, (d) day 28. Scale bar is 50 µm

4.5 **Conclusions**

We developed an approach to encapsulate Hela cells in the thermoresponsive microgel-based droplets, and the cells were further cultured in the hydrogel network to form multicellular spheroids. A LBM simulation method was used to optimise the droplet formation process and a flow ratio between the center stream and two side streams was found to be over 1:4. After MCSs were formed in the microgels, the MCSs were recovered by cooling down to room temperature without introduction of any toxic chemicals. The full recoverability and 3D controlled environment in the system render this approach a promising avenue for multicellular spheroid formation and harvest.

4.6 **Acknowledgements**

The microfluidic channels were made in the ANFF SA node at The University of South Australia and we acknowledge technical supports from the team at the node. XC would like to acknowledge the divisional scholarship given by the University of Adelaide. HZ thanks the financial support from ARC Discovery Project (DP160104632) and The Medical Advancement Without Animal (MAWA) Trust.

4.7 **Reference**

1. Pampaloni, F., E.G. Reynaud, and E.H.K. Stelzer, The third dimension bridges the gap between cell culture and live tissue. Nat Rev Mol Cell Biol, 2007. 8(10): p. 839-845.

2. Bosenberg, M.W. and J. Massagué, Juxtacrine cell signaling molecules. Current Opinion in Cell Biology, 1993. 5(5): p. 832-838.

3. Baraniak, P.R. and T.C. McDevitt, Scaffold-free culture of mesenchymal stem cell spheroids in suspension preserves multilineage potential. Cell and Tissue Research, 2011. 347(3): p. 701-711.

4. Korff, T. and H.G. Augustin, Integration of Endothelial Cells in Multicellular Spheroids Prevents Apoptosis and Induces Differentiation. The Journal of Cell Biology, 1998. 143(5): p. 1341-1352.

5. Lu, H.-F., et al., Three-dimensional co-culture of rat hepatocyte spheroids and NIH/3T3 fibroblasts enhances hepatocyte functional maintenance. Acta Biomaterialia, 2005. 1(4): p. 399-410.

6. Wang, Y. and J. Wang, Mixed hydrogel bead-based tumor spheroid formation and anticancer drug testing. Analyst, 2014. 139(10): p. 2449-2458.

7. Nyberg, S.L., et al., Rapid, large-scale formation of porcine hepatocyte spheroids in a novel spheroid reservoir bioartificial liver. Liver transplantation, 2005. 11(8): p. 901-910.

8. Kim, J.B., R. Stein, and M.J. O'Hare, Three-dimensional in vitro tissue culture models of breast cancer-- a review. Breast Cancer Res Treat, 2004. 85(3): p. 281-91.

9. Ingram, M., et al., Three-dimensional growth patterns of various human tumor cell lines in simulated microgravity of a NASA bioreactor. In Vitro Cellular & Developmental Biology-Animal, 1997. 33(6): p. 459-466.

10. Carpenedo, R.L., C.Y. Sargent, and T.C. McDevitt, Rotary suspension culture enhances the efficiency, yield, and homogeneity of embryoid body differentiation. Stem cells, 2007. 25(9): p. 2224-2234.

11. Manley, P. and P.I. Lelkes, A novel real-time system to monitor cell aggregation and trajectories in rotating wall vessel bioreactors. Journal of biotechnology, 2006. 125(3): p. 416-424.

12. Yuhas, J.M., et al., A simplified method for production and growth of multicellular tumor spheroids. Cancer Research, 1977. 37(10): p. 3639-3643.

13. Napolitano, A.P., et al., Dynamics of the self-assembly of complex cellular aggregates on micromolded nonadhesive hydrogels. Tissue engineering, 2007. 13(8): p. 2087-2094.

14. Baac, H., et al., Submicron-scale topographical control of cell growth using holographic surface relief grating. Materials Science and Engineering: C, 2004. 24(1): p. 209-212.

15. Kamihira, M., et al., Spheroid formation of hepatocytes using synthetic polymer. Annals of the New York Academy of Sciences, 1997. 831(1): p. 398-407.

16. Sakai, S., S. Ito, and K. Kawakami, Calcium alginate microcapsules with spherical liquid cores templated by gelatin microparticles for mass production of multicellular spheroids. Acta biomaterialia, 2010. 6(8): p. 3132-3137.

17. Lee, M.-Y., et al., Three-dimensional cellular microarray for high-throughput toxicology assays. Proceedings of the National Academy of Sciences, 2008. 105(1): p. 59-63.

18. HoáLee, K., et al., Diffusion-mediated in situ alginate encapsulation of cell spheroids using microscale concave well and nanoporous membrane. Lab on a chip, 2011. 11(6): p. 1168-1173.

19. Chen, M.C., M. Gupta, and K.C. Cheung, Alginate-based microfluidic system for tumor spheroid formation and anticancer agent screening. Biomedical microdevices, 2010. 12(4): p. 647-654.

20. Velasco, D., E. Tumarkin, and E. Kumacheva, Microfluidic encapsulation of cells in polymer microgels. Small, 2012. 8(11): p. 1633-1642.

21. Serra, M., et al., Microencapsulation technology: a powerful tool for integrating expansion and cryopreservation of human embryonic stem cells. PLoS One, 2011. 6(8): p. e23212.

22. Tumarkin, E., et al., High-throughput combinatorial cell co-culture using microfluidics. Integrative Biology, 2011. 3(6): p. 653-662.

23. Sakai, S., et al., Cell-enclosing gelatin-based microcapsule production for tissue engineering using a microfluidic flow-focusing system. Biomicrofluidics, 2011. 5(1): p. 013402.

24. Kumachev, A., et al., High-throughput generation of hydrogel microbeads with varying elasticity for cell encapsulation. Biomaterials, 2011. 32(6): p. 1477-1483.

25. Utech, S., et al., Microfluidic Generation of Monodisperse, Structurally Homogeneous Alginate Microgels for Cell Encapsulation and 3D Cell Culture. Advanced healthcare materials, 2015. 4(11): p. 1628-1633.

26. Chan, H.F., et al., Rapid formation of multicellular spheroids in double-emulsion droplets with controllable microenvironment. Scientific reports, 2013. 3.

27. Yoon, S., et al., Droplet-based microfluidic system to form and separate multicellular spheroids using magnetic nanoparticles. Lab on a Chip, 2013. 13(8): p. 1522-1528.

28. Shen, Z., et al., Exploring thermal reversible hydrogels for stem cell expansion in three-dimensions. Soft Matter, 2012. 8(27): p. 7250-7257.

29. Reis, T. and T.N. Phillips, Lattice Boltzmann model for simulating immiscible two-phase flows. Journal of Physics A: Mathematical and Theoretical, 2007. 40(14): p. 4033-4053.

30. Leclaire, S., M. Reggio, and J.-Y. Trépanier, Numerical evaluation of two recoloring operators for an immiscible two-phase flow lattice Boltzmann model. Applied Mathematical Modelling, 2012. 36(5): p. 2237-2252.

31. Anna, S.L., N. Bontoux, and H.A. Stone, Formation of dispersions using "flow focusing" in microchannels. Applied Physics Letters, 2003. 82(3): p. 364-366.

32. Gunstensen, A.K. and D.H. Rothman, Lattice-Boltzmann studies of immiscible two-phase flow through porous media. Journal of Geophysical Research: Solid Earth, 1993. 98(B4): p. 6431-6441.

33. Tan, Y.-C., V. Cristini, and A.P. Lee, Monodispersed microfluidic droplet generation by shear focusing microfluidic device. Sensors and Actuators B: Chemical, 2006. 114(1): p. 350-356.

34. Mazutis, L. and A.D. Griffiths, Selective droplet coalescence using microfluidic systems. Lab on a Chip, 2012. 12(10): p. 1800-1806.

35. Lei, Y. and D.V. Schaffer, A fully defined and scalable 3D culture system for human pluripotent stem cell expansion and differentiation, in Proceedings of the National Academy of Sciences. 2013. p. E5039-E5048.

36. Lin, R.Z. and H.Y. Chang, Recent advances in three-dimensional multicellular spheroid culture for biomedical research. Biotechnol J, 2008. 3(9-10): p. 1172-84.

4.8 **Supporting document**

Chapter 4: Multicellular spheroids formation and recovery in microfluidics-generated thermoresponsive microgel droplets

X. Cui[a], Y. Liu[b], Y. Hartanto[a], J. Bi[a], S. Dai[a] and H. Zhang[a]

a. School of Chemical Engineering, The University of Adelaide, Adelaide SA 5005, Australia

b. School of Biochemical Engineering, East China University of Science and Technology, Shanghai, China

Corresponding :Dr. Hu Zhang

Hu.zhang@adelaide.edu.au

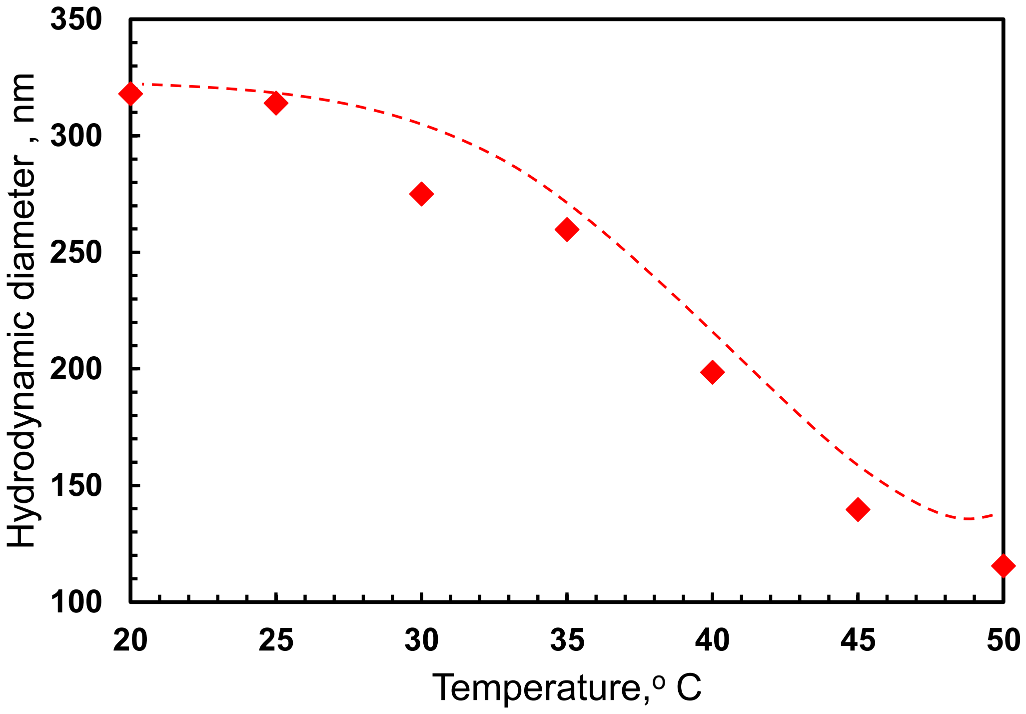

Figure 4-6 Temperature dependent hydrodynamic diameter of P(NIPAM-AA)

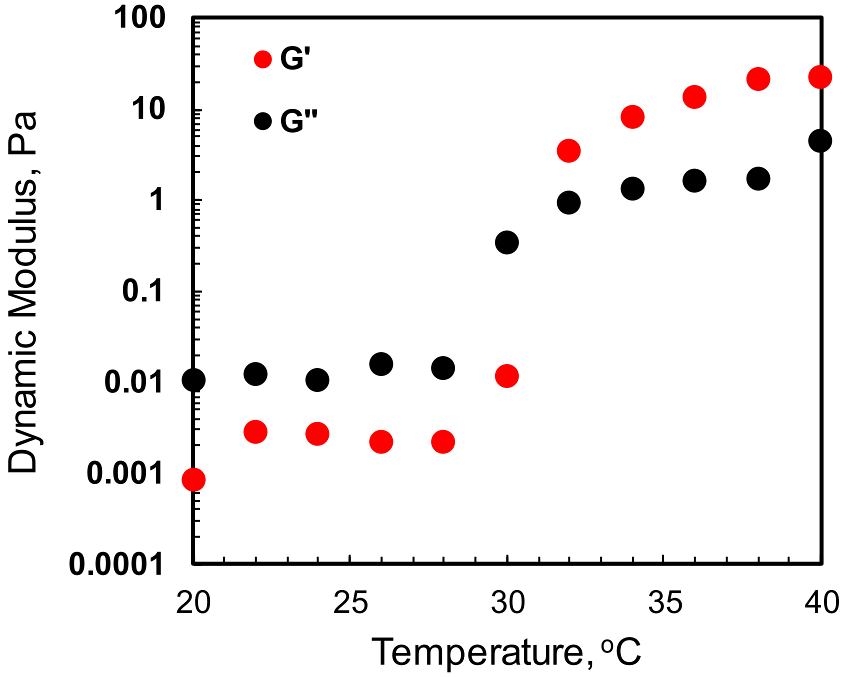

Figure 4-7 The temperature dependence of the dynamic moduli for 30 mg/mL P(NIPAM-AA) in PBS buffer. G’ is elastic (or storage) modulus. G” is viscous (or loss) modulus

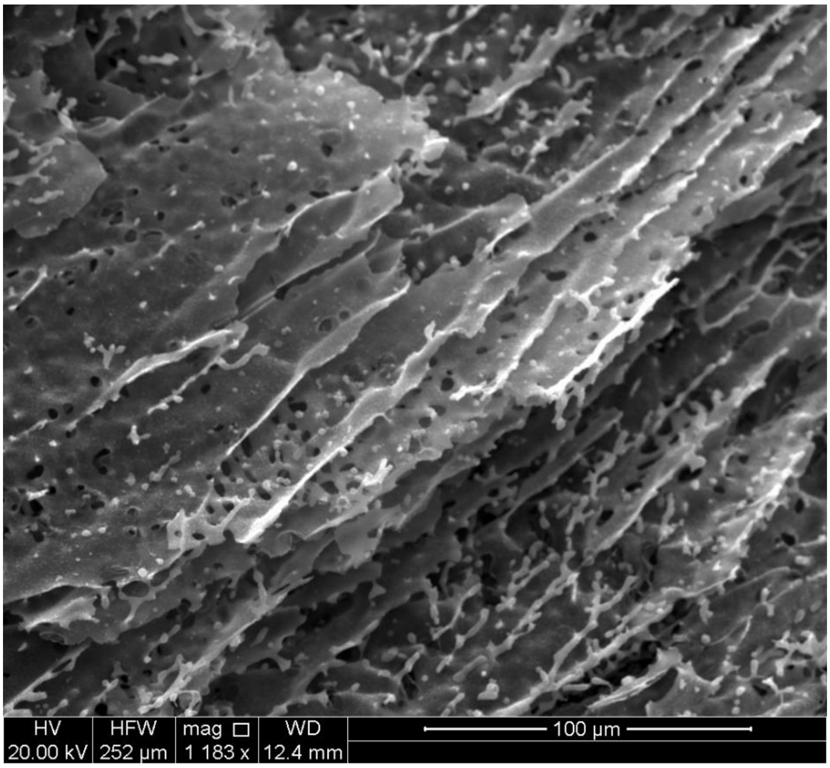

Figure 4-8 SEM of porous microgels scaffold

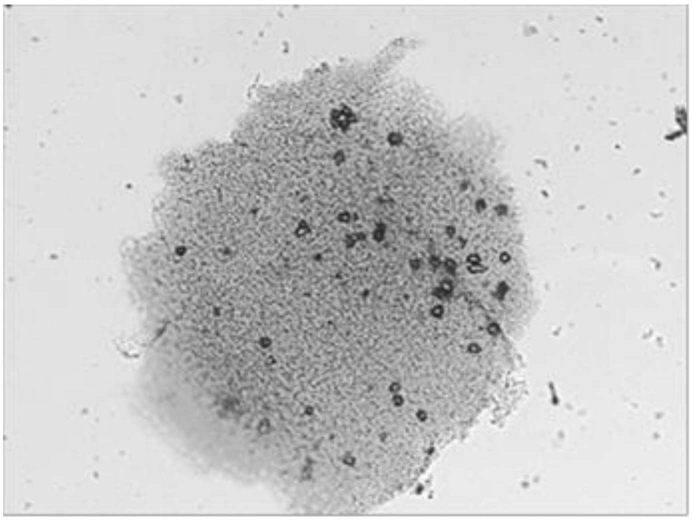

Figure 4-9 Single individual cells are distributed in partially liquefied microgel solution. The single cells are shown in black spots in the solution.

CHAPTER FIVE

5. Tuning the microenvironment for tumour spheroids formation

Chapter 5: Tuning the microenvironment for tumour spheroids formation

X Cui, Y Hartanto, J Bi, S Dai and H Zhang

School of Chemical Engineering, The University of Adelaide, SA 5005, Australia

Graphical Abstract

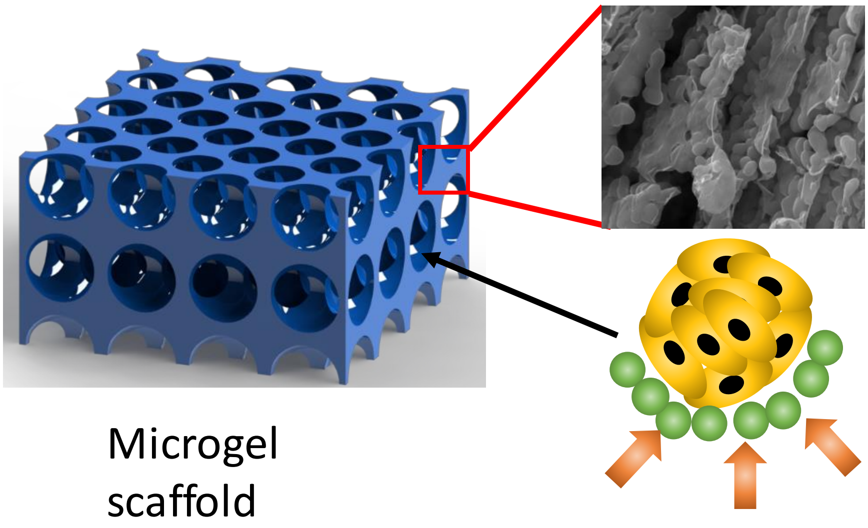

*Corresponding author: Dr Hu Zhang

Email: hu.zhang@adelaide.edu.au

5.1 Abstract

Tumor spheroids are considered as an effective 3D *in-vitro* model in drug screening and evaluation. Three-dimensional scaffolds-based cell culture becomes very promising in producing multicellular spheroids. Different from other approaches, 3D scaffolds mimic the *in-vivo* cellular microenvironment which encourages intercellular and extracellular interactions. The properties of the cellular microenvironment includes the surface wettability, chemistry, and charge of the scaffolds which may influence cell attachment, proliferation as well as migration and these properties are essential for multicellular spheroids formation. Through co-polymerization with different carboxylic acids, we demonstrate that the surface charge density and hydrophobicity of the microenvironment have a great impact on the tumour spheroids formation progress and their size distribution. Our results show that a scaffold with a moderate negative charge density and a highly hydrophilic surface promotes cell proliferation, resulting in the formation of larger spheroids in a more rapid way.

Key words: Thermosensitive microgels, Tissue engineering, Microenvironment, Multicellular spheroids.

5.2 Introduction

Three dimensional tumour spheroids culture is considered as one of the advanced tools to screen and evaluate anti-cancer drugs. It provides a similar complex spatial and temporal structure that is seen in the in vivo environment [1], and duplicates the concentration gradients observed in the tumours spheroids from patients. This 3D spheroid culture has great potential in accelerating the novel drug discovery and development process [2].

Traditional approaches of culturing 3D tumour spheroids, such as liquid overlay based on non-adhesive surfaces [3-5], suspension culture in mechanically stirred spinner flasks [6-8], and hanging drops [9-13], have been explored in the laboratory scale. A rotary cell culture system developed by National Aeronautics and Space Administration (NASA) has demonstrated its potential of commercializing the 3D spheroid culture in a large scale. Nevertheless, these approaches cannot create the *in-vivo* mimicking microenvironment for spheroids formation since they fail to provide the necessary physical support for the cells to replicate cell-extracellular matrix (ECM) interactions which are important for cell behaviors [14]. Furthermore a large variation in the spheroid size distribution and intensive labor demand also impede these conventional approaches for commercial success.

Polymer scaffolds have been pursued for engineering tissues in the lab. Their rich networks and cellular mimicking matrices supply physical and structural support for tumour spheroids formation, facilitate cell-to-cell interactions and provide surfaces for cell attachment [15-17]. Natural hydrogels are one of the best candidates for the scaffold due to their biocompatibility. Most natural hydrogel scaffolds enhance cell proliferation as well as promote spheroids formation[18]. However, lack of design flexibility, expensive cost for some natural polymers, poor handling characteristics and poor reproducibility have hampered their applications in spheroids culture [19]. As a result, synthesized hydrogels have emerged as alternatives for the engineering scaffolds. Apart from the capability of mimicking key features of the extracellular microenvironment, they can also be modified to modulate cell behaviors and promote cell attachment [20]. It was reported that the stiffness of the hydrogels influenced cell viability and proliferation [21]. Proliferation and adhesion of cells on polymer materials were also affected by surface characteristics such as wettability, chemical groups, and surface charge [22]. Therefore, we proposed to synthesize a range of thermosensitive hydrogels to construct the microenvironment for tumour spheroids formation and the microenvironment was tuned for its hydrophobicity/hydrophilicity, surface charge and chemical groups. In addition, cells on their own have different capacities of forming spheroids, and cells are also important for probing the interactions between cells and polymer scaffolds. Therefore, different cell lines were selected for investigating the impact of spheroid formation due to cellular properties.

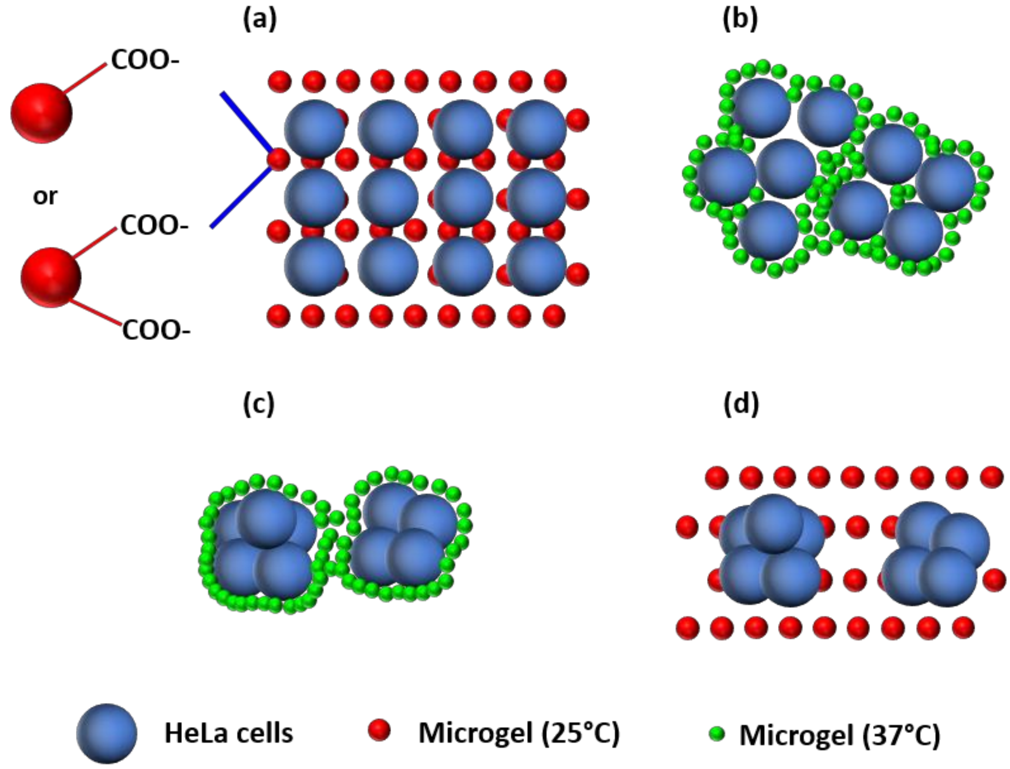

Figure 5-1 Fabrication and release of HeLa cells spheroids in the P(NIPAM) based microgels. (a) Cells are mixed with microgels at room temperature. (b) At 37°C, P(NIPAM) based microgels confine single cells in a three-dimensional network. (c) After placing cell-laden microgels in the cell culture medium for a certain time, tumour spheroids are produced in 3D microgels. (d) Reducing the temperature to room temperature, 3D microgels turn into solution and spheroids are released from the liquefied solution.

Through manipulation of the co-polymerization, different charged microgels have been successfully synthesized for mesenchymal stem cells culture [23-25]. In this study, we synthesized a range of microgels by co-polymerizing poly(NIPAM) with different carboxyl acids that exhibited different levels of hydrophobicity as well as surface charge density. As shown in Fig. 5-1, single cells were homogeneously seeded inside different microgel networks after heating to 37 ˚C. Cells grew in the cell culture medium to form clusters due to the interaction of multiple cells. After the desired size of clusters has been achieved, through cooling the system down to room temperature, the clusters were collected. By tuning the microenvironment, we assessed the impact of hydrophobicity/hydrophilicity, surface charge and other chemical groups on the tumor spheroids formation. We also used the refined microenvironment for culturing different cell lines for spheroids formation. The outcomes will provide great insights into unlocking the mechanisms of tumor spheroids formation and establishing the spheroids model for drug screening and evaluation.

5.3 Materials and Method

5.3.1 Materials

N-Isopopylacrylamide (NIPAM), acrylic acid (AA), itaconic acid (IA), malic acid (MA), methacrylic acid (MAA), N,N'-methylenebis(acrylamide) (MBA), potassium persulphate (KPS) were ordered from Sigma-Aldrich, sodium dodecyl sulphate (SDS) were purchased from VWR. NIPAM was recrystallized in n-hexane and dried in vacuum at room temperature before synthesis. Dulbecco's Modified Eagle's Medium (DMEM), trypsin-EDTA, pencillin-streptomycin (PS) and fetal bovine serum (FBS) were purchased from Gibco. 3-(4,5-Dimethlthiazol-2-yl)-2,5-diphenyltetrazolium bromide (MTT) was obtained from Merck. The LIVE/DEAD® Viability/Cytotoxicity Kit was purchased from Life Technologies.

5.3.2 Microgel synthesized

The P(NIPAM-AA) microgels were synthesized by free radical emulsion polymerization based on the method reported previously[23]. The same method was used for synthesizing P(NIPAM-MA), P(NIPAM-IA), P(NIPAM-MAA), and P(NIPAM) microgels. 9.9 mmol NIPAM, 0.1 mmol AA, MA, IA, or MAA, 0.2 mmol MBA and 0.12 mmol of SDS were dissolved in 97 mL of water. After stirring to thoroughly mix the solution, the mixture was transferred to a 250 mL three-necked flask connected with a condenser and a mechanical stirrer. Prior to the polymerization, the solution was under nitrogen atmosphere for degassing 30 min. After degassing, the flask was placed into a pre-heated oil batch (70 ˚C). 3.0 mL of KPS aqueous solution (0.1 mmol) was injected into the mixture solution to initiate the polymerization. The polymerization was carried out for 5 h under the protection of nitrogen atmosphere with continuous stirring. After the polymerization, the solution was cooled down to the ambient temperature. The microgels were purified by membrane dialysis with a cut-off molecular weight of 12-14 kDa against Milli-Q water for one week with a daily water change. The purified microgels were concentrated at 70 ˚C with continuous stirring.

5.3.3 Conductometric and potentiometric titration

The amount of the carboxyl acidic group, MAA, AA, IA and MA, in the as-synthesized microgels was measured by conductometric and potentiometric titrations. Typically, the pH of a 100 mL microgel dispersion (0.1 mg/mL in Milli-Q water) was adjusted to pH 4.0 using 1.0 M HCl aqueous solution. The solution was then titrated by adding 0.1M NaOH aqueous solution. After each addition of NaOH, the solution conductivity was monitored by a H18733 conductivity meter and the pH was recorded using a pre-calibrated pH/mV meter (smartCHEM-pH, TPS Australia).

5.3.4 Dynamic light scattering measurement

Zetasizer (Malvern, Nano-ZS) was employed to measure the hydrodynamic diameter (d_h) and zeta potential of the synthesized microgels (1.0 mg/mL in physiological saline (pH ≈ 7.4)) by dynamic light scattering (DLS) at different temperatures. The DLS data were collected on an autocorrelator with a detection angle of scattered light at 90°. The intensity autocorrelation function was evaluated by the CONTIN software package. Zeta potential was obtained by conversion of the electrophoresis mobility using the Smoluchowski model. The swelling ratio (SR) of microgels was defined by

$$SR = (\frac{d_h(25°C)}{d_h(40°C)})^3$$

Where SR is the swelling ratio, $d_{h,}$(25° C) is the hydrodynamic diameter of the microgels at 25˚C and d_h(40 °C) is the hydrodynamic diameter of the microgels at 40˚C.

5.3.5 Rheological characterization

Dynamic oscillation experiments of 30 mg/mL microgel dispersions (in physiological saline, pH ≈ 7.4) were carried out by a BA universal stress rheometer SR5 (Rheometric Scientific) with a 40 mm cone plate geometry. The gap was set as 0.0483 mm, and the temperature was controlled by a Peltier system attached to a water bath. The elastic (storage) modulus, G', and the viscous (loss) modulus, G" were obtained at different temperatures from 20 to 40 ^{0}C under a controlled stress of 0.1 Pa and a frequency of 0.1 Hz. The rheological experiments were performed within the linear viscoelastic region.

5.3.6 Hydrogel morphologies

3 mL of each microgel dispersion at 30 mg/mL in PBS buffer placing in a 15 mL plastic centrifuge tube respectively was heated up in an incubator at 37 °C until microgel dispersions

turned into a physical gel. In order to maintain the microstructure of the microgel under the SEM, centrifuge tubes with gels were quenched by liquid nitrogen and dried under vacuum using a Christ Aplha 2-4 DL freeze dryer. The observation of morphologies of hydrogels networks was performed under a FEI Quanta 450 FEG environmental scanning electron microscopy (SEM) after surface platinum coating at an accelerating voltage of 20 kV.

5.3.7 Tumor spheroid formation in microgels

A T-75 flask was used to culture HeLa cells in a growth medium (DMEM with 10% FBS and 1% PS). The culture flask was placed at a 37 ˚C incubator in a humidified atmosphere with 5 % CO_2 until cells became confluent. Trypsin was added into the flask to detach cells from the flask and cells were re-suspended into a complete growth medium at a cell concentration of 1.4×10^6 cells/mL. The HeLa cell dispersion was mixed with 50 mg/mL microgels (in phosphate buffered saline (PBS), pH≈7.2) at a volumetric ratio of 2: 3, which resulted in a final concentration of microgels at 30 mg/mL. 0.5 mL of cell-microgel mixture was seeded into each well of a 24-well plate at a cell density of 4.8×10^5 cells per well. The cell-microgel mixture was placed in an incubator at 37˚C for 2 h until the mixture was converted into gel. 1 mL growth medium was added on the top of the soft gel in each well. Cells were incubated at 37 ˚C in a humidified atmosphere with 5 % CO_2 and the growth medium was changed daily. Cells were harvested for further analysis at day 7, 14, and 21.

5.3.8 Cell proliferation assay

The standard MTT assay was employed to measure the cell viability during the cell harvest process. 100 μL MTT solution (5.0 mg/mL) was added into each well. After another 4 hr incubation, the medium was completely removed. 1 mL DMSO was added to dissolve the formazan crystals. All solutions from each well were transferred to a 96 well plate and the absorbance of the solubilized formazan crystals was recorded using an ELx808 Absorbance Microplate Reader (BioTek Instruments In., USA) at a wavelength of 490 nm.

5.3.9 Spheroid morphology and structure analysis

The spheroids were released and harvested by placing the cell-gel mixture at room temperature for 1 h until gels became solution and centrifuging the cell-microgel solution. An Olympus IX50 inverted microscope (USA) was utilized to observe the morphology of harvested HeLa cell spheroids.

The Live/Dead cell viability/cytotoxicity kit was used to assess live and dead cells in the spheroid structure. Based on the protocol from the supplier, a mixture of 0.75 μL calcein AM (green) and 3 μL Ethidium homodimer-1 (red) was added into 1.5 mL PBS. After removing the culture medium and washing the cell/gel mixture with pre-warmed PBS buffer for two times, 200 μL dye solution was added into each well. After dying, the mixture was incubated at 37 °C for another 30 min before rinsing spheroids with fresh PBS buffer two times. The stained spheroids were observed under a florescent microscopy. The excitation wavelength for calcein Am was selected to be 504 nm-553 nm, and for Ethidium homodimer-1 was 569 nm-619 nm.

5.3.10 Data analysis

All experimental data were shown as mean ± standard deviation. Student's t test was performed for analyzing statistics. Data were considered to be as significantly different when $p<0.05$.

5.4 Results and discussion

5.4.1 Synthesis and characterization of thermo-responsive acidic microgels

Different P(NIPAM) based microgels were synthesized by free radical emulsion polymerization. The crosslinker MBA, SDS emulsifier, and KPS initiator were fixed to be 0.02 mmol, 0.012 mmol, and 0.01 mmol respectively. In this study, different carboxylic acidic monomers were used to represent the different degree of deprotonation of acidic monomers. There are two groups of carboxylic acid monomers. Acrylic acid (AA) and methacrylic acid (MAA) are monocaboxylic acids, while maleic acid (MA) and itaconic acid (IA) are dicarboxylic acids. The feeding amount of carboxylic acidic monomers were fixed at 0.1 mmol. Membrane dialysis was utilized after polymer synthesis to remove all the un-reacted monomers and the emulsifier. The details on the polymerization conditions and microgel characterizations results are shown in Table 5-1. Fig. 5-2 shows the chemical structure for all microgels synthesized in this study.

Table 5-1 Summary on the synthesis and characterization of different P(NIPAM) based microgels

Microgels	NIPAM	Co-monomer	MBA	SDS	KPS	Acid content (× 10^{-4} mol g^{-1} microgels)		Zeta potential (mV)		VPPT
	mmol	mmol	mmol	mmol	mmol	Observed	Theoretical	25°C	37°C	°C
P(NIPAM)	10	0	0.2	0.12	0.1	0	0	-2.3±0.4	-1.8±0.3	32
P(NIPAM-MAA)	9.9	0.1 MAA	0.2	0.12	0.1	0.82	0.89	-6.6±0.3	-9.1±1	30
P(NIPAM-AA)	9.9	0.1 AA	0.2	0.12	0.1	0.64	0.89	-7.3±0.5	-9.3±0.8	33
P(NIPAM-MA)	9.9	0.1 MA	0.4	0.12	0.1	0.61	0.89	-12.3±0.8	-18.4±1.2	34
P(NIPAM-IA)	9.9	0.1 IA	0.2	0.12	0.1	0.66	0.89	-10.2±0.2	-12.8±0.5	34

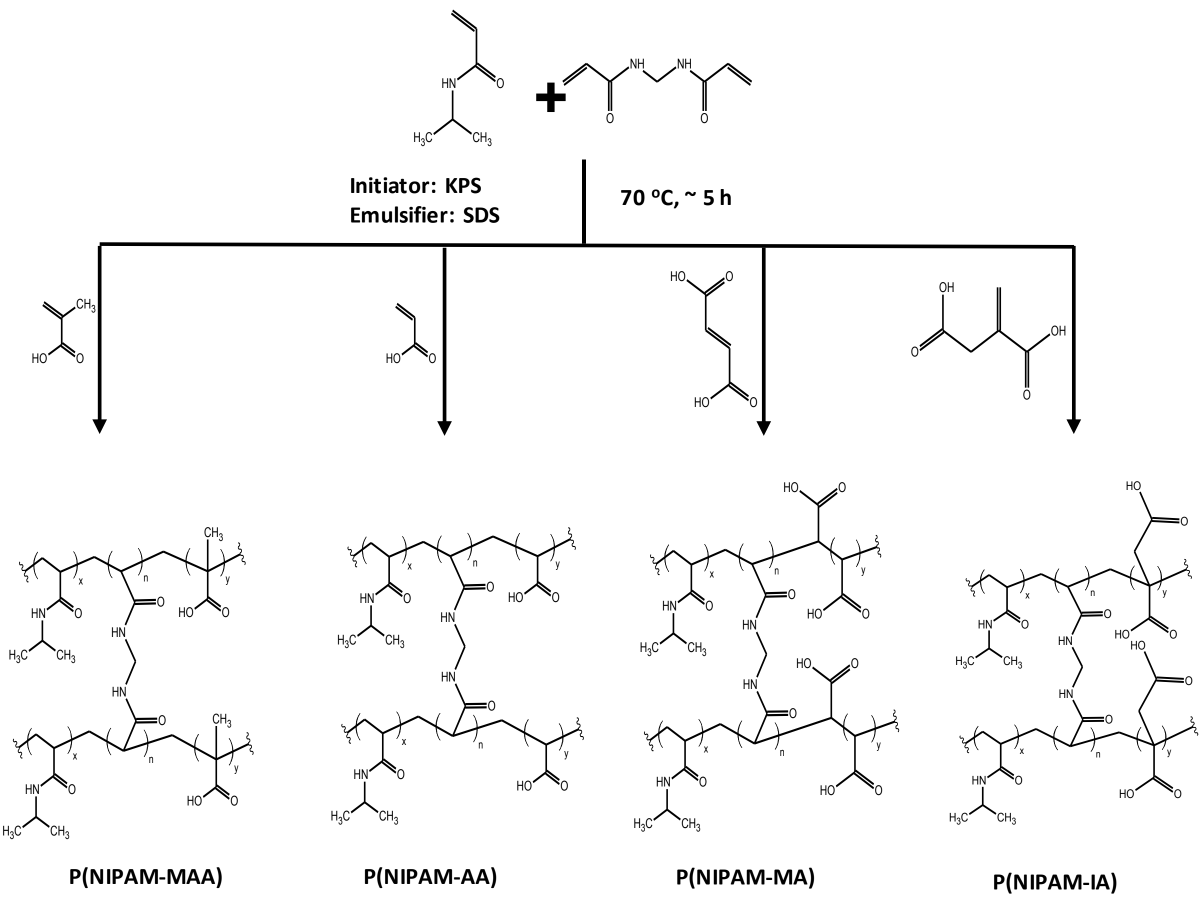

Figure 5-2 Scheme for synthesis of P(NIPAM) based microgels

Conductomertic (Fig. 5-10, supporting document) and pH titrations were used to confirm the success of co-polymerization by the buffer range between the decreasing and increasing legs as shown in Fig. 5-10 (supporting document) for the diluted P(NIPAM) based microgels. In the buffer region, carboxylic acids in the co-polymer neutralized counterion condensation and the conductivity increased slowly upon the alkali addition, while without carboxylic acids, the conductivity of the P(NIPAM) microgels dropped rapidly as the excess HCL was added [23].

5.4.2 Hydrodynamic diameter and swilling ratio

Dynamic light scattering (DLS) was utilized to measure the hydrodynamic diameter, d_h, of the dilute aqueous synthesized microgels (1.0 mg /mL) at different temperatures. The hydrodynamic diameter of the microgels is dependent on temperature as shown in the plot of d_h versus temperature (Fig. 5-3a). The d_h of PNIPAM is the smallest due to the absence of carboxyl acidic monomers in comparison with other microgels [26]. The d_h of five microgels decreases with an increase in the temperature. The d_h of P(NIPAM-MAA) microgels has a sharp decrease between 25-30 °C, while the sharp decrease of d_h occurs around 30-35 °C for the other four microgels. The critical transition temperature for sharp change of d_h is the volume phase transition temperature (VPTT) of microgels, equivalent to the lower critical solution temperature of a linear polymer. Because of addition of functional carboxyl acidic monomers into the microgels, the VPPT of p(NIPAM) is shifted and the extent of shift is determined by the degree of ionization and the hydrophobicities of the co-polymers [27, 28]. The monocarboxyl acid microgels have a lower volume phase transition temperature compared with the dicarboxyl acid microgels.

The swelling ratio is often used to represent the degree of hydrophobicity of the microgels. The swelling ratios of the copolymer microgels are shown in Fig. 5- 3b. Because of the presence of a more hydrophobic methyl group in the P(NIPAM-MAA) microgels, the swelling ratio of P(NIPAM-MAA) is the highest compared with other four microgels. P(NIPAM-MA) and P(NIPAM-IA), on the other hand, have more carboxylic groups which result in a more hydrophilic environment due to the strong hydrogen bonding between $–coo^-$ and water molecule. As a result, they have a lower swelling ratio [29].

5.4.3 Surface charge of microgels

Zeta potential is often employed to measure the surface charge density of microgels and the charge density of as-synthesized microgels is shown in Table 5-1. The introduction of carboxylic acids into the P(NIPAM) influence the zeta potential of microgels. The surface charge density have an order of P(NIPAM-MA) > P(NIPAM-IA) > P(NIPAM-AA) > P(NIPAM-MAA) > P(NIPAM). The partial deprotonation of the carboxyl acid group elevates the negative surface charges, and the introduction of KPS initiator also contributes to the negatives surface charges [30]. More carboxyl acid groups in the P(NIPAM-IA) and P(NIPAM-MA) renders two polymers to exhibit a higher negative charge density while KPS initiator is the only contributor for the negative charge in P(NIPAM) microgels.

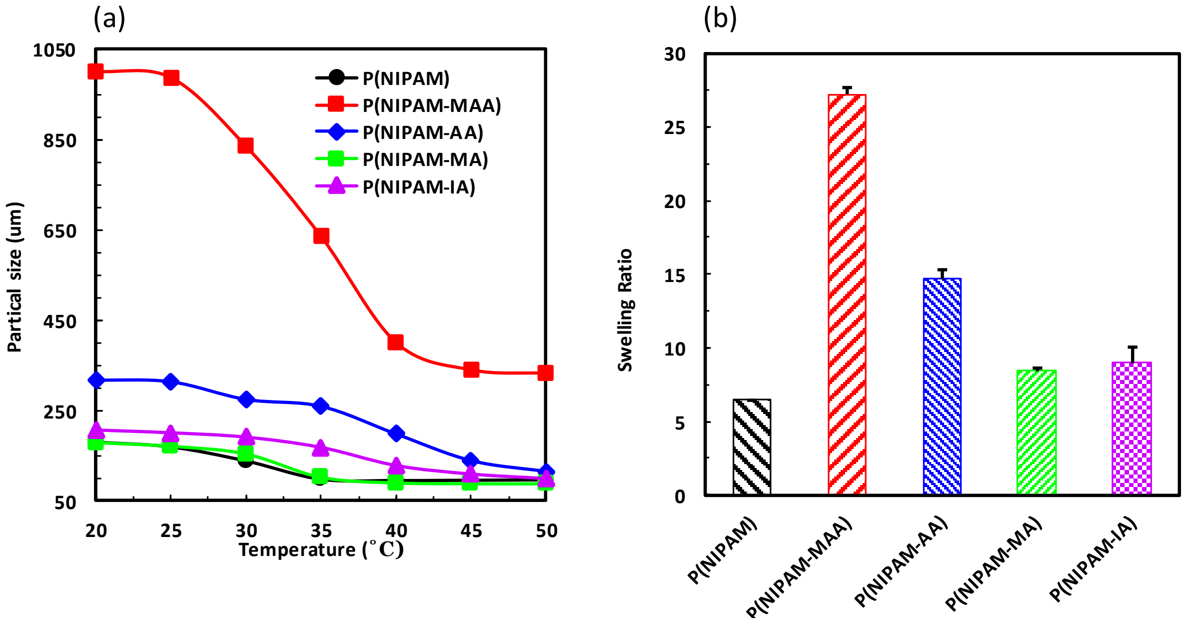

Figure 5-3 Microgel size and swelling ratio are temperature dependent. (a) Hydrodynamic dimeter (d_h). (b) Swelling ratio. (mean ± SD).

5.4.4 Thermal gelation of the microgels

Five microgels at 30 mg mL^{-1} (in PBS buffer) presents as the solution state at room temperature and increasing the temperature to 37 °C, all the microgels form gels. All microgels possess the thermal reversibility. Once the hydrogels are cooled down to room temperature, they exhibit a sol state (Fig. 5-4a). The gelation is caused by the balance of the hydrophobic attractions and electrostatic repulsion [31]. Itaconic acid and malic acid have more hydrophilic groups than other carboxyl acids in this study which weaken the hydrophobic effect and enhance the electrostatic repulsion due to the deprotonation of the carboxyl group. Physiological saline introduces Na^+ and K^+ ions, which can reduce the electrostatic repulsion to mitigate the hydrophobic effect for formation of physical gels.

Dynamic rheometric measurement was used for examining the sol-gel transition properties of these microgel dispersions at different temperatures. P(NIPAM-MAA) and P(NIPAM) microgel solution were excluded for the rheological measurements because phase separation of both mcirogels occurred under the measurement conditions. Fig. 5-4b shows that the dynamic modulus of 30 mg mL^{-1} of the P(NIPAM-AA), P(NIPAM-IA) and P(NIPAM-MA) microgel dispersions (pH, ~7.0) is temperature dependent. At a low temperature (25 to 32°C), viscous modulus (G”) is dominant over elastic modulus (G’), which indicates the microgel dispersion presentes in the liquid form and the solution behavior is predominated by viscous flow characteristics. Because of the domination of in the flow property, G' is not measured accurately at a low oscillation frequency. Both G' and G" increase significantly when the temperature continues to increase but G' increases much faster than G". At a certain temperature, G' is higher than G", which indicates the gel formation.

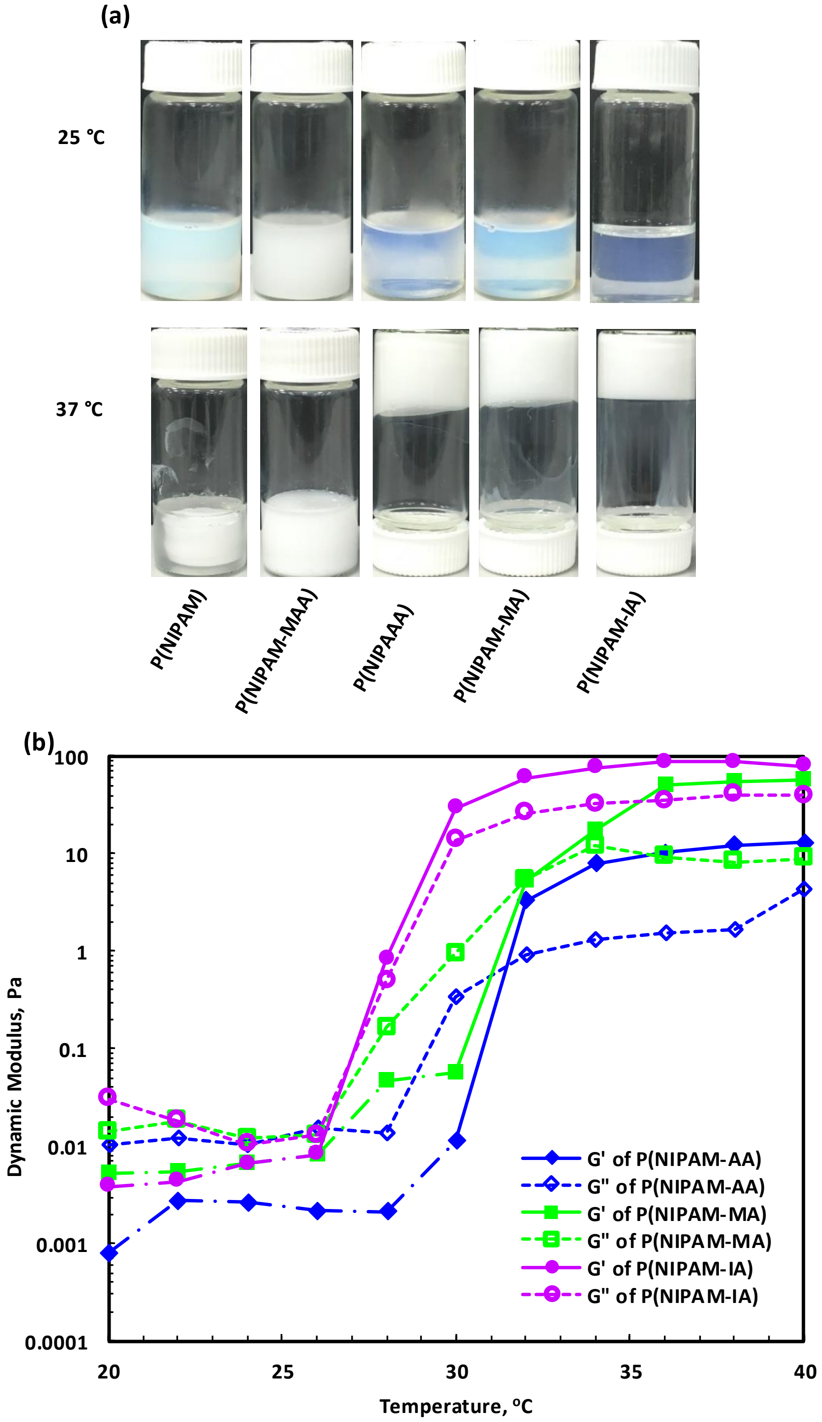

Figure 5-4 Thermal gelation of microgels. (a) Sol-gel thermoreversibility of 30 mg/mL of microgels (in PBS buffer) at the dispersed sol state (25°C) and the gel state (37°C). (b) Temperature dependent dynamic rheological moduli of 30 mg/mL of microgels (in PBS buffer). G' is elastic (or storage) modulus and G" is viscous (or loss) modulus.

The temperature at which G’ and G” intersect during the heating process is defined as the gelation temperature T_g. As shown in Table 5-1, T_g of each microgel is close to the corresponding VPTT of the microgel. This result indicates that hydrophobic interaction among these shrunk microgels is the main driving force for the microgel thermal gelation which is associated with transformation of P(NIPAM) moieties from hydrophilic to hydrophobic beyond VPTTs [32]. In addition, the G’ of P(NIPAM-IA) and P(NIPAM-MA) is higher than that of P(IPAM-AA), which indicates both microgels have stronger mechanical properties compared with P(NIPAM-AA). This may be due to the stronger hydrogen bonds in both P(NIPAM-IA) and P(NIPAM-MA) than P(NIPAM-AA) [33]. The PNIPAM-IA microgel has a higher G’ than P(NIPAM-MA) due to its larger size. The dangling chains of the microgel are relatively longer when the microgel size is bigger. The longer dangling chains are, the stronger inter microgel interaction is in both the number of active junctions and the strength of each junction, which result in a higher elastic modulus shown in the dynamic oscillation measurement [25].

5.4.5 Microstructure of the hydrogels

The microstructure of the microgel network was observed under the SEM. The freezing process by rapid liquid nitrogen quenching results in an amorphous structure instead of a crystalline one [34]. As a result, the minimum damage occurs during the frozen and dry stages. Fig. 5-5 shows that P(NIPAM-IA) and P(NIPAM-MA) have a larger pore size of 40 μm. This was due to higher electrostatic repulsion forces driven by the deprotonation of the carboxyl groups of the microgels. P(NIPAM-AA) has a slightly smaller pore size around 10-20μm. P(NIPAM) has the smallest pore due to the strong hydrophobic attractions and the absence of electrostatic repulsion. The pores of the P(NIPAM-MAA) microgel is also small due to its high hydrophobicity contributed from the co-monomer MAA. This interconnected porous microstructure is valuable for mass transportation such as nutrients, oxygen and wastes, which promotes cell growth and enhance cell survivial. Furthermore, the larger pore size is also beneficial for cell migration for spheroid formation.

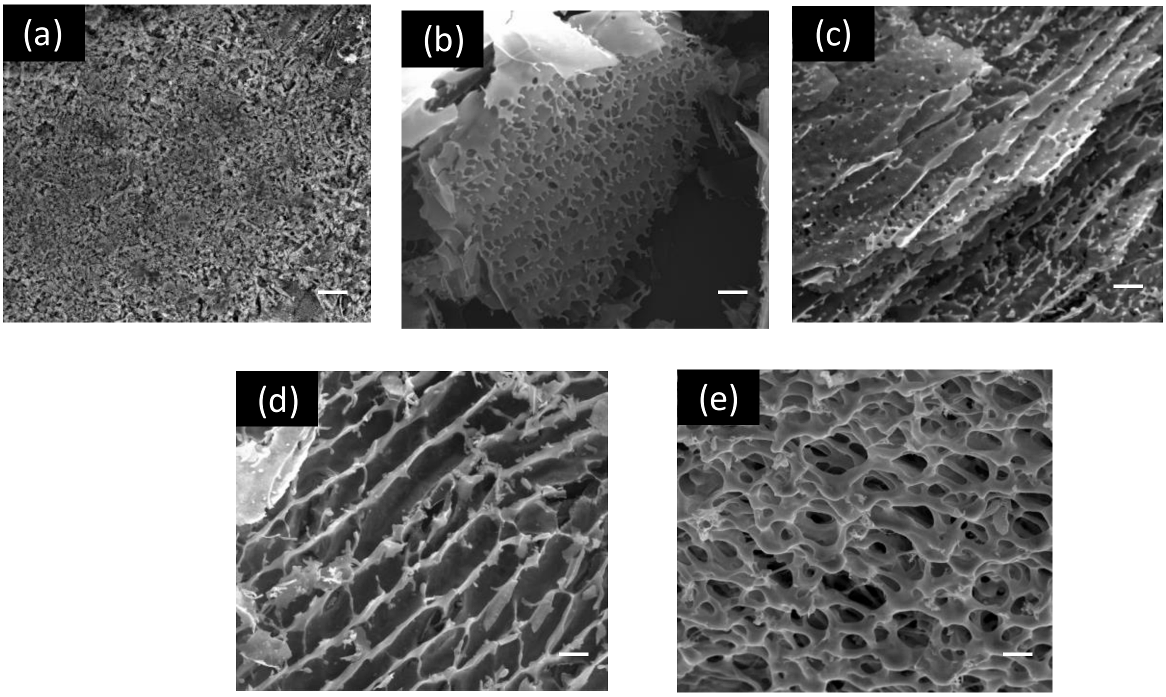

Figure 5-5 SEM morphologies of the in-situ formed P(NIPAM) based hydrogels. (a) P(NIPAM); (b) P(NIPAM-MAA); (c) P(NIPAM-AA); (d) P(NIPAM-MA); (e) P(NIPAM-IA). Scale bar is 20 μm.

5.4.6 Cell proliferation

P(NIAM-AA) microgels have been used by our group to culture mesenchymal stem cells as well as HeLa cell spheroids [23, 35]. The results have shown stem/Hela cells proliferated better in the microgel network than in the conventional two-dimensional petri dishes. This microgel-based cell culture platform was further explored to form tumor spheroids. However, not all tumor cell types are able to form compacted spheroids. Loose aggregates, disconnected or floating cells are observed from spheroid culture [36]. The microenvironment surrounding the cells plays a significant role in facilitating cell-to-cell interactions such as adhesion and junction connections, and the properties of the microenvironment include the extracellular electric charges, hydrophobicity, and special functional chemical groups. In this study, five microgels were synthesized to investigate these microenvironment properties for spheroid formation. We seeded HeLa cells inside the microgels network at a low cell density, and cells generated their own extracellular matrix and proteins for forming compacted spheroids. The cell proliferate rapidly in the first 7 days as shown in Fig. 5-6, and continue at a high proliferation rate from day 7 to day 14.

Afterwards, cell number starts to decrease. This trend is observed for all the microgels, which is in agreement with the growth kinetics of tumours in the *in vivo* environment [37].

At day 1 the MTT result shows cells growing within different microgels at a very similar absorbance rate, which indicates that the same initial cell density was used for different microgels. At day 7, cells seeded in hydrophilic microgels (P(NIPAM-AA), P(NIPAM-IA), and P(NIPAM-MA)) proliferates much faster than those in relatively hydrophobic microgels (P(NIPAM) and P(NIPAM-MAA)). The cell growth kinetics in microgels indicates the microgels pore networks are beneficial for cells growth because of rapid diffusion of the oxygen and nutrients. The extra carboxylic group from IA and MA increases the hydrophilicity of the microgels, which provides a more benign environment for cell growth since the hydrophilic environment is better for cell attachment and proliferation [38]. In addition, a higher negative charged environment results in a lower cell membrane potential which promotes cell functions such as proliferation and migration [38]. However, after day 7 the highest negative charged environment offered by P(NIPAM-MA) starts to lower the cell proliferation rate compared with P(NIPAM-IA) and P(NIAM-AA), which demonstrates that the highly negative charged environment has an adverse effect on cell proliferation. The optimized charged microenvironment is needed for better cell growth and spheroid formation. Besides the localized electric charge of the microenvironment, the hydrophobicity of the microenvironment also plays a role in cell growth [39]. This can be confirmed by that cells growing in P(NIPAM-MA) is higher than those in more hydrophobic hydrogel networks in the P(NIPAM) and P(NIPAM-MAA) microgels. At day 21, a significant drop on the live cell number is observed for all microgels. This may be due to formation of large clusters. The starvation of oxygen and nutrient transportation and the accumulation of toxic wastes in the cluster result in the death of the inner cells [40]. The core surrounding by dead cells and the live cells on the periphery are the characteristic structure of a solid tumor.

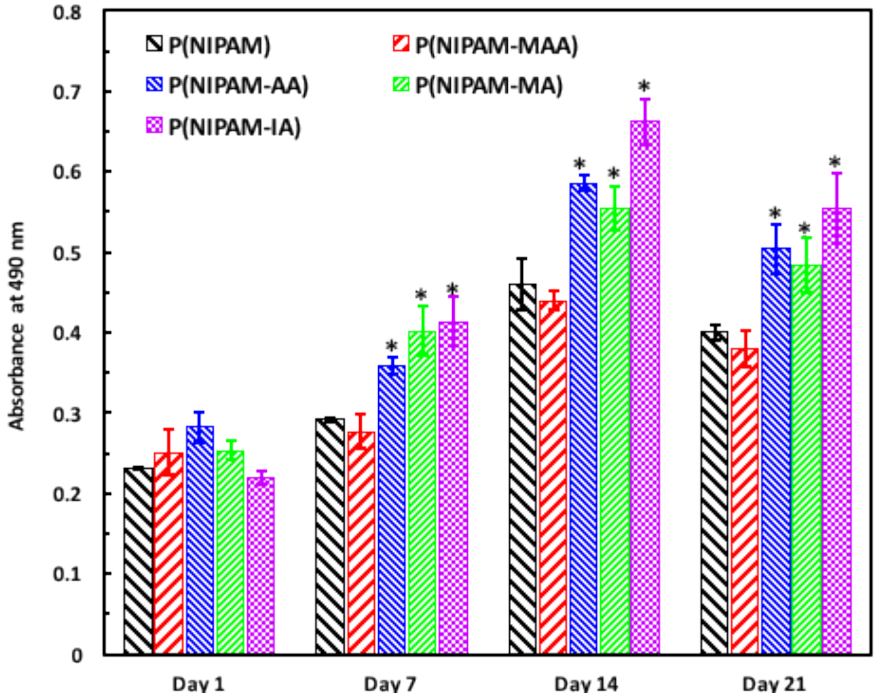

Figure 5-6 HeLa cells proliferation in the 3D microgels. Mean ± SD. n=6. "*" indicates $P < 0.05$ in comparison with P(NIPAM).

5.4.7 Three dimensional culture of tumor spheroids

The size of spheroids and the compacted cell density within the spheroids determine the physiological state of spheroids. Optical images were taken to examine the morphology of the spheroids, and the images are presented in Fig. 5-7 for day 21 and supporting documents (Fig. 5-11, 12, 13) for day 1,7 and 14 respectively. These images were taken at 4x magnification. It can be seen that in the P(NIPAM) and P(NIPAM-MMA) microgels, cells grow slowly and no cluster is observed in both networks due to their high hydrophobicity and small pore size networks. A great number of large clusters are observed in the P(NIPAM-AA), P(NIPAM-IA) and P(NIPAM-MA) networks. The size of the clusters in P(NIPAM-IA) is relatively larger which is around 200-500 μm in comparison with P(NIPAM-AA) and P(NIPAM-MA). This may ascribe to the high cell proliferation rate in the network, as well as the relatively negative charged environment compared with P(NIPAM-AA). The large pore size of P(NIPAM-IA) not only maximizes nutrient, oxygen and waste transportation for supporting HeLa cell growth but also allows cell migration inside the hydrogel network due to the negative charged environment. The P(NIPAM-AA) network also provides a benign environment due to its relative hydrophilicity for cancer cell proliferation and migration, which promotes spheroid formation [41]. Spheroids at a small size are produced on the other hand in the P(NIPAM-MA) microgel due to its much higher negative charge.

The Live/Dead viability and cytotoxicity kit was further employed to examine the structure of individual tumor spheroids. The green cells represents the live cells and the red for the dead cells. The fluorescent images as shown in Fig. 5-7f to Fig. 5-7h illustrate the structure of the spheroids at day 21 in the P(NIPAM-AA), P(NIPAM-IA) and P(NIPAM-MA) networks. Cells have a high degree of viability inside these hydrogels, which indicates the high biocompatibility of these microgels.

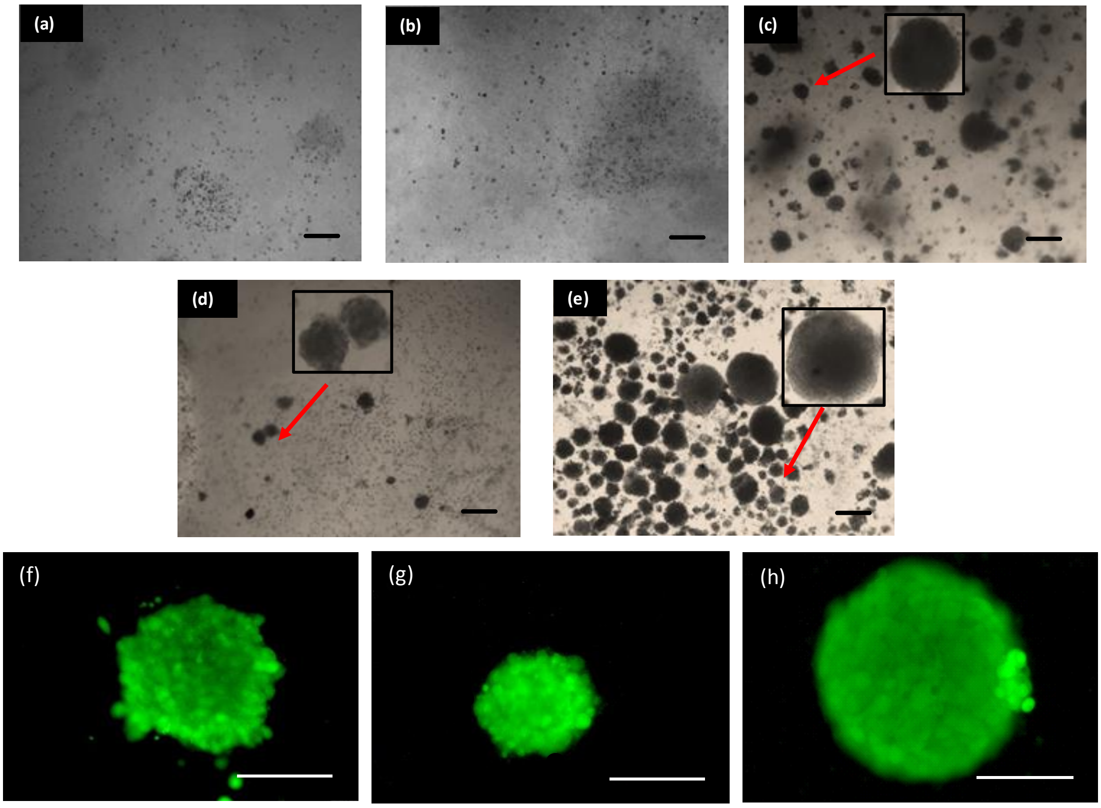

Figure 5-7 HeLa cell spheroids at day 21 in different microgels. (a) P(NIPAM), (b) P(NIPAM-MAA), (c) P(NIPAM-AA), (d) P(NIPAM-MA), (e) P(NIPAM-IA). (f) to (g) are live/dead images for HeLa cell spheroids at day 21 in P(NIPAM-AA), P(NIPAM-MA) and P(NIPAM-IA) microgels respectively. Scale bar is 200 µm.

The HeLa spheroid formation kinetics in the P(NIPAM-IA) microgels shown in Fig. 5-8 with optical images and live/dead images indicate three stages in the cellular spheroid formation. Cells are drawn together and form small loose aggregates in the first 14 days. The initiation of cell aggregation is caused by the cell surface integrin binding between long chain ECM fibers and multiple RGD motifs. At day 14, the size of aggregates becomes around 250 µm, which is 2 times bigger than the cell pellet at day 7. The structure of the aggregates become more compacted. During the process, cadherin expression is upregulated so the protein is accumulated on the surface. After another 7 days, the size of spheroids reaches more than 350 µm. The spheroids become smooth and spherical, which indicates spheroids arrive at their final compaction stage [19]. Homophilic cadherin-cadherin binding leads to strong cell to cell interactions which result in the formation of compacted spheroids [9].

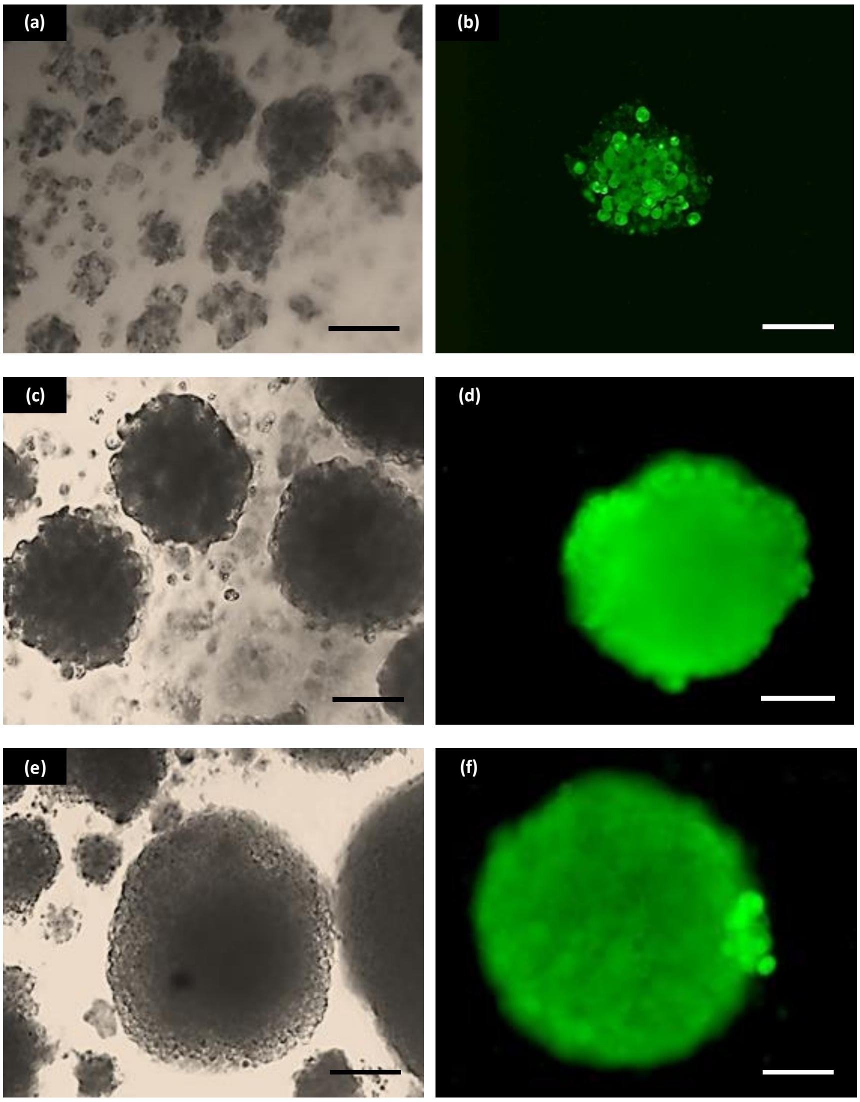

Figure 5-8 Evolution of spheroids formation from single HeLa cells in the P(NIPAM-IA) microgels at different days. (a), (c) and (e) are optical images of spheroids at day 7, day 14, day 21 respectively. (b), (d) and (f) are live/dead images of spheroids at day 7, day 14, day 21 respectively. Scale bar is 100 µm.

The cellular microenvironment can provide an active component of biochemical signals, which regulates cell behavior. Therefore, not all the cells can form spheroids easily within matrix. We expect that cells which cannot easily form spheroids will aggregate into clusters with the aid of our microgels. We further cultured MSC, U-87 and HEK 293T cells in the microgels-based scaffold. Both MSCs and U-87 cells have a similar spheroid formation process as Hela cells, and they form a spheroids structure in P(NIPAM-IA) microgels which is shown in Fig. 5-14 (support document). We noticed that HEK239T cells perform differently in the P(NIPAM-AA) and P(NIPAM-IA) microgels network (Fig. 5-9). At day 14, HEK239T cells form spheroids in the P(NIPAM-IA) scaffold but they proliferate as single individual cells in the P(NIPAM-AA) scaffold. By examining the difference between both microgels, the difference in HEK293T cell performance may be due to the pore size and surface charge. P(NIPAM-IA) negative surface charge may repulse cells away from the microgel surface and the cells are forced to form a loose aggregate in the initial stage and then a compact structure is formed when cadherin is accumulated on the surface. Meanwhile, the large porous network of the P(NIPAM-IA) microgels allows cells to migrate freely which promotes cell-to-cell contact to form spheroids.

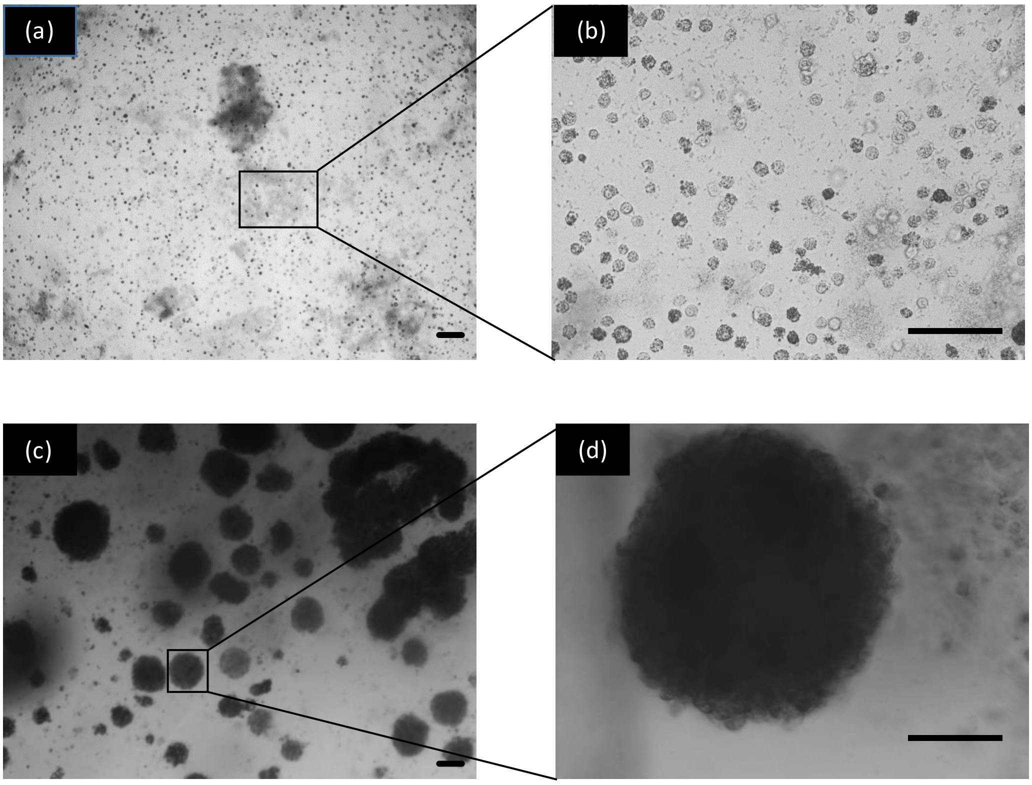

Figure 5-9 Spheroids formation of HEK293T cells within the P(NIPAM-AA) and P(NIPAM-IA) microgel scaffold at day 14. (a) and (b) are HEK239T cells in the P(NIPAM-AA) microgels. (c) and (d) are HEK293T cells in the P(NIPAM-IA) microgels. Scale bar is 100 μm.

5.5 Conclusion

Five microgels with various degrees of hydrophilicity and different charge density are developed and used for culturing cell clusters. We demonstrated a benign the microenvironment created by P(NIPAM-IA), P(NIPAM-AA) and P(NIPAM-MA) with high hydrophilicity and a moderately negative charge density is beneficial for cell proliferation and clusters formation. HeLa, MSC, and U-87 cells were found to form spheroids in P(NIPAM-IA) microgels. HEK 293 cell only form spheroids in the P(NIPAM-IA) microgels which demonstrates that moderate negative charge weakens cell-substrate interactions and promotes the formation of tumor spheroids. However, high hydrophobicity (such as the P(NIPAM) and P(NIPAM-MAA) microgel) decreases the cell proliferation rate, and highly negative charged microenvironment from P(NIPAM-MA) results in spheroids with a small size. Hence the microenvironment experience by cells play a crucial role in spheroids formation.

5.6 Reference

1. Nyga, A., U. Cheema, and M. Loizidou, 3D tumour models: novel in vitro approaches to cancer studies. Journal of cell communication and signaling, 2011. 5(3): p. 239-248.

2. Mehta, G., et al., Opportunities and challenges for use of tumor spheroids as models to test drug delivery and efficacy. J Control Release, 2012. 164(2): p. 192-204.

3. Landry, J., et al., Spheroidal aggregate culture of rat liver cells: histotypic reorganization, biomatrix deposition, and maintenance of functional activities. The Journal of cell biology, 1985. 101(3): p. 914-923.

4. Yuhas, J.M., et al., A simplified method for production and growth of multicellular tumor spheroids. Cancer Research, 1977. 37(10): p. 3639-3643.

5. Hamilton, G.A., C. Westmoreland, and E. George, Effects of medium composition on the morphology and function of rat hepatocytes cultured as spheroids and monolayers. In Vitro Cellular & Developmental Biology-Animal, 2001. 37(10): p. 656-667.

6. Nyberg, S.L., et al., Rapid, large-scale formation of porcine hepatocyte spheroids in a novel spheroid reservoir bioartificial liver. Liver transplantation, 2005. 11(8): p. 901-910.

7. Lazar, A., et al., Extended liver-specific functions of porcine hepatocyte spheroids entrapped in collagen gel. In Vitro Cellular & Developmental Biology-Animal, 1995. 31(5): p. 340-346.

8. Song, H., et al., Spatial composition of prostate cancer spheroids in mixed and static cultures. Tissue engineering, 2004. 10(7-8): p. 1266-1276.

9. Lin, R.-Z., et al., Dynamic analysis of hepatoma spheroid formation: roles of E-cadherin and β1-integrin. Cell and Tissue Research, 2006. 324(3): p. 411-422.

10. Kelm, J.M., et al., Method for generation of homogeneous multicellular tumor spheroids applicable to a wide variety of cell types. Biotechnol Bioeng, 2003. 83(2): p. 173-80.

11. Kelm, J.M. and M. Fussenegger, Microscale tissue engineering using gravity-enforced cell assembly. Trends in biotechnology, 2004. 22(4): p. 195-202.

12. WARTENBERG, M., et al., Tumor-induced angiogenesis studied in confrontation cultures of multicellular tumor spheroids and embryoid bodies grown from pluripotent embryonic stem cells. The FASEB Journal, 2001. 15(6): p. 995-1005.

13. Kelm, J.M., et al., Design of custom-shaped vascularized tissues using microtissue spheroids as minimal building units. Tissue engineering, 2006. 12(8): p. 2151-2160.

14. Ravi, M., et al., 3D cell culture systems: advantages and applications. J Cell Physiol, 2015. 230(1): p. 16-26.

15. Holliday, D.L., et al., Novel multicellular organotypic models of normal and malignant breast: tools for dissecting the role of the microenvironment in breast cancer progression. Breast Cancer Research, 2009. 11(1): p. 1-11.

16. Gurski, L.A., et al., Hyaluronic acid-based hydrogels as 3D matrices for in vitro evaluation of chemotherapeutic drugs using poorly adherent prostate cancer cells. Biomaterials, 2009. 30(30): p. 6076-6085.

17. Talukdar, S., et al., Engineered silk fibroin protein 3D matrices for in vitro tumor model. Biomaterials, 2011. 32(8): p. 2149-2159.

18. Asghar, W., et al., Engineering cancer microenvironments for in vitro 3-D tumor models. Materials Today, 2015. 18(10): p. 539-553.

19. Lin, R.Z. and H.Y. Chang, Recent advances in three-dimensional multicellular spheroid culture for biomedical research. Biotechnol J, 2008. 3(9-10): p. 1172-84.

20. Liu, Z. and G. Vunjak-Novakovic, Modeling tumor microenvironments using custom-designed biomaterial scaffolds. Current Opinion in Chemical Engineering, 2016. 11: p. 94-105.

21. Lee, B.H., et al., Modulation of Huh7.5 Spheroid Formation and Functionality Using Modified PEG-Based Hydrogels of Different Stiffness. PLoS ONE, 2015. 10(2): p. e0118123.

22. Lee, J.H., et al., Cell behaviour on polymer surfaces with different functional groups. Biomaterials, 1994. 15(9): p. 705-711.

23. Shen, Z., et al., Exploring thermal reversible hydrogels for stem cell expansion in three-dimensions. Soft Matter, 2012. 8(27): p. 7250-7257.

24. Mellati, A., et al., A biodegradable thermosensitive hydrogel with tuneable properties for mimicking three-dimensional microenvironments of stem cells. RSC Advances, 2014. 4(109): p. 63951-63961.

25. Shen, Z., et al., A thermally responsive cationic nanogel-based platform for three-dimensional cell culture and recovery. RSC Advances, 2014. 4(55): p. 29146-29156.

26. Saunders, B.R. and B. Vincent, Microgel particles as model colloids: theory, properties and applications. Advances in Colloid and Interface Science, 1999. 80(1): p. 1-25.

27. Hoare, T. and R. Pelton, Highly pH and temperature responsive microgels functionalized with vinylacetic acid. Macromolecules, 2004. 37(7): p. 2544-2550.

28. Pomogailo, A.D., G.I. Dzhardimalieva, and V.N. Kestelʹman, Macromolecular metal carboxylates and their nanocomposites. Vol. 138. 2010: Springer Science & Business Media.

29. Hartanto, Y., et al., Thermoresponsive Acidic Microgels as Functional Draw Agents for Forward Osmosis Desalination. Environ Sci Technol, 2016. 50(8): p. 4221-8.

30. Schwierz, N., D. Horinek, and R.R. Netz, Specific ion binding to carboxylic surface groups and the pH dependence of the Hofmeister series. Langmuir, 2015. 31(1): p. 215-25.

31. Cho, E.C., et al., Highly Responsive Hydrogel Scaffolds Formed by Three-Dimensional Organization of Microgel Nanoparticles. Nano Letters, 2008. 8(1): p. 168-172.

32. Gan, T., Y. Guan, and Y. Zhang, Thermogelable PNIPAM microgel dispersion as 3D cell scaffold: effect of syneresis. Journal of Materials Chemistry, 2010. 20(28): p. 5937-5944.

33. Au, A., et al., Thermally reversible polymer gel for chondrocyte culture. Journal of Biomedical Materials Research Part A, 2003. 67(4): p. 1310-1319.

34. Nègre, M., et al., Characterization of model soil colloids by cryo-scanning electron microscopy. Geoderma, 2004. 121(1): p. 1-16.

35. Cui, X., et al., A mechanistic study on tumour spheroid formation in thermosensitive hydrogels: experiments and mathematical modelling. RSC Advances, 2016. 6(77): p. 73282-73291.

36. Ivascu, A. and M. Kubbies, Diversity of cell-mediated adhesions in breast cancer spheroids. Int J Oncol, 2007. 31(6): p. 1403-13.

37. Sutherland, R.M., Cell and environment interactions in tumor microregions: the multicell spheroid model. Science, 1988. 240(4849): p. 177-184.

38. Arima, Y. and H. Iwata, Effect of wettability and surface functional groups on protein adsorption and cell adhesion using well-defined mixed self-assembled monolayers. Biomaterials, 2007. 28(20): p. 3074-3082.

39. Stevens, M.M. and J.H. George, Exploring and Engineering the Cell Surface Interface. Science, 2005. 310(5751): p. 1135-1138.

40. Wang, D., et al., Thermoreversible Hydrogel for In Situ Generation and Release of HepG2 Spheroids. Biomacromolecules, 2011. 12(3): p. 578-584.

41. Yang, M. and W.J. Brackenbury, Membrane potential and cancer progression. Frontiers in Physiology, 2013. 4: p. 185.

5.7 **Supporting document**

Chapter 5: Tuning the microenvironment for tumour spheroids formation

X Cui, Y Hartanto, J Bi, S Dai and H Zhang

School of Chemical Enigneering, University of Adelaide, Adelaide, Australia 5005

Corresponding :Dr. Hu Zhang

Hu.zhang@adelaide.edu.au

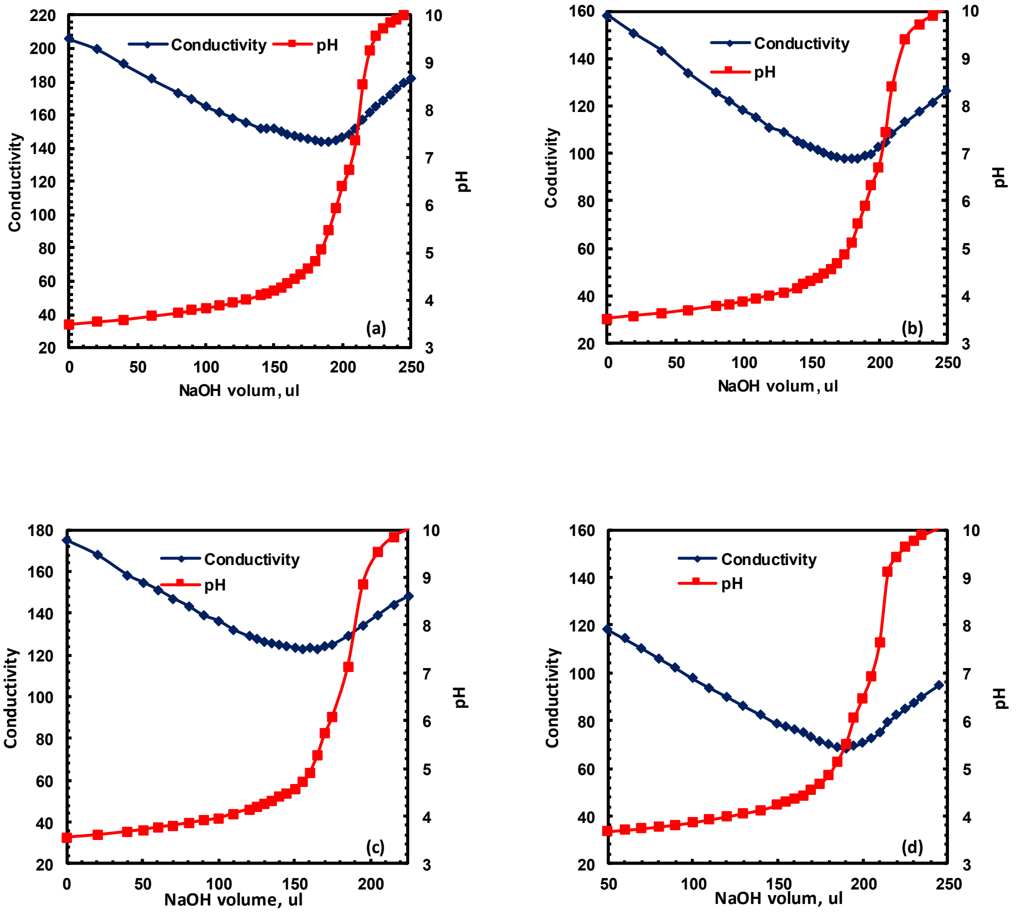

Figure 5-10 Conductivity and pH during back titrations of p(NIPAM)-based microgels at room temperature. (a) for P(NIPAM-MAA); (b) for P(NIPAM-AA); (c) for P(NIPAM-MA) and (d) for P(NIPAM-IA).

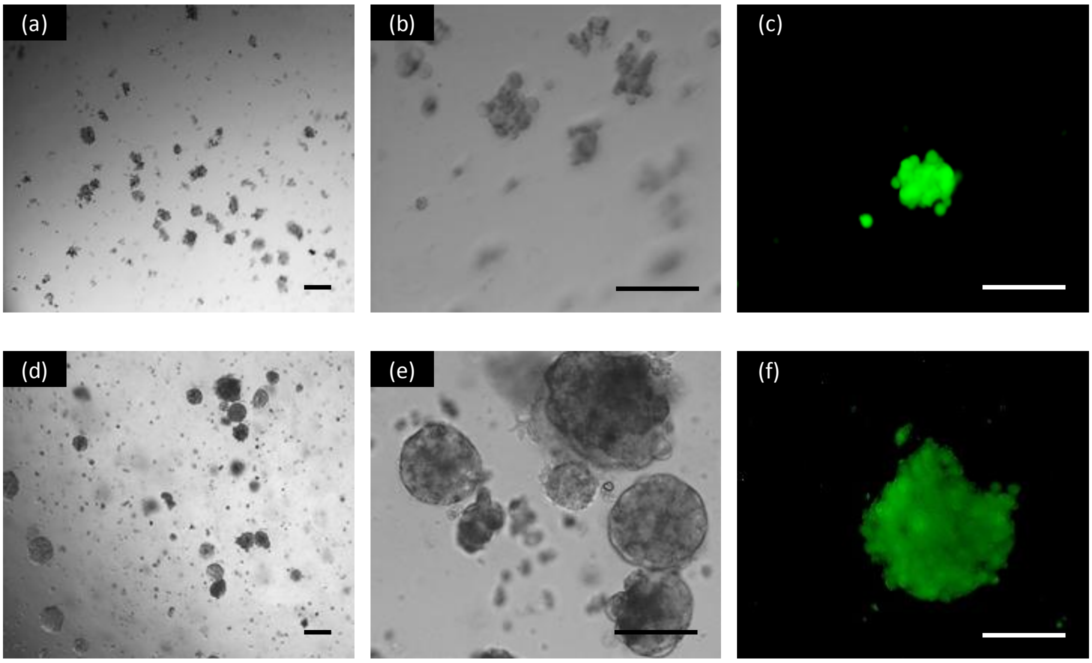

Figure 5-11 HeLa cell spheroids formation in the P(NIPAM-AA) microgels. (a) and (b) are optical images for spheroids at day 7 at different magnifications: (a) for 4x magnification , and (b) for 20x magnification. (c) is the Live/Dead image of spheroids at day 7. (d) and (e) are optical images for spheroids at day 14 at different magnification: (d) for low magnification, and (e) for high magnification. (f) is the Live/Dead image of spheroids at day 14. Scale bar is 100 μm.

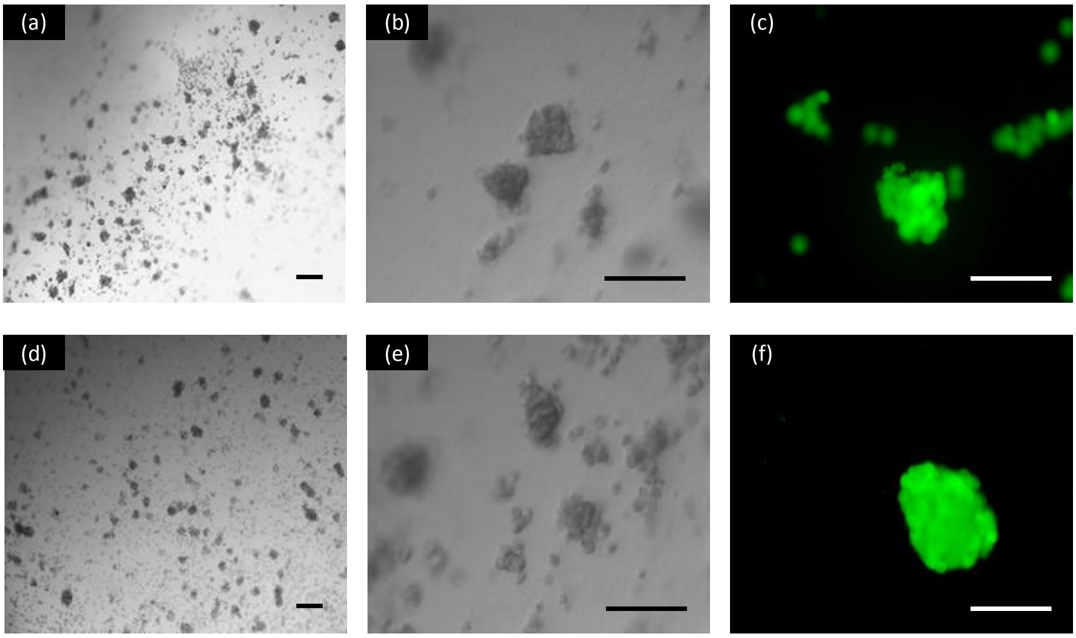

Figure 5-12 HeLa cell spheroids formation in the P(NIPAM-MA) microgels. (a) and (b) are optical images for spheroids at day 7 at different magnifications: (a) for 4x magnification , and (b) for 20x magnification. (c) is the Live/Dead image of spheroids at day 7. (d) and (e) are optical images for spheroids at day 14 at different magnification: (d) for low magnification, and (e) for high magnification. (f) is the Live/Dead image of spheroids at day 14. Scale bar is 100 μm.

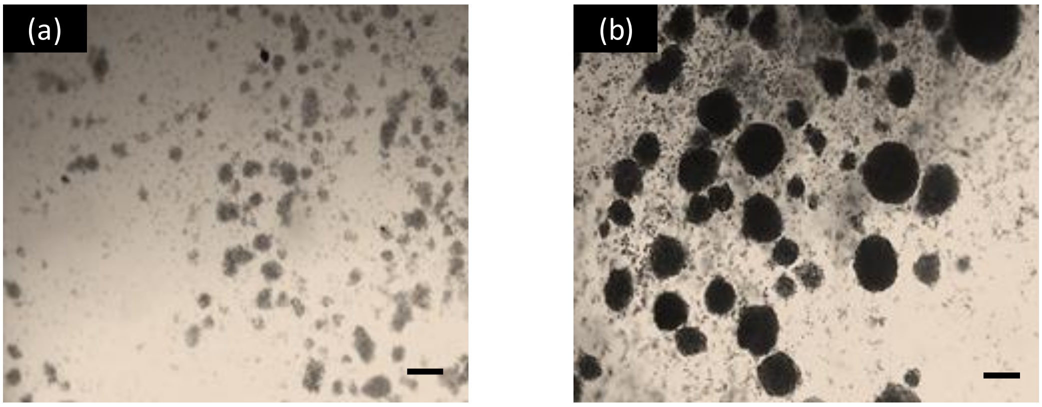

Figure 5-13 HeLa cell spheroids formation in the P(NIPAM-IA) microgels at low magnification (x4): (a) for Day 7 and (b) for Day 14. Scale bar is 100 µm.

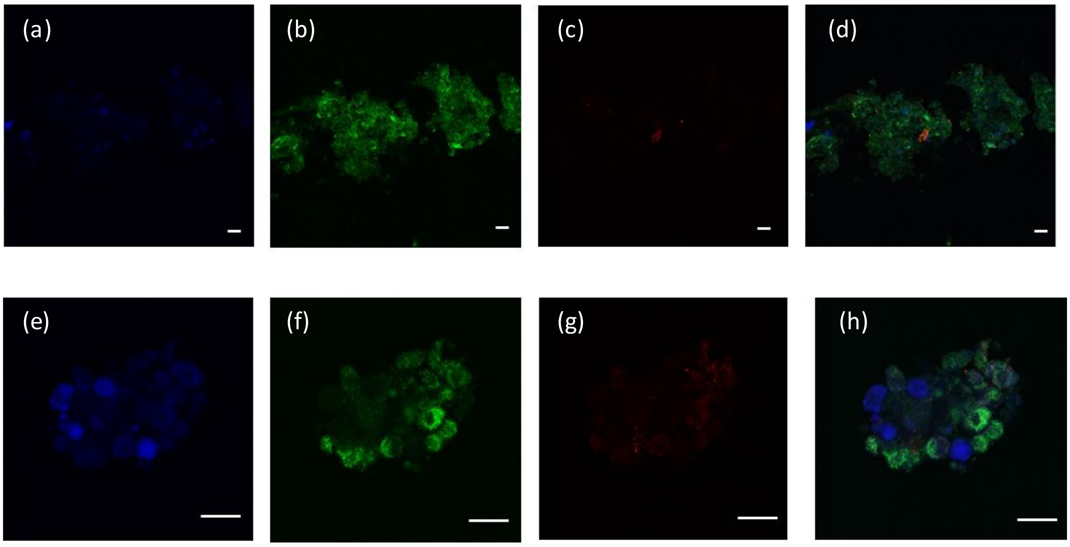

Figure 5-14 Cellular spheroids formation in the P(NIPAM-IA) microgels scaffold. (a) to (d) are for MSC: (a) Hoechst, (b) Calcein, (c) EthD and (d) merged image. (e) to (h) are for U-87 spheroids: (e) Hoechst, (f) Calcein, (g) EthD and (h) merged image. Scale bar is 10 μm.

CHAPTER SIX

6. Exploring thermally reversible hydrogels for heart regeneration

Chapter 6: Exploring thermally reversible hydrogels for heart regeneration

Xiaolin Cui[a], Junnan Tang[b], Yusak Hartanto[a], Jingxiu Bi[a], Sheng Dai[a], Ke Cheng[b] and Hu Zhang[a]

a School of Chemical Engineering, The University of Adelaide, Adelaide, SA, Australia, 5005

b Department of Molecular Biomedical Sciences and Comparative Medicine Institute, North Carolina State University, Raleigh, North Carolina, USA, 27607

Graphical Abstract

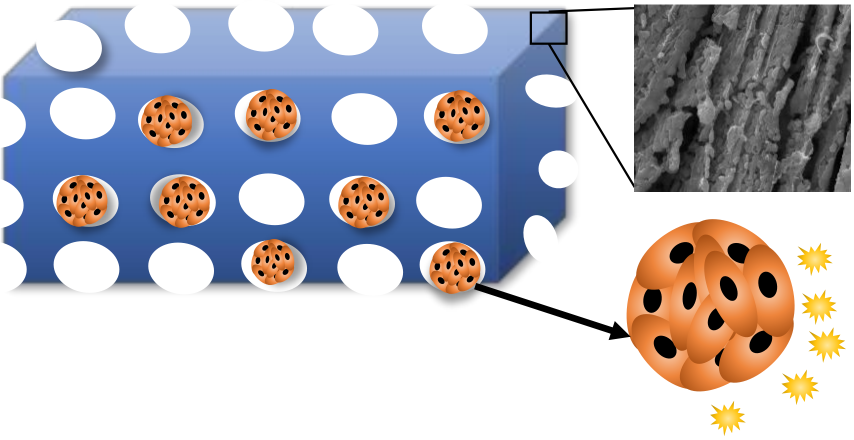

*Corresponding author: Dr Hu Zhang

Email: hu.zhang@adelaide.edu.au

6.1 **Abstract**

Injectable hydrogels for acute myocardial infarction treatment have attracted great attention due to its chronic treatment and effectiveness. Natural polymers as well as few synthetic polymers have been used for post myocardial infarction cardiac repair due to their ability to interact with and facilitate recruitment of cardiac stem cells. However, the impact of microenvironment created by the hydrogel on cardiac stem cells behavior is not yet addressed. since cell will behave differently in different microenvironment. Hence, here we synthesized serials of thermally sensitive microgels exhibiting different electrical charge (cationic, anionic and neutral) and different degrees of hydrophobicity, and explored the impact of the microgel microenvironment on cardiac stem cell viability and functions. The results indicate the negatively charged and hydrophilic microenvironment offered from the microgels is favorable for maintaining high viability of cardiac stem cells and to releasing a large amount of growth factor that is vital for neonatal rat cardiomyocytes growth. In addition, poly(N-Isoproylacrylamide-co- itaconic acid) P(NIPAM-IA) microgels was injected into mice as an injectable hydrogels. The result shows P(NIPAM-IA) not only will not elicit immune response, but also can improve post MI cardiac function and regenerate cardiomyocytes.

Key words: Injectable hydrogels, Thermosensitive microgels, Stem cells, Myocardial infarction.

6.2 Introduction

Acute myocardial infarction (MI) leads to heart failure which is one of the leading causes for death worldwide. More than 3 million people every year suffer from an acute ST-elevation myocardial infarction (STEMI), and the number of people with a non-ST-elevation myocardial infarction (NSTEMI) is estimated to be 4 million [1]. The hospital mortality rate has dropped significantly due to the development of coronary care units in the 1960s, the introduction of pharmacological reperfusion therapy in the 1980s as well as the widespread application of catheter-based interventions in the 1990s [2-4]. Moreover, aspirin [5], β blockers [6], angiotensin-converting enzyme (ACE) inhibitors [7] and statins [8] as chronic treatment, have been employed to improve long-term prognosis for survivors. Despite these advancements, myocardial infarction treatment still remains a challenge and more effective chronic approaches are still being pursued [9].

Introduction of injectable hydrogels into the MI region is considered as a promising approach to treat MI due to its effectiveness and chronic durability. Hydrogels increase the wall thickness and reduce the wall stress in the damaged tissues [10], and according to the LaPlace's Law, they may improve cardiac functions. Natural polymers, such as fibrin [11], collagen [12, 13], matrigel [13, 14], chitosan [15, 16], keratin [17] and hyaluronic acid [18, 19], have been used on the animal model to treat MI. These hydrogels were found to have positive treatment results and improve hear functions after treatment because they are highly biocompatible and their enriched ECM proteins/carbohydrates interact with cells to facilitate stem cell migration into the MI region. The migrated stem cell in the microenvironment created from the hydrogels may continuously release growth factors for regeneration or repair of myocytes in the damaged tissue [20]. However, drawbacks of natural polymer hydrogels such as poor handling characteristics, batch-to batch-variability, inflexibility in design, incompetence in rapid gelation prevents them from unitization in the MI therapy [21]. The synthetic polymer-derived injectable hydrogels are explored to be the replacement of natural polymer hydrogels. Synthetic polymer hydrogels have been developed for tissue engineering applications because they can mimic natural extracellular microenvironment [22-24], and they are also tuned with functional groups in order to modulate cell behaviors [25-27]. Poly(ethylene glycol) (PEG) [28], poly(lactide-co-glycolide) (PLG) [29], ploy(latide-co-glycolic acid) (PLGA) [30], poly(N-isoproylacrylamide) (PNIPAM) [31, 32], and poly(ε-carpolacton) (PCL) [33] are the most intensively studied. However, very few attempts have been made to inject synthetic hydrogels to treat MI. The poly(N-

Isoproylacrylamide-co- acrylic acid) (P(NIPAM-AA)) with hydroxyethyl methacrylate-poly(trimethylene carbonate) (HEMAPTMC) copolymer was used to treat chronic infarcted myocardium [34]. The high mechanical strength of the hydrogel provided physical support for the heart tissue. However, the impact hof other microenvironment properties on the heart regeneration remains to be investigated.

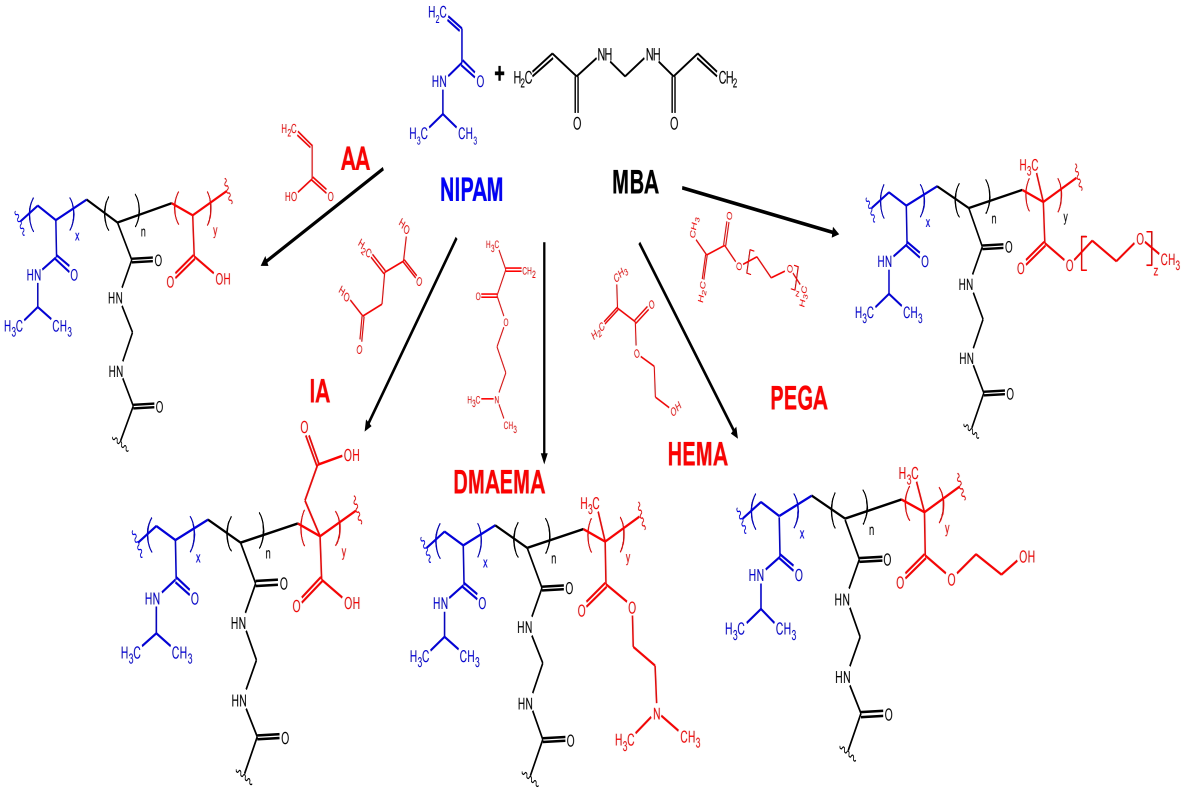

Figure 6-1 Reaction scheme for different charged thermally sensitive microgels

Our group has demonstrated that the cellular microenvironment created from the scaffold, including the surface charge, microstructure, chemical groups, and hydrophobicity/hydrophilicity, affects cell attachment, growth, migration, differentiation, and biological functions [31, 32, 35-37]. Here we proposed to use p(NIPAM)-based synthetic thermosensitive injectable hydrogels for myocardial infarction treatment and examined the effect of the microenvironment offered from the injectable hydrogels on cardiac stem cell attachment, proliferation, growth factor releases, and long-term myocyte viability. Through co-polymerizing the co-monomers with NIPAM (Fig. 6-1), we modified the microgels with different surface charges (cationic, anionic and neutral) and different degrees of hydrophilicity and these microgels were used to form the microenvironment with different properties. Individual human cardiac stem cells (hCSCs) were cultured inside these microgels as shown in Fig. 6-2a, hCSCs proliferated within the microgel (Fig. 6-2c&d) and formed a multicellular spheroid structure (Fig. 6-2e). The biological factors such as vascular endothelial growth factor (VEGF), stromal-derived factor-1 alpha (SDF-1α) and insulin-like growth factor I (IGF-I) released from the hCSC spheroid structure in the microgels were quantified to assess the impact of the microenvironment on the hCSC functions and the conditional culture medium collected from the hCSCs culture in the microgels was applied to culture neonatal rat cardiomyocytes (NRCMs) culture in vitro (Fig. 2b). We future injected the best microgel, P(NIPAM-IA), into immune-competent mice as an injectable hydrogel to evaluate the immune responses and assess the efficacy of the MI repair (Fig. 6-2f&g.

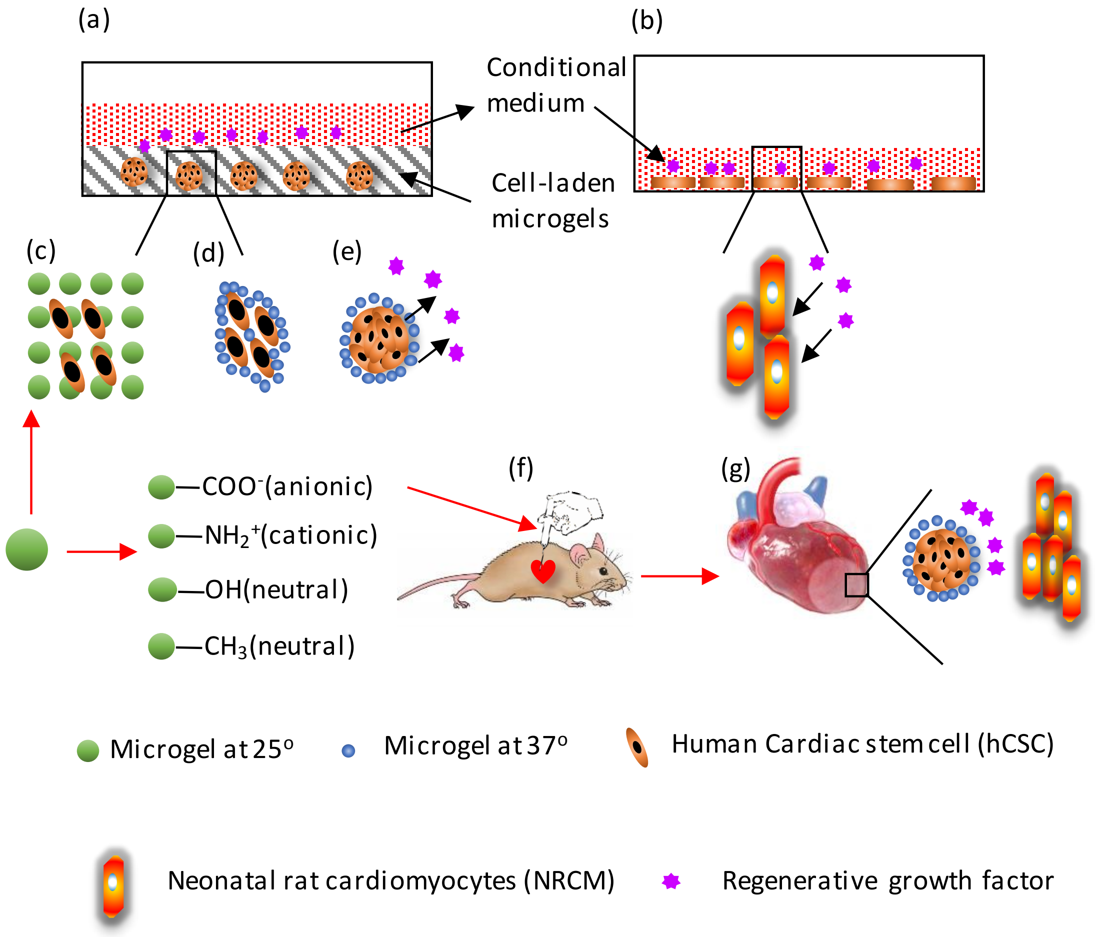

Figure 6-2 The use of thermal sensitive microgel scaffold for human cardiac stem cells (hCSC) spheroid for heart regeneration. (a) hCSCs spheroid culture within microgel network. (b) Conditional medium collected from hCSCs spheroids culture was used for neonatal rat cardiomyocytes (NRCM) culture. The growth factor from hCSC spheroids stimulates NRCM growth. (c) to (e) hCSCs spheroid formation inside microgel scaffold. (c) hCSCs are mixed with microgels at 25°C. (d) At 37°C, microgels confine single cells in a three-dimensional network. (e) After certain days culture regenerative growth factor release

from hCSC spheroids. (f) Assessment of immune responses of microgels and evaluation of MI treatment. (g) Injection of microgels into mouse hearts for MI treatment.

6.3 **Method and materials**

6.3.1 Materials

N-Isoproylacrylamide (NIPAM, 99%+), N,N-methylenebisacrylamide (MBA, 98+), potassium persulfate (KPS, 99%+), sodium dodecyl sulphate (SDS, 98.5%+), itonatic acid (IA, 99%+), 2-hydroxyethyl methacrylate (HEMA), dimethyl amino ethyl methacrylate(DMAEMA) were ordered from Sigma-Aldrich. Acrylic acid (AA, 99.5%) was purchased from Acros Organics Co. (New Jersey, USA). Before synthesis, NIPAM was recrystallized in n-hexane and dried in vacuum at room temperature to achieve high purification. Collagenase solution was bought from Sigma (St. Louis, MO). Fiberonectin was ordered from Biosciences (San Jose, CA). Iscove's Modified Dulbecco's Medium (IMDM), 2-mercaptoethanol, L-glutamine, and LIVE/DEAD® Viability/Cytotoxicity kit were bought from Invitrogen (Carlsbab, CA). Fetal bovine serum and ultralow attachment flask were ordered from Corning (Corning, NY). Gentanicin and trypsin were purchased from Gibco, Life technologies (CA, USA). VEGF and IGF-1 were purchased from R&D Systems (Mineapolis MN) and the SDF-1 ELISA kits from B-Bridge International (Cupertion, CA).

6.3.2 Microgel synthesis

Free radical emulsion polymerization was carried out to synthesize P(NIPAM) based microgels according to our previous study [32]. Based on the recipe in Table 6-1, 9.9 mmol NIPAM, 0.1mmol co-monomer, 0.2 mmol (31 mg) MBA and 0.2 mmol SDS (for positive-charge DMAEMA microgel, no SDS was added to avoid introducing the surfactant with negative charges) were dissolved in 97 mL of water before the mixture was transferred into a 250 mL three-necked flask connected with a condenser and a mechanical stirrer. After 30 min degassing under nitrogen atmosphere, the flask was placed into a pre-heated oil bath at 70°C. 3mL of KPS aqueous solution (0.1 mmol) (for DMAEMA microgel, the positively charged initiator APPS at 0.1 mmol was used instead) was injected into the flask to initiate the reaction. After 5 hr polymerization with continuous stirring under a nitrogen atmosphere at 70ºC, the solution was cooled down to room temperature and purified by membrane dialysis (cut-off M_w 12-14kDa) against Milli-Q water for a week with daily water change.

After purification, the solution was concentrated through heating up to 70 ºC to evaporate the water. An aliquot of solution was totally dried at 70ºC to estimate the concentration.

Table 6-1 Synthesis and characterization of different P(NIPAM) based microgels.

Name	NIPAM	Co-monomer	MBA	SDS	KPS	Zeta potential mV		VPTT	T_{gel}
	mmol	mmol	mmol	mmol	mmol	25 ºC	37ºC	ºC	ºC
P(NIPAM-IA)	9.9	0.1	0.2	0.2	0.1	-10.2±0.2	-12.8±0.5	34	32
P(NIPAM-PEGA)	9.9	0.1	0.2	0.2	0.1	-1.9±1.0	-1.8±0.56	33	30.5
P(NIPAM-HEMA)	9.9	0.1	0.2	0.2	0.1	-3.8±1.1	-4.9±0.4	30	27
P(NIPAM-DMAEMA)	9.9	0.1	0.2	0	0.1	6.49±0.5	7.6±0.2	32	31

6.3.3 Dynamic light scattering measurement and Fourier transform infrared spectroscopy

The hydrodynamic diameter (d_h) and the zeta potential of microgels at 1.0 mg/mL in PBS buffer were measured by a Zetasizer (Malvern, Nano-ZS) at different temperatures. Attenuated total reflectance Fourier transform infrared spectroscopy (ATR-FTIR) was used to identify functional co-monomers in the microgels to confirm the success of co-polymerization. A Thermos Scientific NICOLET 6700 spectrometer equipped with a diamond ATR was used to record FTIR bands. Wavenumber resolution was 4 cm^{-1} in the range of 400–4000 cm^{-1}.

6.3.4 Rheological characterization

Dynamic oscillation experiments were performed in a universal stress rheometer SR5 (Rheometric Scientific) with a 40 mm cone plate geometry for 30 mg/mL microgel dispersions in PBS buffer. The gap was set up at 0.0483mm, and the temperature was controlled by a Peltier system connected to a water bath. The elastic (storage) modulus G' and viscous (loss) modulus G" were measured at different temperatures from 20 to 40 °C. The stress was fixed at 0.1 Pa, and the frequency at 0.1 Hz. The experiments were tested in the linear viscoelastic region.

6.3.5 Hydrogel morphologies

30 mg/mL microgels dispersions in PBS buffer were prepared in centrifuge tubes. The tubes were placed into a water bath at 37°C until the solution was gelled. The samples were quickly quenched by liquid nitrogen then dried under vacuum using a Christ Alpha 2-4 LD free dryer. A FEI Quanta 450 FEG Environmental SEM (scanning electron microscopy) was employed to record microgel morphologies after coating with platinum at an acceleration voltage of 20 kV.

6.3.6 Derivation and culture of human CSCs

The experimental procedures were approved by the Institutional Review Board (IRB) of North Caroline University. Human CSCs were isolated from endomycardial heart biopsies obtained from the ventricular aspect of septum in patients during operating heart transplantation. Heart biopsies were chopped into small pieces (around 2 mm^3). After washing with PBS, the collagenase solution was used to digest the tissue. The tissue pieces were cultured as cardiac explants on a culture plate that was coated with 0.5 mg/mL fiberonectin in culture medium (IMDM with 20% FBS, 0.5% gantanicin, 0.1 m 2-mecaptoethanol and 1% L-glutamine). In 1-2 weeks, a stratum of stromal-like flat cells were observed at the cardiac explant with phase-bright round cells on the top. 0.25% trypsin was used to harvest cells and then cells were seeded at a density of 2×10^4 cells/mL in an ultraLow-attachment flask for cardiosphere formation. It took around one week for cells to spontaneously cluster together and form cardiospheres. The cardiosphere-derived cardiac stem cells (hCSCs) were produced by seeding collected cardiospehres on fibronectin-coated plates. All cultures were under the same conditions with continuous supply of 5% CO_2 in a humidity environment at 37ºC.

6.3.7 Three-dimensional hCSC and NRCM cell culture in the microgel

hCSCs and 50 mg/mL of microgels (in PBS buffer) were mixed at a ratio of 2:3. 500 µL cell/gel mixture was seeded into each well in 24 a well-plate for hCSC culture at a cell density of 10^4 per well. hCSCs were further proliferated in 96 wells plates with 50 µL cell/gel mixture in each well at a cell density of 2,500 cells per well. After incubation at 37 ºC for 1 hr to form gel, 150µL cell culture medium was added to each well of 96 wells plate. Cells were incubated up to 7 days under a humidified environment with 5% CO_2 with a daily medium change. After culturing for pre-determined days, 10 µl CCk-8 (cell count kit 8) was added into each well to perform the cell proliferation assay for hCSCs. After 4 hr incubation at 37°C, the gel/cell mixture was cooled down to room temperature until the gel was liquefied, then the plate was placed into a microplate reader (Tecan sunrise, Switzerland) to read the absorbance at 490nm.

NRCMs culture was performed in 96 wells plate with 50 μL cell gel mixture in each well at a cell density of 1.5×10^5 cells per well. The cell culture and cell proliferation assay were conducted in the same procedure as for hCSCs.

6.3.8 Live/dead cell image

The cell viability test was performed by the Live/Dead cell viability/cytotoxicity kit. After cell culture, the gel / cell mixture was washed with pre-warmed PBS buffer twice. 200 μL (for 24 wells) or 50 μL (for 96 wells) dye solution (0.2% Ethidium homodimer-1 (red) and 0.05% calcein AM (green) in PBS buffer) was added into each well. After incubation for another 30 min? at 37°C, cells were rinsed by PBS buffer twice. Then cells were observed under a ZEISS LSM 880 WITH Airyscan microscope (Carl Zeiss, Oberkochen, Germany).

6.3.9 ELISA and NRCM cell culture with conditional medium

200 μL of cardiac stem cells (hCSCs) was mixed with 300 μL 50 mg/mL of microgels (in PBS buff, 7.2) to seed into each well in 24 well-plates. The cell density was 10,000 in each well. The plate was placed in an incubator at 37°C for 45 min to allow microgel gelation. 1 mL cell culture medium was added into each well. Cells were cultured up to 7 days with medium change every two days. The cell culture medium was replaced by FBS free medium and cells were incubated for another 2 days. The FBS free cell culture medium was collected for ELISA assays and further NRCM cell culture. The concentration of IGF-1, VEGF, and SDF-1 was determined by the ELISA kits following the manufacturer's instructions. The collected conditioned medium was added into wells in a 96 well-plate seeded with 7500 freshly harvested NRCMs in each well. NRCMs were cultured with conditioned medium for 3 days. The LIVE/DEAD vibility/cytotoxicity kit was used to assess the cell viability.

6.3.10 Inflammation and immunogenicity of P(NIPAM-IA) microgel in immune-competent mice

To assess the biocompatibility of P(NIPAM-IA) microgel in vivo, a cohort of immune-competent male CD1 mice were anesthetized with 3% isofluorane combined with 2% oxygen inhalation. Under sterile conditions, the heart was exposed by a minimally invasive left thoracotomy, and the heart was randomized to be injected with 50 μl P(NIPAM-IA) microgel. Mice were sacrificed to harvest the heart and blood at day 7 for immunochemistry, while heart and spleen at day 21 post-injection for H&E stain. The heart or spleen were frozen in the OCT compound and sectioned at 10 μm thickness from the apex to the ligation level with 100 μm intervals for histology analysis. Haematoxylin and Eosin (HE) staining was performed as described in our previous paper [7]. The vein blood was harvested in an Edta tube and centrifuged for 20 min at 2000 rpm to obtain plasma which was stored at -80 °C. The mouse inflammation antibody array C1 (Raybio, Norcross, GA) was used for quantification of inflammatory proteins in the plasma.

6.3.11 Heart morphometry

After the echocardiography study at 3 weeks, animals were euthanized and hearts were harvested and frozen in the OCT compound. Specimens were sectioned at a 10 μm thickness from the apex to the ligation level with 100 μm intervals. Masson's trichrome staining was performed according to the manufacturer's instructions (HT15 Trichrome Staining (Masson) Kit; Sigma-Aldrich). From the Masson's trichrome stained images, morphometric parameters including viable myocardium, scar size and infarct thickness were measured in each section with the NIH ImageJ software. The percentage of viable myocardium as a fraction of the scar area (infarcted size) was quantified based on the previous report [7]. Three selected sections were quantified for each animal.

6.3.12 Cardiac function assessment

The transthoracic echocardiography procedure was performed by an animal cardiologist who was blind to the experimental design using a Philips CX30 ultrasound system coupled with a L15 high-frequency probe. All animals underwent anesthesia by inhaling 1.5% isofluorane-oxygen mixture in the supine position at the 4 hr and 3 weeks. Hearts were imaged in the long-axis views at the level of the longest LV diameter. Ejection fraction (EF) was determined by measurement of the images taken from the infarcted area.

6.3.13 Histology

For immunohistochemistry staining, heart cryosections were fixed with 4% paraformaldehyde, permeabilized and blocked with the Protein Block Solution (DAKO, Carpinteria, CA) containing 1% saponin (Sigma), and then incubated with the following antibodies overnight at 4 °C: rabbit anti-CD3 (ab16669, Abcam, Cambridge, United Kingdom), mouse anti-CD8 alpha (mca48r, abd Serotec, Raleigh, NC), mouse anti-CD68 (ab955, Abcam) and rabbit anti-vWF (ab6994, Abcam). FITC- or Texas-Red secondary antibodies (Abcam) were used in conjunction with the above primary antibodies. For assessment of cell apoptosis, heart cryosections were incubated with the TUNEL solution (Roche Diagnostics GmbH, Mannheim, Germany) and counter-stained with DAPI (Life Technology, NY, USA). Images were taken under an Olympus epi-fluorescence microscopy.

6.3.14 Statistical analysis

All results were expressed as mean ± standard deviation (SD). Comparison between two groups were conducted by two-tailed Student's t test. One-way ANOVA test was used for comparison among three or more groups with Bonferroni post hoc correction. Differences were considered statistically significant when P-values were <0.05.

6.4 Result and discussion

6.4.1 Microgel synthesis

Free radical emulsion polymerization was utilized to synthesize poly(N-Isoproylacrylamide) (P(NIPAM)) based microgels. Fourier transform infrared spectroscopy (FTIR) analysis was employed to identify the functional groups of the co-monomer in the as-synthesized microgels (Fig. 6-3a). C=O asymmetric stretching and C-N bending within N-isopropylacrylamide are shown at 1640 cm^{-1} and 1550 cm^{-1} respectively [38]. The methyl groups of NIPAM associated with C-C stretching and bending as well as asymmetric C-H bonding are assigned to 1450 cm^{-1}. The C=O bond in carboxylic group of itonatic acid (IA) is around 1710-1720 cm^{-1}. The hydroxyl group from 2-hydroxyethyl methacrylate (HEMA) is associated with the peak at 3440 cm^{-1} [39]. The C-O stretching bands in the ether group from polyethylene glycol acrylate (PEGA) are assigned to 1050 cm^{-1} [40]. The C=O bond (around 1640 cm^{-1}) and C-N bond (around 1566 cm^{-1}) in 2-(N,N-dimethylamino)ethyl methacrylate (DMAEMA) [41] are overlapped with those from NIPAM. The FTIR results confirm the co-monomers except DMAEMA have been incorporated into NIPAM. The p(DMAEMA-NIPAM) microgels were assessed through their zeta potential measurements. A highly positive zeta potential value for this microgel demonstrates the DMAEMA monomer has been successfully co-polymerized with NIPAM.

The zeta potential indicates the surface charge of the microgels, which was shown in Table 6-1. The incorporated co-monomers influence the zeta potential of the as-synthesized microgels. The partial deprotonation of the carboxyl group in P(NIPAM-IA) raises the negative surface charge of the microgel. Apart from the carboxyl group contribution to the negative charge, the introduction of the KPS initiator also results in a negative surface charge of the synthesized microgels, and this is the reason for a slightly negative charge of both P(NIPAM-PEGA) and P(NIPAM-HEMA) microgels even they only have neutral monomers. The amino group in the P(NIPAM-DMAEMA) and the positively charged initiator contribute to a positive surface charge of this microgel.

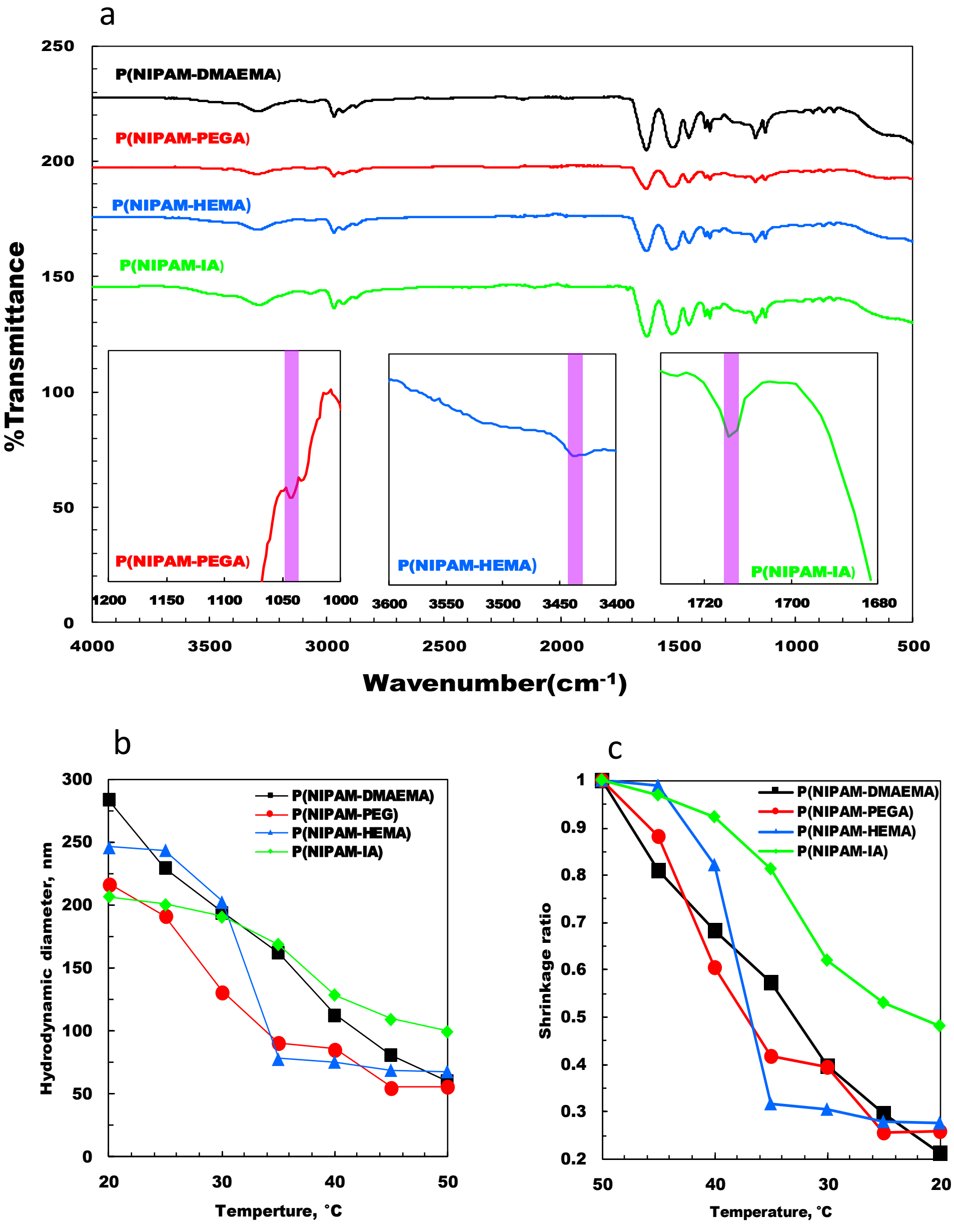

Figure 6-3 FITR and temperature dependent microgel size. (a) FTIR for P(NIPAM) based microgels. The enlarged figures shows the peaks for individual co-monomer functional groups; (b) hydrodynamic diameter (d_h) and (c) the shrinkage ratio $d_h(T)/ d_h(25$ °C) for 1.0 mg mL^{-1} P(NIPAM) based microgels in physiological saline (pH≈7.4).

6.4.2 Hydrodynamic diameter

Dynamic light scattering (DLS) was applied to the diluted synthesized microgels (0.1 mg mL^{-1}) at various temperatures in PBS buffer to obtain the microgels hydrodynamic diameter (d_h) as shown in Fig. 6-3b. The d_h of all microgels shrinks with an increase in temperature because of the presence of the NIPAM moiety. All microgels have a considerable shift of d_h around 30-35°C. This critical transition temperature is termed as the volume phase transition temperature (VPTT) of microgels, which is correspondent to the lower critical solution temperature (LCST) of the linear polymer NIPAM. To further illustrate the phase transition behaviours as a function of temperature, the plot of the shrinkage ratio $d_h(T)/d_h(25°C)$ versus temperature is shown in Fig. 6-3c. The P(NIPAM-DMAEMA) has the largest shrinkage ratio because no SDS surfactant was added during the polymer synthesis procedure, resulting in a large microgel size. P(NIPAM-IA) shows the lowest shrinkage ratio in comparison with P(NIPAM-HEMA) and P(NIPAM-PEGA) due to a high amount of carboxylic groups which lead to stronger hydrogen bonding.

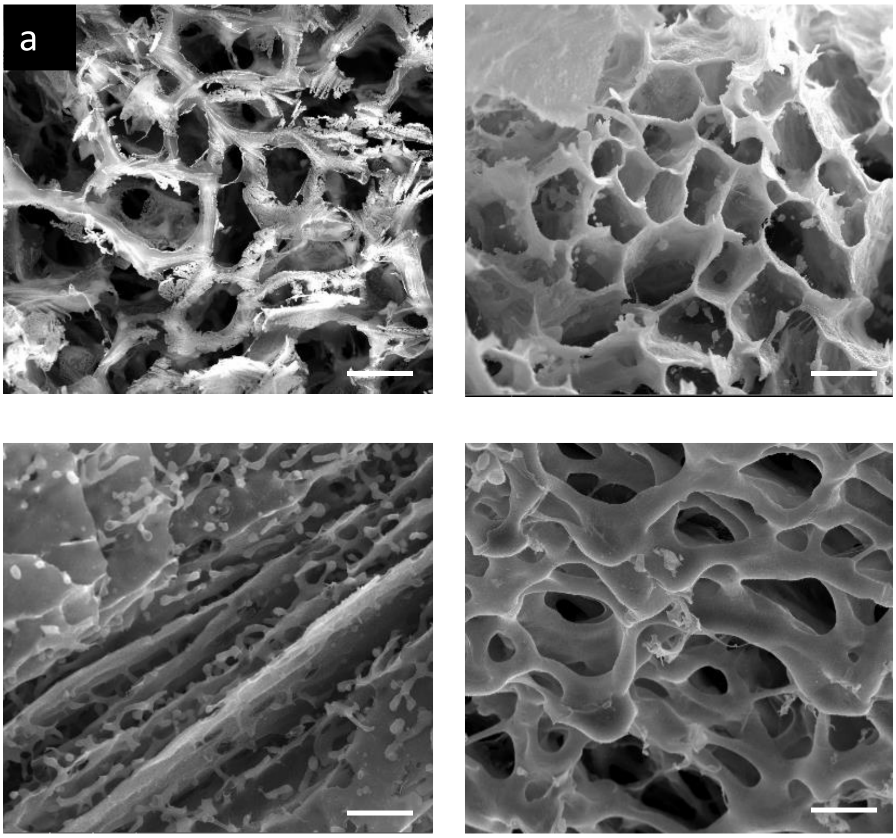

Figure 6-4 SEM morphologies of the in situ formed P(NIPAM) based hydrogels. (a) P(NIPAM-DMAEMA); (b) P(NIPAM-PEGA); (c) P(NIPAM-HEMA); (d) P(NIPAM-IA); scale bar is 20 μm.

6.4.3 Microstructure and thermal gelation of the microgels

SEM was employed to characterize the microstructure and morphology of the synthesized microgels. Through quick quenching in liquid nitrogen to freeze samples, the microgels achieved an amorphous structure rather than a crystalline structure, which maximally preserved the original microgel structure [42]. The SEM shows different morphologies and structures for five microgels (Fig. 6-4). P(NIPAM-IA) has the largest pore size around 50 um because of its highest electrostatic repulsion force which is due to the deprotonation of the carboxyl groups of the microgels. Such a big pore size may allow cell migration inside the network to promote cell-cell interactions. P(NIPAM-HEMA), on the other hand, has the smallest pore size around 10 μm due to its almost neutral charge density and strong hydrophobic attractions. Overall, all the hydrogel networks present a porous structure which allows nutrients, oxygen and wastes to transport into/out of cells inside the microgel.

All the microgel dispersions at 30 mg mL^{-1} (in physiological saline, at a pH of approximate 7.2) change the state from sol to gel once the temperature is over 37 ºC, and reverse back to the sol state again when the gel cools down to room temperature(Fig. 6-14, supporting document). The balance of hydrophobic interactions and electrostatic repulsions results in the physical hydrogel formation[32]. The rheological study reveals the gelation dependence on temperature. The dynamic moduli of all microgels at 30 mg mL^{-1} were plotted against temperature (Fig. 6-5). The stress was fixed at 0.1 Pa and the frequency at 0.1 Hz. At a lower temperature, the microgel dispersions are in the sol state. With an increase in temperature, the elastic modulus (G') and the loss modulus (G") of the microgel dispersions both increase sharply. The point at which the value of G' is greater than G" is considered as the gelation temperature T_{gel}. P(NIPAM-HEMA) has the lowest gelation temperature due to its highest hydrophobicity ascribed to the strong hydrophobic co-monomer HEMA. Other microgels have a T_{gel} at around 32°C to 33°C. All the gelation temperatures are close to their VPTTs. This result implies that hydrophobic interactions are the main driven force for the hydrogel formation. The hydrophilic microgel becomes hydrophobic when the temperature reaches their VPTTs and the hydrophobic attractions drive the gelation of the microgel to form a 3D structure. Furthermore, P(NIPAM-IA) has the highest mechanical strength, around 25 times higher than P(NIPAM-HEMA). Because the crosslink between individual microgels is formed with additional intra- and inter-chain interactions, the highest hydrophilic carboxyl groups from itonatic acid result in the strongest hydrogen bonding in comparison with the most hydrophobic HEMA[43].

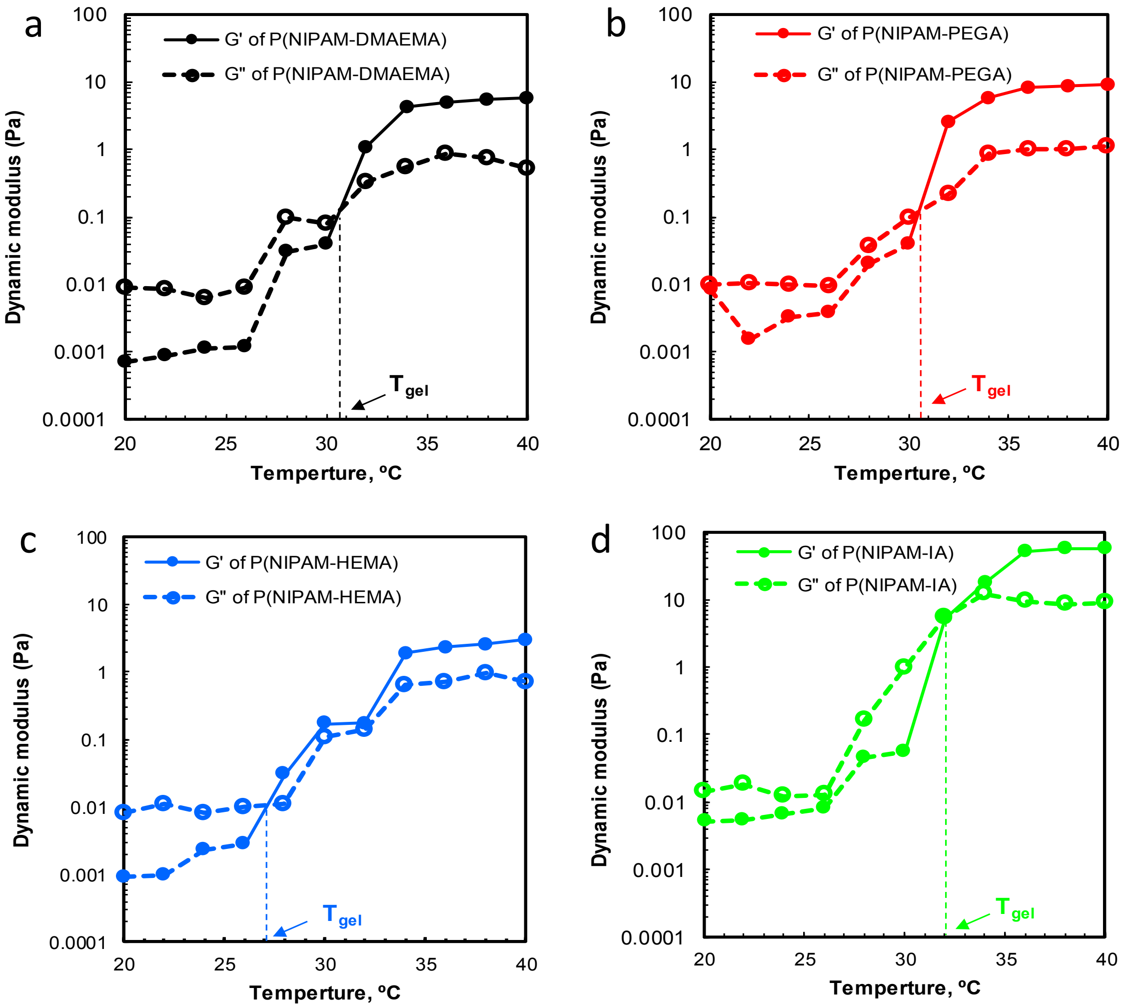

Figure 6-5 The temperature dependence of the dynamic moduli of 30 mg mL^{-1} of P(NIPAM) based microgels (pH≈7.4). (a) P(NIPAM-DMAEMA); (b) P(NIPAM-PEGA); (c) P(NIPAM-HEMA); (d) P(NIPAM-IA); G’ is elastic (or storage) modulus and G” is viscous (or loss) modulus.

6.4.4 Three-dimensional culture of hCSCs

The MTT assay was used to evaluate the viability of hCSCs within the 3D microgel scaffold. The cell proliferation rate is presented as the absorbance at different incubation durations since the absorbance values are well correlated with the number of live cells[44]. As shown in Fig. 6-6, at day one, cells seeded in the microgels exhibit a similar absorbance value compared with the 2D culture, which indicates the high biocompatibility of the synthesized microgels as well as the same initial cell density for all 3D and 2D cultures. P(NIPAM-DMAEMA), on the other hand, halves the absorbance value in comparison with the value in other microgels or the 2D culture wells, which may be due to the slightly positive-charged microenvironment from the DMAEMA monomers. The positive charge has a detrimental effect on the cells viability [45] since the membrane potential of cells is negative and cationic surface charges of the microgel

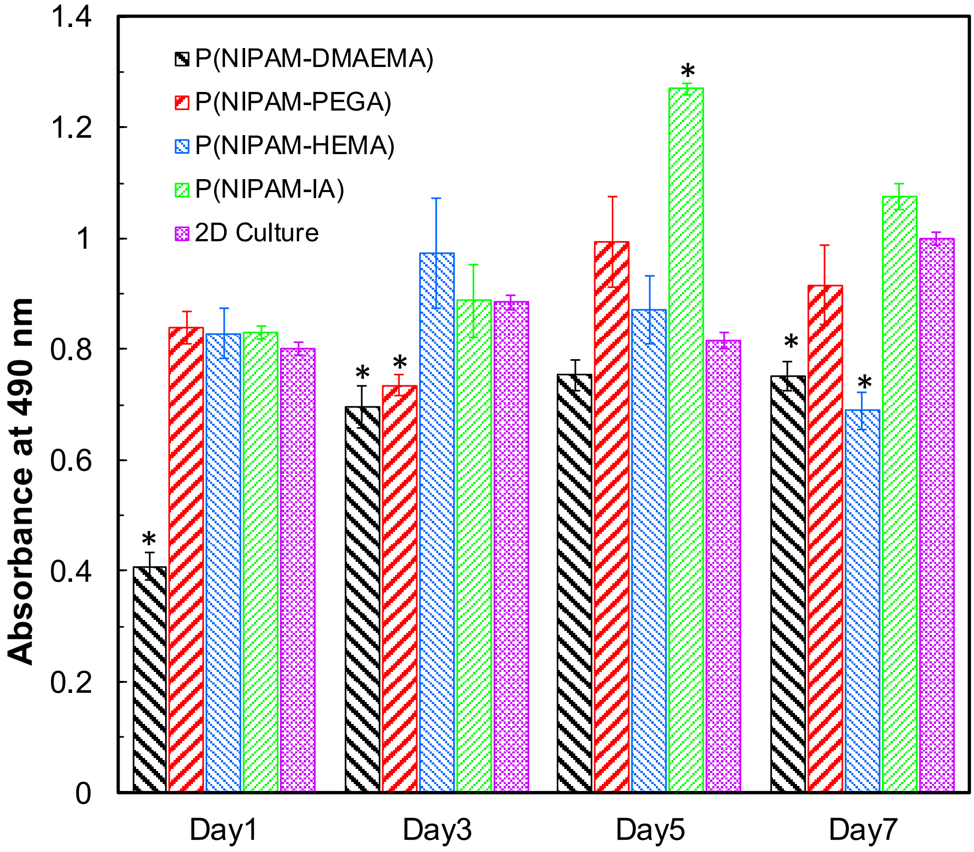

Figure 6-6 Proliferation of hCDCs cultured in the P(NIPAM) based microgel network and 2D culture from day 1 to day 7. (Mean± SD, n=3). '*' indicates $p<0.5$ for cell number of P(NIPAM) based microgels in comparison with that in 2D culture.

may rupture or damage the cell membrane. All cells in the synthesized microgels except the P(NIPAM-HEMA) microgel start to grow in the first 5 days. The cell viability in the P(NIPAM-HEMA) microgel start to drop after day 3. The small pore size of the P(NIPAM-HEMA) microgel has a high resistance for mass transport, which may lead to starvation of nutrients and oxygen while accumulation of toxic wastes around cells. Meanwhile, the highly hydrophobic surface of the P(NIPAM-HEMA) microgel may prevent cell attachment to the microgel surface and therefore, lead to a slow proliferation rate[46]. At day 7, the live cells in both positively charged P(NIPAM-DMAEMA) and the most hydrophobic P(NIPAM-HEMA) microgels are less than those in other microgels, which indicates the microenvironment with positive charges and strong hydrophobicity may not be appropriate for cell proliferation. On the contrast, cells in the P(NIPAM-IA) networks have the highest proliferation rate, which means that the microenvironment with slightly negative charges and high hydrophilicity may stimulate cell proliferation. In addition, the strong mechanical property of the P(NIPAM-IA) microgel may also provide a physical support for facilitating cell attachment and further promoting cell proliferation. The large pore size of the P(NIPAM-IA) network reduces the resistance in transporting oxygen, nutrients and wastes to maintain a high cells viability. Moreover the extra carboxyl (COOH) group introduced to the microgels is also demonstrated to perform better in cell attachment and proliferation in comparison with the ether group in PEGA and the hydroxyl (OH) group from HEMA [47]. Overall, hCSCs are preferable in the microenvironment created by the P(NIPAM-IA) microgel with a slightly negative surface charge, high hydrophilicity, a large pore size, a strong mechanical property and extra carboxyl groups.

To investigate cell viability and morphology inside the microgels, the live/dead images were taken under a fluorescence microscopy as shown in Fig. 6-7a-e and Fig. 6-15, supporting document. Red represents apoptotic cells (EthD positive dead cells), while green indicates the live cells. The smallest percentage of the EthD positive cells from hCSCs in the P(NIPAM-IA) microgel from the images (Fig. 6-7a-e) and the quantitative figure (Fig. 6-7g) further confirms that hCSCs have a high proliferation rate and a high viability in this microgel compared with other microgels. The cell morphology analysis is shown in Fig. 6-7f. The morphology of hCSCs in the 3D microgel culture is a round shape, which is similar to cell morphology in the 3D cell culture [48]. In addition, the negatively charged network of the P(NIPAM-IA) facilitates cell migrations due to the electrostatic repulsion and a large pore size structure, and encourages cell-to-cell interactions that leads to formation of multicellular spheroids (MCSs). The MCSs are spotted in the P(NIPAM-IA) and P(NIPAM-PEGA) microgels. The maximum size of the MCSs in the P(NIPAM-IA) microgel is around 200 μm. The P(NIPAM-HEAM) microgel also has a slight negative charge, but the small pore size (around 5 μm) prevents cells from freely migrating within the microgel and thus hinders MCS formation. The P(NIPAM-DMAEMA) microgel has a positive surface charge which helps cell attachment [35] but restrains cell migration. Therefore, single individual hCSC cells are spotted in both P(NIPAM-HEAM) and P(NIPAM-DMAEMA) microgel networks. hCSCs grown on the 2D culture plates display a flattened and well spread shape. The formation of hCSCs spheroids was reported to improve hCSCs viability and enhance their biological functions [21]. Both the MTT assay and the live/dead images confirm that hCSCs have a better viability and form large clusters by exposing to a microenvironment with negative charges and high hydrophilicity.

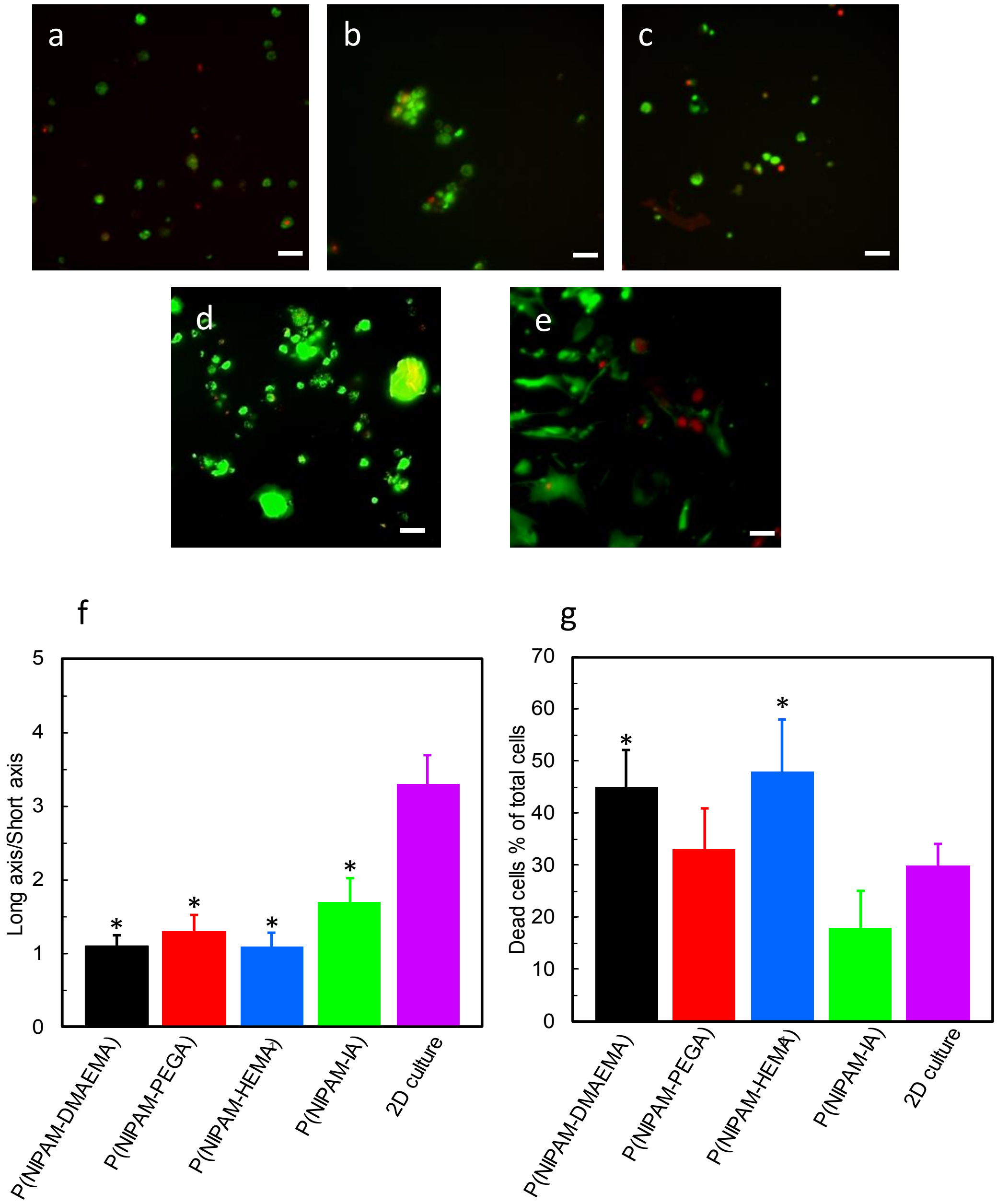

Figure 6-7 hCSCs morphologies and growth in P(NIPAM) based microgels and 2D culture. (a) to (e) Live/Dead images of hCSCs in P(NIPAM) based microgels at day 7; (a) P(NIPAM-DMAEMA); (b) P(NIPAM-PEGA); (c) P(NIPAM-HEMA); (d) P(NIPAM-IA); (e) 2D culture. (f) Enlongated cells morphology was seen in hCSCs culture in different microgels and 2D culture at day 7; (g) Live/Dead assay shows cells viability of hCSCs cultured in different microgels and 2D condition at day 7. Scale bar is 20 µm. Green is Calcein (live cells), Red is EthD (dead cells). Mean± SD(n=3). '*' indicates $p<0.0$ 5 for comparison of cells cultured in P(NIPAM) based microgels with 2D condition.

6.4.5 Biological factor release from hCSCs in microgels

hCSCs in the appropriate microenvironment release regenerative growth factors that play a great role in survival and growth of cardiomyocytes. Therefore, we examine the growth factor release from hCSCs functions in the synthesized microgels. The vascular endothelial growth factor (VEGF) released by hCSCs does not only regulate the activation, proliferation as well as migration of vascular endothelial cells, but also arguments angiogenesis [49, 50]. It contributes to an increase in bloody flow to a healing infarct, which accelerates the healing process [51]. Another regenerative growth factor released by hCSCs, the stromal-derived factor-1 alpha (SDF-1α), guides stem cells to the injured heart tissue. As a result, SDF-1α also augments the angiogenesis [52]. Insulin-like growth factor I (IGF-I) stimulates hCSCs proliferation, somatic growth and hCSC differentiation. Meanwhile IGF-I inhibits apoptotic cell death and enhance stem cell survival [53]. As shown in Fig. 6-8a to Fig. 6-8c, hCSCs incubated in all microgels release a higher amount of IGF-I at three examination days than in the 2D culture, and all four microgels have an equivalent performance by inducing hCSCs to release IGF-I. hCSCs release a similar amount of SDF-1 in two microgels, P(NIPAM-PEGA) and P(NIPAM-IA), as well as in the 2D cell culture. At day 5, VEGF release from the P(NIPAM-IA) is the highest in comparison with other microgels and 2D cell culture, but at day 7, VEGF is produced equivalently in the P(NIPAM-PEGA), P(NIPAM-IA), and the 2D cell culture. The microenvironment created from both P(NIPAM-DMAEMA) and P(NIPAM-HEMA) has a negative impact on both SDF-1 and VEGF release from hCSCs. The conditional medium collected from hCSCs culture in the microgels at day 5 culture experiment was applied to culture neonatal rat cardiomyocytes (NRCMs) for 3 days. The Live/dead assay was employed to assess the NRCMs viability. As shown in Fig. 6-8d to Fig. 6-8h, the number of live NRCMs in the conditional medium from the P(NIPAM-IA) microgel is the highest, while a similar number of live NRCMs is obtained from the conditioned medium from the P(NIPAM-PEGA) microgel and the 2D culture. The fewest NRCMs survive in the medium from the positive charged P(NIPAM-DMAEMA) and the hydrophobic P(NIPAM-HEMA) microgels. This result is in agreement with the ELISA assay for VEGF since VEGF release from hCSCs, which means that these factors from hCSCs contribute significantly to cardiomyocyte activation and proliferation. The microenvironment provided from the microgels are essential for hosting hCSCs and inducing them to produce VEGF and SDF-1 for heart regeneration.

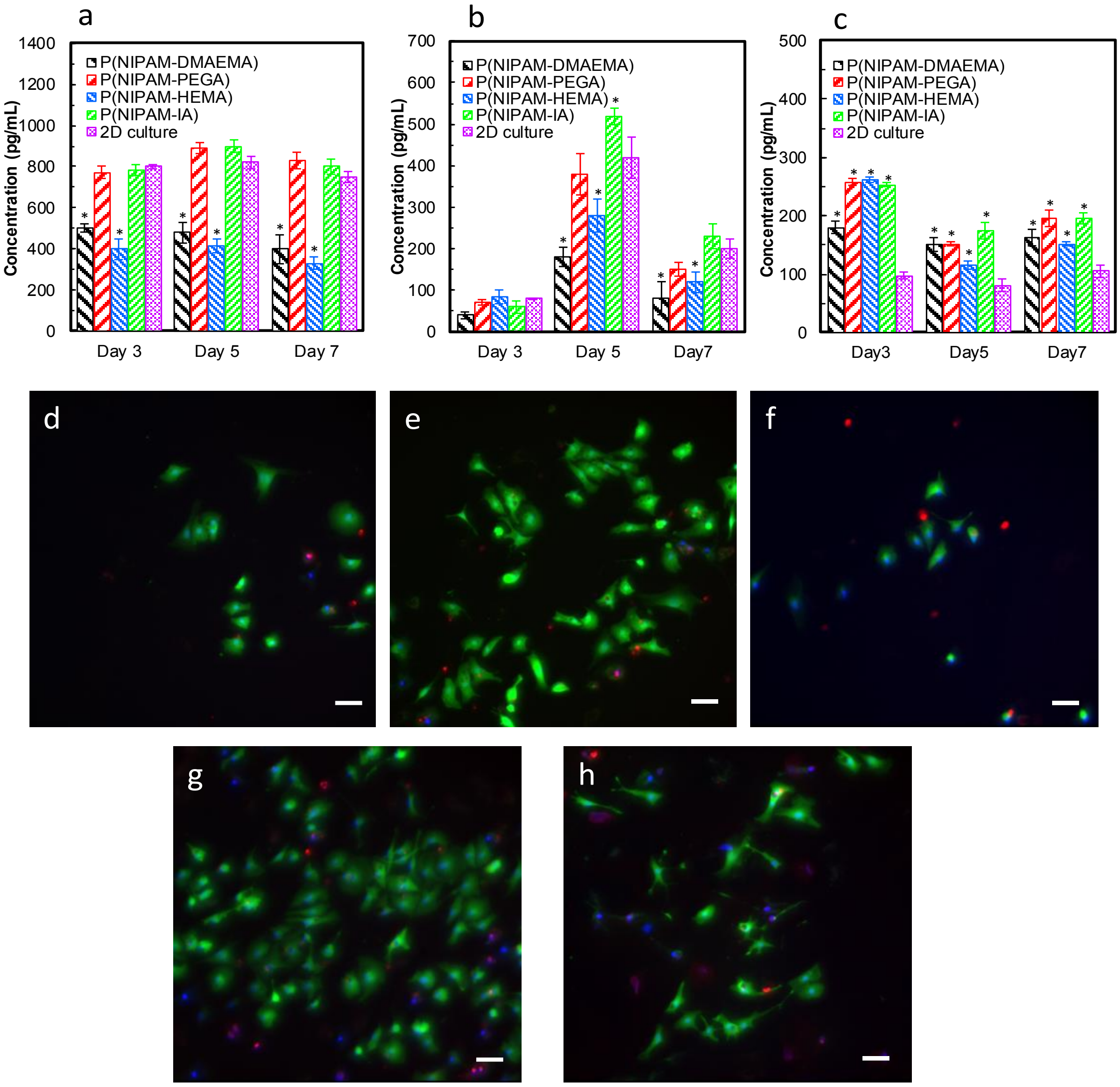

Figure 6-8 Evaluation of hCSCs function in different microgels. (a) to (c) growth factor released from hCSCsin the P(NIPAM) based microgel network and 2D culture at day 3, day 5 and day 7. (a) SDF-1; (b) VEGF; (c) IGF-I. (Mean± SD, n=3). '*' indicates $p<0.05$ for comparing cells in microgels with those in the 2D culture; (d) to (h) NRCMs cell images of conditional medium culture. Conditional medium was collected from different microgel network at day 5. (d) P(NIPAM-DMAEMA); (e) P(NIPAM-PEGA); (f) P(NIPAM-HEMA); (g) P(NIPAM-IA); (h) 2D culture. Green is Calcein (live cells), Red is EthD (dead cells), Blue is hoechest. Scale bar is 20 µm.

6.4.6 In vitro and vivo biocompatible evaluation of P(NIPAM-IA) microgel

In order to evaluate the biocompatibility of microgels in the heart tissue, we cultured neonatal rat cardiomyocytes (NRCMs) inside the microgels or on the 2D culture plates as a control for up to 7 days. The Live/dead assay was employed to assess the viability and morphology of NRCMs inside the microgels (Fig. 6-9, Fig. 6-16 in supporting document).

The result indicates NRCMs have a relatively high viability in all microgels and the highest number of live NRCMs is found in the P(NIPAM-IA) microgel, which indicates the P(NIPAM-IA) microgel is the most biocompatible to NRCMs compared to other microgels. Because the microenvironment from four these microgels has different surface charges, NRCMs in these microenvironments present different morphologies. In an environment with slight positive or negative charges, NRCMs interact with each other to form multicellular spheroids. While under an environment with a high density of negative charges, they present a round shape without cell-cell interactions. NRCMs grown on the 2D culture plate show an elongated shape.

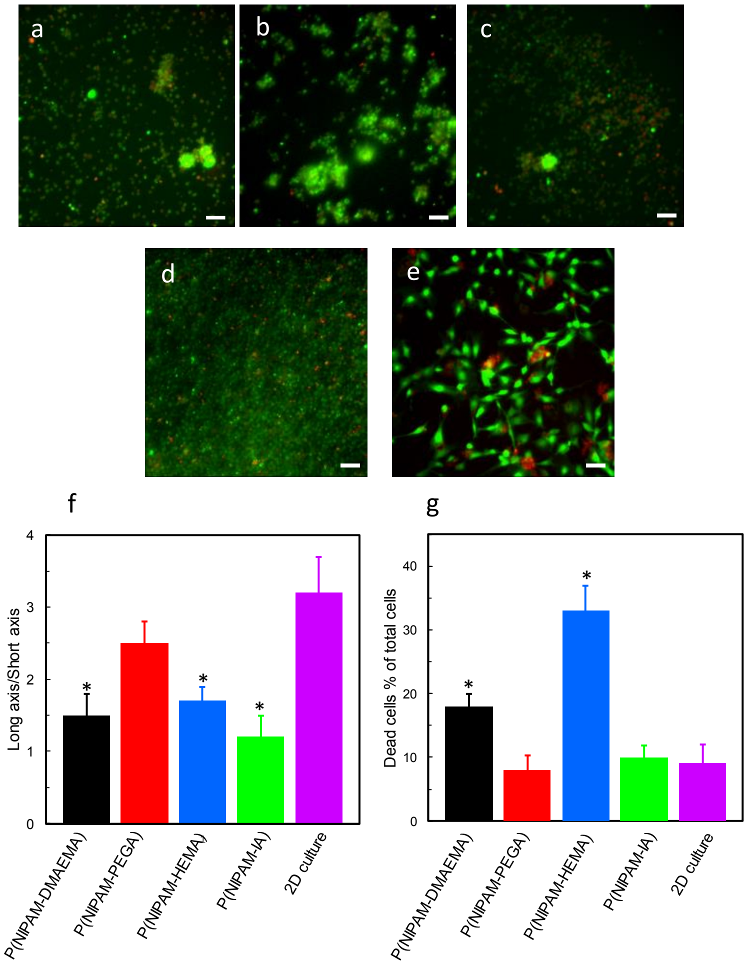

Figure 6-9 NRCMs morphologies and growth in P(NIPAM) based microgels and 2D culture. (a) to (e) Live/Dead images of NRCMsin P(NIPAM) based microgels at day 7; (a) P(NIPAM-DMAEMA); (b) P(NIPAM-PEGA); (c) P(NIPAM-HEMA); (d) P(NIPAM-IA); (e) 2D culture. (f) Enlongated cells morphology was seen in NRCMs culture in different microgels and 2D culture at day 7; (g) Live/Dead assay shows cells viability of NRCMs cultured in different microgels and 2D condition at day 7. Scale bar is 20 µm. Green is Calcein (live cells), Red is EthD (dead cells). Mean± SD(n=3). '*' indicates p<00.5 for comparison of cells cultured in P(NIPAM) based microgels with 2D condition

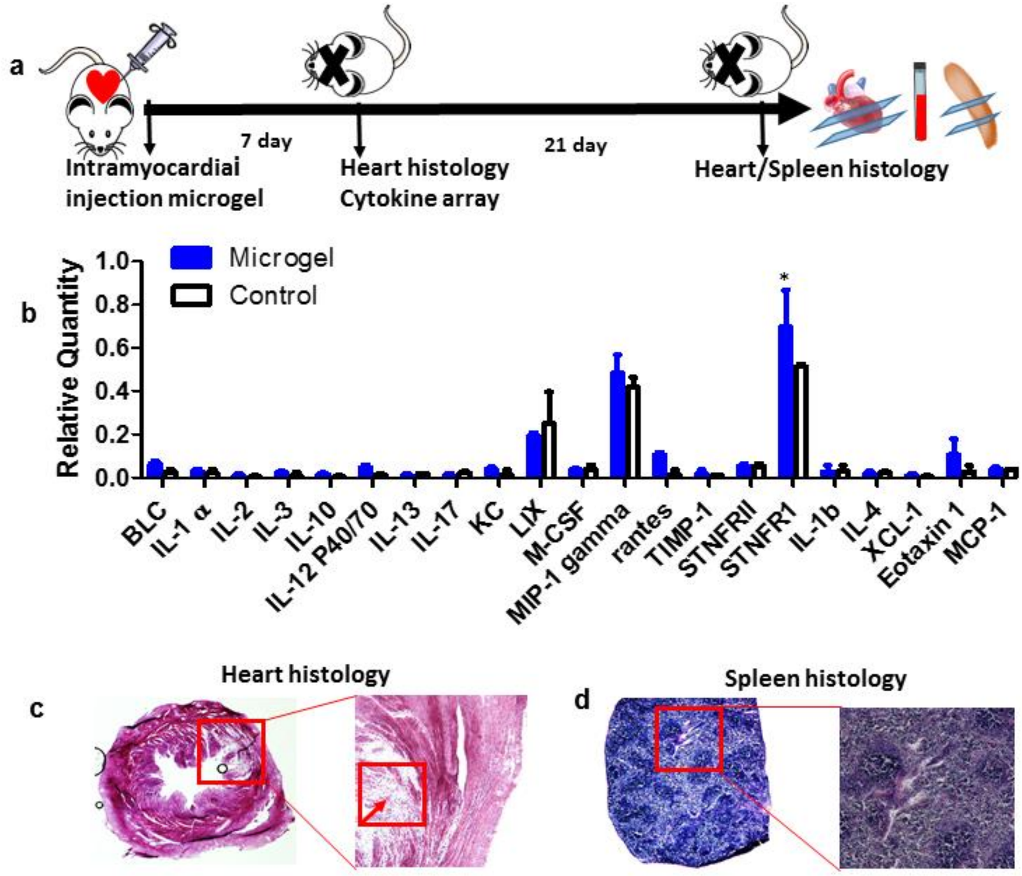

Figure 6-10 Injection of P(NIPAM-IA) microgel does not elicit systematic inflammation in immune-competent mice. (a) Schematic showing the overall animal study design. (b) Relative quantity analysis of circulating levels of proinflammatory factors in mice injected with P(NIPAM-IA) microgel (blue bar) or healthy control mice (white bar) at 7 day (n=3 animals per group). (c) HE staning revealed no inflammation was elicited on the heart section injected with P(NIPAM-IA) microgel at 21 day. Red box indicated the higher magnification of injected area, red arrow indicated the injected P(NIPAM-IA) microgel. (d) HE staining reveals normal spleen function in the mice injected with P(NIPAM-IA) microgel at day 21. * indicates $P < 0.05$.

From the in-vitro evaluation, the P(NIPAM-IA) microgel was selected for further in-vivo assessment of immunogenicity in the immune-competent mice. The immune-competent male CD1 mice were injected with P(NIPAM-IA) microgel (Fig. 6-10a). To evaluate the acute inflammation and T cell immune reaction induced by the microgel, blood and hearts were collected at day 7 after injection. Analysis of mouse inflammatory proteins shows that the plasma levels of pro-inflammatory factors in mice treated with the microgel are comparable to those in normal control mice (Fig. 6-10b), which indicates that injection of the microgel does not induce systematic inflammation. To evaluate the chronic inflammation induced by the microgel, hearts and spleens were collected at day 21 after injection. The HE staining reveals no obvious inflammation in the heart and spleen section of mice injected with the microgel. After injection of the microgel in the liquid solution, the microgel becomes gel and retains in the injected area as shown from the images at a higher magnification (Fig. 6-10c & d). Furthermore, presence of the microgel in mice does not elicit obvious local T cell immune rejection or exacerbate cardiac inflammation. As shown in Fig. 6-11, the amount of CD3+, CD8+, or CD68+ cells (green) detected in the heart treated with the microgel is similar to those in the normal heart. The result indicates that the P(NIPAM-IA) microgel does not elicit obvious inflammation, T cell immune-response and macrophage cell infiltrations.

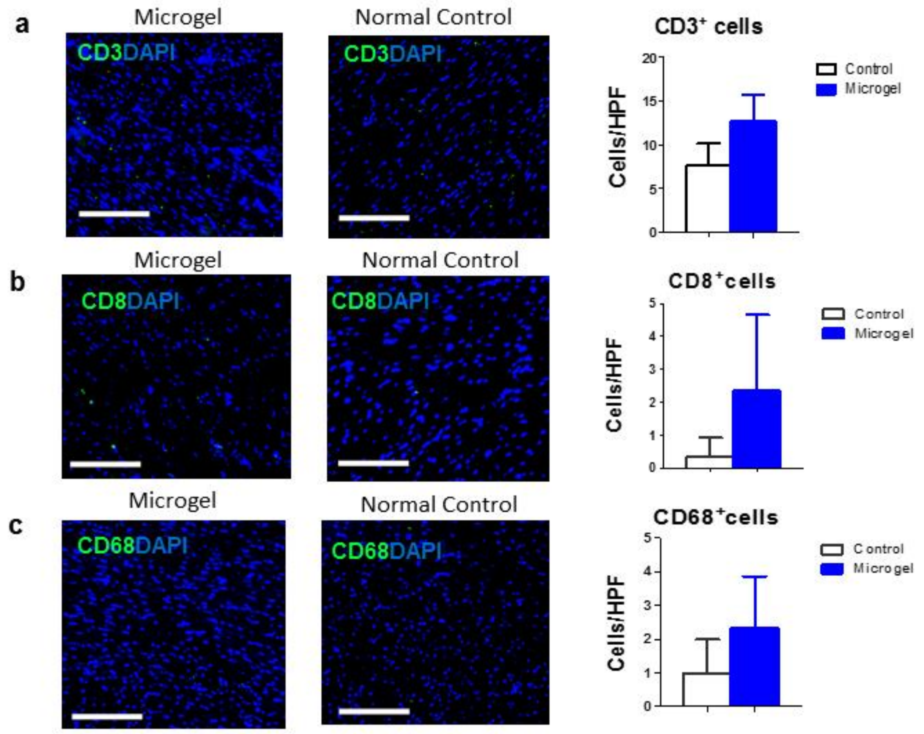

Figure 6-11 Injection of P(NIPAM-IA) microgel does not elicit local T cell immune-response and macrophage cells infiltration in immune-competent mice. (a - b) Representative fluorescent images showing the presence of CD3+ T cells and CD8+ T cells (green) in hearts injected with P(NIPAM-IA) microgel or normal control heart at Day 7. Quantitative analysis indicated that the number of CD3+ T cells and CD8+ T cells were comparable between hearts injected with microgel or normal control (n=3 animals per group). (c) Representative fluorescent images showing the presence of CD68+ macrophage cells (green) in hearts injected with P(NIPAM-IA) microgel or normal control heart at Day 7. Quantitative analysis indicated that the number of CD68+ macrophage cells were comparable between hearts injected with microgel or normal control (n=3 animals per group). Scale bar, 200 μm.

6.4.7 Injectable hydrogel for MI treatment.

We further injected theP(NIPAM-IA) microgel into mice with MI by ligation of the left anterior descending artery (LAD) (Fig. 6-12a). The vWF positive endothelial cells are found to populate into the microgel-treated area after 3 weeks (Fig. 6-12b), and the number of the vWF positive endothelial cells are much more in the microgel-treated area than those in the control heart tissue (Fig. 6-12d). The TUNEL staining reveals the anti-apoptosis effects of the microgel: much less apoptotic nuclei are detected in the microgel treated area than in the controls (Fig. 6-12c & e).

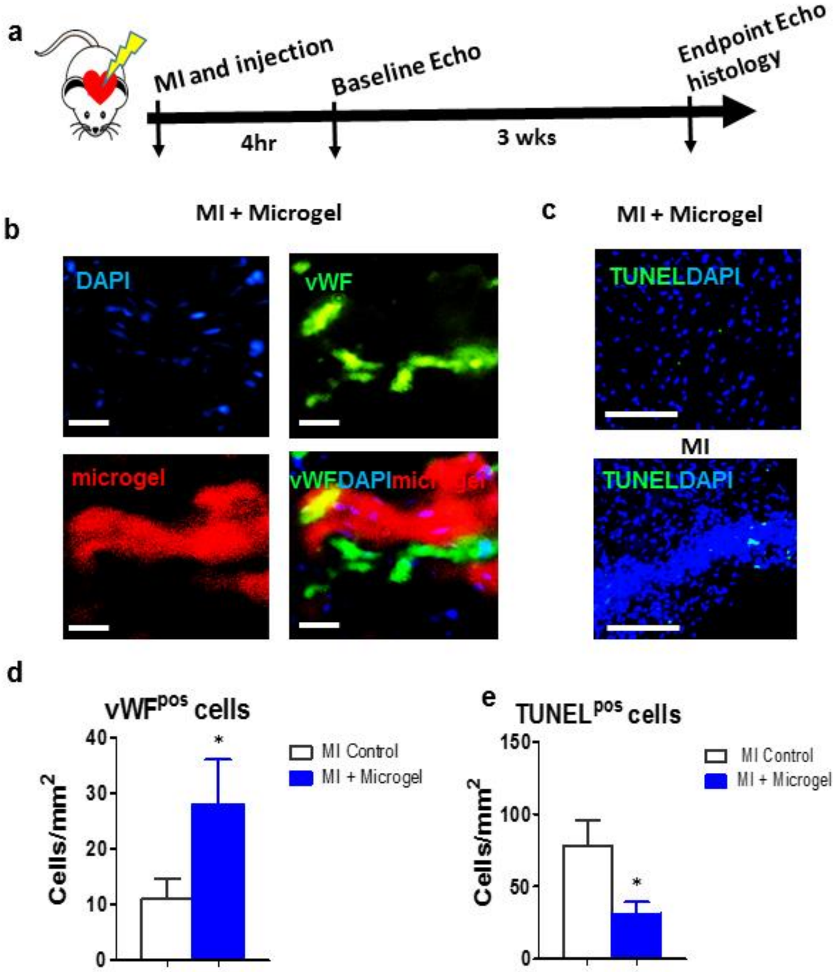

Figure 6-12 Injection of P(NIPAM-IA) microgel reduces myocardial apoptosis but promotes angiogenesis. (a) Schematic showing the overall design of animal experiments to test the therapeutic benefits of microgel in a mouse model of myocardial infarction (MI). (b) Representative images showing vWF-positive endothelial cells (green) in microgel-treated hearts (n=3 hearts per group) after 3 weeks. Scale bar=100 µm. (c) Representative fluorescent micrographs and showing the presence of TUNEL+ apoptotic cells (green) microgel-treated MI heart or PBS control treated MI heart after 3 weeks. Scale bar = 200um. (d) The numbers of vWF-positive endothelial cells were quantified. (n=3 animals per group). (e) The numbers TUNEL+ apoptotic cells were quantified (n=3 hearts per group) * indicates $P < 0.05$.

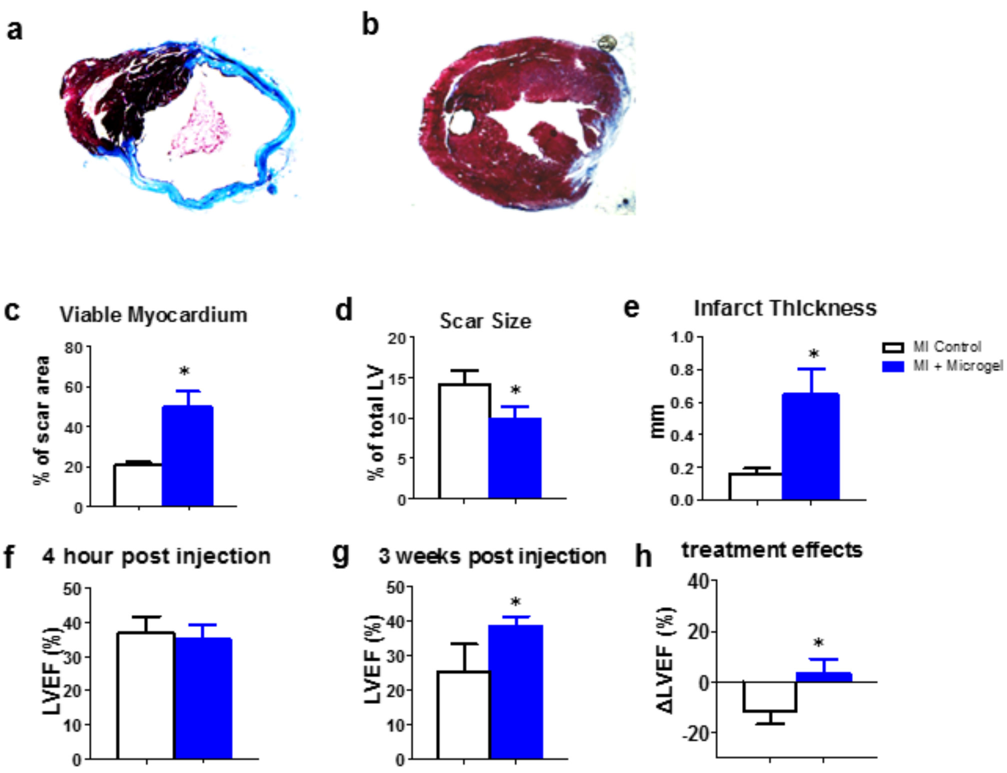

Figure 6-13 Injection of P(NIPAM-IA) microgel could attenuate LV remodeling and preserve cardiac function in myocardial infarction heart. (a, b) Representative Masson's trichrome-stained myocardial sections 3 weeks after PBS control (a) or injection of P(NIPAM-IA) microgel treatment (b) (blue = scar tissue and red = viable myocardium). (c-e) Quantitative analyses of viable myocardium, scar size and infarct thickness from the Masson's trichrome images (n=5 animals per group). (f-g) Left ventricular ejection fractions (LVEFs) measured by echocardiography at baseline (4 hrs post-MI) and 3 weeks afterward. (h) Treatment effects were calculated (n=6 animals per group). * indicated $P<0.05$ when compared to "MI Control" group.

The representative Masson's trichrome-stained myocardial sections 3 weeks after treatment (red = viable myocardium and blue = scar tissue) display severe LV chamber dilation and infarct wall thinning in the non-treated hearts (Fig. 6-13a) in comparison with microgel treated hearts (Fig. 6-13b). Notably, the microgel-treated hearts exhibit attenuated LV remodeling and less abnormal heart morphology is observed with more viable myocardium (Fig. 6-13c), a smaller scar size (Fig. 6-13d) and thicker infarcted walls (Fig. 6-13e). The left ventricular ejection fractions (LVEFs) were measured by echocardiography at the baseline (4 hr post infarct) and 3 weeks afterwards. The LVEFs are indistinguishable at the baseline for all groups (Fig. 6-13f), indicating a similar initial injury degree. Over the 3 week period, the LVEFs in control (white bars, Fig. 6-13g) are decreased while the microgel-treated mice exhibit the enhanced LVEF (blue bar, Fig. 6-13g). The treatment effects was evaluated by changes in LVEFs from the baseline as shown in Figure 6-13h. The controls have a negative treatment effect, while microgel-treated hearts preserve cardiac functions.

6.5 **Conclusion**

We have examined the impact of the microenvironment created from P(NIPAM) based microgels with different degrees of hydrophobic and different surface charge on hCSC growth, growth factor release and NRCMs viability. The results demonstrate hCSCs and NRCMs have higher viability and proliferate better by exposure to a t negative charged and hydrophilic microenvironment from the P(NIPAM-IA) microgel. hCSCs in the P(NIPAM-IA) microgel release regenerative growth factors which are vital for growth and viability of NRCMSs. The initial *in-vivo* results shows that injection of this microgel into mice did not elicit immune system responses and T cells/macrophages infiltrations. The P(NIPAM-IA) microgel attenuate LV remodeling and facilitates heart repair/regeneration in the treatment of MI in the immune competent mice.

6.6 **Reference**

1. White, H.D. and D.P. Chew, Acute myocardial infarction. The Lancet. 372(9638): p. 570-584.

2. Keeley, E.C., J.A. Boura, and C.L. Grines, Primary angioplasty versus intravenous thrombolytic therapy for acute myocardial infarction: a quantitative review of 23 randomised trials. The Lancet, 2003. 361(9351): p. 13-20.

3. Indications for fibrinolytic therapy in suspected acute myocardial infarction: collaborative overview of early mortality and major morbidity results from all randomised trials of more than 1000 patients. Fibrinolytic Therapy Trialists' (FTT) Collaborative Group. Lancet, 1994. 343(8893): p. 311-22.

4. Katz, J.N., et al., Evolution of the coronary care unit: clinical characteristics and temporal trends in healthcare delivery and outcomes. Crit Care Med, 2010. 38(2): p. 375-81.

5. Collaborative meta-analysis of randomised trials of antiplatelet therapy for prevention of death, myocardial infarction, and stroke in high risk patients. BMJ, 2002. 324(7329): p. 71-86.

6. Freemantle, N., et al., β Blockade after myocardial infarction: systematic review and meta regression analysis. Bmj, 1999. 318(7200): p. 1730-1737.

7. Latini, R., et al., Clinical effects of early angiotensin-converting enzyme inhibitor treatment for acute myocardial infarction are similar in the presence and absence of aspirin: systematic overview of individual data from 96,712 randomized patients. Angiotensin-converting Enzyme Inhibitor Myocardial Infarction Collaborative Group. J Am Coll Cardiol, 2000. 35(7): p. 1801-7.

8. Schwartz, G.G., et al., Effects of atorvastatin on early recurrent ischemic events in acute coronary syndromes: The miracl study: a randomized controlled trial. JAMA, 2001. 285(13): p. 1711-1718.

9. Boersma, E., et al., Acute myocardial infarction. The Lancet, 2003. 361(9360): p. 847-858.

10. Nguyen, M.M., N.C. Gianneschi, and K.L. Christman, Developing injectable nanomaterials to repair the heart. Current opinion in biotechnology, 2015. 34: p. 225-231.

11. Christman, K.L., et al., Fibrin glue alone and skeletal myoblasts in a fibrin scaffold preserve cardiac function after myocardial infarction. Tissue engineering, 2004. 10(3-4): p. 403-409.

12. Dai, W., et al., Thickening of the infarcted wall by collagen injection improves left ventricular function in rats: a novel approach to preserve cardiac function after myocardial infarction. Journal of the American College of Cardiology, 2005. 46(4): p. 714-719.

13. Huang, N.F., et al., Injectable biopolymers enhance angiogenesis after myocardial infarction. Tissue engineering, 2005. 11(11-12): p. 1860-1866.

14. Ou, L., et al., Intracardiac injection of matrigel induces stem cell recruitment and improves cardiac functions in a rat myocardial infarction model. Journal of cellular and molecular medicine, 2011. 15(6): p. 1310-1318.

15. Lu, W.-N., et al., Functional improvement of infarcted heart by co-injection of embryonic stem cells with temperature-responsive chitosan hydrogel. Tissue Engineering Part A, 2008. 15(6): p. 1437-1447.

16. Wang, H., et al., Improved myocardial performance in infarcted rat heart by co-injection of basic fibroblast growth factor with temperature-responsive chitosan hydrogel. The Journal of Heart and Lung Transplantation, 2010. 29(8): p. 881-887.

17. Shen, D., et al., The amelioration of cardiac dysfunction after myocardial infarction by the injection of keratin biomaterials derived from human hair. Biomaterials, 2011. 32(35): p. 9290-9299.

18. Ifkovits, J.L., et al., Injectable hydrogel properties influence infarct expansion and extent of postinfarction left ventricular remodeling in an ovine model. Proceedings of the National Academy of Sciences, 2010. 107(25): p. 11507-11512.

19. Yoon, S.J., et al., Regeneration of ischemic heart using hyaluronic acid-based injectable hydrogel. Journal of Biomedical Materials Research Part B: Applied Biomaterials, 2009. 91(1): p. 163-171.

20. McGarvey, J.R., et al., Targeted injection of a biocomposite material alters macrophage and fibroblast phenotype and function following myocardial infarction: relation to left ventricular remodeling. Journal of Pharmacology and Experimental Therapeutics, 2014. 350(3): p. 701-709.

21. Lin, R.Z. and H.Y. Chang, Recent advances in three-dimensional multicellular spheroid culture for biomedical research. Biotechnol J, 2008. 3(9-10): p. 1172-84.

22. Langer, R. and D.A. Tirrell, Designing materials for biology and medicine. Nature, 2004. 428(6982): p. 487-492.

23. Lutolf, M. and J. Hubbell, Synthetic biomaterials as instructive extracellular microenvironments for morphogenesis in tissue engineering. Nature biotechnology, 2005. 23(1): p. 47-55.

24. Griffith, L.G. and M.A. Swartz, Capturing complex 3D tissue physiology in vitro. Nature reviews Molecular cell biology, 2006. 7(3): p. 211-224.

25. Loessner, D., et al., Bioengineered 3D platform to explore cell-ECM interactions and drug resistance of epithelial ovarian cancer cells. Biomaterials, 2010. 31(32): p. 8494-506.

26. Wu, Y., et al., Galactosylated reversible hydrogels as scaffold for HepG2 spheroid generation. Acta biomaterialia, 2014. 10(5): p. 1965-1974.

27. Lei, Y. and D.V. Schaffer, A fully defined and scalable 3D culture system for human pluripotent stem cell expansion and differentiation. Proceedings of the National Academy of Sciences, 2013. 110(52): p. E5039-E5048.

28. Lee, B.H., et al., Modulation of Huh7.5 Spheroid Formation and Functionality Using Modified PEG-Based Hydrogels of Different Stiffness. PLoS ONE, 2015. 10(2): p. e0118123.

29. Chou, M.-J., et al., Application of open porous poly(D,L-lactide-co-glycolide) microspheres and the strategy of hydrophobic seeding in hepatic tissue cultivation. Journal of Biomedical Materials Research Part A, 2013. 101(10): p. 2862-2869.

30. Liu, Z. and G. Vunjak-Novakovic, Modeling tumor microenvironments using custom-designed biomaterial scaffolds. Current Opinion in Chemical Engineering, 2016. 11: p. 94-105.

31. Cui, X., et al., A mechanistic study on tumour spheroid formation in thermosensitive hydrogels: experiments and mathematical modelling. RSC Advances, 2016. 6(77): p. 73282-73291.

32. Shen, Z., et al., Exploring thermal reversible hydrogels for stem cell expansion in three-dimensions. Soft Matter, 2012. 8(27): p. 7250-7257.

33. Fong, E.L.S., et al., Modeling Ewing sarcoma tumors in vitro with 3D scaffolds. Proceedings of the National Academy of Sciences, 2013. 110(16): p. 6500-6505.

34. Fujimoto, K.L., et al., Synthesis, characterization and therapeutic efficacy of a biodegradable, thermoresponsive hydrogel designed for application in chronic infarcted myocardium. Biomaterials, 2009. 30(26): p. 4357-4368.

35. Shen, Z., et al., A thermally responsive cationic nanogel-based platform for three-dimensional cell culture and recovery. RSC Advances, 2014. 4(55): p. 29146-29156.

36. Mellati, A., et al., Poly (N-isopropylacrylamide) hydrogel/chitosan scaffold hybrid for three-dimensional stem cell culture and cartilage tissue engineering. Journal of Biomedical Materials Research Part A, 2016.

37. Mellati, A., et al., Microengineered 3D cell-laden thermoresponsive hydrogels for mimicking cell morphology and orientation in cartilage tissue engineering. Biotechnology and Bioengineering, 2016.

38. Zhang, X.-Z., et al., Preparation and Characterization of Fast Response Macroporous Poly(N-isopropylacrylamide) Hydrogels. Langmuir, 2001. 17(20): p. 6094-6099.

39. Lewis, D. and V. Farmer, Infrared absorption of surface hydroxyl groups and lattice vibrations in lepidocrocite (c-FeOOH) and boehmite (c-AlOOH). Clay Minerals, 1986. 21(1): p. 93-100.

40. Maeda, Y., IR Spectroscopic Study on the Hydration and the Phase Transition of Poly(vinyl methyl ether) in Water. Langmuir, 2001. 17(5): p. 1737-1742.

41. Liu, F. and M.W. Urban, Dual Temperature and pH Responsiveness of Poly(2-(N,N-dimethylamino)ethyl methacrylate-co-n-butyl acrylate) Colloidal Dispersions and Their Films. Macromolecules, 2008. 41(17): p. 6531-6539.

42. Nègre, M., et al., Characterization of model soil colloids by cryo-scanning electron microscopy. Geoderma, 2004. 121(1): p. 1-16.

43. Au, A., et al., Thermally reversible polymer gel for chondrocyte culture. Journal of Biomedical Materials Research Part A, 2003. 67(4): p. 1310-1319.

44. Gan, T., Y. Zhang, and Y. Guan, In Situ Gelation of P(NIPAM-HEMA) Microgel Dispersion and Its Applications as Injectable 3D Cell Scaffold. Biomacromolecules, 2009. 10(6): p. 1410-1415.

45. Bruining, M.J., et al., Biodegradable three-dimensional networks of poly(dimethylamino ethyl methacrylate). Synthesis, characterization and in vitro studies of structural degradation and cytotoxicity. Biomaterials, 2000. 21(6): p. 595-604.

46. Ranella, A., et al., Tuning cell adhesion by controlling the roughness and wettability of 3D micro/nano silicon structures. Acta Biomaterialia, 2010. 6(7): p. 2711-2720.

47. Faucheux, N., et al., Self-assembled monolayers with different terminating groups as model substrates for cell adhesion studies. Biomaterials, 2004. 25(14): p. 2721-2730.

48. Tae, G., et al., Formation of a Novel Heparin-Based Hydrogel in the Presence of Heparin-Binding Biomolecules. Biomacromolecules, 2007. 8(6): p. 1979-1986.

49. Zentilin, L., et al., Bone marrow mononuclear cells are recruited to the sites of VEGF-induced neovascularization but are not incorporated into the newly formed vessels. Blood, 2006. 107(9): p. 3546-3554.

50. Grunewald, M., et al., VEGF-induced adult neovascularization: recruitment, retention, and role of accessory cells. Cell, 2006. 124(1): p. 175-189.

51. Schwarz, E.R., et al., Evaluation of the effects of intramyocardial injection of DNA expressing vascular endothelial growth factor (VEGF) in a myocardial infarction model in the rat—angiogenesis and angioma formation. Journal of the American College of Cardiology, 2000. 35(5): p. 1323-1330.

52. Tang, J., et al., Mesenchymal stem cells over-expressing SDF-1 promote angiogenesis and improve heart function in experimental myocardial infarction in rats. European Journal of Cardio-Thoracic Surgery, 2009. 36(4): p. 644-650.

53. Suleiman, M.S., R.J.R. Singh, and C.E.H. Stewart, Apoptosis and the cardiac action of insulin-like growth factor I. Pharmacology & Therapeutics, 2007. 114(3): p. 278-294.

6.7 Supporting document

Chapter 6: Exploring thermally reversible hydrogels for heart regeneration

Xiaolin Cui[a], Junnan Tang[b], Yusak Hartanto[a], Jingxiu Bi[a], Sheng Dai[a], Ke Cheng[b] and Hu Zhang[a]

a School of Chemical Engineering, The University of Adelaide, Adelaide, SA, Australia, 5005

b Department of Molecular Biomedical Sciences and Comparative Medicine Institute, North Carolina State University, Raleigh, North Carolina, USA, 27607

Corresponding :Dr. Hu Zhang

Hu.zhang@adelaide.edu.au

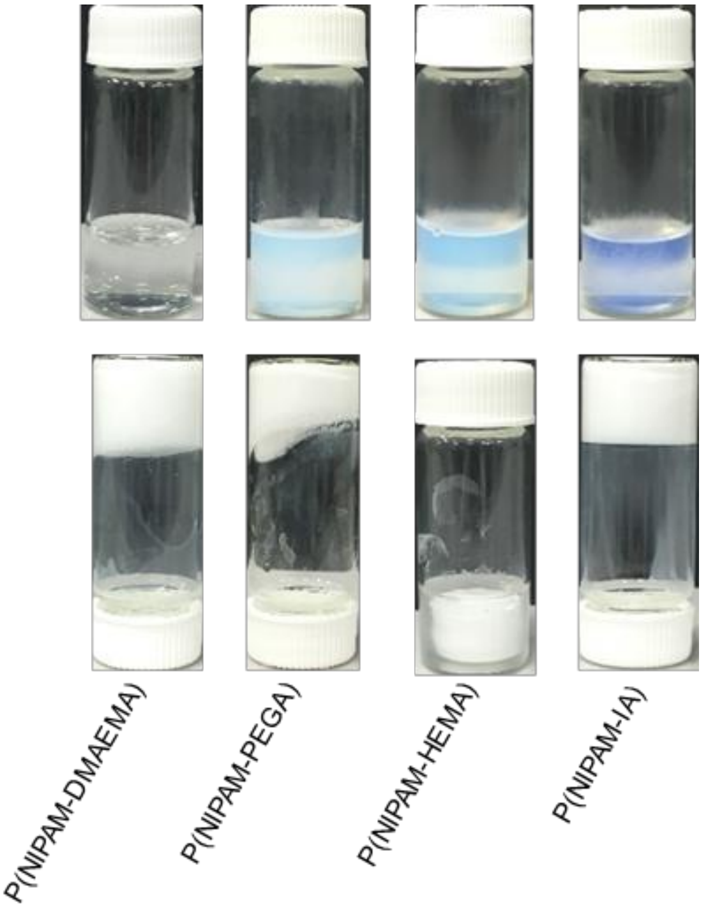

Figure 6-14 Comparison of 30 mg mL^{-1} of P(NIPAM) based microgels (pH, ~7.2) in the dispersed state (25ºC) and the hydrogel state (37ºC)

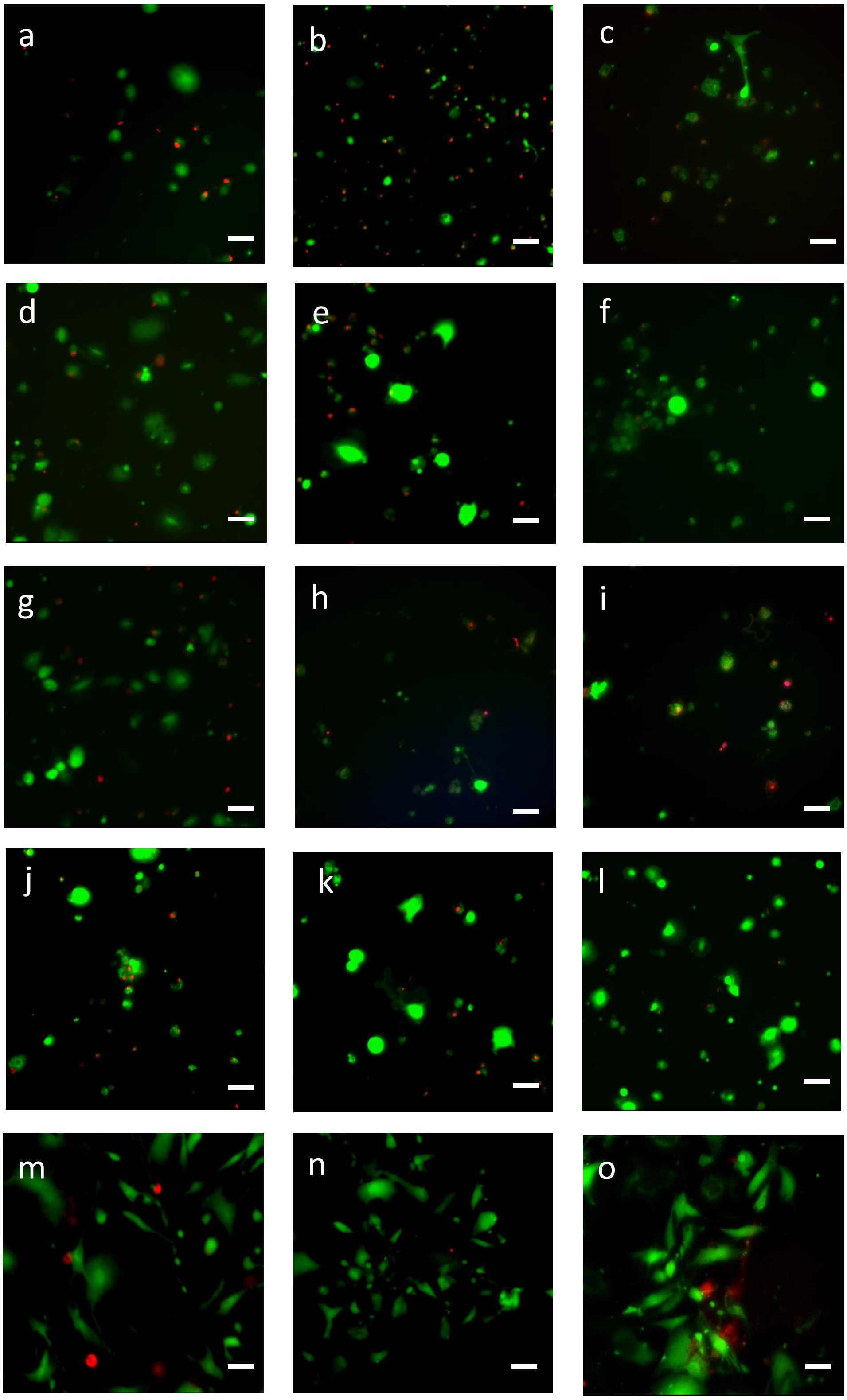

Figure 6-15 hCSCs morphologies and growth in P(NIPAM) based microgels and 2D culture at day 1, day 3 and day 5. (a) to (c) P(NIPAM-DMAEMA); (d) to (f) P(NIPAM-PEGA); (g) to (i) P(NIPAM-HEMA); (j) to (l) P(NIPAM-IA); (m) to (o) 2D culture. Scale bar is 20 µm. Green is Calcein(live cells), Red is EthD (Dead cells).

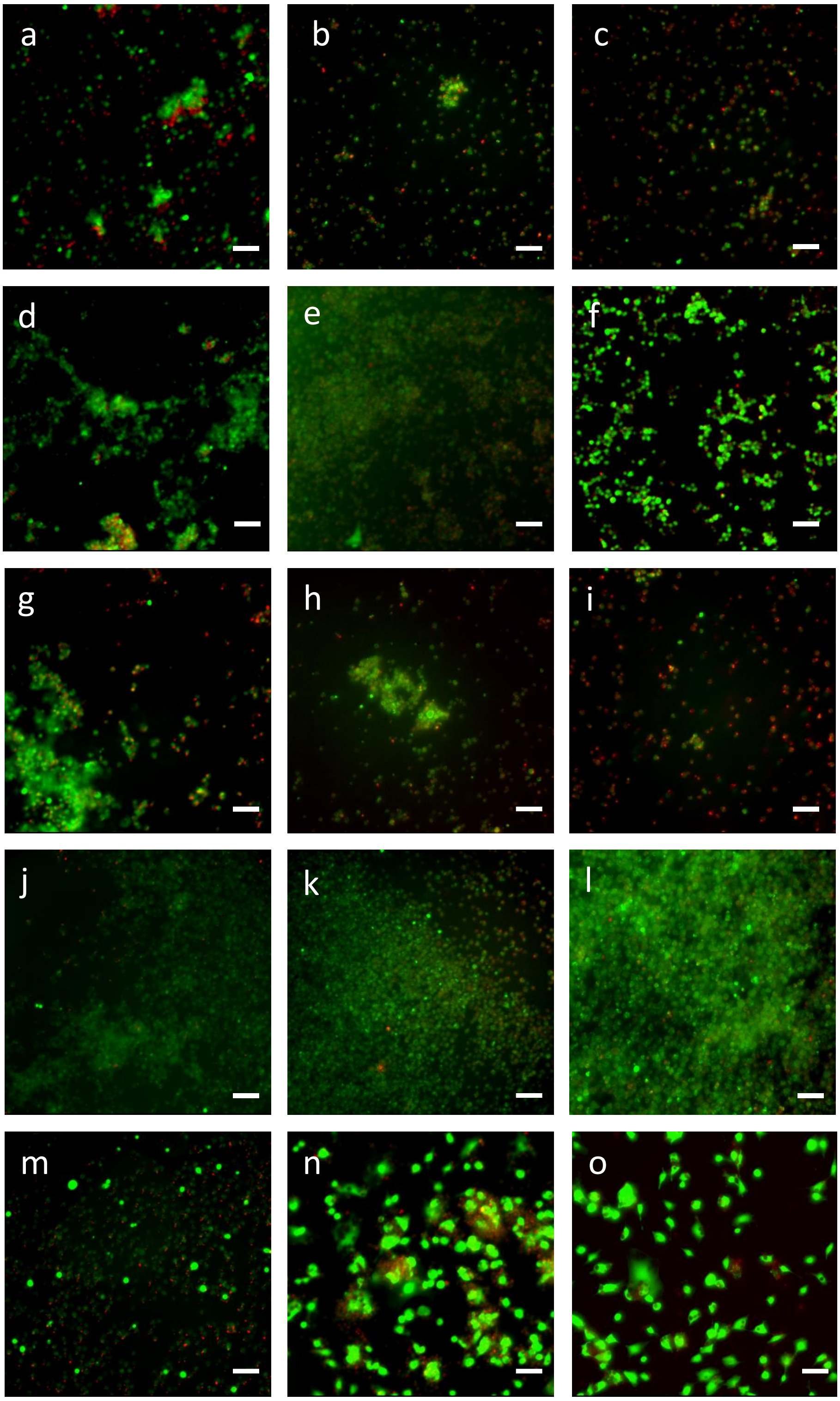

Figure 6-16 NRCMs morphologies and growth in P(NIPAM) based microgels and 2D culture at day 1, day 3 and day 5. (a) to (c) P(NIPAM-DMAEMA); (d) to (f) P(NIPAM-PEGA); (g) to (i) P(NIPAM-HEMA); (j) to (l) P(NIPAM-IA); (m) to (o) 2D culture. Scale bar is 20 µm. Green is Calcein(live cells), Red is EthD (Dead cells).

CHAPTER SEVEN

7. Conclusions and Future directions

Chapter 7: Conclusion and future directions

7.1 Conclusions

The overall objective of this thesis is to apply thermally sensitive microgels to fabricate multicellular spheroids for different bio-applications. The thesis investigates the synthesis of a range of *N*-isopropylacrylamide (NIPAM) based microgels by copolymerizing with different co-monomer materials to examine the impact of microenvironment properties such as surface density and hydrophobicity on formation of different types of multicellular spheroids.

We have explored the mechanics of tumour spheroids formation in the thermally sensitive scaffold. The microgel culture produced more uniform-sized spheroids with a more spherical shape. It may be utilized for scalable production of multicellular spheroids because MCSs were easily released and collected from the microgel. The introduction of the microgel network was able to re-create a stiff environment that is seen *in-vivo*, which is important to restore tumour biological features *in- vivo*. The cellular automata (CA) model combined with experimental results showed the effective initial cell density played a crucial role in determining the MCSs size distribution. The microgel network did not only reduce the effective initial cell density, but also provided the substrate for cellular survival and proliferation.

Basing on the promising results of formation of Hela cell spheroids in the P(NIPAM-AA) microgels in Chapter 3, we developed microgel droplet-based culture of spheroids to obtain uniform-sized spheroids in Chapter 4. The uniform droplet size was achieved by the pre-defined microfluidic channel width. After the droplet was heated to form the gel, the cell-laden gel was cultured in the full medium for formation of MCSs. The MCSs were also released from the droplets by reversing the cell culture temperature to room temperature.

In Chapter 5, we demonstrated the microenvironment with high hydrophilicity and a moderate negative charge density promoted cell proliferation and formation of multicellular clusters. The P(NIPAM-IA) microgel was found to perform the best in cell proliferation and spheroid formation because it provided a benign microenvironment for cell attachment and growth, and its moderate negative charge weakened cell-substrate interactions and facilitated the formation of tumor spheroids. However, high hydrophobicity (such as the P(NIPAM-

HEMA) microgel) decreased the cell proliferation rate, and a highly negative charged microenvironment was also detrimental to cellular growth.

The microenvironment created from the microgels was further examined on the proliferation and biological functions of human cardiac stem cells (hCSCs) for potential applications in tissue engineering and regenerative medicine in Chapter 6. The result demonstrated that hCSCs preferred to a negative charged microenvironment in comparison with a cationic and neutral microenvironment. The hydrophilic microenvironment played an equal role in hCSC growth and biological functions. hCSCs spheroids formation within the anionic microgel with high hydrophilicity, p(NIPAM-IA), significantly improved cell proliferation rate and enhanced release of growth factors. The P(NIPAM-IA) microgel was found to be biocompatible with myocytes *in-vitro* and the immune responses after injection of the P(NIPAM-IA) microgel in the mouse model were negligible. The P(NIPAM-IA) microgel was also found to exhibit attenuated LV remodeling and help MI repair after injection into the MI region in the immune-competent mice.

7.2 **Future directions**

This thesis contributions to cancer cell spheroids formation, including uniform-sized spheroids formation within microgels and microfluidically forming droplets, which is essential for anti-cancer drug screening. Also, the microgels enhance spheroid formation from some cells which are not easy to form spheroids. Another major contribution of this thesis is to form stem cell spheroids for regenerative therapy, especially heart stem cells for MI repair, which offers the potential applications in other cell encapsulation such as beta-cells or T-cells. The copolymerization contributions to polymer synthesis. Different monomers with various charges, functional groups have been incorporated to P(NIPAM) via the emulsion polymerization technique. New polymers synthesized in this thesis study can not only be used for tissue engineering, but also employed in other engineering areas such as water desalination. There are still some limitations: such P(NIPAM) biodegradation and 3D culture for other cell types, especially human primary cancer cells.

Although in this thesis, comprehensive studies on thermal P(NIPAM) based microgels for bioapplications have been conducted, further development derived from this thesis may be made from the following four directions.

1. Large-scale production of tumour spheroids in the microgels for drug screening. The combination of microfluidics with the microgels to culture tumour spheroids offers the great

promise in producing uniform-sized tumour spheroids, however, distribution of even number of cells in each droplet remains a challenge. Modification of current microfluidic configuration may improve the cell distribution.

2. Further studies on the impact of the microenvironment on multicellular spheroids formation may be explored, especially chemical functional groups such as –COOH, $-NH_2$ and –OH on the cell attachment, proliferation, and behaviours.

3. The P(NIPAM) based microgels due to their thermal reversibility may be delivered into patients' injured area as injectable hydrogels for tissue engineering and regeneration medicine. This thesis has demonstrated the safety of using these microgels in the animal model. However more extensive studies on encapsulation of stem cells and protection of stem cells from attack by the immune system are required. The introduction of immunosuppressive drugs within the microgels may achieve local immunosuppression which may generate positive outcomes while the whole body immune system will not be compromised.

4. Biodegradability of the synthetic polymers in the animal models is the most challenging issue. The P(NIPAM) based microgels may be co-polymerized with other biodegradable natural polymers such as chitosan or matrigel for stem cell therapy.

Appendix

Published papers in their Journal style

RSC Advances

PAPER

View Article Online
View Journal | View Issue

Cite this: *RSC Adv.*, 2016, **6**, 73282

A mechanistic study on tumour spheroid formation in thermosensitive hydrogels: experiments and mathematical modelling†

X. Cui,[a] S. Dini,[b] S. Dai,[a] J. Bi,[a] B. J. Binder,[b] J. E. F. Green[b] and H. Zhang*[a]

Received 5th May 2016
Accepted 21st July 2016

DOI: 10.1039/c6ra11699j

www.rsc.org/advances

A tumour is a complex, growing tissue with a dynamic microenvironment. Its shape and size affect mass transport and thus the ability of drugs to penetrate into the tumour. Three-dimensional (3D) tumour spheroid culture has thus been recognised as an advanced tool for anti-cancer drug screening. However, the use of tumour spheroids has been hampered by the large variations in spheroid size, their irregular shape and the labour-intensive culture process. We explore thermosensitive hydrogels, P(NIPAM-AA), for culturing tumour spheroids and compare our approach with a traditional suspension culture method (non-adhesive surface) in terms of cell proliferation, tumour spheroid size distribution and spheroid morphology. Spheroids cultured in the microgel network show a narrower size distribution and a more spherical shape. We hypothesised that these observations could be explained by the fact that cells are homogeneously retained inside the hydrogels, cell aggregate formation is much slower due to network resistance and the cell death rate is smaller in comparison with the suspension culture. We developed a cellular automata (CA) model to validate these hypotheses. Spheroid formation with different parameter values, representing culture in suspension and in microgels, is simulated. Our results are consistent with the hypothesis that the microgel culture produces a more uniform size distribution of spheroids as a result of reduced cell death and the gel network resistance.

Introduction

Cancer is a leading cause of human death: 7.9 million people died of the disease in 2007 and the number is estimated to reach 12 million per year by 2030.[1] This has motivated intense research efforts to develop new drugs over several decades.[2] As part of these efforts, a two dimensional cancer cell culture has been widely used to screen cancer therapeutic drugs. However, these culture methods have limitations when it comes to replicating the cell–cell and cell–extracellular matrix (ECM) interactions which are important regulators of cell behaviour in physiological tissues. Three-dimensional (3D) cell culture methods which mimic, to some extent, the complex spatial structure of tissues observed in *in vivo* models, are increasingly being used to help us understand cancer biology and screen potential treatments. In addition, *in vitro* 3D culture systems can recreate the functional, environmental, and histomorphological features of human tissues.[3]

Numerous 3D culture models currently exist for cancer-related research, such as liquid overlay based culture non-adhesive surfaces,[4–6] suspension culture in mechanically stirred spinner flasks,[7–9] and hanging drops.[10–14] However, these conventional means either have a high labour cost or limited capacity for generating large-scale uniform-sized tumour spheroids. The National Aeronautics and Space Administration developed a rotary cell culture system that can achieve a large scalable production of tumour spheroids. However the microenvironment experienced by cells during spheroid formation is very different to that *in vivo*,[15,16] as without the physical resistance given by ECM, multicellular spheroids grow as individual cell agglomerates and do not interact with their extracellular milieu. Naturally derived hydrogels[17–19] have been employed as scaffolds in tissue engineering to mimic the *in vivo* microenvironments due to their rich networks of ECM proteins and cellular support matrices.[20–22] Cells grown in hydrogels not only interact with each other but also exhibit matrix attachment. The scaffold provides physical and structural support for the formation of tumour spheroids.[23] However, these naturally derived hydrogels lack design flexibility in manipulating individual matrix properties, have poor handling characteristics and display poor reproducibility due to different compositions from batch to batch.[24] Synthetic hydrogels have emerged as a replacement for naturally derived hydrogels for 3D cell culture since they are not only able to mimic the key features of the natural extracellular microenvironment,[25–28] but also can be modified with specific functional groups to modulate cell

---

[a] *School of Chemical Engineering, University of Adelaide, Adelaide, SA 5005, Australia. E-mail: hu.zhang@adelaide.edu.au; Tel: +61-8-83133810*

[b] *School of Mathematical Sciences, University of Adelaide, Adelaide, SA 5005, Australia*

† Electronic supplementary information (ESI) available. See DOI: 10.1039/c6ra11699j

behaviour.[29–33] However, harvesting tumour spheroids from hydrogels for subsequent use in screening potential therapeutic drugs remains a significant challenge.

We have previously developed a range of thermo-reversible hydrogels or microgels, and used them to mimic the extracellular microenvironment for mesenchyme stem cells.[34–36] In this study we employ these thermo-reversible microgels to culture and harvest tumour spheroids. In our method, as shown in Scheme 1, single cells are homogeneously embedded inside the microgel network that have been heated to 37 °C. Cells proliferate in the cell culture medium, and multiple cells interact to form clusters. After the clusters reach the desired size, the spheroids are easily released and collected by cooling the system down to room temperature. In this confined environment, we expect to obtain uniform-sized spheroids with a narrow size-distribution. We characterize the spheroid size, size distribution and shape, and examine the detailed structure of spheroids through fluorescent images and SEM analysis that is missing from the previous study.[37] This approach can be easily adapted for producing large quantities of tumor spheroids for high throughput screening potential drugs.

We put forward possible mechanisms for spheroid formation, which we then investigate using an agent-based or cellular automata (CA) model. CA models have previously been widely used to investigate various biological phenomena,[38,39] including tumour growth.[40–42] However, to our knowledge they have not previously been applied to the study of tumour spheroid formation within hydrogel scaffolds. By changing some of the parameters in our model, we are able to take into account the different environments experienced by cells in hydrogel and suspension cultures, and investigate their effects on spheroid formation. Of particular interest was to determine the factors affecting the uniformity of the spheroid size distribution. Combining the CA model and experimental results, allows us to explore the different mechanisms for tumour spheroid formation in microgel scaffold culture and suspension cultures.

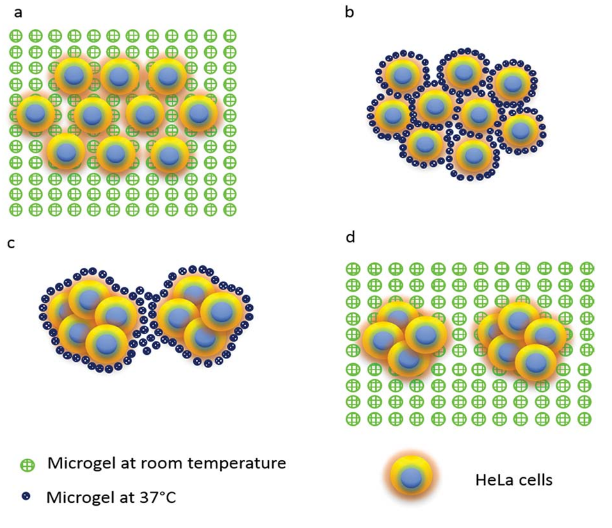

Scheme 1 Thermally sensitive microgels for culturing tumour spheroids: (a) HeLa cells are homogenously mixed with microgels at room temperature; (b) at 37 °C, P(NIPAM-AA) microgels constrain single cells in a three-dimensional network as the microgels are solidified due to the hydrophobic attraction; (c) after incubating HeLa-laden microgels in cell culture medium for a pre-determined period, HeLa multicellular spheroids are generated in P(NIPAM-AA) microgels; (d) by cooling down the temperature to 25 °C, the 3D microgel turns into solution as microgels become hydrophilic again and are re-dispersed into medium, and HeLa spheroids are released from the liquefied solution.

Experimental

Materials

N-Isopropylacrylamide (NIPAM), acrylic acid (AA), *N*,*N*′-methylenebis(acrylamide) (MBA), potassium persulphate (KPS) were purchased from Sigma-Aldrich, sodium dodecyl sulphate (SDS) was purchased from VWR. NIPAM was recrystallized in *n*-hexane and dried in vacuum at room temperature. AA was purified by vacuum distillation. Dulbecco's Modified Eagle's Medium (DMEM), trypsin-EDTA, penicillin–streptomycin (PS) and fetal bovine serum (FBS) were ordered from Gibco. 3-(4,5-Dimethlthiazol-2-yl)-2,5-diphenyltetrazolium bromide (MTT) was purchased from Merck. The LIVE/DEAD® Viability/Cytotoxicity Kit was purchased from Life Technologies.

Microgels synthesis

The P(NIPAM-AA) microgels were synthesized by free radical emulsion polymerization based on the method reported previously[34] and the recipe was shown in Table S1.† 9.9 mmol NIPAM, 0.1 mmol AA, 0.2 mmol MBA and 0.12 mmol of SDS were dissolved in 97 mL of water. After thoroughly mixing, the solution was transferred to a 250 mL three-necked flask fitted with a condenser and a mechanical stirrer. Before the polymerization, the solution was under nitrogen atmosphere for degassing 30 min. After degassing, the flask was placed into a pre-heated oil batch (70 °C). 3.0 mL of KPS aqueous solution (0.1 mmol) was injected into the mixture solution to initiate the polymerization. The polymerization was carried out for 5 h under the protection of nitrogen atmosphere with continuous stirring. After reducing the temperature to the ambient temperature, the microgels were purified by membrane dialysis with a cut-off molecular weight of 12–14 kDa against Milli-Q water for one week with a daily water change. The purified microgels were concentrated at 70 °C with continuous stirring. The success of copolymerization was confirmed by FTIR (Fig. S1) and titration (Fig. S2) in ESI document.†

Tumor spheroid formation from three dimensional cell culture

HeLa cells were cultured in a growth medium (DMEM with 10% FBS and 1% PS) in a T-75 flask. The flask was incubated at 37 °C in a humidified atmosphere with 5% CO_2 until it was confluent. Trypsin was added into the flask to harvest cells. Cells were resuspended in a complete growth medium at a cell concentration of 1.4×10^6 cells per mL.

To prevent HeLa cells attached to the bottom of the 24 well plates, all wells were pre-coated with 400 μL 5% agarose. After coating, HeLa cell dispersion was mixed with 50 mg mL^{-1} microgels (in phosphate buffered saline (PBS), pH $\approx$ 7.2) at a volumetric ratio of 2 : 3. Therefore, the initial concentration of cells was 5.6 × 10^5 cells per mL, and the concentration of microgels was 30 mg mL^{-1}. 0.5 mL of mixture was seeded to each well of a 24-well plate. The cell–microgel mixture was incubated at 37 °C for 2 h until the mixture became soft gel. 1 mL growth medium was added on the top of the soft gel in each well. Cells were incubated at 37 °C in a humidified atmosphere with 5% CO_2 and the growth medium was changed daily. Cells were harvested for further analysis at day 7, 14, and 21. For comparison of cell culture in the absence of microgels, 0.5 mL of the HeLa cell dispersion in the complete growth medium with a concentration of 5.6 × 10^5 cells per mL was seeded to each coated well of a 24-well plate, and then another 1 mL culture medium was added to each well. Other experimental conditions were identical to 3D cell culture in the microgels.

Cell proliferation assay

Cell proliferation was determined by the standard MTT assay. After culturing for a predetermined period, 100 μL MTT solution (5.0 mg mL^{-1}) was added into each well with microgels or without microgels. After further incubating for 4 h, the medium was completely removed. 1 mL DMSO was added to dissolve the formazan crystals. All solutions from each well were transferred to a 96 well plate and the absorbance of the solubilized formazan crystals was recorded using an ELx808 Absorbance Microplate Reader (BioTek Instruments In., USA) at a wavelength of 490 nm.

Spheroid release and collection

After the culture period has elapsed, the scaffold and cells structure are left at room temperature for 1 h. The microgels liquefy when the temperature is below LCST, and the released spheroids can be easily collected through centrifuge.

Spheroid morphology and structure analysis

After the HeLa cells were cultured in the microgels for a fixed time point, the cell-microgel mixture was cooled down to the room temperature. The microgels turned into solution and spheroids were released. The morphology of the HeLa cell spheroids in the microgel solution was observed under an Olympus IX50 inverted microspore (USA). The optical images were analysed by a software package Analysis LSR (USA) to quantify the cell size distribution and sphericity. The spheroids' size was analysed through pictures that were taken from 3 wells (3 pictures per well) for each day and the total number of spheroids analysed was at least 100.

The Live/Dead cell viability/cytotoxicity kit was used to assess live and dead cells in the spheroid structure. The dye solution was prepared according to the protocol from the supplier. 0.3 μL ethidium homodimer-1 (red) and 0.75 μL calcein AM (green) was added 1.5 mL PBS buffer. Before staining, the gel and cells mixture was washed with pre-warmed PBS buffer twice. Then 200 μL dye solution was added to each well. After another 30 minutes incubation at 37 °C, gel and cells mixture was washed with pre-warmed PBS buffer for two more times. A fresh 300 μL PBS buffer was added after rinse process. The stained mixture was observed under confocal microscopy for spheroid morphology examination. The excitation wavelength for calcein AM was selected to be 504–553 nm, and for ethidium homodimer-1 was 569–619 nm. The Leica TCS SP5 confocal microscope was used to record fluorescent images.

The scanning electron microscopy (SEM) was also further employed for spheroid structure analysis. The cellular spheroid was fixed for 30 min in the EM fixative (4% paraformaldehyde/1.25% glutaraldehyde in PBS, and 4% sucrose, pH 7.2). The sample was rinsed in a washing buffer (PBS + 4% sucrose) for 5 min. The spheroid was post-fixed in a 2% OsO_4 aqueous solution for 30 min. After fixing the sample, the sample was dehydrated by rinsing it by 70%, 90% and 100% ethanol thrice and 10 min for each step. The sample was submerged into a mixture of HMDS (hexamethyldisilazane) and 100% ethanol at a volumetric ratio of 1 : 1 for 10 min. The sample was further placed into 100% HMDS for 10 min. HMDS was removed and the sample was dried. The dried sample was coated with platinum and observed under a Philips XL30 Field Emission Scanning Electron Microscope at an accelerating voltage of 10 kV.

Development of CA model

The CA model consists of a lattice, where each site on the lattice can either be empty or occupied by a cell. At the beginning of a simulation, a specified number of cells are placed at random on the lattice. The number and position of the cells are updated at discrete time intervals. During each timestep, cells are selected in random order, and act according to rules for cell behaviour (including cell movement, proliferation and death) that are described in detail below. Our model uses a two-dimensional lattice, as the experimental data derives from two-dimensional images. This has the further advantage of reducing the computational cost compared to a three-dimensional model. The method by which we take into account the three-dimensional nature of the experiments is explained in detail below.

Cell movement. We let the probability that a cell will attempt to move during a time step be P_m. We assume this probability will depend upon the cell's environment. We take a higher value of P_m to represent cells in suspension, and a lower value of P_m for cells in microgels, representing some resistance to movement (such as cell–ECM adhesion, and high viscosity of microgel solution). Cell movement is assumed to involve two component behaviours: unbiased random motion (in which a cell will attempt to move to one of the four neighbouring lattice sites with equal probability) and biased motion (where cells will preferentially move towards other cells). In our model, cells attempt to move according to the biased motion rule with probability P_b (hence the probability of moving according to the unbiased random motion rule is $1 - P_b$). Thus the tendency of cells to aggregation is represented by the probability of biased motion, P_b: for cell types that are strongly inclined to create clusters after seeding, P_b will be close to one, whilst for those that do not tend to aggregate, P_b is close to zero.[43] P_b and P_m are chosen based on the hypothesised characteristics of the cells in the medium before the start of each simulation.

When a cell attempts to move using the biased motion rule, the direction in which it moves is determined as follows. For each of the four directions, we calculate the following probability:

$$P_v(k) = \frac{v(k)}{\sum_{i=1}^{4} v(i)} \quad \text{for } k = 1, 2, 3, 4$$

where $v(k)$ is the number of cells at the right ($k = 1$), left ($k = 2$), up ($k = 3$) and down ($k = 4$) direction of a cell within its range of attraction (l) (see Fig. 1). Note that the $P_v(k)$ sum to unity. We then subdivide the interval [0,1] into four sub-intervals: [0, $P_v(1)$], ($P_v(1)$, $P_v(1) + P_v(2)$], ($P_v(1) + P_v(2)$, $1 - P_v(4)$), ($1 - P_v(4)$, 1], and draw a random number uniformly distributed on [0,1]. If the number chosen lies in the first interval, the cell attempts to move right, if in the second, it attempts to move left, *etc.*

Area exclusion is accounted for in the cell movement rules:[44] two or more cells cannot occupy a site at a time. Therefore, if at any point a cell attempts to move to an already occupied site, the movement is aborted.

Mombach and Glazier[45] suggest that in unbiased motion a cell moves 1/6 of its diameter in 30 minutes. Therefore, in 3 hours each cell moves one site in the lattice when $P_m = 1$.

The probability of biased motion is set to $P_b = 0.9$ with the range of attraction, $l = 3$ for both types of culture. Thus, it is very likely that the cells move towards each other when they are very close to each other (*e.g.* close enough that some parts of the cell may make physical contact). Long range attractions are not considered here as chemotactic signals are assumed to be negligible.

Cell proliferation. The probability of proliferation, P_p, determines the rate of proliferation at each timestep. When proliferation occurs for a cell, the parent cell keeps its position and the daughter cell occupies one of the four adjacent sites. Area exclusion is accounted for in the proliferation rules as well, *i.e.* if a cell already occupies the chosen site for the daughter, the proliferation event is aborted.

We follow the model of Qi *et al.*[40] who take into account the effects of nutrient depletion as cancer cells proliferate by making the probability of proliferation dependent upon the total number of cells. We define the two-dimensional cell density, ρ, as the area fraction occupied by the cells, given by

$$\rho = \frac{N(t)B}{A}$$

where $N(t)$ is the number of cells at time t, B is the cell area (15^2 µm^2) and A is the area of the lattice in µm^2. The area of a well in the experiments is around 20 mm^2. Thus, the length of each side of the well is $a = \sqrt{A} \approx 4.5$ mm. Therefore, a lattice representing the wells has a length of $L = a/0.015 = 300$ sites. As the proliferation rate is assumed to decrease when cell density increases, due to lack of nutrients, we define the probability of proliferation as

$$P_p = k\left(1 - \frac{\rho(t)}{C}\right)$$

where C is carrying capacity and k is growth rate. Qi *et al.*[40] suggest $0.26\ \mathrm{d}^{-1} < k < 0.48\ \mathrm{d}^{-1}$. From the experimental data shown in Fig. 2, cells have approximately the same rate of proliferation in suspension and microgel: we hence use the same probability of proliferation for both types of culture with $k = 0.48\ \mathrm{d}^{-1} = 0.06\ (3\ \mathrm{h})^{-1}$. C is estimated to be 0.6 by processing the images of the experiments to obtain the maximum area fraction that may occur.

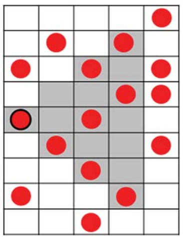

Fig. 1 A sample distribution of cells is depicted. For example, the red cell marked out with the black border senses 7 cells at its right side, $v(k = 1) = 7$, where $l = 3$ is the radius of the attraction range, illustrated by the shaded sites.

Cell death. Cells need to adhere to another cell or a surface to survive and proliferate.[46] As the cells in suspension culture are prevented from adhering to the substrate, we assume that they are likely to die after one day if they do not adhere to other cells.[47,48] In the model, we assume a cell is adhered to another cell if there is a least one cell in the four squares adjacent to it. However, in microgel culture, the cells can survive and proliferate by adhering to the microgel. We thus considered two different death probabilities, P_d, in simulations of suspension and microgel experiments. In suspension simulations, P_d for an isolated cell is low during the first day of culture, increasing rapidly to unity thereafter. For microgel simulations, for the sake of simplicity, P_d is taken to be zero.

Thus, the probability of death for isolated cells in suspension and microgel culture respectively can be defined as follows

$$P_d = \begin{cases} \dfrac{1}{1 + e^{-100(\Delta t - 8)}}, & \text{suspension} \\ 0, & \text{microgel} \end{cases} \tag{1.1}$$

where Δt is the number of timesteps (each timestep represents 3 h) where a cell is not adhered to another cell. This equation gives a rapid increase in the death probability after $\Delta t = 8$ (1 day) for suspension culture, whilst $P_d = 0$ for microgel cultures for $0 \le \Delta t \le 168$ timesteps, see Fig. 2. Note that the functional

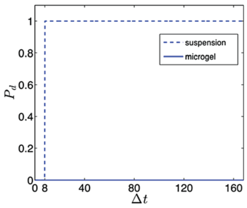

Fig. 2 The probability of death (P_d) applied in the CA model, described in eqn (1.1). Δt is the number of timesteps (each of 3 h) where a cell is not adhered to another cell.

form of P_d in eqn (1.1) is simply chosen to reproduce the assumed qualitative behaviour of the cells in the two different culture environments described above. In the case of suspension culture, other functions that increase rapidly to unity after a period of 1 day would be expected to produce similar results.

The CA model was run with a timestep, T_s, of 3 hours. The initial population was set to $\rho_0 = \rho(0) = 0.05$ in suspension and $\rho_0 = 0.005$ in microgel to have the best fit to the experiments. The reason for this difference is that in suspension most cells settle down and interact in a layer close to the substrate, whereas the cells in microgels lie in multiple layers. Note that ρ_0 represents the effective initial population of cells in our 2D CA model, *i.e.* the cells that interact with each other within a layer, not the total population of cells in a well. This leads to a considerably higher effective ρ_0 for the suspension culture case where the cells are mainly within one layer, compared to the microgel, where they are distributed more evenly throughout the gel.

The length of the lattice side was scaled down to half: 150 sites, similar to the size of the images of the experiments. Moreover, a periodic boundary condition was applied in the simulations. This means that when a cell moves out of the domain at one side, it will re-enter from the opposite side. Applying periodic boundary conditions mitigates the effect of boundaries on the distribution of cells,[43] since there is no physical boundary present at the edge of the experimental images with which we aim to compare our results.

The size of the clusters (cluster diameter) was calculated as follows. Firstly, the areas of the clusters were computed, using the function #bwarea in MATLAB. This function gives an estimate of the area, n, created from adjacent connected pixels, using the algorithm explained in ref. 49. Multiplying the area by 15^2 (area of a cell), gave the area of a cluster in μm^2. The cluster diameter, D, was then calculated as the diameter of a circular cluster of equivalent area – *i.e.*:

$$D = 30\sqrt{\frac{n}{\pi}}$$

Data analysis

All experimental data were expressed with mean ± standard deviation. Student's t test was used to for statistical analysis. Data were considered to be significantly different at $p < 0.05$.

Results and discussion

Cell proliferation

We have previously used synthesized microgels to culture mesenchymal stem cells and promote cell proliferation in the three dimensional network.[34–36] We again employed this novel three-dimensional cell culture platform in this study to form HeLa tumor spheroids and compare them with suspension culture controls. When HeLa cells are cultured in the microgels, the cells display rapid proliferation in the first 7 days, maintain a dynamically balanced cell growth from day 7 to 14, and start to decrease in cell number from day 14 to 21 as shown in Fig. 3. A similar trend of cell proliferation was also observed for the cells in suspension culture. Interestingly, the growth kinetics for HeLa cells in microgels are quite similar to those of tumour *in vivo*.[50]

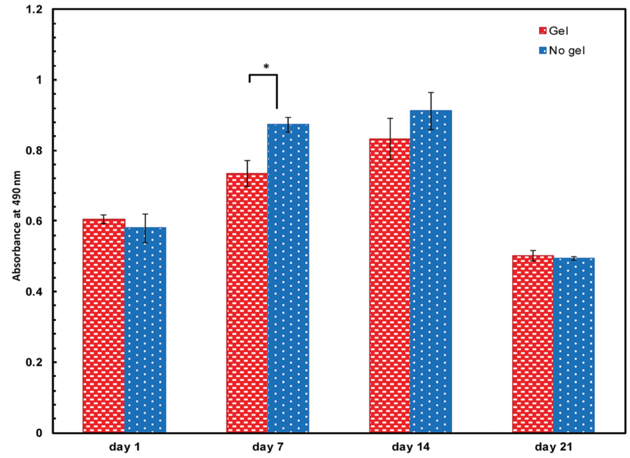

Fig. 3 HeLa cell proliferation inside the microgel network. The experiment was performed in parallel (mean ± SD, $n = 12$). '*' indicates $p < 0.05$.

At day 1 the MTT result shows cells growing within microgels or in suspension have a very similar absorbance rates which indicates good biocompatibility of the P(NIPAM-AA) microgels with HeLa cells. At day 7, cells in suspension proliferate relatively faster than those within the microgels. However, the number of viable cells increases significantly in microgels, which means oxygen and nutrients can diffuse through the microgel pore networks to support cell growth. As cell growth progresses, the number of proliferating cells starts to decrease and the proportion of non-proliferating (quiescent) cells starts to increase.[50] This may be due to the maximum cell density being achieved in each well.[37] However, the lower growth rate in the microgels in the previous 7 days results in more rapid growth from day 7 to day 14 in comparison with suspension culture. At day 21, the viable cell number with and without gels shows a dramatic drop. This may be due to formation of large clusters in which the inner cells are dead because of limited oxygen and nutrients. At this stage, the maximum size of clusters is reached, and there are many more inner dead cells. Cell death may also due to toxic products discharged by the cells.[37]

Spheroid structure analysis

The Live/Dead viability and cytotoxicity kit was further employed to examine the structure of individual tumour spheroids. Live cells are coloured green, whilst dead cells are red. The fluorescent images clearly show the inner structure of the spheroids. Fig. 4a–d illustrates the progression of spheroid development. At day 1, the single cells are dispersed in the microgel network. At day 7, as shown in Fig. 4b, small clusters are able to be seen and the inner cells become dead due to starvation of oxygen, glucose and other nutrients as well as accumulation of toxic metabolites secreted by cells.[50] A solid

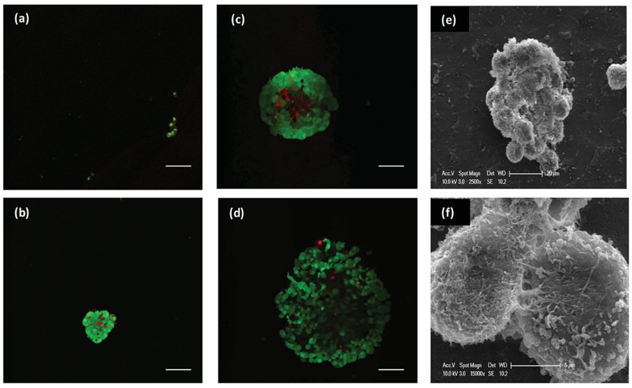

Fig. 4 HeLa cell Live/Dead and SEM images. (a–e) HeLa cells fluorescent images within microgel network at day 1, day 7, day 14, day 21 respectively. Scale bar is 100 μm. (e and f) SEM of a HeLa cell spheroid at day 7 at different scale, 20 μm for (e) and 5 μm for (f).

and compact spheroid structure appears at day 14, and dead cells in the central core are distinguishable from those in the outer layers. At day 21, the compact structure becomes loose and some cells detach from it and start to migrate away. High-resolution SEM images in Fig. 4 clearly reveal the spheroid structure. Cells are tightly bound to each other to form a nearly spherical structure (Fig. 4e). The strong interaction between cells results in the compact spheroid structure (Fig. 4f and S3†). This confirms that the cell adhesion is one of the key driving forces to maintain the structure.

Spheroid size analysis

The physiological state of spheroids is dependent on their size and the cell density within them. Three dimensional cell–cell and cell–matrix interactions are established when the spheroid size reaches 150 μm and gene expression profiles are significantly altered, compared to 2D culture. Chemical gradients, such as oxygen, nutrients and catabolizes, are developed at diameters between 200 μm and 500 μm, and a central secondary necrosis is established for a diameter greater than 500 μm. Thus, spheroid size has a great impact on drug screening. Optical images were used to study the morphology of the spheroids, and the images are presented in Fig. 5. 4× magnification images reveal the evolution of cluster sizes at each time stage. It can be seen that cells remaining inside of microgels tend to form a cluster structure at a slower rate than those in suspension. At day 7, without the control of microgels, cells cultured in the suspension medium have formed a cluster structure (Fig. 5a), while cells grown in the microgels form a much smaller cluster containing two or three cells (Fig. 5b). At day 14, a clear spheroid structure can be observed both within and without microgels. However, the size of the clusters in microgels (Fig. 5c) is considerably less than those in suspension medium (Fig. 5d). A number of single cells are seen in the microgel system. After culturing for 21 days, the number of clusters within microgels increases although some single cells can still be observed (Fig. 5e). In suspension culture, the number of clusters begins to drop but the size of the clusters continues to increase (Fig. 5f).

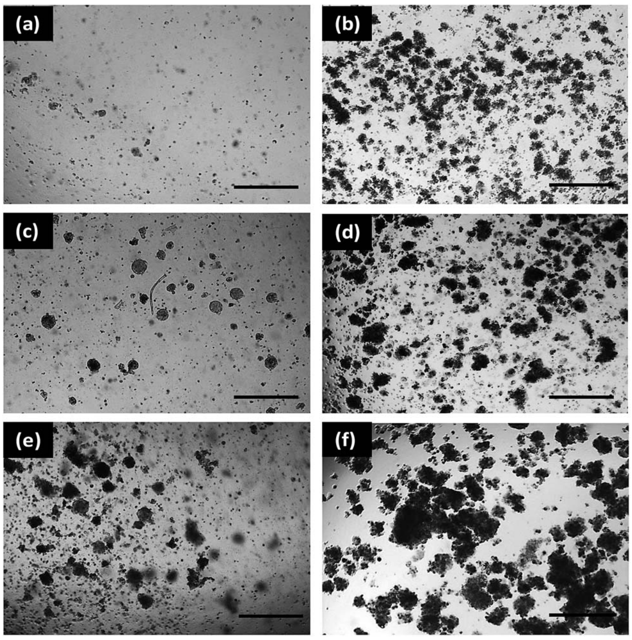

Fig. 5 HeLa cells in microgel (a, c and e) and suspension culture (b, d and f) at different culture days at room temperature. Scale bar is 500 μm. (a), (c) and (e) show HeLa cells within microgel culture after 7 days, 14 days and 21 days respectively. (b), (d) and (f) show HeLa cells in suspension culture after 7 days, 14 days and 21 days respectively.

Clusters may be formed due to interactions between two neighbouring cells or between parent and the daughter cells, depending on their physical locations and the secretory molecules surrounding them.[31] Clusters in the suspension medium may be formed due to interactions between parent and daughter cells as well as neighbouring cells. Further increases in cluster size may be due to cluster–cluster, cluster–cell and cell–cell interactions. However, inside the microgels, the restraint provided by the microgel networks slows down the formation of cell clusters. Neighbouring cells inside the scaffold are separated by the physical barriers formed by the microgel network and they cannot migrate freely to form clusters. Most likely, clusters are formed by parent cells and their adjacent daughters. On the first day, the cell density is low, and cells are scattered inside the microgel network. Gradually cells start to proliferate and two-cell clusters are formed. As the culture time increases, multicellular spheroid structures are generated.

Cluster size distribution

The optical images were further analysed using an imaging software package to obtain the size distribution of the clusters which is shown in Fig. 6. At the first 7 days, cells grown in microgels form clusters with a size range of 20 μm to 70 μm (Fig. 6a). By contrast, cells grown in suspension form larger clusters more rapidly. More than 60% of the clusters are bigger than 70 μm. Most clusters are around 70 μm to 120 μm (Fig. 6b).

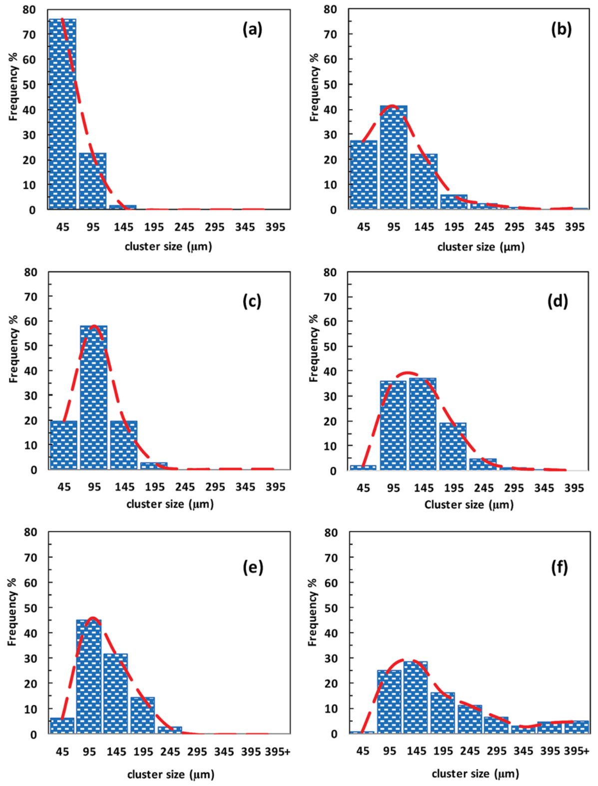

Fig. 6 HeLa cell spheroid size distribution. (a), (c) and (e) show results for HeLa cells within microgel culture after 7 days, 14 days, and 21 days respectively. (b), (d) and (f) show results for HeLa cells in suspension culture after 7 days, 14 days and 21 days respectively.

At day 14, a shift in spheroid size towards larger sizes becomes more evident in both types of culture. The majority of clusters in microgels are around 70 μm to 120 μm with a narrow size distribution, while the cluster size in the suspension medium shows a much wider distribution. Equal numbers of spheroids are found in the range of 70 μm to 120 μm and 120 μm to 170 μm. Bigger-sized clusters can be observed in the suspension medium than in microgels. At day 21, the cluster size increases again. The incremental rate of cluster size growth in the suspension medium is much faster than that in the microgels. In microgel scaffold culture, the majority of the cluster sizes are in the range 70 μm to 120 μm, with a relatively narrower size distribution than that for suspension culture.

The stiff microenvironment formed by the microgels has a significant impact on the size distribution of spheroids. It has been reported that a higher stiffness surrounding cells results in much smaller spheroids.[51] The microgels generated in the study are relatively soft, with an elastic modulus (G') of around 1 Pa, far less than the values reported ranging from 241 to 1201 Pa G' of other hydrogels.[51] It would be expected that a higher stiffness may also lead to a very narrow size distribution. However, spheroids with a size below 150 μm generated in the *in vitro* environment may not be able to represent the tumours in the human body. It is clearly shown that the soft microgels in our study can significantly reduce variability in spheroid size and also produce spheroids with a size range similar to the *in vivo* environment.

Sphericity

The measurement of sphericity was based on the central moment, and the sphericity is defined as the ratio of the perimeter of the circle with the same projected area as the cluster (πd_{eq}) to the perimeter of the cluster (P):[52]

$$s = \pi d_{\mathrm{eq}}/P$$

The calculated sphericities for spheroids with and without microgels are shown in Fig. 7. It can be seen from Fig. 7 that the sphericity in the suspension does not vary with the culture time. Above 70% of clusters have sphericity of 0.4 to 0.6, which means the shape of the clusters is far from spherical. In the microgel culture, at day 7, the sphericity seems similar to that in the suspension medium. However, over 70% of clusters present sphericity of 0.8–1.0, showing that the most of clusters exhibit a spherical shape. As the culture time extends to 21 days, the sphericity shifts from 0.8–1.0 to 0.6–0.8, with the frequency of eccentric shapes increasing after 14 days in culture. The results demonstrate the stiffness of the microenvironment formed by microgels also plays a role in maintaining the spherical shape of spheroids.

CA model

Fig. 8 shows the pattern and distribution of clusters in suspension and microgel simulations. Here, we consider extreme cases where P_{m} is 1 for suspension and 0 for microgels

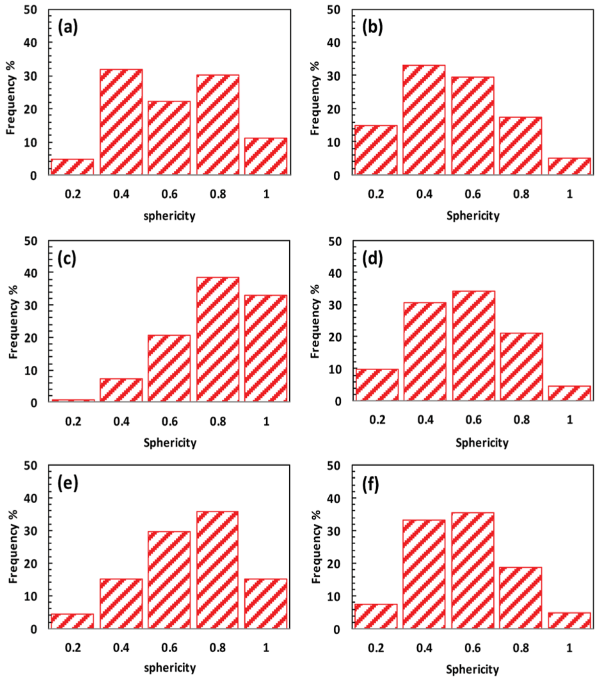

Fig. 7 Sphericity of HeLa clusters in microgel and suspension culture. (a), (c) and (e) show results for HeLa cells within microgel culture after 7 days, 14 days, and 21 days respectively. (b), (d) and (f) show results for HeLa cells in suspension culture after 7 days, 14 days and 21 days respectively.

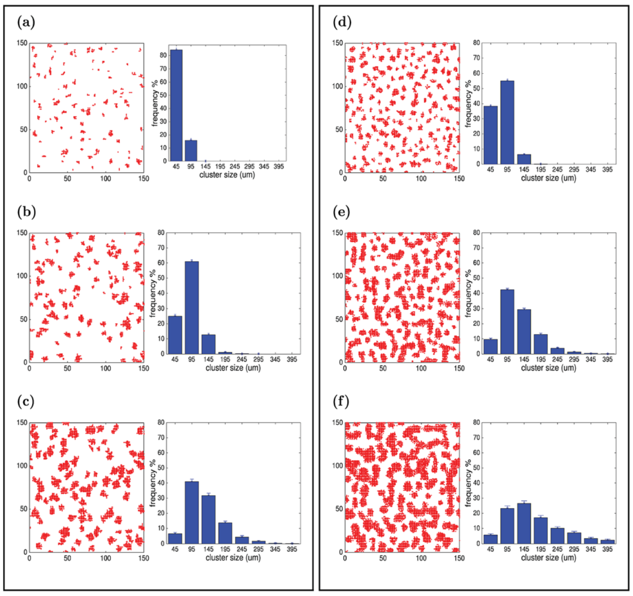

Fig. 8 Visualisations of spheroid formation and the distribution of cluster sizes in microgel (left box) and suspension (right box) simulations. (a and d) day 7, (b and e) day 14 and (c and f) day 21. The average with the 95% confidence intervals of the *t*-distribution are depicted for 50 simulations. In suspension: $P_m = 1$ and $\rho_0 = 0.05$. In microgel: $P_m = 0$ and $\rho_0 = 0.005$. The lattice has side of $L = 150$ sites, the range of attraction is $l = 3$, the probability of biased movement is $P_b = 0.9$, the proliferation constant is $k = 0.06$, the carrying capacity is $C = 0.6$ and the death probability is defined in eqn (1.1). The dead cells are not shown in the images. Time lapses of the evolving distribution of cells for suspension and microgel cultures are shown in the ESI document.†

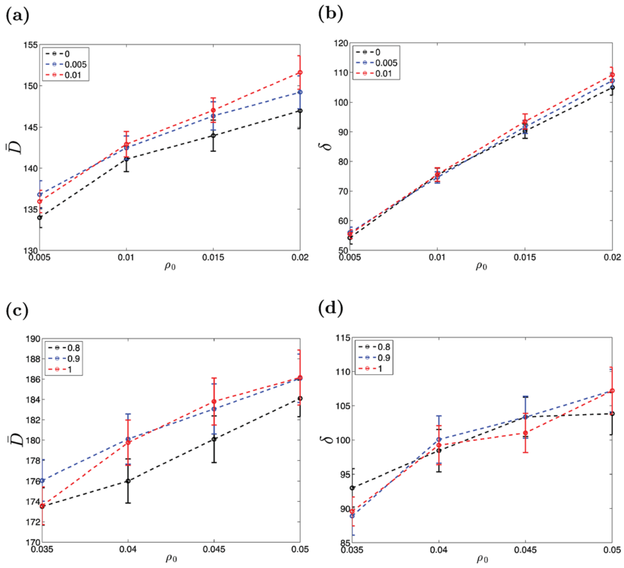

Fig. 9 Parameter sweeping tests. Standard deviation, δ, and average, $\bar{D}$, of cluster size are depicted. (a and b) Microgel: $\rho_0 = \{0.005, 0.01, 0.015, 0.02\}$. $P_m = 0$ black, $P_m = 0.005$ blue and $P_m = 0.01$ red. (c and d) Suspension: $\rho_0 = \{0.035, 0.04, 0.045, 0.05\}$. $P_m = 0.8$ black, $P_m = 0.9$ blue, $P_m = 1$ red. The points in the graphs are averages over 50 simulations and the error bars are 95% confidence intervals of the *t*-distribution. The values of the other parameters are the same as in Fig. 8.

respectively. Thus, the cells are very motile in suspension and the cells in microgels do not move at all. Note that in the histograms clusters with $n < 7$ are not included, since they are too small to be considered as spheroids.

Comparing Fig. 8 with 5 shows that the simulation results are in good agreement with the experimental results. At day 21, the average cluster size is $\bar{D} \approx 186$ μm and the standard deviation of the cluster size is $\delta \approx 107$ μm for simulated suspension cultures, while $\bar{D} \approx 133$ μm and $\delta \approx 54$ μm for simulated microgel cultures. Hence, the distribution of clusters is more uniform in the microgel with a lower standard deviation and the average cluster size is smaller as well.

The main differences between the simulated suspension and microgel experiments are in the motion of cells and the initial cell density. We aim to understand how each of them affects the distribution of cluster size, and so, parameter-sweeping tests were carried out in which one of the parameters is varied while the others are kept constant. We swept the parameters in a physically plausible region, *i.e.* where their values are within a range that is consistent with the physical properties of the medium. Small variations about the previous values of P_m and ρ_0 (see the caption of Fig. 9) are analysed.

We have also examined general cases where the parameter ranges are not necessarily in the plausible region, see ESI Fig. S4 and S5.† This allows us to analyse other different media that might be used for spheroid formation in future work.

The parameter sweeping was done for 150 × 150 lattice with $\rho_0 = \{0.005, 0.01, 0.015, 0.02\}$ and $P_m = \{0, 0.005, 0.01\}$ in the microgel and $\rho_0 = \{0.035, 0.04, 0.045, 0.05\}$ and $P_m = \{0.8, 0.9, 1\}$ in suspension. Fig. 9 shows that $\bar{D}$ and δ increase with ρ_0. Thus our model suggests that using a higher initial cell density, ρ_0, leads to formation of bigger clusters, which is desirable, but this has the unwanted effect of reducing the uniformity of cluster size. Hence the choice of ρ_0 would involve a trade-off between cluster size and size-variability.

As illustrated in Fig. 9b and d, our model predicts that the rate of increase of δ with ρ_0 for microgel culture is greater than for suspension culture. Thus, increasing the initial population would have a more deleterious effect on the uniformity of the clusters in microgels compared to suspension culture.

Sweeping the values of P_m in a wider range, we determined that motility of cells can strongly affect $\bar{D}$ and δ. Fig. S4† in ESI shows that increasing P_m leads to the formation of bigger clusters. The reason is that, when P_m is high enough, randomly moving cells can find bigger clusters nearby and attach to them. In addition, the highly motile cells in small clusters are more likely to find bigger clusters and attach to them. Therefore, increasing P_m can reduce the number of small clusters and increase the number of larger ones. Further details can be found in the ESI.†

Conclusion

In summary, we conducted a series of experiments to demonstrate the advantages of using microgel scaffolds to culture tumour spheroids instead of conventional suspension culture methods. Microgel culture produces more uniformly-sized spheroids, with a more spherical shape. Also it could be used for scalable production of multicellular spheroids. The introduction of the microgel network can be helpful to mimic the stiff environment of tumour growth *in vivo*. Spheroids produced by our technique can be easily released and collected. Further study on the details of cells' behaviour in microgels can be conducted, and the mechanism of spheroid formation will help understanding of the spheroid formation progress in real tissue. This material, with some modifications, could be used to re-create a controlled microenvironment for other scaffold applications such as regenerative medicine, tissue engineering and so forth.

We developed a CA model to explore the reasons for the different size distributions observed in spheroids grown in microgels and suspension culture. In the model, the cells behave according to rules for movement, proliferation and death. We tried to keep the model as simple as possible in order to focus on the effect of the major parameters on spheroid formation. The CA model was developed in two-dimensions, since this facilitates comparison with the two-dimensional experimental images, and also reduces the computation time required.

Our CA model was successfully able to reproduce the experimental results for spheroid formation rate and size distribution, for both microgel and suspension cultures. Our results are thus consistent with the main differences between cells in the two different cultures being in their proliferation and death rates, and their initial effective density. Hence, the more uniform size distribution of spheroids produced by microgel culture could be due to its ability to separate the cells into multiple layers, reducing the effective initial density. However, even when the number of cells is low, the microgel provides a substrate for cells to survive and proliferate, so spheroids can still be produced. By contrast it is not possible to reduce the initial population of cells significantly in suspension cultures, since the cells would die out and spheroid formation would not occur.

The model predicts that the initial cell density plays a crucial role in determining the features of the formed spheroids. For the parameter ranges we considered, higher initial densities led to larger spheroids, but at the cost of introducing greater variability in spheroid size. This effect was predicted to be more pronounced for microgel cultures than suspension cultures. Further experiments will be required to test these predictions.

Acknowledgements

X. C. acknowledges financial support from a University of Adelaide scholarship. H. Z. would like to acknowledge the financial support from ARC Discovery Project (DP160104632) and The Medical Advancement Without Animal (MAWA) Trust. The work of S. D. and J. E. F. G. was supported by an ARC Discovery Early Career Researcher Award (DE130100031) to J. E. F. G. S. D. also acknowledges a University of Adelaide Full Fees Scholarship. B. J. B. was supported by an ARC Discovery Project Grant (DP160102644). H. Z. and J. E. F. G. thank the Faculty of Engineering, Computer & Mathematical Sciences of the University of Adelaide for multidisciplinary research collaboration funding.

References

1 A. Nyga, U. Cheema and M. Loizidou, *Journal of Cell Communication and Signaling*, 2011, **5**, 239–248.
2 C. Wang, Z. Tang, Y. Zhao, R. Yao, L. Li and W. Sun, *Biofabrication*, 2014, **6**, 022001.
3 F. Hirschhaeuser, H. Menne, C. Dittfeld, J. West, W. Mueller-Klieser and L. A. Kunz-Schughart, *J. Biotechnol.*, 2010, **148**, 3–15.
4 J. Landry, D. Bernier, C. Ouellet, R. a. Goyette and N. Marceau, *J. Cell Biol.*, 1985, **101**, 914–923.
5 J. M. Yuhas, A. P. Li, A. O. Martinez and A. J. Ladman, *Cancer Res.*, 1977, **37**, 3639–3643.
6 G. A. Hamilton, C. Westmoreland and E. George, *In Vitro Cell. Dev. Biol.: Anim.*, 2001, **37**, 656–667.
7 S. L. Nyberg, J. Hardin, B. Amiot, U. A. Argikar, R. P. Remmel and P. Rinaldo, *Liver Transplant.*, 2005, **11**, 901–910.
8 A. Lazar, H. J. Mann, R. P. Remmel, R. A. Shatford, F. B. Cerra and W.-S. Hu, *In Vitro Cell. Dev. Biol.: Anim.*, 1995, **31**, 340–346.
9 H. Song, O. David, S. Clejan, C. L. Giordano, H. Pappas-Lebeau, L. Xu and K. C. O'connor, *Tissue Eng.*, 2004, **10**, 1266–1276.
10 R.-Z. Lin, L.-F. Chou, C.-C. M. Chien and H.-Y. Chang, *Cell Tissue Res.*, 2006, **324**, 411–422.
11 J. M. Kelm, N. E. Timmins, C. J. Brown, M. Fussenegger and L. K. Nielsen, *Biotechnol. Bioeng.*, 2003, **83**, 173–180.
12 J. M. Kelm and M. Fussenegger, *Trends Biotechnol.*, 2004, **22**, 195–202.
13 M. Wartenberg, F. Dönmez, F. C. Ling, H. Acker, J. Hescheler and H. Sauer, *FASEB J.*, 2001, **15**, 995–1005.
14 J. M. Kelm, V. Djonov, L. M. Ittner, D. Fluri, W. Born, S. P. Hoerstrup and M. Fussenegger, *Tissue Eng.*, 2006, **12**, 2151–2160.
15 M. Ingram, G. Techy, R. Saroufeem, O. Yazan, K. Narayan, T. Goodwin and G. Spaulding, *In Vitro Cell. Dev. Biol.: Anim.*, 1997, **33**, 459–466.
16 V. I. Khaoustov, G. J. Darlington, H. E. Soriano, B. Krishnan, D. Risin, N. R. Pellis and B. Yoffe, *In Vitro Cell. Dev. Biol.: Anim.*, 1999, **35**, 501–509.
17 H. K. Kleinman and G. R. Martin, *Semin. Cancer Biol.*, 2005, **15**, 378–386.
18 R. H. Kramer, K. G. Bensch and J. Wong, *Cancer Res.*, 1986, **46**, 1980–1989.
19 R. Castelló-Cros, D. R. Khan, J. Simons, M. Valianou and E. Cukierman, *BMC Cancer*, 2009, **9**, 94.
20 D. L. Holliday, K. T. Brouilette, A. Markert, L. A. Gordon and J. L. Jones, *Breast Cancer Res.*, 2009, **11**, R3.
21 L. A. Gurski, A. K. Jha, C. Zhang, X. Jia and M. C. Farach-Carson, *Biomaterials*, 2009, **30**, 6076–6085.
22 S. Talukdar, M. Mandal, D. W. Hutmacher, P. J. Russell, C. Soekmadji and S. C. Kundu, *Biomaterials*, 2011, **32**, 2149–2159.

23 M. J. Paszek, N. Zahir, K. R. Johnson, J. N. Lakins, G. I. Rozenberg, A. Gefen, C. A. Reinhart-King, S. S. Margulies, M. Dembo and D. Boettiger, *Cancer cell*, 2005, **8**, 241–254.

24 B. Weigelt and M. J. Bissell, *Semin. Cancer Biol.*, 2008, **18**, 311–321.

25 R. Langer and D. A. Tirrell, *Nature*, 2004, **428**, 487–492.

26 M. Lutolf and J. Hubbell, *Nat. Biotechnol.*, 2005, **23**, 47–55.

27 L. G. Griffith and M. A. Swartz, *Nat. Rev. Mol. Cell Biol.*, 2006, **7**, 211–224.

28 M. P. Lutolf, *Integr. Biol.*, 2009, **1**, 235–241.

29 D. Loessner, K. S. Stok, M. P. Lutolf, D. W. Hutmacher, J. A. Clements and S. C. Rizzi, *Biomaterials*, 2010, **31**, 8494–8506.

30 Y. Lei and D. V. Schaffer, *Proc. Natl. Acad. Sci. U. S. A.*, 2013, **110**, E5039–E5048.

31 Y. Wu, Z. Zhao, Y. Guan and Y. Zhang, *Acta Biomater.*, 2014, **10**, 1965–1974.

32 M. Ehrbar, S. C. Rizzi, R. Hlushchuk, V. Djonov, A. H. Zisch, J. A. Hubbell, F. E. Weber and M. P. Lutolf, *Biomaterials*, 2007, **28**, 3856–3866.

33 M. Ehrbar, S. C. Rizzi, R. G. Schoenmakers, B. San Miguel, J. A. Hubbell, F. E. Weber and M. P. Lutolf, *Biomacromolecules*, 2007, **8**, 3000–3007.

34 Z. Shen, J. Bi, B. Shi, D. Nguyen, C. J. Xian, H. Zhang and S. Dai, *Soft Matter*, 2012, **8**, 7250–7257.

35 Z. Shen, A. Mellati, J. Bi, H. Zhang and S. Dai, *RSC Adv.*, 2014, **4**, 29146–29156.

36 A. Mellati, S. Dai, J. Bi, B. Jin and H. Zhang, *RSC Adv.*, 2014, **4**, 63951–63961.

37 D. Wang, D. Cheng, Y. Guan and Y. Zhang, *Biomacromolecules*, 2011, **12**, 578–584.

38 G. B. Ermentrout and L. Edelstein-Keshet, *J. Theor. Biol.*, 1993, **160**, 97–133.

39 T. Toffoli and N. Margolus, *Cellular automata machines: a new environment for modeling*, MIT press, 1987.

40 A.-S. Qi, X. Zheng, C.-Y. Du and B.-S. An, *J. Theor. Biol.*, 1993, **161**, 1–12.

41 A. A. Patel, E. T. Gawlinski, S. K. Lemieux and R. A. Gatenby, *J. Theor. Biol.*, 2001, **213**, 315–331.

42 Y. Jiao and S. Torquato, *PLoS Comput. Biol.*, 2011, **7**, e1002314.

43 D. Agnew, J. Green, T. Brown, M. Simpson and B. Binder, *J. Theor. Biol.*, 2014, **352**, 16–23.

44 B. J. Binder and K. A. Landman, *J. Theor. Biol.*, 2009, **259**, 541–551.

45 J. C. Mombach and J. A. Glazier, *Phys. Rev. Lett.*, 1996, **76**, 3032.

46 B. Alberts, A. Johnson, J. Lewis, M. Raff, K. Roberts and P. Walter, *Molecular Biology of the Cell*, 4th edn, 2002.

47 A. Gilmore, *Cell Death Differ.*, 2005, **12**, 1473–1477.

48 Q. Wei, V. Hariharan and H. Huang, *PLoS One*, 2011, **6**, e27064.

49 W. K. Pratt, *Digital Image Processing: PIKS Inside*, 3rd edn, 1991, pp. 551–587.

50 R. M. Sutherland, *Science*, 1988, **240**, 177–184.

51 D. Loessner, J. A. Flegg, H. M. Byrne, J. Clements and D. Hutmacher, *Integr. Biol.*, 2013, **5**, 597–605.

52 A. Asundi, *Digital holography for MEMS and microsystem metrology*, John Wiley & Sons, 2011.

Colloid and Interface Science Communications 14 (2016) 4–7

Contents lists available at ScienceDirect

Colloid and Interface Science Communications

journal homepage: www.elsevier.com/locate/colcom

Rapid Communication

Multicellular Spheroids Formation and Recovery in Microfluidics-generated Thermoresponsive Microgel Droplets

X. Cui [a], Y. Liu [b], Y. Hartanto [a], J. Bi [a], S. Dai [a], H. Zhang [a],*

[a] School of Chemical Engineering, The University of Adelaide, Adelaide, SA 5005, Australia
[b] School of Biochemical Engineering, East China University of Science and Technology, Shanghai, China

ARTICLE INFO

Article history:
Received 10 August 2016
Received in revised form 24 August 2016
Accepted 11 September 2016
Available online xxxx

Keywords:
Biomaterials
Thermal response microgels
Droplet
Microfluidics
Multicellular spheroids

ABSTRACT

Multicellular spheroids (MCSs) have a unique structure to represent the in vivo tissues and they have many potential applications, such as in drug screening and evaluation. Traditional methods of fabricating MCSs are incapable of controlling the MCS size and size distribution. For MCS formation in the ion- or photo-crosslinked hydrogel, recovery of MCSs from these hydrogels may need strong chemicals or enzymes to break the crosslinked network for release of MCSs. We are the first to develop a microfluidic approach to encapsulate Hela cells in thermoresponsive microgel-based droplets to generate Hela MCSs. The microgel network provided a physical scaffold for cells so that cell aggregates formed in a biomimicking condition. Due to the thermal reversibility of microgels, MCSs were released and harvested from the microgels droplets by simply cooling the droplets down to room temperature. This approach may open a new door for generating uniform-sized MCSs.

Most cells in the human body are living in a three-dimensional (3D) environment through interacting with neighboring cells and extracellular matrices (ECM) which are missing in traditional two dimensional monolayer culture [1]. Cell-cell and cell-ECM interactions have a great impact on many biological activities such as homeostasis and cell signaling through functional junctions between cells [2]. The 3D cell culture model based on multicellular spheroids (MCSs) is a powerful tool to recapitulate the cell-cell and cell-matrix interactions that have been found in vivo to preserve cellular viability, functionality and phenotype [3], and the MCSs serve a building bridge to connect the two-dimensional cell culture and animal-based studies [4]. Hence, a myriad of methods have been developed for fabrication of MCSs. Conventional methods such as the hanging drop [5], the gyratory method [6], non-adhesive culture [7], micro-fabricated confined culture [8], accelerated aggregate-forming method [9] as well as liquid overlay culture [10] have been explored. Among them, the micro-fabrication technology has been recently pursued due to manipulatable sizes and shapes of MCSs in the confined environment. Microarrays [11], microwells [12] and microfluidic devices [13] are designed to seed a high cell density in a small cavity so that cells aggregate in the cavity to form MCSs. However, in this method, cells tend to settle in the bottom of the cavity due to gravity and the formed MCSs are unable to easily recover from the microfabrication devices.

Cell encapsulation in microfluidic channels is achieved by mixing the cell-laden hydrogels in one channel with crosslinking agents from another channel(s). This approach allows rapid formation, high-throughput [14] and miniaturized bioreactors for cell culture [15]. To date, hydrogels like alginate, agarose, gelatin and poly (ethylene glycol) [16–19], as well as double emulsion [20] have been attempted to encapsulate cells in these hydrogels. Very few attempts are reported to culture cells in the crosslinked gel for a long term. Since the polymers are chemical crosslinked, potent chemicals may be required to break the shell to release MCSs [21]. For the double emulsion encapsulation since the middle layer between cells and the culture medium is an oil phase, the oxygen and nutrient diffusion rate is low, and this becomes the constraints for MCS growth. We are the first group to propose a droplet-based microfluidics system to form and release spheroids using thermal-responsive synthetic polymers. Different from natural polymers, this unique thermoresponsive material can release MCSs easily after long-term culture without introduction of toxic chemicals. In addition, through copolymerizing different co-monomers, the properties of the synthesized polymers can be tuned for different types of cells.

As described in Fig. 1, HeLa cells were encapsulated inside the Poly (N-Isopropylacrylamide-co-acrylic acid) (P(NIAM-AA)) microgel based droplets. P(NIPAM-AA) has a unique amphiphilic structure so the microgel network is thermally reversible, which was confirmed from the temperature dependence of its hydrodynamic size (Fig. S1) and elastic/viscous modulus (Fig. S2). The SEM image (Fig. S3) shows a porous structure which not only provides the physical support for

---

* Corresponding author.
E-mail address: hu.zhang@adelaide.edu.au (H. Zhang).

http://dx.doi.org/10.1016/j.colcom.2016.09.001
2215-0382/

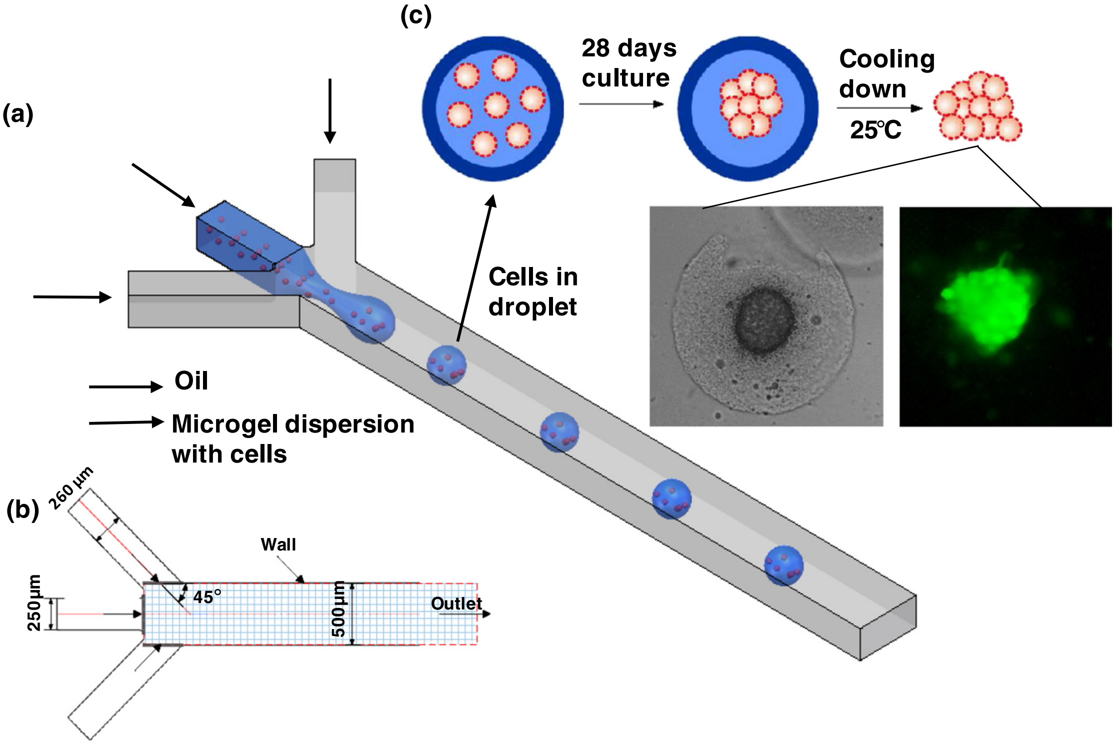

Fig. 1. Droplet generation and cell encapsulation through microfluidics (a) Droplet generation process inside a micro-channel (b) Dimension and geometry of the micro-channel (c) Multicellular spheroids formation inside the droplet.

embedding cells in a 3D microenvironment but also allows sufficient oxygen and nutrient transportation.

The cell-laden P(NIPAM-AA) microgel aqueous solution was squeezed into individual droplets by the oil phase from two side channels. The polydimethylsiloxane (PDMS) microfluidic microchannel was fabricated using the soft-lithography technique. The PDMS microchannel was designed as a flow-focusing device, which was composed of one water channel in the middle and two oil channels at both sides to produce the immiscible interfaces when the two flows were focused at the intersection. Two streams of continuous oil phase flowed through two sides and squeezed the forefront stream of the dispersed fluid into droplets. The Lattice Boltzmann model was applied to two immiscible phases for simulation of the droplet formation within the microchannel, and the optimized flow rate to generate discrete droplets for both phases was used for the following experiments (Fig. S4). Compared to experimental data, the LBM simulation can accurately predict the flow phenomenon within microchannel. When the flowrate ratio is at 1:1 between the dispersed phase and the continuous phase, jetting flow was observed without droplet generation. At a flowrate ratio of 1:4, the majority (more than 40%) of the droplets have the size around 260 μm. More than 80% of the droplets are in the range between 250 and 350 μm. When increasing the continuous phase flow rate, at flowrate ratio of 1:6, the droplet size is around 100 μm. In order to obtain reasonable size of droplets to culture MCSs, the flowrate ratio at 1:4 was chosen for future experiments.

After droplets were generated inside the microchannel and collected at the exit, the droplets were heated up to 37 °C, and their colour changed from transparent (Fig. 2a) into white which is shown at Fig. 2b. When the temperature of the microgels within the droplets was above the volume phase transition temperature of the microgels (VPTT, around 32 °C from our previous report [22]), the microgels became hydrophobic from hydrophilic due to the presence of N-isopropylacrylamide. In additional, due to hydrophobic attractions and electrostatic repulsions, physical gel was formed [22]. The physical gel presented a white cloudy colour, which is shown darkness under an optical microscope. The size of the droplet slightly decreased during the heating up process since the microgels shrank due to loss of surrounding water molecules. After washing the microgels with pre-warmed PBS buffer (37 °C) to remove the oil residue, the droplets were transferred into a pre-warmed culture medium. The physical gel was able to maintain its spherical shape as shown in Fig.2c, since at 37 °C, the hydrophobic nature of the microgel prevented water from

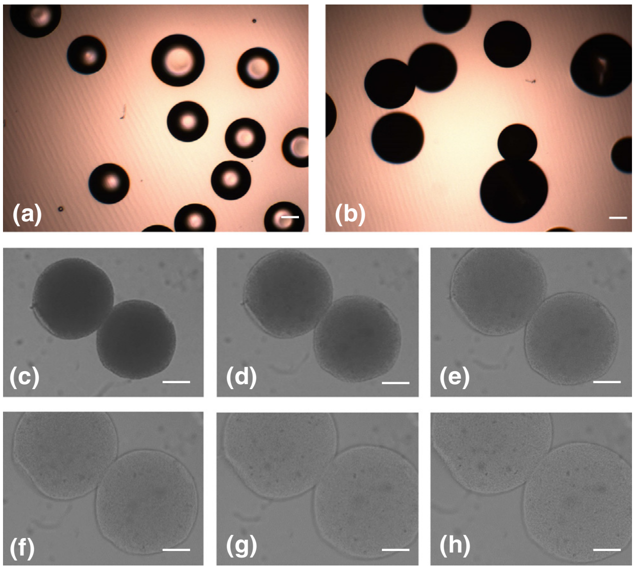

Fig. 2. Droplets collection and thermal response for elevating and decreasing temperature. (a) Microgel solution droplets collection at room temperature in the oil. The dark edge of droplets is seen due to light reflection between oil and water. (b) The changes of hydrophobicity of droplets from hydrophilic to hydrophobic at 37 °C in oil. Opaque hydrophobic droplets show complete darkness. (e) to (h) Droplets in culture media cool down to temperature every 2 min. Scale bar is 100 μm.

entering into its inner structure. Fig. 2d–h demonstrate the collapse process of the microgel structure every 2 min when the temperature reduces to the room temperature. During the first 6 min, the colour of the droplet gradually changed into transparent and the droplets were able to maintain their size and shape. After 6 min, the droplets started to lose their shape, and the size of the droplets expanded, which indicated microgels were dispersed into water.

We hypothesized that cells are encapsulated into the uniform-sized droplets generated from the microchannel, and then the droplets gel at 37 °C and disperse in the cell culture medium for cell growth and cellular spheroid formation, finally the cellular spheroids are released from the droplets after the temperature reduces to the room temperature for harvest, as shown in Fig. 1. Comparing with other previous reports using droplet encapsulation of cells [19,21], in which MSCs are unable to release from droplets without strong or toxic chemicals. We encapsulated HeLa cells inside the microgel-containing droplets. After suspending droplets in the cell culture medium for the pre-set days, we collected the droplets and cooled down to the room temperature to harvest the MCSs. We found out that it took 20 min to dissolve the droplets and release the MCSs. Fig.3 shows the HeLa MCS formation process inside the droplets for up to 28 days. The porous structure inside the droplet provided a 3D structure to support cell growth due to sufficient nutrient, oxygen and biowaste transportation (Fig. S3). At day 7, cells proliferated and aggregated to form a few cell clusters in each droplet, and the cell cluster size varied depending on the initial cell distribution within the droplets, which was similar to cluster formation in the 3D scaffold [23] in comparison with single individual cells at day 1 as shown in Fig. S5. After continuing cell culture for another 7 days (Fig.3b), the size of the big cluster increased to 40–50 μm while a few small clusters scattered around the big clusters. The loose structure indicates the first step of multicellular spheroid formation where cells are drawn together due to the combination of ECM fibres with multiple RGD motifs [24]. At day 21 (Fig. 3c), smaller clusters aggregated into the big cluster to have a size of 50 μm and very few smaller clusters were observed within the droplet. At day 28, the edge of the big cluster become smoother which indicates spheroid compaction stage was reached [24] where the homophilic cadherin-cadherin binding and microfilaments of cells become localized along the cell. Due to controlled microenvironment provided from the droplet, the spheroid size can be manipulated by adjusting the droplet size, initial cell density and cell culture duration. Compared with the normal HeLa cluster size around 250 μm and the size variations of 50 μm in the conventional culture condition, this approach can provide more uniform-sized multicellular spheroids.

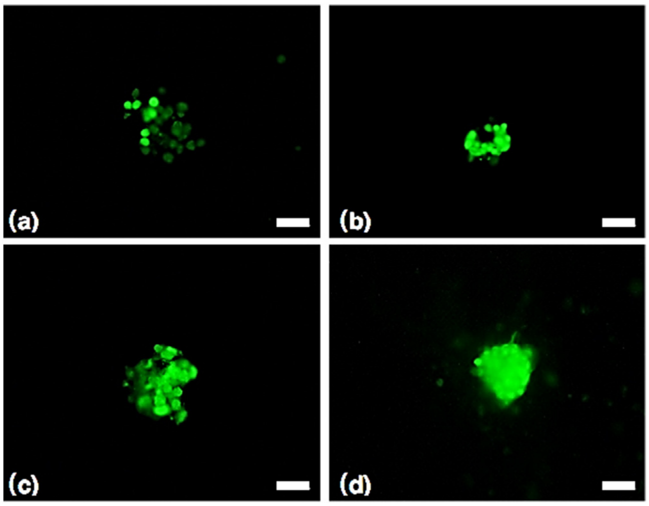

Fig. 4. Live/dead images of the MCSs inside the droplets at (a) day 7, (b) day 14, (c) day 21, (d) day 28. Scale bar is 50 μm.

To further investigate the cluster morphology, live/dead cells images were taken by staining cells with the Live/Dead cell kit. Fig. 4 shows the cluster formation process from the encapsulated cells within a droplet. This approach was benign to cells and most cells were still green up to 28 day culture, which means cells have a high viability. At day 7, within the droplet, smaller clusters started to form (Fig. 4a), and these clusters were drawn together due to their extracellular matrices. After another 7-day culture (Fig. 4b), small clusters aggregated to form a loose structure, and a few single cells or small clusters were observed around the loose structure. At day 21 (Fig. 4c) the loose structure started the compaction process, but the cavities were seen inside the structure. After 28 day culture (Fig. 4d), mature spheroids were obtained with a spherical shape and a very compact structure was observed.

In this hydrogel-based droplet microenvironment, Hela cells are confined in the given space and aggregated to form the spheroids.

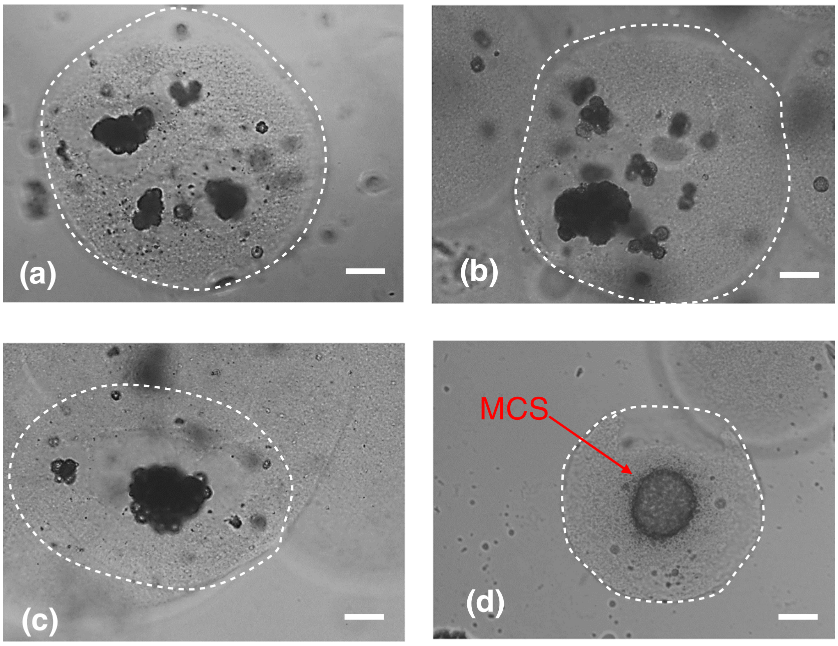

Fig. 3. MCSs formation inside the droplets at (a) day 7, (b) day 14, (c) day21, (d) day 28. Scale bar is 50 μm. Dash line is droplet boundary.

Meanwhile the nutrients and wastes are transferred to the cell clusters to maintain cellular activities. Importantly, the spheroids are harvested simply by reversing the temperature to the room temperature without physical or chemical damage. Therefore, the full recoverability and the 3D controlled microenvironment render our approach very promising for size-controllable multicellular spheroid formation.

The microfluidic channels were made in the ANFF SA node at The University of South Australia and we acknowledge technical supports from the team at the node. XC would like to acknowledge the divisional scholarship given by the University of Adelaide. HZ thanks the financial support from ARC Discovery Project (DP160104632) and The Medical Advancement Without Animal (MAWA) Trust.

Appendix A. Supplementary data

Supplementary data to this article can be found online at http://dx.doi.org/10.1016/j.colcom.2016.09.001.

References

[1] F. Pampaloni, E.G. Reynaud, E.H.K. Stelzer, The third dimension bridges the gap between cell culture and live tissue, Nat. Rev. Mol. Cell Biol. 8 (2007) 839–845.

[2] M.W. Bosenberg, J. Massagué, Juxtacrine cell signaling molecules, Curr. Opin. Cell Biol. 5 (1993) 832–838.

[3] H.-F. Lu, K.-N. Chua, P.-C. Zhang, W.-S. Lim, S. Ramakrishna, K.W. Leong, H.-Q. Mao, Three-dimensional co-culture of rat hepatocyte spheroids and NIH/3T3 fibroblasts enhances hepatocyte functional maintenance, Acta Biomater. 1 (2005) 399–410.

[4] Y. Wang, J. Wang, Mixed hydrogel bead-based tumor spheroid formation and anticancer drug testing, Analyst 139 (2014) 2449–2458.

[5] S.L. Nyberg, J. Hardin, B. Amiot, U.A. Argikar, R.P. Remmel, P. Rinaldo, Rapid, large-scale formation of porcine hepatocyte spheroids in a novel spheroid reservoir bioartificial liver, Liver Transpl. 11 (2005) 901–910.

[6] R.L. Carpenedo, C.Y. Sargent, T.C. McDevitt, Rotary suspension culture enhances the efficiency, yield, and homogeneity of embryoid body differentiation, Stem Cells 25 (2007) 2224–2234.

[7] J.M. Yuhas, A.P. Li, A.O. Martinez, A.J. Ladman, A simplified method for production and growth of multicellular tumor spheroids, Cancer Res. 37 (1977) 3639–3643.

[8] A.P. Napolitano, P. Chai, D.M. Dean, J.R. Morgan, Dynamics of the self-assembly of complex cellular aggregates on micromolded nonadhesive hydrogels, Tissue Eng. 13 (2007) 2087–2094.

[9] M. Kamihira, K. Yamada, R. Hamamoto, S. Iijima, Spheroid formation of hepatocytes using synthetic polymer, Ann. N. Y. Acad. Sci. 831 (1997) 398–407.

[10] S. Sakai, S. Ito, K. Kawakami, Calcium alginate microcapsules with spherical liquid cores templated by gelatin microparticles for mass production of multicellular spheroids, Acta Biomater. 6 (2010) 3132–3137.

[11] M.-Y. Lee, R.A. Kumar, S.M. Sukumaran, M.G. Hogg, D.S. Clark, J.S. Dordick, Three-dimensional cellular microarray for high-throughput toxicology assays, Proc. Natl. Acad. Sci. 105 (2008) 59–63.

[12] K. HoáLee, D. YoonáNo, J. HeeáRyoo, S. FungáWong, Diffusion-mediated in situ alginate encapsulation of cell spheroids using microscale concave well and nanoporous membrane, Lab Chip 11 (2011) 1168–1173.

[13] M.C. Chen, M. Gupta, K.C. Cheung, Alginate-based microfluidic system for tumor spheroid formation and anticancer agent screening, Biomed. Microdevices 12 (2010) 647–654.

[14] D. Velasco, E. Tumarkin, E. Kumacheva, Microfluidic encapsulation of cells in polymer microgels, Small 8 (2012) 1633–1642.

[15] M. Serra, C. Correia, R. Malpique, C. Brito, J. Jensen, P. Bjorquist, M.J. Carrondo, P.M. Alves, Microencapsulation technology: a powerful tool for integrating expansion and cryopreservation of human embryonic stem cells, PLoS One 6 (2011), e23212.

[16] E. Tumarkin, L. Tzadu, E. Csaszar, M. Seo, H. Zhang, A. Lee, R. Peerani, K. Purpura, P.W. Zandstra, E. Kumacheva, High-throughput combinatorial cell co-culture using microfluidics, Integr. Biol. 3 (2011) 653–662.

[17] S. Sakai, S. Ito, H. Inagaki, K. Hirose, T. Matsuyama, M. Taya, K. Kawakami, Cell-enclosing gelatin-based microcapsule production for tissue engineering using a microfluidic flow-focusing system, Biomicrofluidics 5 (2011) 013402.

[18] A. Kumachev, J. Greener, E. Tumarkin, E. Eiser, P.W. Zandstra, E. Kumacheva, High-throughput generation of hydrogel microbeads with varying elasticity for cell encapsulation, Biomaterials 32 (2011) 1477–1483.

[19] S. Utech, R. Prodanovic, A.S. Mao, R. Ostafe, D.J. Mooney, D.A. Weitz, Microfluidic generation of monodisperse, structurally homogeneous alginate microgels for cell encapsulation and 3D cell culture, Adv. Healthcare Mater. 4 (2015) 1628–1633.

[20] H.F. Chan, Y. Zhang, Y.-P. Ho, Y.-L. Chiu, Y. Jung, K.W. Leong, Rapid formation of multicellular spheroids in double-emulsion droplets with controllable microenvironment, Scientific Reports, 3, 2013.

[21] S. Yoon, J.A. Kim, S.H. Lee, M. Kim, T.H. Park, Droplet-based microfluidic system to form and separate multicellular spheroids using magnetic nanoparticles, Lab Chip 13 (2013) 1522–1528.

[22] Z. Shen, J. Bi, B. Shi, D. Nguyen, C.J. Xian, H. Zhang, S. Dai, Exploring thermal reversible hydrogels for stem cell expansion in three-dimensions, Soft Matter 8 (2012) 7250–7257.

[23] Y. Lei, D.V. Schaffer, A fully defined and scalable 3D culture system for human pluripotent stem cell expansion and differentiationProceedings of the National Academy of Sciences 2013, pp. E5039–E5048.

[24] R.Z. Lin, H.Y. Chang, Recent advances in three-dimensional multicellular spheroid culture for biomedical research, Biotechnol. J. 3 (2008) 1172–1184.

Engineering in Life Sciences

Eng. Life Sci. **2015**, *15*, 582–592 www.els-journal.com

Hu Zhang[1]
Xiaolin Cui[1]
Jingxiu Bi[1]
Sheng Dai[1]
Haitao Ye[2]

[1] School of Chemical Engineering, University of Adelaide, Adelaide, Australia

[2] School of Engineering and Applied Science, Aston University, Birmingham, United Kingdom

Review

Single-cell analysis for bioprocessing

Cell population heterogeneity has attracted great interest for understanding the individual cellular performances in their response to external stimuli and in the production of targeted products. Physical characterization of single cells and analysis of dynamic gene expression, synthesized proteins, and cellular metabolites from one single cell are reviewed. Advanced techniques have been developed to achieve high-throughput and ultrahigh resolution or sensitivity. Single cell capture methods are discussed as well. How to make use of cellular heterogeneities for maximizing cellular productivity is still in the infant stage, and control strategies will be formulated after the causes for heterogeneity have been elucidated.

Keywords: Gene expression / Population heterogeneity / Protein expression / Single-cell analysis / Single-Cell isolation

Received: September 23, 2014; *revised:* December 8, 2014; *accepted:* April 29, 2015

DOI: 10.1002/elsc.201400155

1 Introduction

Population cells have been traditionally employed to evaluate the cellular responses to the external environment stimuli, cell–cell interactions, and cellular performance in the bioprocessing to achieve the maximum process efficiency and product yield. Nevertheless, heterogeneous cells are present in the large-scale bioreactor, which may generate substantial consequences in industrial fermentation and cell culture processes. Even genetically identical bacteria display different levels of resistance to antibiotics, and clonal yeast populations demonstrate morphological and growth-rate heterogeneity [1]. Cell population heterogeneity has been reduced by modern cell culture and fermentation technology, such as continuous cultivation at the distinct growth rate and synchronously growing culture, while understanding and then employing cell heterogeneity to control and manipulate cell heterogeneous features for maximizing benefit are gaining more interests from bioprocess engineers [2]. Single-cell analysis plays a significant role in understanding the mechanisms and the information from single-cell analysis will become the foundation for process control and optimization. Since the single-cell analysis provides the individual characteristics so that it offers the opportunity to explore discrete cellular or biological phenomena which cannot be found from the bulk-averaged measurements.

Population heterogeneity can be attributed to several factors, and a recent review paper has addressed the origin of heterogeneity [2]. Three factors have been considered to be responsible for the heterogeneity of cells distributed inside a large-scale bioreactor: cell cycle phase, age distribution, and extracellular micro-environmental conditions. Replication and cell division are essential for cellular biomass growth within a certain specific time frame. They are independent of the prevailing growth conditions, while the remaining of the cell cycle varies substantially, especially when the overall cell growth rate is low. During these cell cycles, physiological changes may lead to an asymmetric division of genetic materials from the parent cell to the daughter cell, which may give rise to larger and smaller cells. Newly born daughter cells from young mother cells are also different from those from old mother cells. For some cells, aged parent cells show reduction in the cell growth rate on average and loss of regenerative capacity. Cells also respond differently to the rapid micro-environmental changes in the nutrient/toxin concentration, osmolarity, shear stress, pH, and temperature, which are typically presented in a large-scale bioreactor [3]. The different responses lead to cell differentiation and population fragmentation, resulting in the population heterogeneity.

A range of tools and techniques has been developed to monitor and detect the population heterogeneity and single-cell analysis becomes one of the most important methods. Biochemical, chemical, physical, immunological, and integrated methods have been developed for single-cell analysis as schemed in Fig. 1. In this review paper, these methods will be discussed and compared for single-cell analysis. These methods have been primarily developed for general biological basic research, but they can be adapted for applications in cell culture and fermentation process. One of the challenging issues for single-cell analysis is to isolate the single cells from the samples for the following analysis. The single-cell isolation methods are reviewed first and then single-cell analysis methods will be detailed. We finish the review paper with concluding remarks.

Correspondence: Dr. Hu Zhang (hu.zhang@adelaide.edu.au), School of Chemical Engineering, University of Adelaide, SA 5005, Australia

Abbreviations: AFM, atomic force microscope; **cDNA**, complementary DNA; **EYFP**, enhanced yellow fluorescence protein; **FACS**, fluorescence-activated cell sorting; **FISH**, fluorescent *in situ* hybridization; **mRNA**, messenger ribonucleic acid

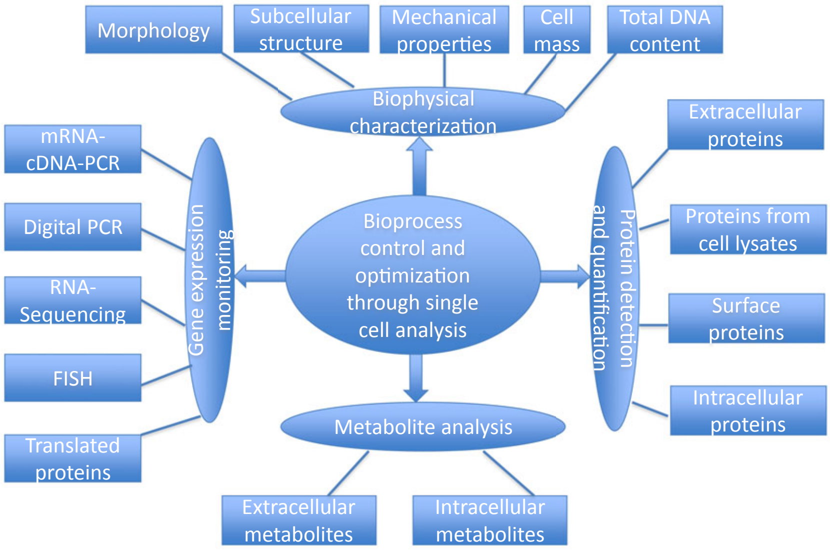

Figure 1. Overview of single-cell analysis for bioprocess control and optimization.

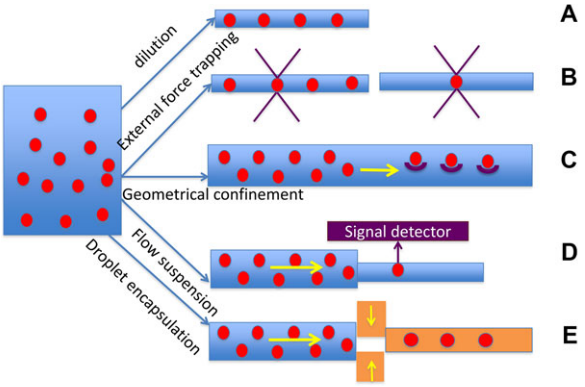

Figure 2. Techniques for isolating single cells. (A) Diluting population cells for microscopic analysis. (B) Trapping single cells using external forces. (C) Confining single cells by geometrical constraints. (D) Flowing one single cell through the microchamber for signal detection. (E) Encapsulating single cells in one droplet.

2 Single-cell isolation

In order to carry out the single-cell analysis, each single cell has to be isolated from the population cells. The isolation methods have been schematically described in Fig. 2, including dilution, physical trapping, geometrical confinement, droplet encapsulation, and flow-driven single suspension. Traditionally the population cells are diluted in the solution and these cells are observed from the microscope. The method can distinguish each single cell but the information provided from the microscope is limited, only including morphology, or live/dead state. This dilution method has been recently used for single cell isolation with the help of fluorescence signals. To avoid labeling the cell with fluorophores which severely affect cell viability, the cell carries a reporter gene which can encode a fluorescent protein. Cells from the sample are diluted and distributed into microchambers so that one single cell is located inside a microchamber. The single cell is further confirmed by the weak fluorescence intensities. The cell is further taken out by a glass capillary for single-cell breeding [4].

Alternatively, one or a few individual cells taken from large-scale bioreactors can be trapped by field gradient traps such as optical tweezers, magnetic tweezers, and dieletrophoretic traps. The trapped single cell(s) can be taken out for further analysis, such as single-cell PCR, or measured *in situ* by Raman spectrometry or other methods. Gradient traps can arbitrarily holding single cells in three dimensions. Optical tweezers are 3D traps which use a highly focused beam of light to trap and manipulate microscopic, neutral objects, such as small dielectric spherical particles like biological cells ranging from ten of nanometers to ten of micrometers [5]. The advantages of using tweezers for manipulating biological cells include noncontact force for cell manipulation and amiability to liquid medium environments. Magnetic tweezers [6] and dieletrophoretic traps [7] are similar to optical tweezers, trapping cells in electromagnetic field gradients that impose a local magnetic force on magnetic beads attached to the single cell surface or in a high-gradient electric field with the subtle trapping force determined from the electrode shape and excitation. Another advantage for the trapped cells is to easily change the microenvironment of the trapped cells including physical or chemical external stimuli, and then monitor cellular responses upon these changes. In this way, specific information about cellular physiological responses upon microenvironment changes can be obtained and fundamental causes for cellular heterogeneity can be understood. However, this method may not be applicable for high-throughput cell analysis.

Since a large enough number of single cells to represent the population are needed to accurately reveal the underlying mechanisms of cell heterogeneities, high-throughput methods have been developed to isolate single cells from samples for further analysis [8]. The widely applied method is to flow the population cells into a narrow microchannel and then force one single cell to pass the detection chamber or confine one single cell in a compartment for further analysis. When one single cell is passed the detection chamber, physical signals, such as fluorescence, are captured and reported for that cell. This method has the capacity for a large number of cells and has been widely used in flow cytometers. This method, fluorescence-activated cell sorting (FACS), has been widely used for analyzing single mammalian cells [9]. However, this method requires pretreatment of the cells by attaching reporting signals and it cannot capture the cellular responses after exposing to external stimuli *in situ*. To make advantage of high-throughput of microfluidic channels, one can confine one single cell in one droplet so that the cell can be further cultivated, manipulated, and detected as shown in [10]. For example, after individual mouse mast cells have been lysed in droplets by heating/photolysis, and cell contents were released into the picoliter container without any interference from other cells [11]. In this small compartment, cellular responses can be monitored for a longer cultivation time or after cells are exposed to a modified microenvironment. Yeast cells and their expression of β-galactosidase [12], and single bacterial cells and their alkaline phosphatase expression [13] have been monitored to provide time series analysis of heterogeneous cell growth rates and expression variation. Such time-resolved variations obtained from a large number of individual cells can be used to explore the heterogeneity in the large-scale bioreactors.

3 Single-cell biophysical characterization

Single cells can be physically characterized through their morphology, fine subcellular structure, electrical and mechanical properties, viability, and physiological states. The cellular morphology including size and shape is often obtained from the optical microscopes. This basic method reveals the phenomena of heterogeneities in a cell sample [14]. Along with the improvements in the microscope, cellular internal fine structure and molecular distribution can be observed. Advancements in microscope analysis of single cells can be found in a recent critical review paper [15]. However, this method is very limited and only few cells can be measured simultaneously. The atomic force microscope (AFM) technique is such an example which maps the surface topology and membrane structure of a single cell based on the physical interactions between the cell and the tip of a few nanometers attached to the cantilever. A resolution for the mammalian cells of approximately 50 nm can be achieved [16]. By varying the external simulations, AFM could be able to detect the surface changes so that dynamic process of cellular responses can be monitored.

AFM also allows the measurement the mechanical properties of single cells at any region of the membrane surface by controlling the position of AFM tips, and it can be further used for characterizing the rheology of single cells adherent to flat surfaces by subjecting to fluid shear stress [17]. Because this technique requires contacting the single cell onto a surface, it is restricted to those cells that can adhere tightly to a substrate over the course of an experiment. Hydrodynamic and optical methods can be used to assay cell mechanical properties of adherent or nonadherent cells. This method is primarily based on the ability of cells to change shape with an applied load. Optical tweezers can exert exquisitely controllable forces in the pN range on a single cell, and they are often used for a variety of sub-nano-mechanical measurements, such as cell membrane deformability and cell adhesion [5]. Except optical forces, other structure-induced, fluid-induced, and electric-induced deformation for a large number of cells has been reported recently. For example, when one single cell passes a microfluidic constriction channel, the cell is squeezed by the constriction channel walls. High-speed recording of the cell deformation process can reveal the duration for cell transit, elongation, and recovery. The deformation characterization can be further correlated to the membrane mechanical properties [18]. These mechanical properties could be correlated with cellular responses to shear stress or normal stress present in the large-scale bioreactors.

Another physical parameter is cell mass which indicates the cellular metabolic rate and its physiological state. For example, cell mass of a single cell can inform of the cell cycle regulation and this information can be used for deriving cell growth rates. The cell mass can be tracked by the suspended microchannel resonator for a single cell. As the cell passes the suspended microchannel resonator, changes in the resonant frequency are detected by measuring the deflection of a laser beam. Since the changes in the resonate frequency depend on the buoyant mass and position of the cell, cell mass and cell growth can be precisely characterized. This method allows simultaneously measuring single cell mass and cell cycle progression over multiple generations for up to 1000 h from mouse lymphoblast and pro-B-cell lymphoid cell line [19].

Cell mass can also be quantified through total DNA content, which can be measured by stoichiometrically staining individual cells with fluorescent dyes and analyzing through FACS. FACS analysis showed that different DNA amount for *Pseudomonas putida* mt-2 during growth on toluene [2]. During the lag phase, around 60% of the cells in the population contained only a single chromosome equivalent. When the cells entered into exponent growth phase, this major subpopulation at the lag phase disappeared while the percentage of cells containing the double chromosome equivalents and more than that considerably increased. This technique can also be applied to study the effect of cellular microenvironment on the growth effect. More DNA contents are expected under optimal microenvironment than the limiting conditions.

Raman spectrometry provides information about the chemical bonds in molecules in a single cell by identifying spectral patterns excited by a near-infrared laser beam in a noninvasive and label-free way, therefore, the Raman fingerprint of a biological cell can yield a vast amount of information about cell's structural makeup, and chemical/biological changes. Raman microscopes have been used to distinguish cell morphology and subcellular organelles [20]. Cell state can be differentiated from the Raman spectra when it is coupled with principal component analysis [21].

4 Single-cell gene expression analysis

Gene expression analysis for single cells can be used to provide great insights to gene expression variations, gene regulatory mechanisms, and protein synthesis dynamics. It has been reported that in microorganisms, variable gene expression for cell to survive antibiotic treatment has led to heterogeneous cell growth profiles within one clonal population [22]. To trace the gene expression inside one single cell, the messenger ribonucleic acid (mRNA) needs to be detected. However, the major challenge for a single-cell gene expression analysis is the small amount of mRNA obtained from an individual cell. The mRNA amount needs to be amplified so that low abundance of mRNA molecules can be detected. Single cell RT-PCR is often used due to its sensitive detection and the method is able to capture as low as one mRNA molecule.

The general procedure for single cell gene expression analysis starts with single-cell capture and lysis, and the released mRNA is transcribed to complementary DNA (cDNA) by reverse transcriptase, and the cDNA is hybridized to a primer for amplification by DNA polymerase. The amplified DNA is detected by fluorescence signals [23]. The specific gene expression level is normalized through a house gene. During the procedure, extra care must be taken to prevent any contamination in mRNA sample preparations since only a few mRNA molecules are present in the samples. mRNA should also be completely converted to cDNA. Using this technique, siRNA knockdown of one specific gene expression from individual Jurkat cells was found to present two distinct groups: partial knockout (50%) and complete knockout (100%). The average result from 50 cells (21%) was not representative of any one individual cell as shown in Fig. 3A [24].

Many techniques have been developed to improve the single-cell RT-PCR method. To improve mRNA quantification from single cells, direct qPCR from a cDNA pool without pre-amplification was performed for four house-keeping genes [25]. 14 single cells were used to quantify these gene expressions. The amount of each of the four genes was different for each cell, which supported the evidence of population heterogeneity [25].

In a recent protocol, microfluidic single-cell quantitative RT-PCR offers real-time analysis of gene expression for a single cell, providing a novel approach for testing large numbers of cells and genes simultaneously and also allowing quantitative high-content analysis and comparison of variations in gene expression patterns at the single-cell level [26]. In this method, single live cells sorted from FACS were directly mixed with the RT-specific target amplification master mix in 96-well plates. The sample from each well was partitioned into 48 (or 96) microfluidic chambers and qPCR detection and quantification were performed for a specific gene in each chamber.

Different from the above approach in which microfluidic chambers were used for detection and quantification only, a microfluidic device for integrating cell encapsulation and lysis, and one single copy RT-PCR within agarose droplets was developed by Zhang et al. as shown in Fig. 3B [27]. RT-PCR reagents and cell lysis solution from one inlet and target cells in aqueous agarose solution from another inlet were mixed in a T-junction and the mixed solution formed mono-disperse picoliter agarose emulsion droplets in carrier oil. Within the agarose droplet, the single cell was lysed to release DNA and RT-PCR was performed at the single copy level. After amplification, the droplets was turned into solid beads at 4°C to remove oil for further fluorescence signal analysis.

Digital PCR employs compartmentalization of single molecules at limiting dilution followed by PCR amplification and end-point detection to make precise measurement of single cell transcription. Special microfluidic devices have been designed to allow cell capture, cell lysis, mRNA purification, cDNA synthesis, cDNA purification within one device (Fig. 3C). For example, Quake's group designed parallel chambers formed by micromechanical valves to act as independent PCR reactors and they have employed such devices to measure the gene expression from the single NIH/3T3 cell and single bacterial cells [28, 29]. White et al. designed 1020 chambers with a volume of 25 pL using surface tension-based sample partitioning. Their 10 cm^2 small device can run the analysis of 200 single cells with 204 000 PCR reactions [30]. Alternatively, after a reverse-transcription and polyA-tailing sample preparation procedure, single molecules were sequenced to generate a single read per transcript. Through this method using spiked-in RNA, the sequencing of yeast transcriptome in a single run was demonstrated and an average of 12 million aligned reads per channel were generated [31]. This will be used for high-throughput, amplification-free transcriptome quantitation.

Single-cell RNA sequencing is an emerging technology that is poised to yield insights about expression-level variability. In this method, all mRNA molecules are converted to cDNA, and the cDNA is then sequenced, providing the complete transcriptome of the single cell. This method is able to provide great insights into the transcriptional architecture, sequential order of gene activation, and tempospatial gene expression profiles. Xue et al. applied the single-cell RNA sequencing to quantitatively reveal the expression defects from embryos which cannot be detected by DNA sequencing [32]. While this method is limited to 100–200 cells per experiment and is applicable to medium-abundance or high-abundance transcripts [33].

RNA transcription can also be measured indirectly through RNA fluorescent *in situ* hybridization (FISH). Fluorescence-labeled nucleic acid probes are hybridized to the target RNA sequences. FISH can preserve spatial information regarding the location of cells within a tissue or subcellular organelles inside one cell. Remarkable differences in transcription and replication in mitochondria were found from individual single cells or even several mitochondria in the same cell [34]. The FISH-positive cells can be sorted through flow cytometry for high-throughput analysis. However, to perform FISH, fluorophore-tagged nucleotide probes are required to insert into the cell, and the cell has to be fixed and permeable, resulting in cell death.

The conventional gene expression analysis involves lysis of single cells and gene expression dynamics cannot be continuously monitored for the same cell. One approach to monitor gene expression dynamics in single cells is to continuously stain single cells with specially treated antibodies. The antibodies interact with the surface proteins expressed by the single cell. The cell can be distinguished from the signals generated by the antibodies. Alternatively, cells containing a green fluorescence plasmid produce a fusion protein composed of a reporter fluorescence protein and a target protein. Gene expression can be monitored through the fluorescence signals generated from the reporter proteins. Transcription as well as translational regulation can be analyzed through this technology. Dynamic gene expression from single HeLa cells has been monitored using this technology when the cell were simulated by soluble molecules with concentration gradients generated from upstream microfluidic

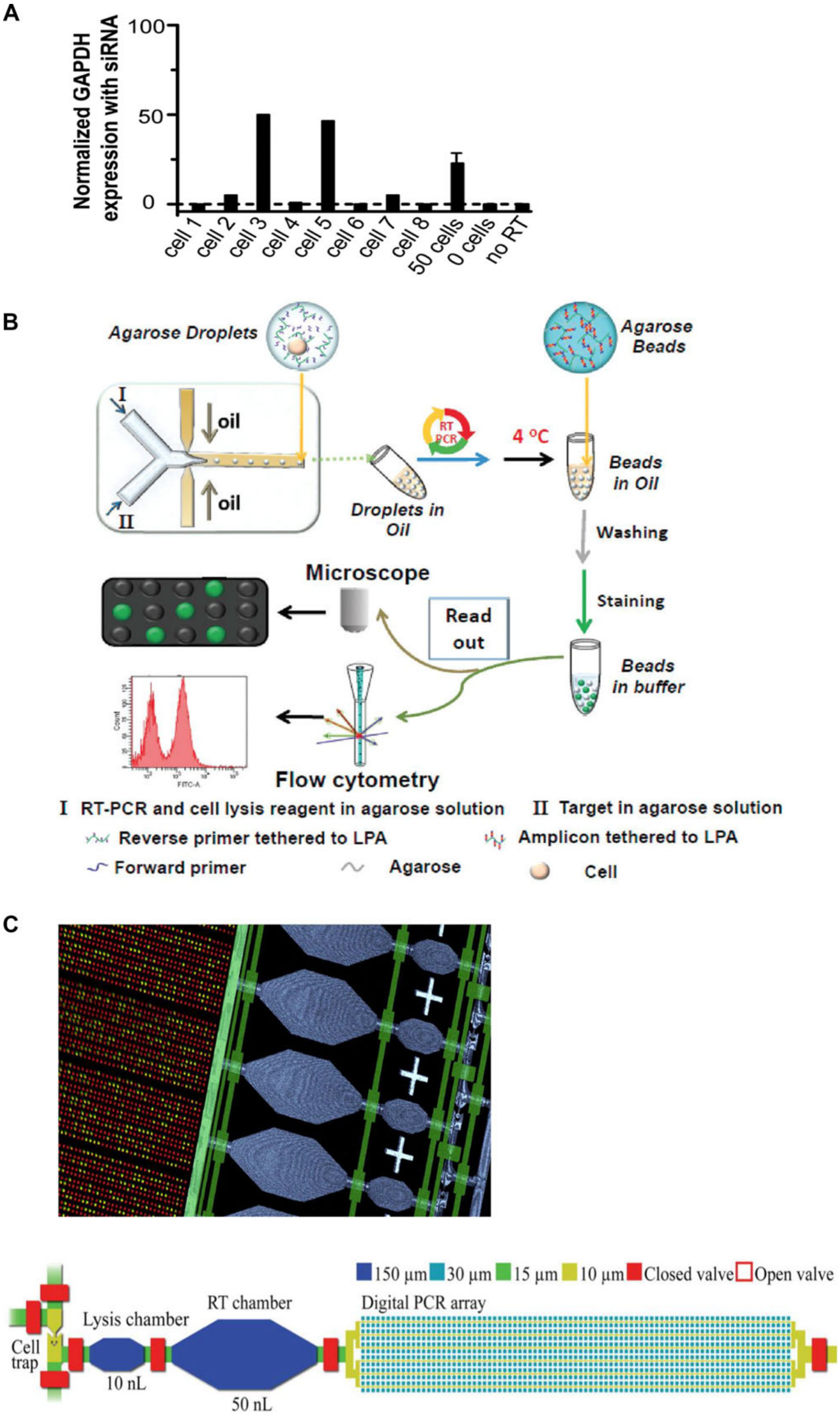

Figure 3. Single-cell dynamic gene expression. (A) Single cell gene expression to demonstrate population heterogeneity [24]. mRNA expression of glyceraldehyde-3-phosphate dehydrogenase (GAPDH) from individual Jurkat cells after siRNA knockout. Responses from averaged 50 cells, 12 individual cells, zero cells, and no reverse transcription (RT) are different. A representative bulk measurement from 50 cells shows GAPDH expression at 21 ± 4%. (B) Droplet-based PCR [27]. Carrier oil in the microfluidic channel squeezes an aqueous agarose solution containing one single cell mixed with PCR reagents and cell lysis solution into single droplets. The droplets are further processed for gene amplification before solidifying into microbeads for gene expression detection via flow cytometry. (C) Microfluidic-digital PCR [30] with a detailed single microfluidic module with dimensions for chambers and channels for single-cell digital PCR analysis. Fifty identical modules are capable of parallel process up to 200 single cells. After cell capture, lysis, and reverse transcription, a fluorinated oil is then used to displace the remaining PCR solution in the channels and compartmentalize individual PCR digital chambers for detection. The resulting cDNA is quantified by positive hits (green) in chambers with a high S/N, while a passive dye (red) is visible in all chambers.

network, and dynamic outputs from the adherent cells can be obtained through the fluorescence signals generated from the reporter protein [35].

5 Single-cell protein analysis

In biological processes, proteins are important in regulating cellular functions or some of them are the products of great interest for curing human diseases. Gene expression analysis can provide indicative information of proteins, but cannot offer the information on protein concentration, protein distribution, protein post-translational modifications, and protein interactions [36]. Different techniques have been developed for intracellular, surface, and extracellular protein analysis from one single cell, either by disrupting cells or keeping cell intact.

MS is the most preferable choice to analyze the intracellular or extracellular proteins, protein interactions, and modifications. For low-abundance proteins, proteins enrichment from the cell lysates is critical for MS analysis. A miniaturized LC column was used to separate proteins from other impurities and the separated proteins were characterized by MS. More than 6000 proteins of nanogram quantities from single pancreatic islets containing 2000–4000 cells were detected with high accuracy (1–2 ppm) and sensitivity (attomole to femtomole) [37]. This method can be further extended to one single cell. Another pretreatment was carried out in 1D and 2D porous layer open-tubular-LC to solid-phase extract protein mixture from around 20 HeLa cells, approximately 2.5 ng of protein in 2 μL of solution was further analyzed using a linear ion trap MS [38]. Two hundred and thirty seven peptides associated with 163 unique proteins were identified based on this technique.

Modified MS methods have been developed for identification and quantification of proteins for single cells. Mass cytometry described in Fig. 4A is a combination of atomic MS and flow cytometry. It offers quantitation, specificity, and dynamic range of MS in a similar format as flow cytometry. Instead of fluorescence signals, the mass cytometer quantifies the stable isotope tags attached to antibodies using metal-chelating labeling reagents [39]. One single cell is stained with epitope-specific 20–30 antibodies, and then the labeled cell is injected and nebulized and the metal tags are quantified using MS. Thirty one different antibodies have been profiled from this powerful technique for single bone marrow cells as well as viability, DNA content, and cell size [40].

Microfluidics or droplet-based technology combined with fluorescence signal detection was developed to detect specific intracellular proteins. In a specially designed microfluidic device, single cells were manipulated and lysed with lysis buffer; the cell lysate was labeled with fluorescent antibodies and separated. The protein contents of a single cell were quantified using single-molecule fluorescence counting [41]. Similar principles were applied to a droplet-based protein analysis [42]. Cells were controlled to flow into the chamber in which cells were electrically lysed. The cell lysate and special-treated microbeads were encapsulated into water-in-oil droplets. Inside the droplets, target proteins were selectively bound to antibody-functionalized beads. Two intracellular proteins were able to be quantified and the protein concentrations range over five orders of magnitude, from 50 pM to 1 μM. Although this method is not applied to one individual cell, this method can be further developed for analysis of low-abundance proteins within one single cell.

The proteins can also be measured without cell lysis by staining with fluorescence antibodies. Changes in fluorescence signals inside the single cell can be monitored in milliseconds. The levels and locations of up to 1000 different endogenously tagged proteins were reported for a cancer cell at a high temporal resolution [43]. Upon external stimulation (anticancer drug in this case), proteins sensitive to these drugs were found to show rapid translocation. Temporal and spatial protein degradation and accumulation were shown inside the single cell. Differences in the behavior of a subset of proteins were identified for individual cells. To analyze telomerase expression, a general cancer biomarker, an optical fiber sensor was immobilized with antitelomerase antibodies and placed in the targeted cell in the precisely controlled region [44]. The telomerase was further measured by a sandwich ELISA in a single cancer cell. It was found that the telomerase was overexpressed in the nucleus of the cancer cells compared to that of normal cells. This optical fiber sensor provides the protein concentration in the special cellular compartment.

Based on the same antibody detection principle, DNA-encoded antibody library microarrays or DNA-barcoded antibody chips are also used to detect secreted proteins or surface proteins. Antibodies against proteins including cell surface marker or secreted proteins are labeled with distinct DNA oligomers. These conjugates then bind to their cognate antigens. A detection limit of 10 fM for the protein IL-2, 150 times more sensitive than the analog ELISA, was demonstrated [45]. DNA-encoded antibody library microarrays were used to analyze cytoplasmic membrane protein contents in a single-cell well and the protein–protein interactions were assessed [46]. Single-cell sensitivity was achieved by isolating single cells in 2 nL volume chambers and two copies of a miniature antibody array were patterned in each chamber. After cells were trapped into individual wells and lysed, the levels of released proteins were assays using the antibody arrays. The DNA-barcoded antibody chips shown in Fig. 4B contained 1040 3 nL volume microwells containing DNA-barcoded antibodies. More than ten cytokines were profiled from tumor antigen-specific cytotoxic T cells [47]. The tip of AFM can be further conjugated with specific antibodies or ligands to detect and localize recognized proteins on the cell membrane surface [48].

The antibody-based technique has been applied for real-time analysis of cellular dynamics in a bioreactor. A fully automated real-time flow injection – flow cytometry (FI-FCM) system has been developed to qualify and quantify variations on the single cell level during cell culture in a bioreactor through monitoring the expression of a fluorescence-protein tagged target protein expressed by *Pichia pastoris* [49]. It was found that very few cells with high fluorescence and many cells with low fluorescence intensity were observed from flow cytometry analysis even they are cultivated in the same bioreactor under the same process conditions.

6 Single-cell metabolite analysis

Small molecules that one single cell contains or generates during cellular metabolic processes can be analyzed through chemical,

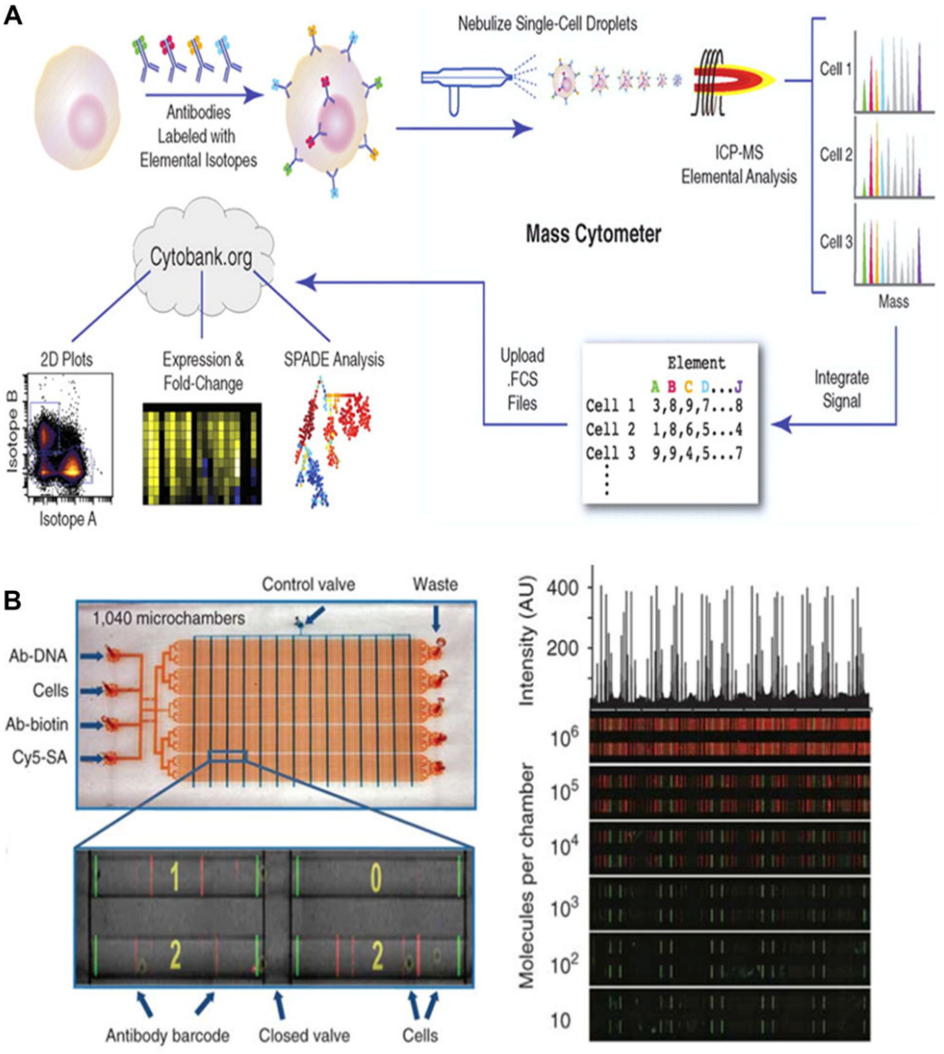

Figure 4. Single-cell protein analysis. (A) Workflow summary of mass cytometry [40]. Cells are stained with epitope-specific antibodies conjugated to transition element isotope reporters, each with a different mass. Cells are nebulized into single-cell droplets, and an elemental mass spectrum is acquired for each cell. (B) DNA-barcoded antibody chips [47]. An optical micrograph showing cells loaded and isolated within the microchambers, overlaid with the fluorescence micrograph of the developed assay barcode for those same microchambers. Numbers of cells per microchamber are indicated by the yellow numbers. Scanned fluorescent images used for the antibody barcode calibration measurements using spiked recombinant proteins. The protein concentrations (in numbers of molecules per chamber) are given to the left of each row of images. The plot at the top is a line profile of the top row of images and represents the reproducibility of the barcodes across the antibody array of a single cell barcode chip.

biochemical, and immunological methods. Dynamic monitoring of cellular metabolites is essential in understanding cell behaviors, and thus elucidating the causes for cell heterogeneous performance. However, the detection of these metabolites can be significantly challenging since release of the metabolites from one single cell occurs very rapidly, within less than a few hundred milliseconds after cell stimulation [50]. There are two different metabolites to be analyzed: intracellular and extracellular. To analyze these metabolites, different techniques have been developed, and they can be categorized into tag-free, tagged or reagent-assisted, and senor-based. The metabolites are analyzed after extraction from cell lysis or *in situ*.

Raman spectrometry and MS, often used in the intracellular or extracellular metabolite analysis for single cells, belong to tag-free methods, which do not require any labeling of metabolites. Raman spectroscopy coupled with stable isotope probing was used to analyze the center carbon metabolism of *Protochlamydia amoebophila* [51]. However, Raman scattering signals are inherently weak. The signals can be intensified when the detected molecules are in close proximity to a metal surface (gold or silver), which is termed as surface-enhanced Raman spectrometry as shown in Fig. 5A. For the single-cell analysis, gold or silver nanoparticles are often transported into the cellular structures and metabolites close to these gold nanoparticles can be detected with high sensitivity. Recently carbon nanotubes of 200 nm in diameter and 5–20 μm in length are decorated with 20 nm gold nanoparticles. The conical shaped nanotube probe can minimize cell damage and the metabolites can be continuously monitored under cell normal physiological conditions. Glycine can be detected down to 1 pM [52].

MS is also applied to characterize small extracellular or intracellular metabolites presented in the single cell. Normally these metabolites have to be isolated from the cell lysis mixture for further analysis by MS. Sample preparation and pretreatment can be a challenge due to a minute amount of metabolites produced from one single cell. CE was coupled with MS to identification of 36 intracellular metabolites [53].

To avoid special pretreatment of metabolites, MALDI MS technology is developed for visualizing metabolites in a specific location within a single cell without cell lysis. Single HeLa cells grown on an indium tin oxide coated glass substrate was metabolically profiled using MS imaging measurement with a

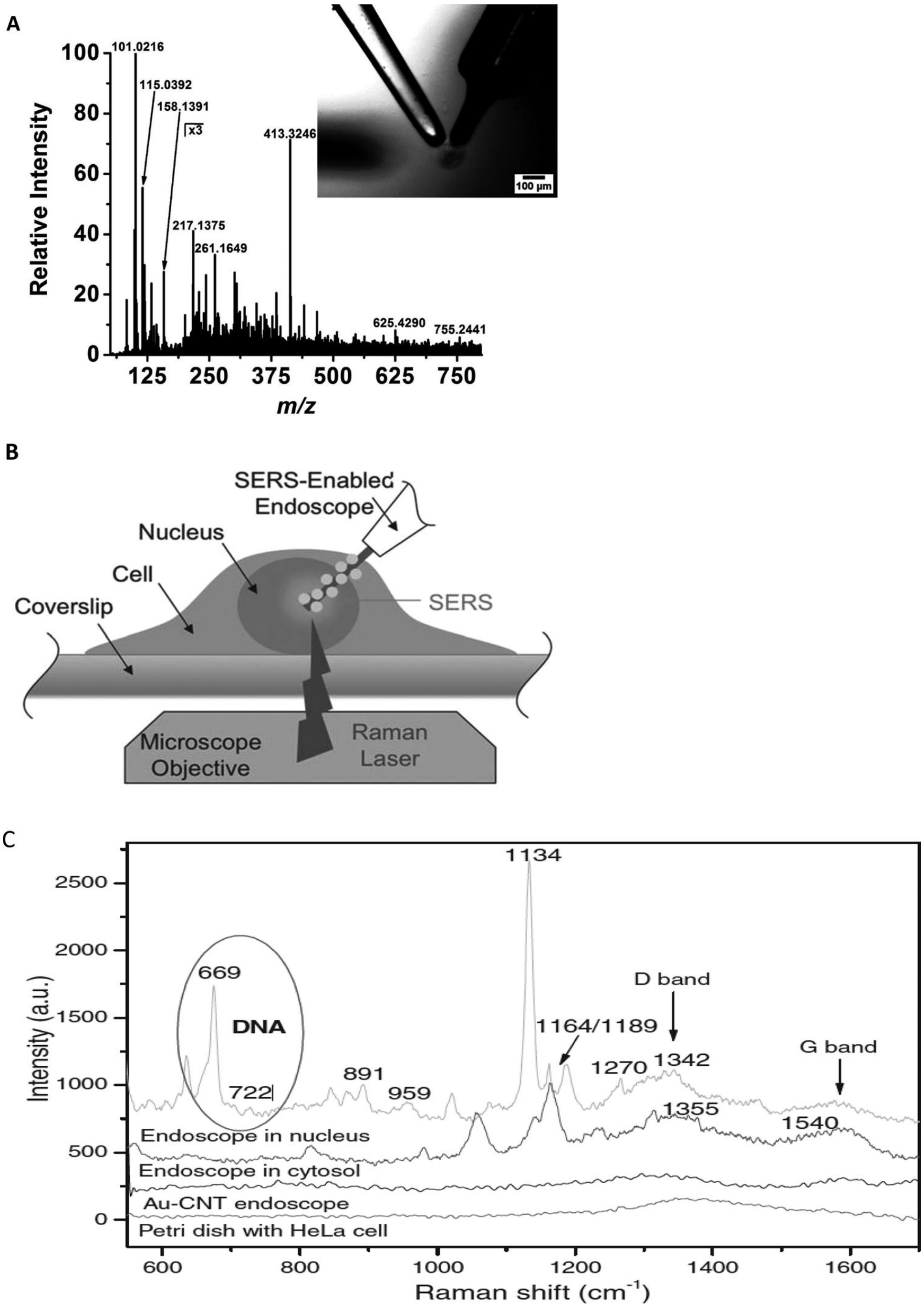

Figure 5. Single-cell metabolite analysis. (A) Positive ion laser ablation ESI mass spectrum of a single egg cell of ~100 μm in diameter [55]. The inset shows the egg immobilized by the holding pipet and touched by the sharpened optical fiber. (B) Surface enhanced Raman spectrometry enabled endoscope for detection of intracellular metabolites in different cellular compartment [52]. (C) The Surface enhanced Raman spectrometry enabled endoscopes into nucleus and cytosol generated different Raman fingerprints in comparison with those from Au–carbon nanotube endoscope and petri dish with HeLa cell.

high spatial resolution, very high mass accuracy, and a very high mass resolution [54]. Numerous components including small metabolites such as adenine, guanine, and cholesterol as well as different lipids such as phosphatidylcholine, sphingomyelin, diglycerides were identified from mass spectrum acquired from an individual spot of 7 μm in diameter. Laser ablation ESI MS (Fig. 5B) is also developed for monitoring metabolites of cells *in situ*. Single cell ablation was obtained by delivering mid-IR laser pulses through the etched tip of a GeO_2-based glass fiber, and metabolic analysis was performed from single cells of *Allium cepa* [55]. Of the 332 peaks detected, 35 were assigned to metabolites with the help of MS. They also applied this method to detect different metabolites from two adjacent individual cells with a difference in pigmentation.

The recently developed nano secondary ion MS has the great potential in applications in metabolite analysis of a single cell. The primary focused laser beam bombs off the upper one to three atomic layers from the cell surface, approximately 1 nm, and the ejected secondary ions are collected and analyzed. This technique does not affect the cell metabolism and is very applicable for continuously analyzing the extracellular metabolites in the real time. Behrens et al. [56] combined enhanced element labeling-catalyzed reporter deposition FISH (EL-FISH) and nano secondary ion MS to study the metabolic interactions of a dual-species microbial consortium. They found evidence for metabolic interactions by visualizing the fate of substrates labeled with ^{13}C carbon and ^{15}N nitrogen, while individual cells were identified simultaneously by halogen labeling via EL-FISH.

Tagged or reagent-assisted methods are formulated for special metabolites which can be reacted with signal-generated molecules or special biochemical reagents to generate signals for detection. The commonly used tagged molecules are fluorescence-based tags that have high sensitivity and can be easily detected from established methods, such as flow cytometry and fluorescence microscopes. We present a few examples in which nonfluorescence tags are used to detect the intracellular and extracellular metabolites. Level of lactate is often raised when cells are exposed to detrimental microenvironments. Lactate was analyzed through an enzyme-linked electrochemical assay based on lactate oxidase in a microfluidic device [57]. An immobilized microfabricated enzyme-modified sensor was developed. After the extracellular lactate produced from one single stimulated heart cell reacted with the immobilized enzyme, the reaction product hydrogen peroxide was detected by amperometrically. The sensor can detect as low as 4.8 fmol (equivalent to 7.4 μM) of lactate produced from one single cell. To detect the same lactate, a nanosensor immobilized with lactate dehydrogenase was located in close vicinity to the target cell membrane, lactate secreted was immediately converted to pyruvate while reducing the cofactor NAD$^+$ to NADH. The byproduct NADH produced fluorescence signals excited by the evanescent field at the nanosensor tip, and the signals were used to calculate the lactate concentration [58]. The low-level concentration of ascorbic acid and amino acids was detected through chemiluminescence method. In this method, reactions of luminol with different oxidizers to reveal enhanced luminescence, and Trp, Gly, and Asp were measured in a single rat hepatocyte to be 5.15, 3.78, and 3.84 fmol, respectively [59].

Special sensors and techniques with sufficient sensitivity and specificity have been developed to detect intracellular metabolites *in situ*. A sensor for a cytosolic metabolite, L-lysine, was developed based on gene transcription regulation. The metabolite sensor contained *lysG,* a transcription regulator that regulates the transcription of its target gene *LysE* and promotes driving transcription of *eyfp* coding for enhanced yellow fluorescence protein (EYFP). The concentration of L-lysine can be correlated with the EYFP protein expressed [60]. Cells with expressed EYFP can be further picked up from FACS for screening purpose. Coupling transcription of the target gene to a reporter protein offered a molecular device for recognition.

7 Concluding remarks

Advanced single-cell analysis techniques have assisted in understanding cellular heterogeneity in bioprocessing. However, challenges are still remaining for the analysis itself and making use of cell population heterogeneity for control of biological processes to maximize product yield. For the single-cell analysis, ultrasensitive detection, and high throughput are still the main theme of pursuit. Minute biological molecules from small-molecular-weight metabolites to large-molecule-weight proteins push the detection limits and novel techniques are and will be developed for this purpose. Combination of several techniques offers new ways of measuring single cell contents *in situ* with high sensitivity. To be able to interpret data from single cells statistically, a significant number of cells must be processed. High-throughput methods are required. Except from flow cytometry and other technique derived from flow cytometry, microfluidics integrate sorting single cell into microchambers and analyzing single cells in each microchamber, including single cell biophysical characterization, dynamic gene expression, and protein and metabolite detection.

Pretreatment including isolation of single cells and samples preparation including DNA, proteins, and metabolites from the isolated single cells are equally challenging. To enrich a trace amount of analytical compounds from cell lysates requires complete recovery of these compounds and removal of impurities as much as possible for further analysis. Specific adsorption and purification methods will be developed and integrated with detection methods. For high-throughput analysis, the sorted cells are required to stain with signal reporters. Multiple reporters can be conjugated with the single cells to reveal more information from one single pass. Future integration of proteomic and metabolic methods with genomic methods at the level of single cells will also expand our understanding of the heterogeneity in genetic lesions and the associated protein and metabolic pathways affected.

To make use of the phenomena of population heterogeneities in large-scale manufacturing is still in the infant stage. Through understanding of the causes of cellular heterogeneities, control, and design strategies are able to formulate to reduce the levels of heterogeneities. Most importantly, we can carefully manipulate the bioprocesses for producing the highest yield even in the presence of heterogeneities.

Author HZ would like to acknowledge the support from the 111 Project (B12034), The MAWA Trust, and the Visiting Fund from Aston University in the UK.

The authors have declared no conflicts of interest.

8 References

[1] Geiler-Samerotte, K. A., Bauer, C. R., Li, S., Ziv, N. et al., The details in the distributions: Why and how to study phenotypic variability. *Curr. Opin. Biotechnol.* 2013, *24*, 752–759.

[2] Muller, S., Harms, H., Bley, T., Origin and analysis of microbial population heterogeneity in bioprocesses. *Curr. Opin. Biotechnol.* 2010, *21*, 100–113.

[3] Zhang, H., Wang, W. X., Quan, C. S., Fan, S. D., Engineering considerations for process development in mammalian cell cultivation. *Curr. Pharm. Biotechnol.* 2010, *11*, 103–112.

[4] Yoshimoto, N., Kida, A., Jie, X., Kurokawa, M. et al., An automated system for high-throughput single cell-based breeding. *Sci. Rep.* 2013, *3*, 1191.

[5] Zhang, H., Liu, K. K., Optical tweezers for single cells. *J. R. Soc. Interface* 2008, *5*, 671–690.
[6] Laurent, V. M., Henon, S., Planus, E., Fodil, R. et al., Assessment of mechanical properties of adherent living cells by bead micromanipulation: Comparison of magnetic twisting cytometry vs optical tweezers. *J. Biomech. Eng.* 2002, *124*, 408–421.
[7] Fiedler, S., Shirley, S. G., Schnelle, T., Fuhr, G., Dielectrophoretic sorting of particles and cells in a microsystem. *Anal. Chem.* 1998, *70*, 1909–1915.
[8] Devonshire, A. S., Baradez, M. O., Morley, G., Marshall, D., Foy, C. A., Validation of high-throughput single cell analysis methodology. *Anal. Biochem.* 2014, *452*, 103–113.
[9] Herzenberg, L. A., Parks, D., Sahaf, B., Perez, O., et al., The history and future of the fluorescence activated cell sorter and flow cytometry: A view from Stanford. *Clin. Chem.* 2002, *48*, 1819–1827.
[10] Brouzes, E., Medkova, M., Savenelli, N., Marran, D. et al., Droplet microfluidic technology for single-cell high-throughput screening. *Proc. Natl. Acad. Sci. U.S.A.* 2009, *106*, 14195–14200.
[11] He, M. Y., Edgar, J. S., Jeffries, G. D. M., Lorenz, R. M. et al., Selective encapsulation of single cells and subcellular organelles into picoliter- and femtoliter-volume droplets. *Anal. Chem.* 2005, *77*, 1539–1544.
[12] Schmitz, C. H. J., Rowat, A. C., Koster, S., Weitz, D. A., Dropspots: A picoliter array in a microfluidic device. *Lab Chip* 2009, *9*, 44–49.
[13] Huebner, A., Olguin, L. F., Bratton, D., Whyte, G. et al., Development of quantitative cell-based enzyme assays in microdroplets. *Anal. Chem.* 2008, *80*, 3890–3896.
[14] Jakobs, S., Stoldt, S., Neumann, D., Light Microscopic Analysis of mitochondrial heterogeneity in cell populations and within single cells. *Adv. Biochem. Eng. Biotechnol.* 2011, *124*, 1–19.
[15] Galler, K., Brautigam, K., Grosse, C., Popp, J., Neugebauer, U., Making a big thing of a small cell—recent advances in single cell analysis. *Analyst* 2014, *139*, 1237–1273.
[16] Shi, X., Zhang, X., Xia, T., Fang, X., Living cell study at the single-molecule and single-cell levels by atomic force microscopy. *Nanomedicine (Lond.)* 2012, *7*, 1625–1637.
[17] Okajima, T., Atomic force microscopy for the examination of single cell rheology. *Curr. Pharm. Biotechnol.* 2012, *13*, 2623–2631.
[18] Zheng, Y., Nguyen, J., Wei, Y., Sun, Y., Recent advances in microfluidic techniques for single-cell biophysical characterization. *Lab Chip* 2013, *13*, 2464–2483.
[19] Son, S., Tzur, A., Weng, Y., Jorgensen, P. et al., Direct observation of mammalian cell growth and size regulation. *Nat. Methods* 2012, *9*, 910–912.
[20] Krafft, C., Knetschke, T., Funk, R. H. W., Salzer, R., Studies on stress-induced changes at the subcellular level by Raman microspectroscopic mapping. *Anal. Chem.* 2006, *78*, 4424–4429.
[21] Ichimura, T., Chiu, L. D., Fujita, K., Kawata, S. et al., Visualizing cell state transition using raman spectroscopy. *Plos One* 2014, *9*, e84478.
[22] Bishop, A. L., Rab, F. A., Sumner, E. R., Avery, S. V., Phenotypic heterogeneity can enhance rare-cell survival in 'stress-sensitive' yeast populations. *Mol. Microbiol.* 2007, *63*, 507–520.
[23] Zhang, H., Kay, A., Forsyth, N. R., Liu, K.-K., El Haj, A. L., Gene expression of single human mesenchymal stem cell in response to fluid shear. *J. Tissue Eng.* 2012, *3*, 2041731412451988.
[24] Toriello, N. M., Douglas, E. S., Thaitrong, N., Hsiao, S. et al., Integrated microfluidic bioprocessor for single-cell gene expression analysis. *Proc. Natl. Acad. Sci. U.S.A.* 2008, *105*, 20173–20178.
[25] Taniguchi, K., Kajiyama, T., Kambara, H., Quantitative analysis of gene expression in a single cell by qPCR. *Nat. Methods* 2009, *6*, 503–506.
[26] Sanchez-Freire, V., Ebert, A. D., Kalisky, T., Quake, S. R., Wu, J. C., Microfluidic single-cell real-time PCR for comparative analysis of gene expression patterns. *Nat. Protoc.* 2012, *7*, 829–838.
[27] Zhang, H. F., Jenkins, G., Zou, Y., Zhu, Z., Yang, C. J., Massively parallel single-molecule and single-cell emulsion reverse transcription polymerase chain reaction using agarose droplet microfluidics. *Anal. Chem.* 2012, *84*, 3599–3606.
[28] Marcus, J. S., Anderson, W. F., Quake, S. R., Microfluidic single-cell mRNA isolation and analysis. *Anal. Chem.* 2006, *78*, 3084–3089.
[29] Ottesen, E. A., Hong, J. W., Quake, S. R., Leadbetter, J. R., Microfluidic digital PCR enables multigene analysis of individual environmental bacteria. *Science* 2006, *314*, 1464–1467.
[30] White, A. K., Heyries, K. A., Doolin, C., VanInsberghe, M., Hansen, C. L., High-throughput microfluidic single-cell digital polymerase chain reaction. *Anal. Chem.* 2013, *85*, 7182–7190.
[31] Lipson, D., Raz, T., Kieu, A., Jones, D. R. et al., Quantification of the yeast transcriptome by single-molecule sequencing. *Nat. Biotechnol.* 2009, *27*, 652–658.
[32] Xue, Z. G., Huang, K., Cai, C. C., Cai, L. B. et al., Genetic programs in human and mouse early embryos revealed by single-cell RNA sequencing. *Nature* 2013, *500*, 593–597.
[33] Tang, F. C., Barbacioru, C., Nordman, E., Li, B. et al., RNA-Seq analysis to capture the transcriptome landscape of a single cell. *Nat. Protoc.* 2010, *5*, 516–535.
[34] Chatre, L., Ricchetti, M., Large heterogeneity of mitochondrial DNA transcription and initiation of replication exposed by single-cell imaging. *J. Cell. Sci.* 2013, *126*, 914–926.
[35] Thompson, D. M., King, K. R., Wieder, K. J., Toner, M. et al., Dynamic gene expression profiling using a microfabricated living cell array. *Anal. Chem.* 2004, *76*, 4098–4103.
[36] Wu, M. Y., Singh, A. K., Single-cell protein analysis. *Curr. Opin. Biotechnol.* 2012, *23*, 83–88.
[37] Waanders, L. F., Chwalek, K., Monetti, M., Kumar, C. et al., Quantitative proteomic analysis of single pancreatic islets. *Proc. Natl. Acad. Sci. U.S.A.* 2009, *106*, 18902–18907.
[38] Luo, Q., Yue, G., Valaskovic, G. A., Gu, Y. et al., On-line 1 D and 2 D porous layer open tubular/LC-ESI-MS using 10-microm-i.d. poly(styrene-divinylbenzene) columns for ultrasensitive proteomic analysis. *Anal. Chem.* 2007, *79*, 6174–6181.
[39] Bandura, D. R., Baranov, V. I., Ornatsky, O. I., Antonov, A. et al., Mass cytometry: Technique for real time single cell multitarget immunoassay based on inductively coupled plasma time-of-flight mass spectrometry. *Anal. Chem.* 2009, *81*, 6813–6822.
[40] Bendall, S. C., Simonds, E. F., Qiu, P., Amir el, A. D. et al., Single-cell mass cytometry of differential immune and drug responses across a human hematopoietic continuum. *Science* 2011, *332*, 687–696.

[41] Huang, B., Wu, H., Bhaya, D., Grossman, A. et al., Counting low-copy number proteins in a single cell. *Science* 2007, *315*, 81–84.

[42] Martino, C., Zagnoni, M., Sandison, M. E., Chanasakulniyom, M. et al., Intracellular protein determination using droplet-based immunoassays. *Anal. Chem.* 2011, *83*, 5361–5368.

[43] Cohen, A. A., Geva-Zatorsky, N., Eden, E., Frenkel-Morgenstern, M. et al., Dynamic proteomics of individual cancer cells in response to a drug. *Science* 2008, *322*, 1511–1516.

[44] Zheng, X. T., Li, C. M., Single living cell detection of telomerase over-expression for cancer detection by an optical fiber nanobiosensor. *Biosens. Bioelectron.* 2010, *25*, 1548–1552.

[45] Bailey, R. C., Kwong, G. A., Radu, C. G., Witte, O. N., Heath, J. R., DNA-encoded antibody libraries: A unified platform for multiplexed cell sorting and detection of genes and proteins. *J. Am. Chem. Soc.* 2007, *129*, 1959–1967.

[46] Shi, Q., Qin, L., Wei, W., Geng, F. et al., Single-cell proteomic chip for profiling intracellular signaling pathways in single tumor cells. *Proc. Natl. Acad. Sci. U.S.A.* 2012, *109*, 419–424.

[47] Ma, C., Fan, R., Ahmad, H., Shi, Q. et al., A clinical microchip for evaluation of single immune cells reveals high functional heterogeneity in phenotypically similar T cells. *Nat. Med.* 2011, *17*, 738–743.

[48] Hinterdorfer, P., Garcia-Parajo, M. F., Dufrene, Y. F., Single-molecule imaging of cell surfaces using near-field nanoscopy. *Acc. Chem. Res.* 2012, *45*, 327–336.

[49] Broger, T., Odermatt, R. P., Huber, P., Sonnleitner, B., Real-time on-line flow cytometry for bioprocess monitoring. *J. Biotechnol.* 2011, *154*, 240–247.

[50] Wang, Y., Chen, Z. Z., Li, Q. L., Microfluidic techniques for dynamic single-cell analysis. *Microchim. Acta* 2010, *168*, 177–195.

[51] Haider, S., Wagner, M., Schmid, M. C., Sixt, B. S. et al., Raman microspectroscopy reveals long-term extracellular activity of Chlamydiae. *Mol. Microbiol.* 2010, *77*, 687–700.

[52] Niu, J. J., Schrlau, M. G., Friedman, G., Gogotsi, Y., Carbon nanotube-tipped endoscope for in situ intracellular surface-enhanced raman spectroscopy. *Small* 2011, *7*, 540–545.

[53] Nemes, P., Rubakhin, S. S., Aerts, J. T., Sweedler, J. V., Qualitative and quantitative metabolomic investigation of single neurons by capillary electrophoresis electrospray ionization mass spectrometry. *Nat. Protoc.* 2013, *8*, 783–799.

[54] Schober, Y., Guenther, S., Spengler, B., Rompp, A., Single cell matrix-assisted laser desorption/ionization mass spectrometry imaging. *Anal. Chem.* 2012, *84*, 6293–6297.

[55] Shrestha, B., Vertes, A., In situ metabolic profiling of single cells by laser ablation electrospray ionization mass spectrometry. *Anal. Chem.* 2009, *81*, 8265–8271.

[56] Behrens, S., Losekann, T., Pett-Ridge, J., Weber, P. K. et al., Linking microbial phylogeny to metabolic activity at the single-cell level by using enhanced element labeling-catalyzed reporter deposition fluorescence in situ hybridization (EL-FISH) and NanoSIMS. *Appl. Environ. Microbiol.* 2008, *74*, 3143–3150.

[57] Cheng, W., Klauke, N., Sedgwick, H., Smith, G. L., Cooper, J. M., Metabolic monitoring of the electrically stimulated single heart cell within a microfluidic platform. *Lab Chip* 2006, *6*, 1424–1431.

[58] Zheng, X. T., Yang, H. B., Li, C. M., Optical detection of single cell lactate release for cancer metabolic analysis. *Anal. Chem.* 2010, *82*, 5082–5087.

[59] Zhao, S., Huang, Y., Liu, Y. M., Microchip electrophoresis with chemiluminescence detection for assaying ascorbic acid and amino acids in single cells. *J. Chromatogr. A* 2009, *1216*, 6746–6751.

[60] Binder, S., Schendzielorz, G., Stabler, N., Krumbach, K. et al., A high-throughput approach to identify genomic variants of bacterial metabolite producers at the single-cell level. *Genome Biol.* 2012, *13*, R40.

Journal of Membrane Science 518 (2016) 273–281

Contents lists available at ScienceDirect

Journal of Membrane Science

journal homepage: www.elsevier.com/locate/memsci

Thermoresponsive cationic copolymer microgels as high performance draw agents in forward osmosis desalination

Yusak Hartanto [a], Masoumeh Zargar [a], Xiaolin Cui [a], Yinghua Shen [b], Bo Jin [a,*], Sheng Dai [a,*]

[a] *School of Chemical Engineering, The University of Adelaide, SA 5005, Australia*
[b] *College of Chemistry & Chemical Engineering, Taiyuan University of Technology, Taiyuan 030024, China*

ARTICLE INFO

Article history:
Received 10 April 2016
Received in revised form
1 June 2016
Accepted 9 July 2016
Available online 16 July 2016

Keywords:
N-isopropylacrylamide
Cationic microgels
Hansen solubility parameters
Forward osmosis
Desalination

ABSTRACT

Thermoresponsive cationic copolymer microgels with aliphatic and aromatic cationic comonomers are synthesized and applied as the draw agents in forward osmosis (FO) desalination for the first time. The results show the FO desalination performance depends on the chemical structures and the dissociation constants (pK_a) of the cationic comonomers. Cationic copolymer microgel containing 2-(diethylamino) ethyl methacrylate has the best overall performance with an initial water flux of 45.6 LMH and water recovery of 44.8%. This microgel also shows the shortest equilibrium swelling time which in turn reveals significant improvement in apparent flux of 5.5 LMH compared to other cationic and anionic copolymer microgels. Furthermore, Hansen solubility parameters are used to correlate the solvation behavior of these cationic microgels and their performance in forward osmosis desalination. Our results show Hansen solubility parameters and the dissociation constants of cationic comonomers can be used to estimate the performance of microgels in microgel-driven FO desalination systems.

1. Introduction

Forward osmosis (FO) is an emerging membrane-based separation process that has the potential to lower energy consumption in desalination process compared to reverse osmosis (RO) process due to the absence of highly applied hydraulic pressure [1]. However, low cost water recovery is the major problem associated with this technology [2]. In order to solve this issue, thermolytic solutes were proposed as the FO draw agents [3,4] due to their phase separation ability at mild temperature. The heating energy can be provided by low grade heat to reduce the overall energy cost. Although this strategy can reduce the energy cost of FO desalination, several drawbacks such as membrane stability [5], membrane scaling [6], final water quality [7] and reverse solute flux [8] still exist which hinder the practical application of these draw agents. In order to overcome the drawbacks of thermolytic solutes, various materials such as linear polymers [9–11], magnetic nanoparticles [12–14], synthetic organic solutes [5,15,16], ionic liquids [17,18] and switchable polarity solvents [19] were proposed as FO draw agents. Although reduced reverse solute flux can be achieved due to their large molecular sizes, these molecules always lead to severe concentration polarization that decreases the performance of these materials in water-drawing process. Furthermore, pressure-driven membrane processes such as ultrafiltration, nanofiltration and reverse osmosis are still required at the water recovery process which might further increases the cost of process [2].

Thermoresponsive polymer hydrogels which are able to reversibly swell and deswell in respond to external temperature change have been recently proposed as effective FO draw agents [20–22]. The absence of reverse solute flux is one of the advantages of using hydrogels as FO draw agents [23]. However, the water flux generated from these hydrogels is much lower than other materials mentioned previously which could be caused by the poor contact between hydrogels and membranes [24,25]. Furthermore, poor liquid water recovery is another problem when bulk hydrogels are used as FO draw agents due to the formation of dense skin during hydrogel deswelling [26]. Although some strategies have been launched to improve the performance of these hydrogels in adsorbing water such as composite hydrogels [25,27–29], semi-interpenetrating network [21] and bifunctional layers formation [30], the water flux generated is still low compared to small molecules as draw materials.

Recently, thermoresponsive copolymer microgels of N-isopropylacrylamide and acrylic acid were proposed as the FO draw agents to overcome the problems associated with thermoresponsive bulk hydrogels [31,32]. Due to their small sizes and large surface areas, these microgels promote better contact with membranes, which results in significant improvement in water flux performance. Furthermore, the amount of acrylic acid plays an

---

* Corresponding authors.
E-mail addresses: bo.jin@adelaide.edu.au (B. Jin), s.dai@adelaide.edu.au (S. Dai).

http://dx.doi.org/10.1016/j.memsci.2016.07.018
0376-7388/© 2016 Published by Elsevier B.V.

important role on water flux and dewatering performance. Although there was improvement in water flux, the swelling kinetics of those microgels is still low which will impact the overall performance of the microgels. Therefore, improving the swelling kinetics of microgels is needed to achieve high apparent water flux.

A study investigating the FO performance of cationic polyelectrolytes of poly 2-(dimethylamino) ethyl methacrylate demonstrated that these polyelectrolytes were able to generate very high osmolality compared to weak acidic polyelectrolytes such as polyacrylic acid [9] in their protonated state [33]. In this paper, we prepared a series of thermoresponsive cationic copolymer microgels and applied them as FO draw agents for the first time. Our results show the FO performance of these cationic microgels depends on the chemical structures of cationic comonomers and their dissociation constants (pK_a). Microgels with aliphatic cationic comonomers show higher water flux than those with aromatic cationic comonomers and the opposite behavior is observed in dewatering process. Copolymer microgel with 2-(diethylamino) ethyl methacrylate as a cationic comonomer shows the highest water flux and the fastest equilibrium swelling kinetics among other cationic copolymer microgels.

2. Experimental section

2.1. Materials

N-Isopropylacrylamide (NP, >98%), purchased from Tokyo Chemical Industry, was purified by recrystallization using n-hexane and dried overnight at room temperature. N-N′-methylenebisacrylamide (BIS, >98%), 2-(dimethylamino) ethyl methacrylate (DMAEMA, 98%), 2-(diethylamino) ethyl methacrylate (DEAEMA, 99%) and 4-vinylpyridine (VP, 95%) were purchased from Sigma-Aldrich. 1-vinylimidazole (VI, 99%) was purchased from VWR International. 2,2′-Azobis (2-methylpropionamidine dihydrochloride (V-50) was purchased from Novachem, Australia. Sodium chloride was purchased from VWR. Cellulose triacetate forward osmosis (CTA-FO) membranes were purchased from Hydration Technologies Inc. (HTI, USA).

2.2. Synthesis of cationic thermoresponsive copolymer microgels

Different thermoresponsive cationic copolymer microgels were synthesized using surfactant-free semi-batch emulsion polymerization. In a typical experiment, 0.735 g of NP, 0.015 g of cationic comonomer, 0.0075 g of BIS and 75 mL of DI water were mixed in a 250 mL three-necked flask fitted with a condenser, a mechanical stirrer and gas inlet and outlet. The semi-batch feeding solution was prepared by dissolving 2.205 g of NP, 0.045 g of cationic comonomer and 0.0225 g of BIS in 45 mL of DI water. After degassing the solution for 45 min with nitrogen, the three-necked flask was immersed into a preheated oil bath at 70 °C under nitrogen protection and a 3 mL of V-50 aqueous solution (0.03 g) was injected to the flask to start the polymerization. The feeding solution was injected at a rate of 3 mL/hour using a syringe pump one hour after the batch solution turned cloudy. The polymerization was carried out overnight under continuous stirring and nitrogen protection. After cooling, the microgels were purified using membrane dialysis (MWCO 12–14 kDa) against DI water for several days to remove any unreacted compounds. Finally, the purified microgels were dried at 65 °C and grounded into fine powders. The nomenclature used in this study is MCG-Monomer I-Monomer II.

2.3. Characterization of thermos-responsive cationic microgels

2.3.1. Dynamic light scattering and zeta potential measurements

The hydrodynamic diameters (d_h) of the cationic microgels at different temperatures (20–50 °C) and their zeta potentials at pH ~6.8 and 20 °C were measured using a Zetasizer (Malvern, Nano-ZS). The swelling ratios (SR) of microgels are calculated using the following equation:

$$SR = \left(\frac{d_{h,To}}{d_{h,Ti}}\right)^3 \tag{1}$$

where SR is the swelling ratio of the microgel, $d_{h,\ To}$ (nm) is the hydrodynamic diameter of the microgel at To °C (20 °C) and $d_{h,\ Ti}$ (nm) is the hydrodynamic diameter of the microgels at Ti °C.

2.3.2. Conductometric and potentiometric titration

The amounts of functional cationic comonomers in the microgels were determined using conductometric and potentiometric titration. Typically, the pH of a 100 mL MCG-NP-DMAEMA microgel dispersion (~1 mg/mL) was adjusted to 3 using concentrated hydrochloric acid. The solution was then back titrated using a 0.1 M NaOH solution. After each addition of NaOH, the conductivity and pH of the solution were measured using a pre-calibrated Aqua-CP/A pH and conductivity meter.

2.4. Forward osmosis desalination evaluation

2.4.1. Water flux evaluation

100 mg dried microgel was loaded in a homemade FO membrane setup equipped with an on-line conductivity monitoring system [31]. The membrane configuration adopted in this experiment was the active layer facing draw solute (AL-DS). The active membrane area is 3.16 cm^2. A conductivity probe (probe cell constant, k=1.0) was immersed in the feed solution of 2000 ppm NaCl to continuously monitor the change in conductivity of the feed solution against time for two hours. The system was conditioned by immersing the membrane in the feed solution for 30 min before loading the microgels on the membrane. The conductivity data was converted into the concentration of sodium chloride in the feed solution through a calibration curve. The water flux is calculated using the concentration data based on the following equations:

$$V_t = \frac{C_i V_i}{C_t} \tag{2}$$

$$J_w = \frac{V_i - V_t}{A\ \Delta t} \tag{3}$$

where V_t (mL) is the volume of feed at time t, V_i (mL) is the initial volume of feed, C_i (ppm) is the initial feed concentration, C_t (ppm) is the feed concentration at time t, J_w (LMH) is the water flux, A (m^2) is the effective membrane surface area and Δt (h) is the time interval where the conductivity of the feed solution changes.

2.4.2. Water recovery

Water-saturated microgels were transferred to centrifuge tubes and weighed after two-hour water adsorption period. The microgels were then centrifuged at 40 °C and 10,000 rpm for 10 min to separate adsorbed water from the microgels. The recovered water was measured using gravimetric method. The water recovered from the deswelled microgels was calculated using the following equations:

$$C_p = \frac{W_d}{W_d + W_w} \tag{4}$$

$$W_g = W_m(1 - C_p) \tag{5}$$

$$R = \frac{W_R}{W_g} x100\% \tag{6}$$

where C_p (g microgels/g water) is the concentration of microgels in the centrifuge tube, W_d (g) is the weight of dry microgel, W_w (g) is the weight of water adsorbed by the microgels calculated from water flux data, W_g (g) is the weight of water in the microgels, W_m (g) is the weight of microgels in the centrifuge tube, W_R (g) is the weight of adsorbed water recovered from the tube and R (%) is the percentage of water recovered from the microgels.

2.4.3. Apparent water flux

Apparent water flux is defined as the amount of water that can be released from the microgels per unit area per unit cycling time and written as follows [23]:

$$J_{app} = \frac{m_W}{(T_{eq} + T_R)A} \tag{7}$$

where J_{app} (LMH) is the apparent water flux, m_W (L) is the volume of water that can be released during dewatering process, T_{eq} (h) is the time needed to reach equilibrium condition, T_R (h) is the time needed to dewater the microgels and A (m^2) is the effective membrane area.

2.4.4. Microgel recycling evaluation

The evaluation of microgel reusability was evaluated using the method published elsewhere [27]. The microgels were removed from the membrane setup and dried in oven until constant weight after the first evaluation. The dried microgels were grounded into fine powders and placed again on the membrane for the second cycle measurement, where the conductivities of feed solution against time were recorded to calculate water flux. The same approach was repeated for the subsequent cycles. The water recovery cycle measurement was conducted using similar fashion using gravimetric method.

2.5. Hansen solubility parameter (HSP) analysis

The solubility parameter components predicted using group contributions can be calculated using the following equations:

$$\delta_d = \frac{\sum F_{di}}{V} \tag{8}$$

$$\delta_p = \frac{\sqrt{\sum F_{pi}^2}}{V} \tag{9}$$

$$\delta_h = \sqrt{\frac{\sum E_{hi}}{V}} \tag{10}$$

$$\delta_{total} = \sqrt{\delta_d^2 + \delta_p^2 + \delta_h^2} \tag{11}$$

where δ_d ($MPa^{1/2}$) is the dispersion interaction parameter, F_{di} ($[MJ/m^3]^{1/2} \cdot mol^{-1}$) is molar attraction constant for the dispersion component, δ_p ($MPa^{1/2}$) is the polar interaction parameter, F_{pi} ($[MJ/m^3]^{1/2} \cdot mol^{-1}$) is the group contribution constant for the polar component, δ_h ($MPa^{1/2}$) is the hydrogen bonding interaction parameter, E_{hi} ($J \cdot mol^{-1}$) is the hydrogen bonding energy, V (cm^3/mol) is the molar volume and δ_{total} ($MPa^{1/2}$) is overall value of the solubility parameter.

The distance of solubility parameter, relative energy difference (RED) and ratio of cohesion energy densities (H), can be calculated using the following equations [34]:

$$(R_a)^2 = 4(\delta_{d2} - \delta_{d1})^2 + (\delta_{p2} - \delta_{p1})^2 + (\delta_{h2} - \delta_{h1})^2 \tag{12}$$

$$RED = \frac{R_a}{R_o} \tag{13}$$

$$RA = \frac{R_a}{2}; R_M = \frac{R_o}{2} \tag{14}$$

$$H = \left(\frac{RA}{R_M}\right)^2 \tag{15}$$

where R_a ($MPa^{1/2}$) is a modified difference between HSP for water (1) and monomer (2). R_o ($MPa^{1/2}$) is the radius of interaction of an HSP solubility sphere.

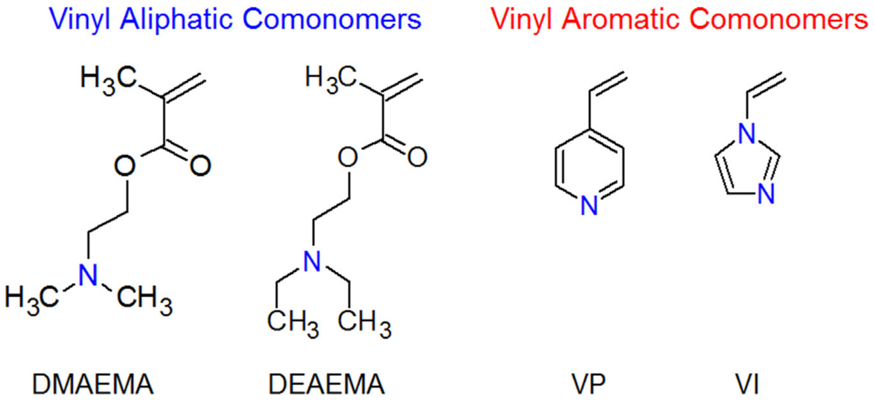

Fig. 1. Chemical structures of different cationic comonomers used in synthesized cationic copolymer microgels.

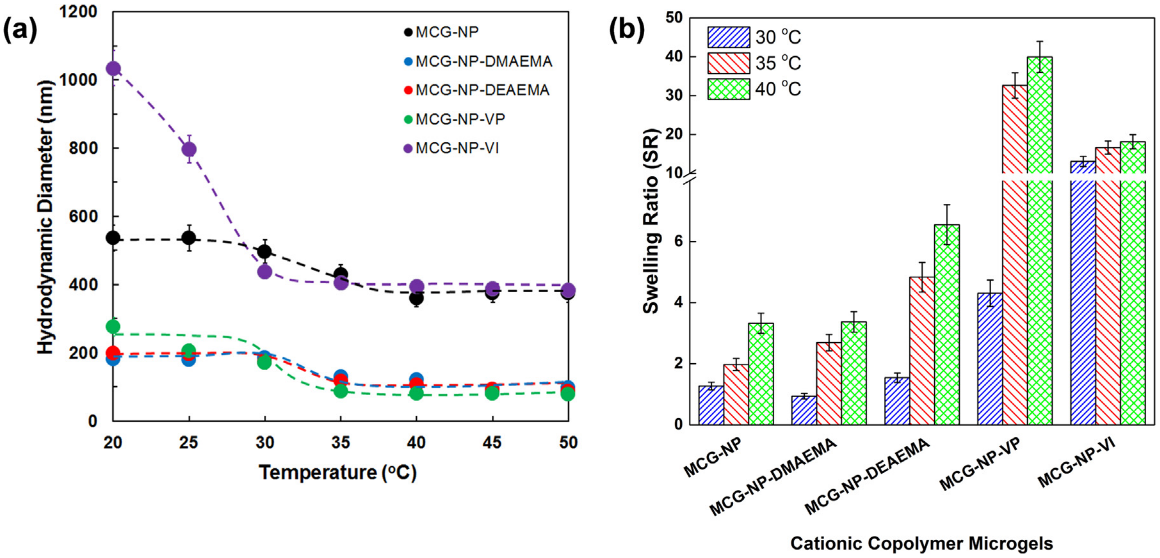

Fig. 2. (a) Hydrodynamic diameters of thermoresponsive microgels at different temperatures and pH 6.8; (b) Swelling ratios of cationic thermoresponsive microgels at 30 °C, 35 °C and 40 °C at pH 6.8.

Table 1
Dissociation constants (pKa) of different cationic comonomers.

Cationic comonomers	pK_a	Ref.
DMAEMA	8.40	[40]
DEAEMA	9.50	[41]
VP	5.39	[38]
VI	6.95	[42]

3. Results and discussions

3.1. Synthesis and characterization of thermoresponsive cationic copolymer microgels

Thermoresponsive cationic copolymer microgels were prepared via semi-batch surfactant-free emulsion polymerization to eliminate the influence of surfactants on final physicochemical properties of these microgels. The comonomer feed ratio used in this study was 2 wt% because excessive amount of ionic moieties will eliminate the thermoresponsive properties of the microgels [31]. The initial pH of the reaction mixture was adjusted to ~4 to partially protonate the cationic comonomer, which assists particle stabilization [35]. After the synthesis, the microgels were transferred to dialysis bags for purification before characterization and evaluation studies. We choose two different groups of cationic comonomers shown in Fig. 1, vinyl aliphatic and vinyl aromatic comonomers, in this study to examine the effect of different chemical structures of cationic comonomers on the FO performance.

Dynamic light scattering measurements were performed to determine the apparent diameters of the microgels at different temperatures and their volume phase transition temperatures (VPTTs). Cationic N-isopropylacrylamide microgel was also synthesized as a control to compare its swelling/deswelling behavior with other cationic copolymer microgels. Fig. 2a shows the hydrodynamic diameters of various cationic copolymer microgels as a function of temperature. The incorporation of different cationic comonomers shifts the VPTTs of resulting cationic microgels due to the different degrees of ionization of cationic comonomers indicated by their different pK_a values [36]. The pK_a of different cationic comonomers used in this study is shown in Table 1. Copolymerization with vinyl aliphatic comonomers leads to the less shift of the VPTTs to lower temperature than those with vinyl aromatic comonomers due to the stronger solvation [37] of these aliphatic comonomers than aromatic counterparts [38,39].

Swelling ratios of the cationic microgels at specific temperatures near their VPTTs are shown in Fig. 2b. MCG-NP-DMAEMA has the lowest swelling ratio among other cationic microgels at 30 °C. However, the swelling ratio of this microgel is slightly higher than the swelling ratio of MCG-NP at 35 °C and 40 °C. Furthermore, the swelling ratio of MCG-NP-DEAEMA is higher at all temperatures than that of MCG-NP and MCG-NP-DMAEMA due to hydrophobic characteristic of PDEAEMA [41]. On the other hand, the cationic copolymer microgels with vinyl aromatic comonomers show higher swelling ratios than the cationic microgels with vinyl aliphatic comonomers at all temperatures due to the increase in hydrophobicity. MCG-NP-VP shows remarkable swelling ratio at 40 °C due to the hydrophobic characteristic of this comonomer at its deprotonated state [43] while MCG-NP-VI microgels have slightly lower swelling ratio than MCG-NP-VP at 40 °C due to slight protonation of its tertiary amines.

The incorporation of cationic comonomers into copolymer microgels can be characterized qualitatively and quantitatively using pH and conductivity titrations. The highlighted areas in Fig. S1 showing the presence of tertiary amines confirm the successful incorporation of cationic comonomers in the microgels. The calculated amounts of tertiary amines in the microgels determined from pH and conductivity titration shown in Table S1 are close to the feeding amounts indicating high conversion of these comonomers (80–90%). In addition, zeta potential measurements at 20 °C and pH ~6.8 were also carried out to elucidate the surface charges of cationic microgels and to further confirm the presence of cationic comonomers in the microgels. The values of zeta potential measurements for each cationic microgel in Fig. S3 show cationic copolymer microgels have higher zeta potentials than cationic N-isopropylacrylamide microgel except for the MCG-NP-VP due to its deprotonated state at pH ~6.8.

3.2. Water flux and water content profiles for thermoresponsive cationic copolymer microgels

Water flux and water content profiles for each thermoresponsive cationic microgel are shown in Fig. 3. Incorporation of

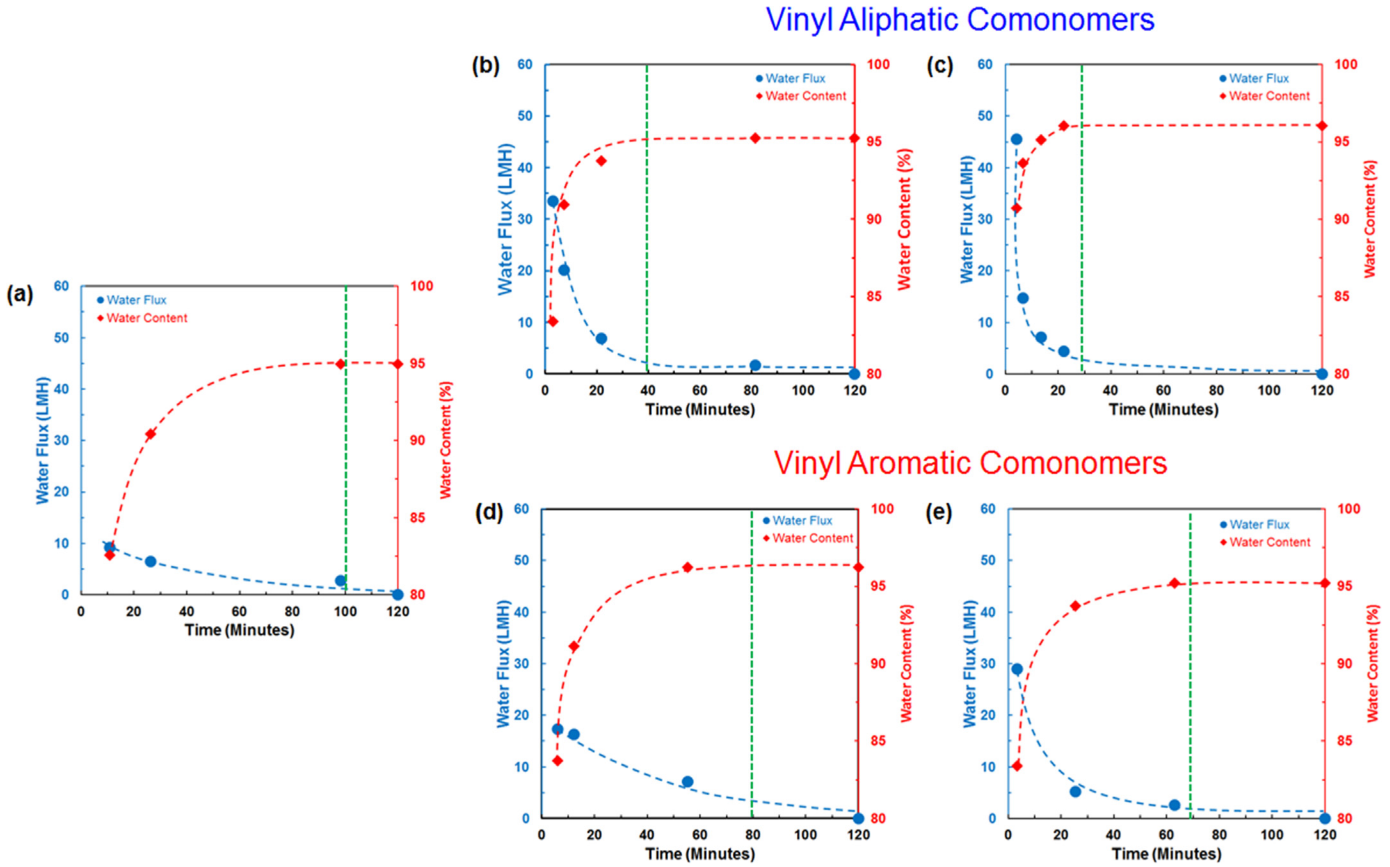

Fig. 3. Water flux and water content profiles of different cationic co-polymer thermoresponsive microgels: (a) MCG-NP, (b) MCG-NP-DMAEMA, (c) MCG-NP-DEAEMA, (d) MCG-NP-VP and (e) MCG-NP-VI, during two-hour water adsorption period. Feed solution is 2000 ppm NaCl and the room temperature was maintained at 20 ± 1 °C. The green vertical lines show the time needed to reach equilibrium water content (T_{eq}). (For interpretation of the references to color in this figure legend, the reader is referred to the web version of this article.)

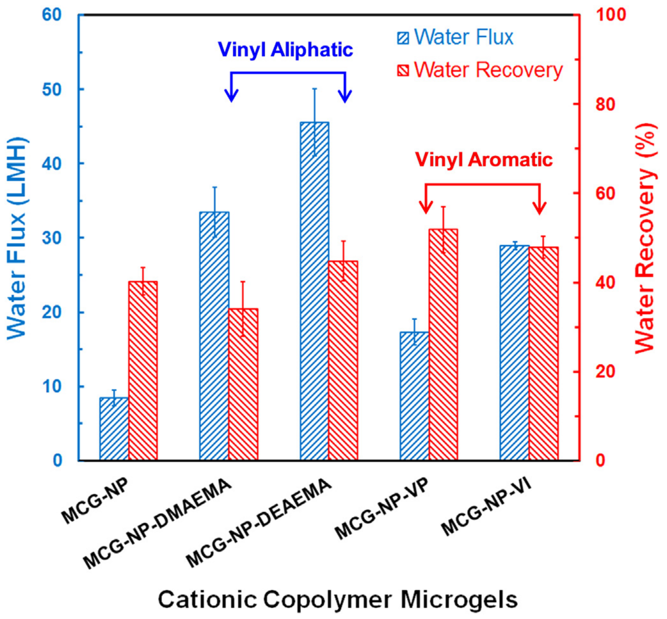

Fig. 4. Initial water flux and water recovery for different cationic thermoresponsive co-polymer microgels. Feed solution concentration is 2000 ppm, pH of the feed solution is 6.8 and the feed temperature is 20 ± 1 °C.

different cationic comonomers leads to varied water adsorption rates, water contents and equilibrium swelling time. MCG-NP-DMAEMA shows faster equilibrium swelling time and higher water flux than MCG-NP due to improved solvation behavior of this microgel caused by the tertiary amines. The equilibrium swelling times for MCG-NP-DMAEMA and MCG-NP are 40 min and 100 min, respectively. Furthermore, the shortest equilibrium swelling time (30 min) and highest water flux are observed in MCG-NP-DEAEMA due to its highest pK_a in Table 1 which results in strong solvation behavior of this copolymer microgel.

On the other hand, cationic microgels with vinyl aromatic comonomers have lower water flux than those with vinyl aliphatic comonomers due to the presence of aromatic ring which contributes to solvation interaction of the microgels [44]. In addition, the increase in hydrophobicity also results in longer equilibrium swelling time in these microgels than the microgels with vinyl aliphatic comonomers. The equilibrium swelling time for MCG-NP-VP (80 min) is longer than MCG-NP-VI (70 min) due to hydrophobic characteristic of 4-vinylpyridine in its deprotonated state [45]. The shorter equilibrium swelling time in MCG-NP-VI is caused by the stronger solvation of this microgel than MCG-NP-VP as indicated by its higher pK_a value in Table 1.

The final water content of MCG-NP-DEAEMA is higher than the final water contents of MCG-NP-DEAEMA and MCG-NP. Similar result is also observed in microgels with aromatic comonomers where MCG-NP-VP had slightly higher final water content than MCG-NP-VI despite the hydrophobic characteristic of VP in its deprotonated state. This phenomenon can be explained by the microphase separation during the polymerization when slightly hydrophobic comonomers such as DEAEMA and VP are introduced during polymerization process. This results in MCG-NP-DEAEMA and MCG-NP-VP have less compact structures which cause these copolymer microgels retain more water than MCG-NP-DMAEMA and MCG-NP-VI [46,47].

3.3. Initial water flux and water recovery of thermoresponsive cationic copolymer microgels

The initial water flux and water recovery for various cationic thermoresponsive microgels are shown in Fig. 4. MCG-NP has the lowest water flux (8.5 LMH) among other cationic copolymer microgels while its water recovery is 40.2%. This water recovery is lower than the previously synthesized anionic N-isopropylacrylamide microgel [31] which can be caused by the strong hydrogen bonding between water and the primary and secondary amines from 2,2′-azobis(2-methylpropioaminidine dihydrochloride) [48]. MCG-NP-DMAEMA and MCG-NP-DEAEMA show higher water fluxes than MCG-NP due to the contribution of protonated tertiary amines from the cationic comonomers. However, the water flux for MCG-NP-DEAEMA is higher than MCG-NP-DMAEMA due to the presence of more tertiary amines in MCG-NP-DEAEMA than MCG-NP-DMAEMA which results in higher osmotic pressure in MCG-NP-DEAEMA than MCG-NP-DMAEMA. The water fluxes for MCG-NP-DMAEMA and MCG-NP-DEAEMA are 33.5 LMH and 45.6 LMH, respectively while their water recovery are 34.1% and 44.8%, respectively. The higher water recovery in MCG-NP-DEAEMA could be from the more hydrophobic character of DEAEMA. In addition, high swelling ratio of MCG-NP-DEAEMA above the VPTT shown in Fig. 2 confirms the higher water recovery in MCG-NP-DEAEMA than MCG-NP-DMAEMA [41].

On the other hand, MCG-NP-VP microgel shows reduced water flux (17.3 LMH) but improved water recovery due to its deprotonated tertiary amines which results in strong hydrophobic properties from the aromatic ring dominates the physicochemical properties of the microgel. The water recovery of MCG-NP-VP microgel is 51.9%. Interestingly, MCG-NP-VI microgel shows higher water flux (28.9 LMH) than MCG-NP-VP despite the presence of aromatic ring structure in this comonomer. However, its water flux is less than MCG-NP-DMAEMA and MCG-NP-DEAEMA due to the lower pK_a value of this comonomer which results in low amount of protonated tertiary amines for this microgel [42]. The water recovery of MCG-NP-VI (47.9%) is comparable with that observed in MCG-NP-VP implying this microgel has balanced water flux and water recovery performance.

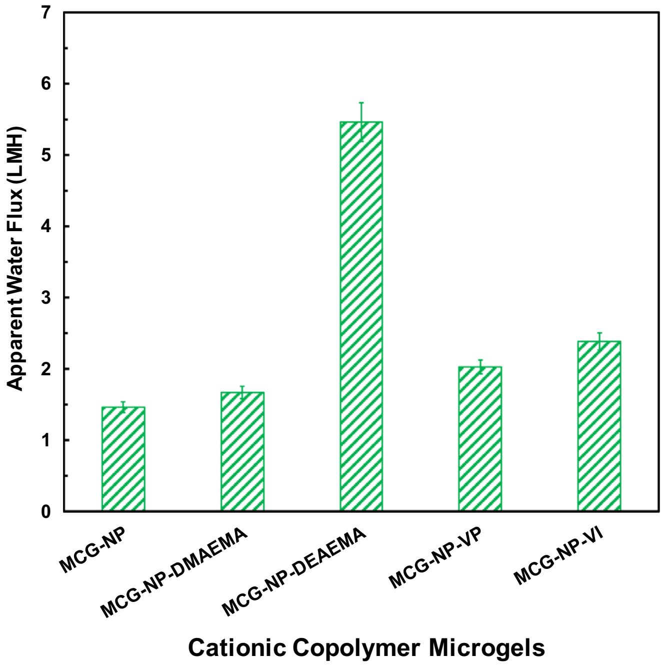

Fig. 5. Apparent water fluxes of different thermoresponsive cationic copolymer microgels.

3.4. Apparent water flux of thermoresponsive cationic copolymer microgels

Apparent water flux can be used to measure the overall performance of microgel-driven FO desalination. This variable measures the amount of water per unit time that can be recovered from the microgel at one cycle [23]. The apparent water fluxes for thermoresponsive cationic copolymer microgels are shown in Fig. 5. The apparent water flux of MCG-NP is 1.5 LMH which is the

Table 2
Comparison of FO draw agents for different polymer hydrogels.

Polymer hydrogels	Experimental Conditions	FO performance		Ref.
		Flux	Water recovery	
N-Isopropylacrylamide-*co*-2-(diethylamino) ethyl methacrylate microgels	PRO Mode Feed: 2000 ppm NaCl Draw Mass: 0.1 g	45.6 LMH	44.8%	This work
N-Isopropylacrylamide-*co*-itaconic acid microgels	PRO Mode Feed: 2000 ppm NaCl Draw Mass: 0.1 g	44.8 LMH	47.2%	[32]
N-Isopropylacrylamide-*co*-acrylic acid microgels	PRO Mode Feed: 2000 ppm NaCl Draw Mass: 0.1 g	23.8 LMH	52%	[31]
Semi-interpenetrating network poly(N-isopropylacrylamide) and polyvinyl alcohol	Feed: 2000 ppm NaCl Draw Mass: 0.4 g	0.24 LMH	98%	[21]
N-Isopropylacrylamide-*co*-sodium acrylate hydrogels	PRO Mode Feed: 2000 ppm NaCl Draw Mass: 1 g	0.60 LMH	62%	[20]
Tributylhexylphosphonium p-styrenesulfonate hydrogels	PRO Mode Feed: 2000 ppm NaCl Draw Mass: 0.6 g	2 LMH	50%	[23]
Tributyl-4-vinylbenzylphosphonium hydrogels	PRO Mode Feed: 2000 ppm NaCl Draw Mass: 0.04 g	0.30 LMH	80%	[49]

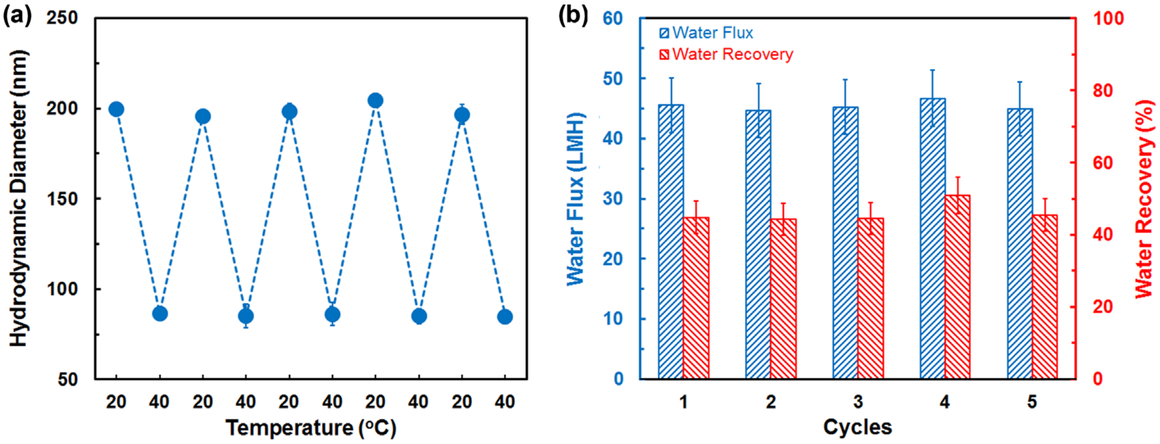

Fig. 6. (a) Swelling – deswelling cycles for MCG-NP-DEAEMA and (b) Water flux and water recovery cycles for MCG-NP-DEAEMA.

lowest among other cationic copolymer microgels due to its low water adsorption and water recovery. Incorporating DMAEMA and DEAEMA into the microgels improves their apparent fluxes due to improved water flux and recovery performance. The apparent water flux of MCG-NP-DMAEMA and MCG-NP-DEAEMA are 1.7 LMH and 5.5 LMH, respectively. The apparent flux of MCG-NP-DEAEMA is significantly higher than MCG-NP-DMAEMA due to its faster equilibrium swelling time and higher water recovery than MCG-NP-DMAEMA.

Although MCG-NP-VP and MCG-NP-VI have higher water recovery than MCG-NP-DEAEMA, their apparent fluxes are lower than MCG-NP-DEAEMA due to their long equilibrium swelling time. The apparent water fluxes of MCG-NP-VP and MCG-NP-VI are 2.0 LMH and 2.4 LMH, respectively. Therefore, MCG-NP-DEAEMA has the best overall performance among other cationic copolymer microgels due to its fast equilibrium swelling times and relatively high water recovery. Furthermore, the apparent water flux of this microgel is significantly higher than bulk hydrogels published in the literature [23,32]. Table 2 summarizes the performance of different polymer hydrogels as FO draw agents.

3.5. Swelling – deswelling cycles and recyclability of thermo-responsive cationic copolymer microgels

The microgel recycling test was conducted to assess the recyclability performance of our thermoresponsive cationic copolymer microgels. We choose to study the recyclability of MCG-NP-DEAEMA as this microgel has the best apparent water flux. Swelling – deswelling cycles conducted using dynamic light scattering by cycling the temperatures of the microgel solution shows that this microgel is fully swellable and deswellable as shown in Fig. 6a. The water flux and water recovery tests were also carried out to confirm the reusability of this microgel following dynamic light scattering study. The cycles of water flux and water recovery shown in Fig. 6b confirm that this microgel is able to maintain its water flux and water recovery performance.

3.6. Relationship between the performance of cationic copolymer microgels in FO desalination and their Hansen solubility parameters

To gain insight on microgel – water interaction, we calculated the Hansen solubility parameters for the monomer and comonomers used in this study. This will assist in designing which monomer/comonomer pair that will lead to optimized FO performance in the future. Hansen solubility parameters consist of three terms, the dispersion, δ_d, polar, δ_p, and hydrogen bonding, δ_h, interaction parameters [34]. The values of individual parameter can be determined directly from experimental data or numerical estimation. Estimation using group contribution method such as the Hoftyzer – Van Kreleven method has reasonable accuracy for most polymer – solvent systems [50]. The calculated values of Hansen solubility parameters using the Hoftyzer – Van Krevelen method are presented in Table 3.

Table 3
Hansen solubility parameters of water and various monomer and comonomer used in this study predicted using Hoftyzer – Van Krevelen method.

Chemical species	δ_d (MPa)$^{1/2}$	δ_p (MPa)$^{1/2}$	δ_h (MPa)$^{1/2}$	δ_{total} (MPa)$^{1/2}$
Water[a]	18.1	12.9	15.5	27.1
NP	16.7	7.8	7.0	19.7
DMAEMA	14.3	7.0	7.7	18.4
DEAEMA	14.7	5.9	7.1	17.9
VP	13.3	7.4	6.8	17.6
VI	13.0	12.5	10.5	21.7

[a] The values were obtained from ref. [34].

The simple way to determine whether a molecule can dissolve in a given solvent is by looking at the difference between total solubility parameter, δ_{total}. This difference must be small enough for the molecule to dissolve in a given solvent. From Table 3, the differences between δ_{total} for water and δ_{total} for all monomers are quite large. For example, the difference between δ_{total} for water and δ_{total} for NP is 7.4 while it is known that water is a good solvent for poly(N-isopropylacrylamide) at the temperature below the lower critical solution temperature (LCST) of this homopolymer [51]. As a result, this approach cannot be used to determine the solubility behavior of the monomers in water.

To determine the monomer – water interaction, plotting the dispersion solubility parameter, δ_d, vs. the sum of polar and hydrogen bonding component, $(\delta_p^2+\delta_h^2)^{1/2}$ allows us to further examine the water affinity towards individual monomers [52]. As can be seen from Fig. 7, VI has the closest distance to water among other comonomers which means that this monomer can be solvated easily while DMAEMA has further distance from NP and water. Furthermore, DEAEMA and VP have less interaction with water as evidenced by their further distance from water than DMAEMA and VI.

The distance in Fig. 7 can be measured quantitatively using relative energy difference (RED) and cohesion energy density (H) parameters calculated using Eqs. (12)–(15). The values of RED and H of N-isopropylacrylamide and various cationic comonomers are summarized in Table 4. It can be seen that all the values of RED and H for the monomers used in this study are less than 1 except for VP which implies that all the microgels are water swellable. VP

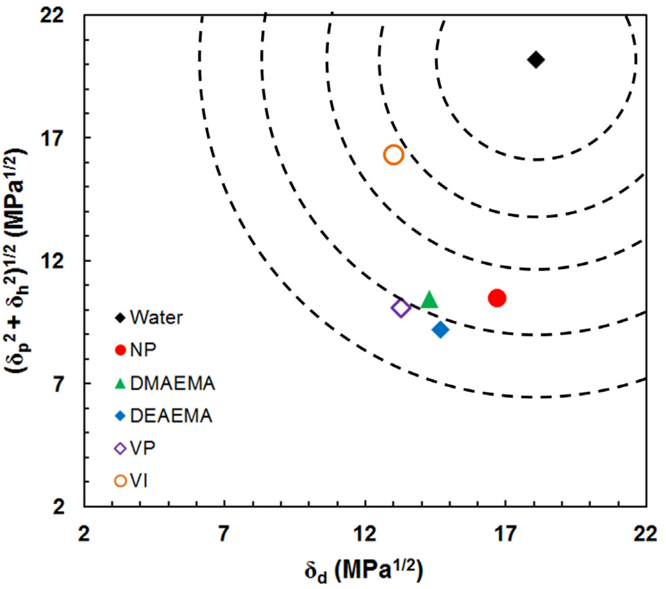

Fig. 7. Hansen solubility plot for determining water affinity toward N-Isopropylacrylamide and cationic comonomers. The dotted lines are the guided lines as a measure of the radial distance of the monomers from water.

Table 4
The solubility distance parameter (Ra), relative energy difference (RED) parameter and the cohesion energy densities (H) parameter of monomer/co-monomer with water.

Monomer/comonomer – water	Ra	RED	H
NP – water	10.3	0.74	0.55
DMAEMA – water	12.4	0.89	0.79
DEAEMA – water	12.9	0.93	0.87
VP – water	14.1	1.01	1.03
VI – water	11.3	0.81	0.66

has the largest values of RED and H which means that this comonomer is close to the boundary of Hansen solubility space and has more hydrophobic character than other monomers.

The analysis of Hansen solubility parameter is generally aligned with the observed FO performance of thermoresponsive cationic copolymer microgels in this work. In detail, MCG-NP-VP shows improved water recovery but less water flux compared to other cationic copolymer microgels due to the high values of RED and H for VP which indicates very weak interaction between water and this microgel. Furthermore, the smallest value of hydrogen bonding interaction parameter (δ_h) of VP in Table 3 further confirms the weak interaction of this comonomer with water. In contrast, VI has smaller values of RED and H than VP which means that MCG-NP-VI has better water interaction than MCG-NP-VP. This analysis is in agreement with the higher water flux generated by MCG-NP-VI than MCG-NP-VP.

On the other hand, microgels with vinyl aliphatic comonomers, MCG-NP-DEAEMA and MCG-NP-DMAEMA, generated higher water flux than MCG-NP despite their relatively high RED and H values. This means the protonation of tertiary amines also plays a key role in determining water flux performance of cationic microgels as discussed in previous section. However, the contribution of RED and H values for these microgels is more significant during the deswelling process where the higher amount of water can be recovered in MCG-NP-DEAEMA than MCG-NP-DMAEMA. This means the interaction of water with DEAEMA is weaker than the water interaction with DMAEMA above the VPTTs of these cationic copolymer microgels. These results also confirm the swelling ratio of MCG-NP-DEAEMA is higher than the swelling ratio of MCG-NP-DMAEMA above the phase transition temperature as shown in Fig. 2.

4. Conclusions

Thermoresponsive cationic copolymer microgels with different cationic comonomers have been synthesized and used as draw agents for forward osmosis desalination. The FO performance of these cationic microgels strongly depends on the chemical structures of the cationic comonomers and the dissociation constants (pK_a). Furthermore, short equilibrium time can be achieved by microgel with 2-(diethylamino) ethyl methacrylate due to its balanced performance in water flux and water recovery which makes this microgel has the highest overall performance among other cationic copolymer microgels. We also carry out in-depth analysis of the relationship between Hansen solubility parameters for each monomer and the FO performance of these microgels. Our results show Hansen solubility parameters and the dissociation constants (pK_a) of cationic comonomers have contribution to the FO performance of the cationic copolymer microgels in water flux and water recovery. This study might assist in designing optimized microgel materials that will lead to optimized microgel-driven FO desalination performance.

Acknowledgement

The authors would like to thank the financial support from the Australian Research Council, Australia (DP110102877). YH would like to appreciate the support of Adelaide Graduate Research Scholarships (AGRS). SD and YS would like to acknowledge the International Scientific & Technological Cooperation Project in Shanxi Province (2014081007-2).

Appendix A. Supplementary material

Supplementary data associated with this article can be found in the online version at http://dx.doi.org/10.1016/j.memsci.2016.07.018.

References

[1] B.D. Coday, P. Xu, E.G. Beaudry, J. Herron, K. Lampi, N.T. Hancock, T.Y. Cath, The sweet spot of forward osmosis: Treatment of produced water, drilling wastewater, and other complex and difficult liquid streams, Desalination 333 (2014) 23–35.

[2] D.L. Shaffer, J.R. Werber, H. Jaramillo, S. Lin, M. Elimelech, Forward osmosis: where are we now? Desalination 356 (2015) 271–284.

[3] J.R. McCutcheon, R.L. McGinnis, M. Elimelech, A novel ammonia—carbon dioxide forward (direct) osmosis desalination process, Desalination 174 (2005) 1–11.

[4] C. Boo, Y.F. Khalil, M. Elimelech, Performance evaluation of trimethylamine–carbon dioxide thermolytic draw solution for engineered osmosis, J. Membr. Sci. 473 (2015) 302–309.

[5] M. Noh, Y. Mok, S. Lee, H. Kim, S.H. Lee, G.-w Jin, J.-H. Seo, H. Koo, T.H. Park, Y. Lee, Novel lower critical solution temperature phase transition materials effectively control osmosis by mild temperature changes, Chem. Commun. 48 (2012) 3845–3847.

[6] Z. Li, R. Valladares Linares, S. Bucs, C. Aubry, N. Ghaffour, J.S. Vrouwenvelder, G. Amy, Calcium carbonate scaling in seawater desalination by ammonia–carbon dioxide forward osmosis: mechanism and implications, J. Membr. Sci. 481 (2015) 36–43.

[7] Q.C. Ge, M.M. Ling, T.S. Chung, Draw solutions for forward osmosis processes: developments, challenges, and prospects for the future, J. Membr. Sci. 442 (2013) 225–237.

[8] L. Chekli, S. Phuntsho, J.E. Kim, J. Kim, J.Y. Choi, J.-S. Choi, S. Kim, J.H. Kim, S. Hong, J. Sohn, H.K. Shon, A comprehensive review of hybrid forward osmosis systems: performance, applications and future prospects, J. Membr. Sci. 497 (2016) 430–449.

[9] Q. Ge, J. Su, G.L. Amy, T.-S. Chung, Exploration of polyelectrolytes as draw solutes in forward osmosis processes, Water Res. 46 (2012) 1318–1326.
[10] R. Ou, Y. Wang, H. Wang, T. Xu, Thermo-sensitive polyelectrolytes as draw solutions in forward osmosis process, Desalination 318 (2013) 48–55.
[11] E. Tian, C. Hu, Y. Qin, Y. Ren, X. Wang, X. Wang, P. Xiao, X. Yang, A study of poly (sodium 4-styrenesulfonate) as draw solute in forward osmosis, Desalination 360 (2015) 130–137.
[12] Q. Zhao, N. Chen, D. Zhao, X. Lu, Thermoresponsive magnetic nanoparticles for seawater desalination, ACS Appl. Mater. Interfaces 5 (2013) 11453–11461.
[13] Y. Na, S. Yang, S. Lee, Evaluation of citrate-coated magnetic nanoparticles as draw solute for forward osmosis, Desalination 347 (2014) 34–42.
[14] P. Dey, E.L. Izake, Magnetic nanoparticles boosting the osmotic efficiency of a polymeric FO draw agent: Effect of polymer conformation, Desalination 373 (2015) 79–85.
[15] M.L. Stone, A.D. Wilson, M.K. Harrup, F.F. Stewart, An initial study of hexavalent phosphazene salts as draw solutes in forward osmosis, Desalination 312 (2013) 130–136.
[16] Q. Long, G. Qi, Y. Wang, Synthesis and application of ethylenediamine tetrapropionic salt as a novel draw solute for forward osmosis application, AIChE J. 61 (2015) 1309–1321.
[17] Y. Zhong, X. Feng, W. Chen, X. Wang, K.W. Huang, Y. Gnanou, Z. Lai, Using UCST ionic liquid as a draw solute in forward osmosis to treat high-salinity water, Environ. Sci. Technol. (2015).
[18] Y. Cai, W. Shen, J. Wei, T.H. Chong, R. Wang, W.B. Krantz, A.G. Fane, X. Hu, Energy-efficient desalination by forward osmosis using responsive ionic liquid draw solutes, Environ. Sci.: Water Res. Technol. 1 (2015) 341–347.
[19] M.L. Stone, C. Rae, F.F. Stewart, A.D. Wilson, Switchable polarity solvents as draw solutes for forward osmosis, Desalination 312 (2013) 124–129.
[20] D. Li, X. Zhang, J. Yao, G.P. Simon, H. Wang, Stimuli-responsive polymer hydrogels as a new class of draw agent for forward osmosis desalination, Chem. Commun. 47 (2011) 1710–1712.
[21] Y. Cai, W. Shen, S.L. Loo, W.B. Krantz, R. Wang, A.G. Fane, X. Hu, Towards temperature driven forward osmosis desalination using Semi-IPN hydrogels as reversible draw agents, Water Res. 47 (2013) 3773–3781.
[22] D. Li, X. Zhang, G.P. Simon, H. Wang, Forward osmosis desalination using polymer hydrogels as a draw agent: Influence of draw agent, feed solution and membrane on process performance, Water Res. 47 (2013) 209–215.
[23] Y. Cai, R. Wang, W.B. Krantz, A.G. Fane, X.M. Hu, Exploration of using thermally responsive polyionic liquid hydrogels as draw agents in forward osmosis, RSC Adv. 5 (2015) 97143–97150.
[24] A. Razmjou, G.P. Simon, H.T. Wang, Effect of particle size on the performance of forward osmosis desalination by stimuli-responsive polymer hydrogels as a draw agent, Chem. Eng. J. 215 (2013) 913–920.
[25] R. Ou, H. Zhang, G.P. Simon, H. Wang, Microfiber-polymer hydrogel monolith as forward osmosis draw agent, J. Membr. Sci. 510 (2016) 426–436.
[26] X.-Z. Zhang, Y.-Y. Yang, T.-S. Chung, The Influence of Cold Treatment on Properties of Temperature-Sensitive Poly(N-isopropylacrylamide) Hydrogels, J. Colloid Interface Sci. 246 (2002) 105–111.
[27] D. Li, X. Zhang, J. Yao, Y. Zeng, G.P. Simon, H. Wang, Composite polymer hydrogels as draw agents in forward osmosis and solar dewatering, Soft Matter 7 (2011) 10048–10056.
[28] A. Razmjou, M.R. Barati, G.P. Simon, K. Suzuki, H. Wang, Fast deswelling of nanocomposite polymer hydrogels via magnetic field-induced heating for emerging FO desalination, Environ. Sci. Technol. 47 (2013) 6297–6305.
[29] Y. Zeng, L. Qiu, K. Wang, J. Yao, D. Li, G.P. Simon, R. Wang, H. Wang, Significantly enhanced water flux in forward osmosis desalination with polymer-graphene composite hydrogels as a draw agent, Rsc Adv. 3 (2013) 887–894.
[30] A. Razmjou, Q. Liu, G.P. Simon, H. Wang, Bifunctional polymer hydrogel layers as forward osmosis draw agents for continuous production of fresh water using solar energy, Environ. Sci. Technol. 47 (2013) 13160–13166.
[31] Y. Hartanto, S. Yun, B. Jin, S. Dai, Functionalized thermo-responsive microgels for high performance forward osmosis desalination, Water Res. 70 (2015) 385–393.
[32] Y. Hartanto, M. Zargar, H. Wang, B. Jin, S. Dai, Thermoresponsive acidic microgels as functional draw agents for forward osmosis desalination, Environ. Sci. Technol. 50 (2016) 4221–4228.
[33] Y.F. Cai, W.M. Shen, R. Wang, W.B. Krantz, A.G. Faneb, X. Hu, CO_2 switchable dual responsive polymers as draw solutes for forward osmosis desalination, Chem. Commun. 49 (2013) 8377–8379.
[34] C.M. Hansen, Hansen Solubility Parameters: A User's Handbook, Second ed., CRC Press, 2007.
[35] L. Zha, J. Hu, C. Wang, S. Fu, A. Elaissari, Y. Zhang, Preparation and characterization of poly (N-isopropylacrylamide-co-dimethylaminoethyl methacrylate) microgel latexes, Colloid Polym. Sci. 280 (2002) 1–6.
[36] M. Das, E. Kumacheva, From polyelectrolyte to polyampholyte microgels: comparison of swelling properties, Colloid Polym. Sci. 284 (2006) 1073–1084.
[37] T. Hoare, R. Pelton, Highly pH and temperature responsive microgels functionalized with vinylacetic acid, Macromolecules 37 (2004) 2544–2550.
[38] V.T. Pinkrah, M.J. Snowden, J.C. Mitchell, J. Seidel, B.Z. Chowdhry, G.R. Fern, Physicochemical properties of poly(n-isopropylacrylamide-co-4-vinylpyridine) cationic polyelectrolyte colloidal microgels, Langmuir 19 (2003) 585–590.
[39] M. Nichifor, X.X. Zhu, Copolymers of N-alkylacrylamides and styrene as new thermosensitive materials, Polymer 44 (2003) 3053–3060.
[40] P. van de Wetering, N.J. Zuidam, M.J. van Steenbergen, O.A.G.J. van der Houwen, W.J.M. Underberg, W.E. Hennink, A mechanistic study of the hydrolytic stability of poly(2-(dimethylamino)ethyl methacrylate), Macromolecules 31 (1998) 8063–8068.
[41] S. Dai, P. Ravi, K.C. Tam, pH-Responsive polymers: synthesis, properties and applications, Soft Matter 4 (2008) 435–449.
[42] X. Li, S.H. Goh, Y.H. Lai, A.T.S. Wee, Miscibility and interactions in blends of carboxyl-containing polysiloxane with poly(1-vinylimidazole), Polymer 42 (2001) 5463–5469.
[43] A.M. Mika, R.F. Childs, Acid/base properties of poly(4-vinylpyridine) anchored within microporous membranes, J. Membr. Sci. 152 (1999) 129–140.
[44] T. Mauser, C. Déjugnat, G.B. Sukhorukov, Balance of hydrophobic and electrostatic forces in the pH response of weak polyelectrolyte capsules, J. Phys. Chem. B 110 (2006) 20246–20253.
[45] H. Nur, V.T. Pinkrah, J.C. Mitchell, L.S. Benée, M.J. Snowden, Synthesis and properties of polyelectrolyte microgel particles, Adv. Colloid Interface Sci. 158 (2010) 15–20.
[46] K. Kabiri, H. Omidian, S.A. Hashemi, M.J. Zohuriaan-Mehr, Synthesis of fast-swelling superabsorbent hydrogels: effect of crosslinker type and concentration on porosity and absorption rate, Eur. Polym. J. 39 (2003) 1341–1348.
[47] Q. Zhao, J. Sun, Q. Zhou, Synthesis of macroporous poly(N-isopropylacrylamide) hydrogel with ultrarapid swelling–deswelling properties, J. Appl. Polym. Sci. 104 (2007) 4080–4087.
[48] F.A. Carey, Organic Chemistry, McGraw-Hill, 2000.
[49] X. Fan, H. Liu, Y. Gao, Z. Zou, V.S.J. Craig, G. Zhang, G. Liu, Forward-osmosis desalination with poly(ionic liquid) hydrogels as smart draw agents, Adv. Mater. (2016), http://dx.doi.org/10.1002/adma.201600205.
[50] D.W. Van Krevelen, K. Te Nijenhuis, Chapter 7 - cohesive properties and solubility (D.W.V.K. by), in: K.T. Nijenhuis (Ed.), Properties of Polymers, Fourth ed.,Elsevier, Amsterdam, 2009, pp. 189–227.
[51] J. Brandrup, E.H. Immergut, E.A. Grulke, Polymer Handbook, Wiley, 1999.
[52] M. Gu, J.E. Kilduff, G. Belfort, High throughput atmospheric pressure plasma-induced graft polymerization for identifying protein-resistant surfaces, Biomaterials 33 (2012) 1261–1270.

RSC Advances

PAPER

View Article Online
View Journal | View Issue

Cite this: *RSC Adv.*, 2016, **6**, 89764

On-line monitoring of the aggregate size distribution of *Carthamus tinctorius* L. cells with multi-frequency capacitance measurements

Yu Liu,[a] Ze-Jian Wang,[ab] Lan Li,[a] Xiaolin Cui,[c] Ju Chu,[a] Si-Liang Zhang*[a] and Ying-Ping Zhuang[a]

Received 25th May 2016
Accepted 25th August 2016

DOI: 10.1039/c6ra13527g

www.rsc.org/advances

This study provided an effective methodology for the aggregate size distribution measurement of *Carthamus tinctorius* L. cells during suspension culture. The results demonstrated that the changes of the cell aggregate size could be reflected in the β-dispersion by the multi-frequency capacitance measurements. Furthermore, a non-linear optimization model was established and validated for predicting the cell aggregate size distribution. In addition, the on-line predicted data agreed well with off-line measurements using microscopic observation and laser-based image analysis.

Introduction

Production of valuable medicinal metabolites through plant cell suspension cultivation has proven to be an effective method in many industrial processes.[1–3] Cell aggregate distribution is one of the most important, yet also the most difficult to obtain, physiological parameters that can provide valuable information for process development, optimization and control.[2–4] The plant cell aggregation diameter has a broad range from 10 to 2000 μm.[5] The cell aggregation state not only has serious effects on the nutrient and oxygen transfer rate, but also improves the cell sensitivity to shear force.[6,7]

Much research has been carried out on quantifying the effect of aggregates on plant cell growth and secondary metabolite biosynthesis.[4,8–13] Kolewe's study demonstrated that smaller aggregates could significantly enhanced higher paclitaxel production than that with larger aggregates in *Taxus* suspension cultures, similar results has also been found in *Vaccinium pahalae* and *C. tinctorius* L. cultures.[4,9] These researches revealed that high oxygen transfer rate and nutrient supply in the center of the aggregated cell with small size would promote the cell growth rate and the secondary metabolite biosynthesis. However, some researches showed that the growth rate of larger aggregates are more rapid than that of small one, because the larger aggregates are facilitate well for the signal transduction from cell-to-cell.[9,11,12]

Microscopy and mechanical sieving were commonly applied in most studies to precisely analyse the plant cell aggregates size distribution.[14,15] However, direct on-line size distribution analysis in the bioreactor would be more advantageous to get real-time information and avoid any interference with external sample manipulations. In recent years, many *in situ* probes have been developed for the direct on-line determination of cells size distribution and concentration based on several principles: *in situ* microscopy image analysis, laser-based image analysis, flow particle image analysis and so on.[16–19] But, these equipment are big in volume, precision, also very expensive. *E.g.* FPIA (Flow Particle Image Analysis) method, also need additional recycle system to sample the cells to the devices. Furthermore, sterilizing process is another limitation, normally they are not easy to sterilize and apply in industrial process.

The capacitance measurements is becoming an established tool for the estimation of viable biomass in many different cells

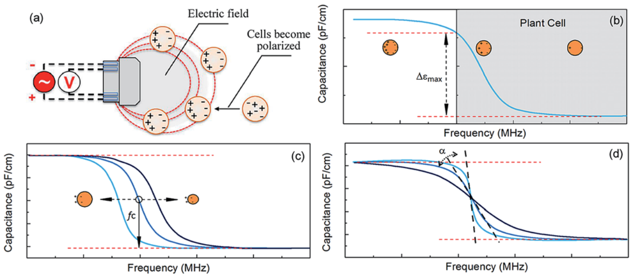

Fig. 1 Principle of culture capacitance measurements at several frequencies. $\Delta\varepsilon_{max}$ is mostly a function of the biomass concentration. The characteristic (or critical) frequency fc is the frequency at which the rate of polarization is one-half complete. fc depends mainly on the cell diameter and the conductivity. α means the homogeneous degree of the aggregation (figure adapted from Cannizzaro *et al.*[24]).

---

[a] *State Key Laboratory of Bioreactor Engineering, East China University of Science & Technology, P.O. Box 329, 130 Meilong Road, Shanghai 200237, China. E-mail: siliangz@ecust.edu.cn*

[b] *Department of Biotechnology, Delft University of Technology, 2628 BC Delft, The Netherlands*

[c] *School of Chemical Engineering, The University of Adelaide, Adelaide, SA, 5005, Australia*

culture.[20–23] The measuring capacitance at different frequencies causes a spectrum called "β-dispersion" (Fig. 1), which is proven to be related with the cell size distribution.[24,25] The underlying theory on the dielectric properties of biological cells has been extensively described elsewhere.[24] Many researches had illustrated that the cell size distribution could be predicted through the β-dispersion parameters, like characteristic frequency (fC) (the frequency at which the rate of polarization is one-half complete) shown in Fig. 1c, and α-angle of β-dispersion curve in fC (Fig. 1d).[25] The sensitivity of dielectric spectroscopy towards cell size has been used to monitor the major transition points of the culture in CHO perfusion cluture process.[24] It was further utilized by Sven Ansorge to estimate the cell size changes of CHO cells,[17] and by Hauttmann and Müller to estimate the radius of hybridoma, yeast, and bacterial cells.[26] On the other hand, in Henry and Sven Ansorge's work,[25] they used multi-frequency capacitance measurements method with partial least square (PLS) models to monitor cell size distribution of mammalian cell cultures. The results demonstrate the method is accurately enough. But until now, hardly any information could be found for this method applying in the field of plant cell suspension culture process.

The objective of this study was to demonstrate that the utility of multi-frequency capacitance measurements spectrum for plant cell size monitoring. More specifically, correlated capacitance performed at multi-frequency with changes in the cell size distribution, a constrained non-linear optimization model was built and used to predict the aggregates size distribution during the suspension culture process.

Materials and methods

Cell line and bioreactor setup

C. tinctorius L. were maintained in Murashige and Skoog (MS) medium supplemented with sucrose (30 g L^{-1}), 1-naphthylacetic acid (NAA) (10^{-2} mM), and 6-benzylaminopurine (6-BA) (10^{-3} mM). The pH of the medium was adjusted to 6.2 prior to sterilization. Cell suspension culture was initially conducted in 1000 mL Erlenmeyer flasks and subculture every 7 days.

Then exponentially growing cells were inoculated into two parallel 5L stirred tank bioreactor with a working volume of 3L. It was equipped with two standard six blade Rushton turbines with a diameter of 72 m (0.45T). During the entire cultivation period, air flow rates (0.8 L $\min^{-1}$), temperature (25 °c), stirring speeds (100, 250 rpm) were maintained at constant levels, corresponding to impeller Reynolds numbers $Re_{imp} = \rho_l N D^2/\mu$, (where N is the rotation speed, D is the impeller diameter) from 0.86×10^4 to 2.16×10^4. Under the conditions described above, two bioreactor runs were conducted in batch mode, inoculated cell densities was covered a range from 1.6 to 1.7 g L^{-1}. Each experiments were operated until the end of logarithmic phase (about 7 days), samples were taken daily for analysis.

Cell number and cell size distribution determination

A laboratory scale focused beam reflectance FBRM (model G400) coupled with iC FBRM software from Mettler Toledo was implemented to detect the particle size distribution. The measurement range is from 0.5 to 1000 μm. The time interval of the measurement is 3 s, our data point is the average result of over 50 measurements on every sample.

In addition, Image-Pro Plus 6.0 software (Media Cybernetics, Bethesda, MA) was used to automatically determine the cell count and cell size based on microscopic observation. First of all, light microscope images of bacteria acquired by a CCD camera (cells are magnified 10 × 4 times) are handled with best-fit equalization and contrast enhancement. Then, the effects of edge enhancement, noise cancellation and smooth are realized by binarization processing. Finally, the counted dark areas are projected cell areas. In parallel, the objects that are not interested in must be hidden, and the adhesive objects must be split. In this investigation, three repetitions are conducted to accomplish 50 microscope images taken from a cell sample at every time point.

On-line capacitance measurements

β-Dispersion of capacitance were measured under an real-time bioreactor operations using a capacitance probe (Biomass Monitor 220, Hamilton Switzerland). The Hamilton software automatically analyzes the capacitance over a total of 17 frequencies from 0.3 to 10 MHz. Two data sampling type were used to monitor the normal viable biomass and cell size distribution. Low frequency data sampling type was acquired in intervals of 6 min, which was used for daily monitoring and high frequency data sampling type was acquired in interval of 6 s along 5 min measurement. All the data were saved in a comma-separated values (CSV) format file for subsequent analysis using Hamilton Software.

Standard capacitance β-dispersion measurement

In order to obtain the standard β-dispersion under different ranges of aggregate size, mechanical sieving was carried out to separate the aggregation to different range. A known volume sample was sieved through 6 cm diameter sieves of 1400, 880, 600, 425 and 96 μm (d_1, d_2…d_6 in Table 1) sieve apertures by rinsing with small volumes (40–50 mL) of 15 mM $CaCl_2$ solution. At least 300 n mL^{-1} cell number was conducted in the smallest classification of 1400 μm aggregation size. Then, each classification was measured over the full range frequency.

Capacitance data analysed method

The matrix of the standard capacitance β-dispersion ($A_{eq}[x]$) means the β-dispersion produced by the specific cell aggregate in some certain size under different frequencies. So A_{eq} is a matrix composed of these standard β-dispersion under different ranges of aggregate size (d_1, d_2…d_6). Assume that an

Table 1 Aggregate size of the mechanical sieving

	d_1	d_2	d_3	d_4	d_5	d_6
Mesh number (n)	12	18	28	35	60	160
Aggregate diameter (μm)	1400	880	600	425	250	96

mixture cell aggregate sample was composed by these size classification (d_1, $d_2 \ldots d_6$). And if we have known the percentage of cell numbers in different size classifications ($x = x_1, x_2 \ldots x_6$). Then, the measured β-dispersion by this sample (b_{eq}) can be described by the standard β-dispersion (A_{eq}) using a mathematical equation ($b_{\text{eq}} = A_{\text{eq}}x$).

To facilitate the description of the algorithm, the size distribution is included into a vector $x = [x_1, x_2 \ldots x_6]$. Based on linear algebra principles, determination of x needs at least 6 independent equations. While, the β-dispersion were measured over a range of 0.1–10 MHz at 17 different frequency channels. For this case, the non-linear optimization model will provide the best fitting to the measurements, which is expressed by $f(x)$ in eqn (1), and constraint conditions in eqn (2). The algorithm is easily implemented in the MATLAB.

$$\min_x f(x) = \text{abs}(A_{\text{eq}}x - b_{\text{eq}}) \tag{1}$$

$$\text{Constraint condition} \left[\begin{array}{c} c(x) \leq 0 \\ c_{\text{eq}}(x) = 0 \\ \text{lb} \leq x \leq \text{ub} \end{array} \right. \tag{2}$$

Where $c(x)$, and $c_{\text{eq}}(x)$ are non-linear functions. $c(x)$ means the different capacitance between adjacent frequency. $c_{\text{eq}}(x)$ ensure the sum of x is equal to one. lb and ub is the lower and upper bounds in x, which is $[0, 0 \cdots 0]$ and $[1, 1 \cdots 1]$ in this research.

If the calculation follows a non-linear model, the $f(x)$ as described by eqn (1) may have multiple local minima, but only the true value of x corresponds to its global minimum, *i.e.*, the smallest one among all local minima. The presence of local minima often represents a problem because the initial setting for x at start would determine where the solution converges. When the initial x setting is close enough to its true value, x will converge to the global minimum. For this reason, a general known of the cell size distribution needs to be identified first, based on which a series of initial values can be selected. Theoretically, more frequency channels' data or independent equations will help the solution but the measuring error at high frequency maybe make the results more accurate or worse.

For comparing this capacitance method to other experimental data, a residual error, γ, was calculated as follows:

$$\gamma = \frac{\sum_{i}^{n} \text{abs}(x(i) - \hat{x}(i))}{\sum_{i}^{n} x(i)} \tag{3}$$

where x and $\hat{x}$ are the cell size distribution based on capacitance measurement and other experimental method, respectively. This residual allows for a direct comparison of results between different method, and values of γ were used to judge the quality of the optimization function.

Result and discussion

Calibration curves of β-dispersion under different aggregate size

In order to build the calibration capacitance β-dispersion matrix A_{eq}, mechanical sieving was used to separate the aggregates to different range (d_1, $d_2 \ldots d_6$ in Table 1). The original unit of the measurement was in pF cm^{-1}, which means capacitance value in a certain volume. Then the results was divided by the cell counting numbers in n ml^{-1} to obtain the specific capacitance, the unit of which is pF n^{-1}. The specific capacitance means the capacitance produced by a single cell aggregate, and the specific β-dispersion curves have the character of each aggregate size. This curves are correlated with the total volume of the cells or the size of the cell aggregate. Fig. 2 presents the specific capacitance β-dispersion of different ranges of aggregate size obtained through mechanical sieving. The results showed that they are corresponding well with the theory mentioned above, capacitance value increase with larger aggregate size.

In the double logarithm coordinate, the relation between the measurement frequencies and the specific capacitance is linear and the capacitance β-dispersion is almost parallel to each other. Signals corresponding to the lower frequencies have the higher amplitudes. Fortunately, with the homogeneous aggregate size distribution in the determination, the measuring error is less than 5% of the average data (relative error).

Initiation and frequency optimization

If the calculation follows a non-linear model, the $f(x)$ as described by eqn (1) may have multiple local minima, but only the true value of x corresponds to its global minimum, *i.e.*, the smallest one among all local minima. The presence of local minima often represents a problem because the initial setting for x at start would determine where the solution converges. When the initial x setting is close enough to its true value, x will converge to the global minimum. For this reason, a general known of the cell size distribution needs to be identified first, based on which a series of initial values can be selected. Based on the maximum change range of the aggregate size from previous experience, three initial value were chosen to investigate the effect of the initiation on the capacitance data analysed method. First one is a value close to the normal distribution; in addition, a zero x and a relatively

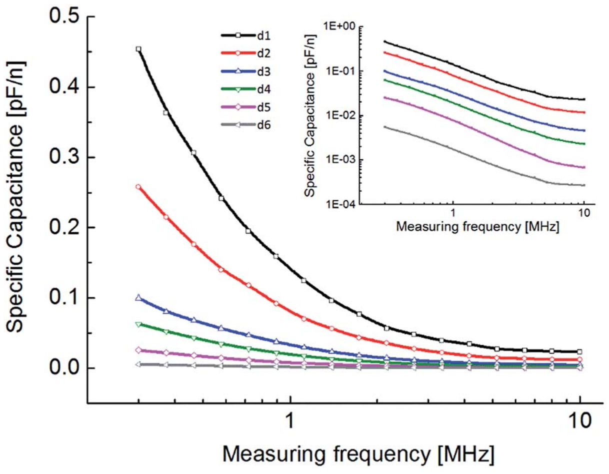

Fig. 2 Calibration curves of β-dispersion under different cell aggregate size.

opposite to the distribution value were chosen. A set of capacitance data from an unknown aggregate size are utilized to validate the detected method. These three initial values are used as initial setting points to solve the non-linear optimization model, respectively. The aggregate size distributions determined by microscopic observation and laser-based image analysis were used to judge the quality of the model predictions. The laser-based image analysis method used as the control result, considering of fewer manual steps.

The results are presented in Fig. 3, and the residual errors γ were calculated based on the laser-based image analysis results. The capacitance based method provide accurate prediction of the distribution in all three initial value. The smallest $\gamma = 0.06$ contributed from the initial value close to the distribution (Fig. 3a). When the initial value is far from the distribution and the zero, $\gamma = 0.08$ will be slightly higher (Fig. 3b and c), and the major error is from the large aggregate prediction. However, for laser-based image method itself is accurate to the small particles (<1 mm), but because of the principle of this electrode, they are insensitive to the particle above 1 mm. On the other hand, the microscopic observation results also showed large different from the laser-based image analysis results ($\gamma = 0.24$). Accurately, in the microscopic observation determine process, there are some cell aggregates overlapped each other, some of which are two or three aggregates merged together in the image. So the results shown there are more large aggregates. However, these results indicate that initial value have limited influence on the analysed method over a broad range.

Furthermore, theoretically, more frequency channels' data or independent equations will help the solution. But, capacitance in high frequencies always have the great amplitudes due to the inhomogeneous of the cell distribution. These measuring errors maybe cause the overdetermined error to the solution. To estimate the influenced of selected frequency channels on the detected results, three different frequency range are used to solve the nonlinear optimization model, respectively. The spectra are measured over the range from 0.3 to 10 MHz with 17 different frequency channels, so the frequency ranges are set to from 0.3 to 1.1 (7 channels), 0.3 to 4.2 (13 channels) and 0.3 to 10 MHz (17 channels). These different frequency range are used to solve the nonlinear optimization model, respectively. The results are shown in Fig. 4, the residual error are also calculated based on the laser-based image analysis results. Three different frequency range calculation results were significant different, and the smallest $\gamma = 0.06$ contributed from the 13 channels' data, and this results were used for further calculation. In addition, it is evident in Fig. 4a and c that less frequency channels' data would decrease the accurate of the non-linear optimization model, and full frequency channels' data slightly overdetermined error to the solution.

Evaluation of method sensitivity to the measurements data

The distribution of the β-dispersion cell aggregate has a broad range, so the mixed gradient changing of the plant cell aggregate distribution caused by the flow field always result in the fluctuation on the capacitance measurement. 50 times of capacitance β-dispersion data with a sample are shown in Fig. 5A. These measurements data present a remarkable difference in a single scan, especially during the high frequency data (double logarithm coordinate). To evaluate the sensitivity of the method to the fluctuant measurements data, some manual interventions to the measurements were performed to simulate the fluctuation in the real measurement process. Although the average of many sample points will reduce this effect, the influence taken from the measurement fluctuation is still necessary for evolution the validity of this method. Three different fluctuations were applied to mimic the measurement fluctuation in the real process. The first fluctuation is the whole frequency data increase and decrease 7 percentage of the average data, the second fluctuation is 7 percentage improvement and decrement of the data at a random low frequency. And the third fluctuations are the 20 percentage improvement and decrement of the data at a random high frequency.

These fluctuation capacitance data are used to solve the nonlinear optimization model, respectively. Results are shown in Fig. 5B, the fluctuation improve significantly the residual error γ. In the first case, the whole frequency data change showed a remarkable increase in prediction errors, which ranged from $\gamma = 0.13$ to 0.19 compared with the average result $\gamma = 0.06$ by the positive or negative fluctuation. In the point data change case, the average prediction errors are $\gamma = 0.40$ and $\gamma = 0.09$, respectively in low and high frequency change. Low frequency data change improve more error compared with the high frequency data. With the frequency selected rule mentioned

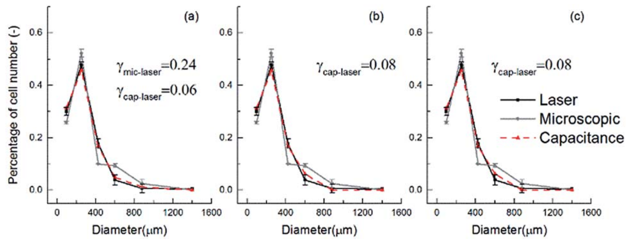

Fig. 3 Effect of size distribution dependence on initial value, using microscopic observation and laser-based image analysis experiments result to judge the quality of the model predictions. Three initial value were chosen: (a) close to the distribution $x = [0.2, 0.4, 0.2, 0.1, 0.05, 0.05]$, (b) zero $x = [0, 0, 0, 0, 0, 0]$ and (c) a relatively opposite to the distribution value $x = [0.05, 0.05, 0.1, 0.2, 0.4, 0.2]$.

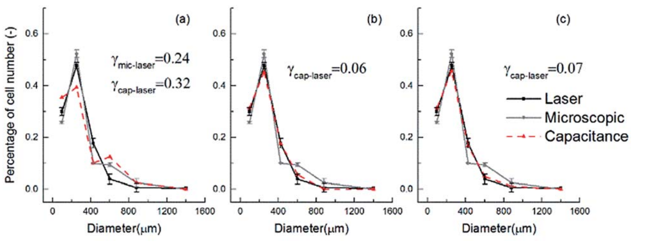

Fig. 4 Effect of size distribution dependence on frequency selected, using microscopic observation and laser-based image analysis experiments result to judge the quality of the model predictions. Three frequency band were chosen: (a) 300–897 kHz, (b) 300–3342 kHz and (c) 300–10000 kHz.

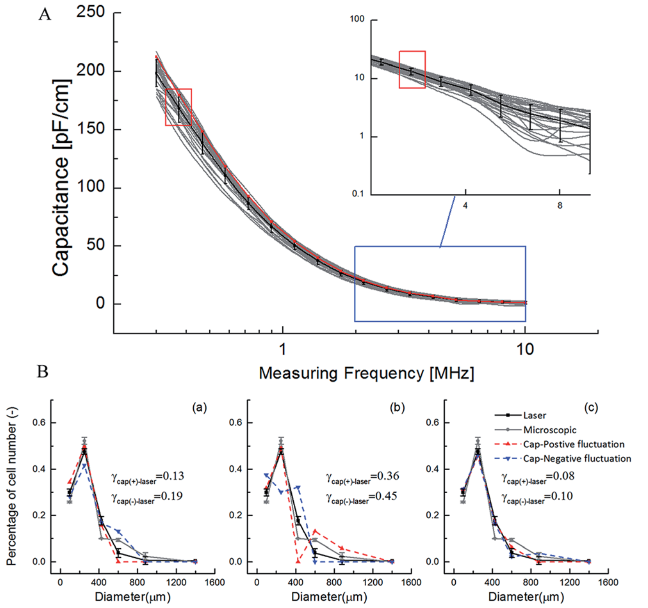

Fig. 5 (A) 50 times of capacitance β-dispersion data with a sample, black line means the average result. (B) Model sensitivity of the size distribution to the measurements data, some manual intervention to the measurements were performed. (a) is the whole frequency data increase and decrease 7 percentage of the average data, (b) is 7 percentage improvement (red dash line) and decrement (blue dash line) of the data at a random low frequency. (c) is the 20 percentage improvement and decrement of the data at a random high frequency.

above, it was evidenced that capacitance data in high frequencies contribute less influence to the result. Therefore, though the capacitance in high frequency fluctuate a lot in the measurement, the capacitance based method can also provide accurate prediction.

Fermentation validation

To examine the performance of the capacitance measurements based method of monitoring of aggregate size distribution in the real fermentation process, we hence performed two batches cultures at different shear environment, expecting that aggregate size distribution would different. Fig. 6 shows the comparisons of profiles under low and high shear conditions for: biomass growth curve, residual sugar concentration, the average aggregate diameter, and the number of aggregate. The results revealed that the cell growth and the lag phase could be serious inhibited and postponed with the increased shear force. Meanwhile, the aggregation diameter encountered great difference under various shear environments during the former culture phase. At the start point of 4 h, the cell aggregation diameter was 225 μm under the lowest shear stress, which is much close to the mean diameter in shaken flask cultures.

While with shear stress up, the particle diameter in 4 h decreased to 165 μm, which was 36% lower than that in low shear conditions. In the whole process, the average aggregation diameter increases with the time until reaching the highest diameter level of 300 μm.

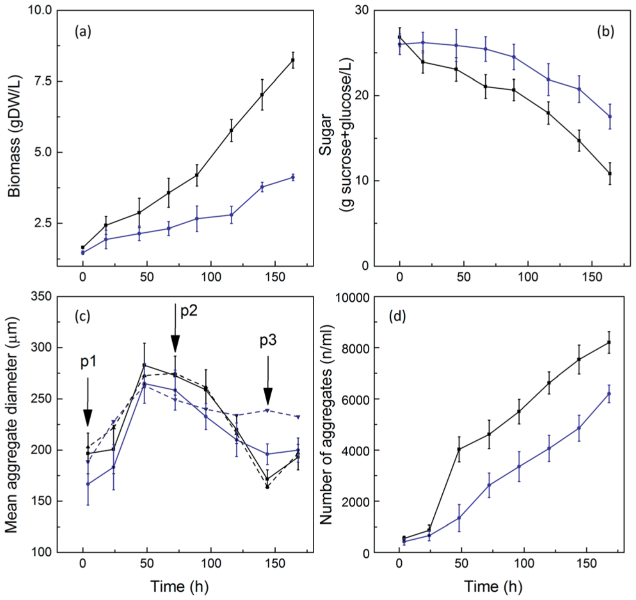

Fig. 6 The fermentation validation is conducted under two shear conditions: black line-low shear conditions and blue line-high shear conditions. (a) Biomass growth curve (b) residual sugar concentration, (c) the comparison between the FBRM results (solid line) and the multi-frequency capacitance measurements results (dash line) of the mean aggregate size, (d) number of aggregates.

Fig. 7 shows the comparisons of laser-based image analysis, microscopic observation and capacitance measurements based results for the aggregate distributions at 4, 72, 144 h in the real fermentation process. Compare with laser-based method the capacitance analysis method provided accurate predictions, particularly during the beginning of the culture, indicating that the model worked well under normal processing conditions. However, in the latter stages of the growth curve in the high shear condition, the capacitance based method failed to provide a reliable prediction of the distribution. This is because capacitance measurements method can only measure alive cells, so in the later sate of the culture, cell programmed death and shear related death make the measurement influences a lots. A similar phenomenon was happened in Holland's study when using this probe to monitor plant cell biomass.[22] They stated that dead cells do not contribute to the capacitance value, but may contribute to the overall signal obtained by conventional measurements of PCV, FW and DW. So it is in an aggregate, some dead cells do not contribute to the capacitance measurement, but the particle is still in its size. This make capacitance measurement result did not agreed well with the other off-line measurements in the later stage of the culture. But the conventional off-line results did not influence a lot. In a similar work, Ansorge and Olivier Henry first using a partial least square (PLS) model to predict the cell concentration, cell viability, cell diameter and size distribution. They demonstrated that the model were validated to provide real-time quantitative information about the mean cell diameter and also cell size distribution. For the small range of the animal cell distribution (10 to 20 μm), the model can only described three volume clusters.

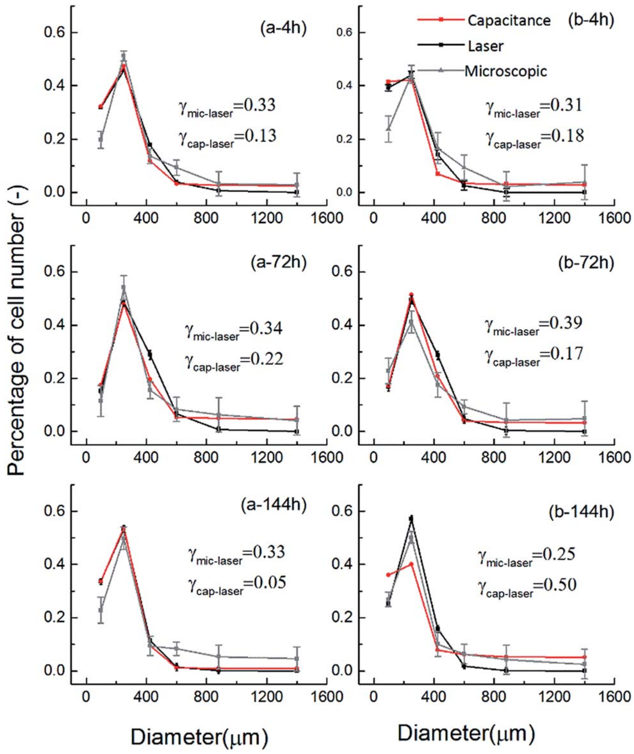

Fig. 7 Comparison of laser-based image analysis experimental data, microscopic observation and capacitance predictions for the aggregate distributions at 4, 72, and 144 h.

Conclusions

Aggregate size distributions of plant cell culture was commonly considered as one of the important physiological parameter, which has key relationship with the cell growth, metabolism and productivity. Therefore, determination and control of the aggregate cell size distribution play a significant role on *C. tinctorius* L. cells suspension cultivation. The present work demonstrated that the capacitance measurement sensor not only was an established tool for the online estimation of viable cell concentration, but also could be applied to determine the aggregate size distribution. A feasible and effective model was established for analysing the aggregate size distributions based on the capacitances measurements obtained under the multiple frequencies. The real time viable cell concentration and aggregate size distributions determination and control could be effective applied on the process optimization control and scale up achievement in suspension culture of *C. tinctorius* L.

Acknowledgements

This work was financially supported by a Grant from the National Natural Science Foundation of China (Grant No. 31200024), the National High Technology Research and Development Program (2015AA021005), and 973 Program No. 2013CB733600. The Royal DSM and partially supported by NOW-MoST Joint Program (2013DFG32630). We also thank pharmacy corporation Practical Bio Co., Ltd. (DALIAN, China) for donating the industrial strain.

References

1 A. M. Nosov, *Appl. Biochem. Microbiol.*, 2012, **48**, 609–624.
2 T. K. Huang and K. A. McDonald, *Biochem. Eng. J.*, 2009, **45**, 168–184.
3 T. K. Huang and K. A. McDonald, *Biotechnol. Adv.*, 2012, **30**, 398–409.
4 M. E. Kolewe, M. A. Henson and S. C. Roberts, *Biotechnol. Prog.*, 2011, **27**, 1365–1372.
5 P. Doran, in *Bioprocess Design and Control*, Springer, Berlin, Heidelberg, 1993, ch. 5, vol. 48, pp. 115–168.
6 P. M. Kieran, P. F. MacLoughlin and D. M. Malone, *J. Biotechnol.*, 1997, **59**, 39–52.
7 M. I. Georgiev, J. Weber and A. Maciuk, *Appl. Microbiol. Biotechnol.*, 2009, **83**, 809–823.
8 J.-i. Edahiro and M. Seki, *J. Biosci. Bioeng.*, 2006, **102**, 8–13.
9 N. Hanagata, A. Ito, H. Uehara, F. Asari, T. Takeuchi and I. Karube, *J. Biotechnol.*, 1993, **30**, 259–269.
10 A. C. Hulst, M. M. T. Meyer, H. Breteler and J. Tramper, *Appl. Microbiol. Biotechnol.*, 1989, **30**, 18–25.
11 M. Keßler, H. J. G. ten Hoopen and S. Furusaki, *Enzyme Microb. Technol.*, 1999, **24**, 308–315.
12 R. Madhusudhan and G. A. Ravishankar, *Biotechnol. Lett.*, 1996, **18**, 1253–1256.
13 M. F. Pépin, M. A. L. Smith and J. F. Reid, *In Vitro Cell. Dev. Biol.: Plant*, 1999, **35**, 290–295.
14 F. Mavituna and J. M. Park, *Chem. Eng. J.*, 1987, **35**, B9–B14.
15 D. Zhao, Y. Huang, Z. Jin, W. Qu and D. Lu, *Plant Cell Rep.*, 2003, **21**, 1129–1133.
16 K. Joeris, J.-G. Frerichs, K. Konstantinov and T. Scheper, *Cytotechnology*, 2002, **38**, 129–134.
17 S. Ansorge, G. Esteban and G. Schmid, *Cytotechnology*, 2010, **62**, 121–132.
18 D. Raschke and D. Knorr, *J. Microbiol. Methods*, 2009, **79**, 178–183.
19 V. Camisard, J. P. Brienne, H. Baussart, J. Hammann and H. Suhr, *Biotechnol. Bioeng.*, 2002, **78**, 73–80.
20 K. Konstantinov, S. Chuppa, E. Sajan, Y. Tsai, S. Yoon and F. Golini, *Trends Biotechnol.*, 1994, **12**, 324–333.
21 G. H. Markx, H. J. G. ten Hoopen, J. J. Meijer and K. L. Vinke, *J. Biotechnol.*, 1991, **19**, 145–157.
22 T. Holland, D. Blessing, S. Hellwig and M. Sack, *Biotechnol. J.*, 2013, **8**, 1231–1240.
23 H. W. Lee, J. Carvell, K. Brorson and S. Yoon, *J. Chem. Technol. Biotechnol.*, 2015, **90**, 273–282.
24 C. Cannizzaro, R. Gügerli, I. Marison and U. von Stockar, *Biotechnol. Bioeng.*, 2003, **84**, 597–610.
25 S. Ansorge, O. Henry, M. Aucoin, R. Voyer, J. P. Carvell and A. Kamen, in *Cells and Culture: Proceedings of the 20th ESACT Meeting, Dresden, Germany, June 17-20, 2007*, ed. T. Noll, Springer Netherlands, Dordrecht, 2010, pp. 853–859, DOI: 10.1007/978-90-481-3419-9_150.
26 S. Hauttmann and J. Müller, *Bioprocess Biosyst. Eng.*, 2001, **24**, 137–141.

Macromolecules
Article
pubs.acs.org/Macromolecules

Generation of Fluorescent and Stable Conjugated Polymer Nanoparticles with Hydrophobically Modified Poly(acrylate)s

Liang Yan,[†] Xiaolin Cui,[‡] Takaaki Harada,[†,§] Stephen F. Lincoln,[†] Sheng Dai,[‡] and Tak W. Kee*[,†]

[†]Department of Chemistry, University of Adelaide, Adelaide, South Australia 5005, Australia
[‡]School of Chemical Engineering, University of Adelaide, Adelaide, South Australia 5005, Australia

Ⓢ *Supporting Information*

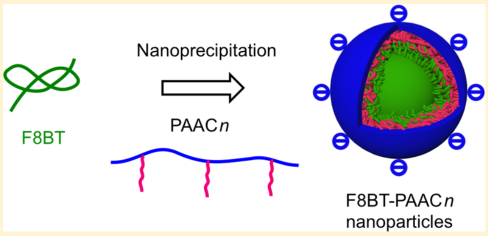

ABSTRACT: Conjugated polymer nanoparticles hold promise as fluorescence imaging agents because of their high brightness and photostability. However, their aggregation and precipitation at the high ionic strengths in physiological conditions present an impediment to their applications in biological imaging. In this study, hydrophobic linear alkyl group substituted poly(acrylate)s, PAAC*n*, are synthesized and employed as amphiphilic stabilizers. The carboxylate groups of PAAC*n* increase the surface charge of conjugated polymer nanoparticles, stabilizing the particles in phosphate buffer saline, PBS. Nanoparticles of the green-yellow emitting conjugated polymer, F8BT, stabilized with PAAC*n* (F8BT-PAAC*n*) are prepared using nanoprecipitation. In contrast to the significant aggregation with a negligible yield (~0%) of bare F8BT nanoparticles in PBS, high yields approaching 90% are observed for F8BT nanoparticles stabilized with PAAC18 at 1%, PAAC16 at 3%, and PAAC10 at 10% substitution. The F8BT-PAAC*n* nanoparticles have a small size ranging from 50 to 70 nm in diameter, highly negative surface charge and high colloidal stability in PBS. These properties pave the way for the deployment of F8BT-PAAC*n* nanoparticles in biological applications. Spectroscopic results indicate that PAAC*n* has no adverse effect on the absorptivity and fluorescence brightness of F8BT-PAAC*n* nanoparticles relative to bare F8BT nanoparticles. In addition, F8BT-PAAC*n* nanoparticles are internalized by HEK 293 cells and exhibit low toxicity. In short, PAAC*n* are versatile and robust stabilizing materials that facilitate the application of F8BT-PAAC*n* nanoparticles as fluorescent probes in cell imaging.

■ INTRODUCTION

The broad UV−visible absorption cross-section, high fluorescence brightness and photostability of conjugated polymer nanoparticles have attracted substantial interests that have resulted in a wide range of applications.[1−18] An interesting application is to use conjugated polymer nanoparticles with emissions ranging from visible to near-infrared (NIR) spectral regions as fluorescent probes in cell imaging. Streptavidin modified conjugated polymer nanoparticles have been developed for labeling EpCAM, a cell-surface receptor and diagnostic marker for cancer cells, selectively.[2,3] Similarly, the integration of the NIR emitting chromophores dithienylbenzoselenadiazole and quinoxaline into conjugated polymer nanoparticles results in a high NIR fluorescence brightness and excellent photostability for deployment in cell imaging.[4,5] An alternative strategy for preparing brightly emitting NIR conjugated polymer nanoparticles involves the doping of these nanoparticles with either NIR fluorescence dyes[6] or quantum dots,[7] which accept energy from the conjugated polymer matrix through efficient Förster resonance energy transfer, FRET. In addition to their use in fluorescence imaging, conjugated polymer nanoparticles have also been used as ratiometric pH,[8,9] temperature,[10] oxygen,[11,12] fluoride,[13] and mercury[14] sensors. These sensors are based on efficient FRET from conjugated polymer nanoparticles to either surface conjugated, doped or covalently attached functional groups. The change of environmental pH, temperature, oxygen level or concentration of fluoride or mercury ions triggers variation of emission properties of the corresponding functional group, thereby disrupting FRET to give rise to sensing function. In therapeutic applications, several conjugated polymer nanoparticle systems have been used as drug delivery vehicles, photothermal and photodynamic therapy agents while providing simultaneous fluorescence imaging capability.[15−18]

Although conjugated polymer nanoparticles exhibit a wide range of biological applications, their large-scale aggregation and precipitation under the high ionic strength conditions in physiological conditions are substantial challenges to advance their biological applications. Ionic surfactants and phospholipids including sodium dodecyl sulfate[19] and 1,2-dipalmitoyl-*sn*-glycero-3-phosphocholine[20,21] have been used to increase the surface charge and colloidal stability of conjugated polymer nanoparticles. However, the required high concentration of surfactants (up to 0.16 M) may result in either cytotoxicity or perturbations to cell membranes. To address this issue, Wu et al. developed a coprecipitation strategy, in which amphiphilic polymers bearing functional groups and hydrophobic conjugated polymers are co-condensed into single nanopar-

Received: September 11, 2016
Revised: October 31, 2016
Published: November 10, 2016

DOI: 10.1021/acs.macromol.6b02002
Macromolecules 2016, 49, 8530−8539

ticles.[2,22] In the resultant conjugated polymer nanoparticles, the hydrophobic segments of the amphiphilic polymers are most likely anchored inside the hydrophobic nanoparticles while the hydrophilic segments bearing functional groups are located on the surface either to enhance surface charge, or supply reactive sites for further bioconjugation, or both. A challenge in this approach is the limited number of amphiphilic polymers that are soluble in an organic solvent. More recently, conjugated polymer nanoparticles with both enhanced surface charge and bioconjugation sites were reported.[23] However, two polyelectrolytes are required; poly(styrenesulfonate) serves as a stabilizer to improve colloidal stability and poly(sodium methacrylate) provides carboxylate groups as bioconjugation sites. Owing to the issues highlighted above, there is significant motivation to develop a single-component stabilizer that can provide conjugated polymer nanoparticles with both colloidal stability in physiological conditions and bioconjugation sites.

In this work, poly(acrylate)s that are randomly substituted with hydrophobic linear alkyl groups, PAAC*n*, are synthesized and used as stabilizing materials. The carboxylate groups of PAAC*n* offer not only a negatively charged nanoparticle surface and enhanced colloidal stability, but also supply potential reactive sites for biomolecule conjugation as described by Wu et al.[23] A green-yellow emitting conjugated polymer, poly[(9,9-dioctylfluorenyl-2,7-diyl)-*alt-co*-(1,4-benzo-[2,1,3]-thiadiazole)], F8BT, is used to prepare nanoparticles stabilized with PAAC*n*. The F8BT-PAAC*n* nanoparticles have hydrodynamic diameters ranging from 49 ± 5 to 70 ± 3 nm and a high colloidal stability in phosphate buffered saline, PBS, at pH 7.4 over 4 weeks. In addition, the F8BT-PAAC*n* nanoparticles have a negatively charged surface arising from the carboxylate groups of PAAC*n*, as reflected by a ζ potential value of approximately -58 ± 2 mV. The sub-100 nm size and negative surface charge hold the promise to facilitate the accumulation of F8BT-PAAC*n* nanoparticles in tumors through the enhanced permeability and retention effect, which is desired in tumor imaging or therapy.[24,25] The F8BT-PAAC*n* nanoparticles can be internalized by cells and exhibit low cytotoxicity. Confocal fluorescence images show their high fluorescence brightness, indicating the potential use of F8BT-PAAC*n* nanoparticles as fluorescent probes for cell imaging.

EXPERIMENTAL SECTION

Materials. Poly[(9,9-dioctylfluorenyl-2,7-diyl)-*alt-co*-(1,4-benzo-[2,1,3]-thiadiazole)], F8BT, average molecular weight: 42,000 g mol^{-1}) was purchased from American Dye Source, Inc. Poly(acrylic acid) (35 wt % aqueous solution, average molecular weight: 250,000 g mol^{-1}), hexylamine, decylamine, dodecylamine, tetradecylamine, hexadecylamine, octadecylamine and fluorescein at 95% purity were purchased from Sigma-Aldrich. 1-Methyl-2-pyrrolidione and dicyclohexylcarbodiimide were purchased from Merck Schuchardt. Dulbecco's modified Eagle's medium (DMEM), penicillin and fetal bovine serum were purchased from Gibco-BRL. 3-(4,5-Dimethylthiazol-2-yl)-2,5 diphenyltetrazolium bromide (MTT) was purchased from Merck. All chemicals were used as received. Tetrahydrofuran was freshly distilled from sodium benzophenone ketyl before use. Deionized water obtained using a Millipore NANO pure water system and filtered through a 0.22 μm nylon membrane (Merck Millipore) was used in all experiments. A stock phosphate buffered saline, PBS, solution was prepared at five times the standard concentration, 5 × PBS, by dissolving 40 g of NaCl, 1 g of KCl, 7.2 g of Na_2HPO_4, and 1.2 g of KH_2PO_4 in 800 mL of deionized water. The pH of this solution was adjusted to 7.4 with 0.1 M NaOH and a final volume of 1 L was achieved by addition of deionized water.

Preparation of Alkyl-Substituted Poly(acrylate)s, PAAC*n*. Poly(acrylate)s randomly substituted with linear alkyl groups were synthesized according to a reported method.[26] Poly(acrylic acid) (1.50 g, 20.8 mmol repeating units) was added into 30 mL of 1-methyl-2-pyrrolidone and the solution was stirred at 60 °C for 16 h, after which decylamine (0.33 g, 2.1 mmol) and dicyclohexylcarbodiimide (0.56 g, 2.7 mmol) were added and the solution was stirred for 120 h at 60 °C. The solution was then cooled to room temperature. Subsequently, 40 mL of 40% w/w aqueous NaOH solution were added and the formation of a precipitate was observed. The precipitate was then collected by vacuum filtration and washed thoroughly twice with 30 mL of 1-methyl-2-pyrrolidone at 60 °C and twice with 50 mL of methanol at room temperature. The collected precipitate was then dissolved in 15 mL deionized water and reprecipitated through addition of 200 mL of methanol. The dissolution and precipitation were repeated three times. The crude product was dissolved in 20 mL of deionized water and dialyzed (Spectr/Por 3, molecular weight cutoff: 3500 g/mol) against deionized water for 4 days with daily change of water. The final product was collected through lyophilization as a white solid. The substitution percentage of alkyl chain substituent was determined using ^{1}H NMR spectroscopy according to eq 1:

$$\text{substitution percentage} = \frac{S_{\text{methyl group}}/3}{S_{\text{methine group}}} \times 100\% \tag{1}$$

where $S_{\text{methyl group}}$ denotes the integrated area of the resonances of alkyl amine terminal CH_3 groups and $S_{\text{methine group}}$ denotes that of the resonances of poly(acrylate) backbone CH groups.

Preparation of F8BT-PAAC*n* Nanoparticles. Dispersions of F8BT-PAAC*n* nanoparticles in PBS were prepared using a modified nanoprecipitation method.[1] The procedure involved dissolving 10 mg F8BT in 100 mL of freshly distilled THF under sonication to obtain a ~100 ppm F8BT solution. A 1 mL portion was rapidly injected into 10 mL 50 ppm aqueous solution of 1% substituted PAAC18 under vigorous stirring. Subsequently, THF was removed under vacuum using a rotary evaporator at ~40 °C to yield the F8BT-PAAC18 nanoparticles. This product was mixed with 2 mL of 5 × PBS solution and deionized water to give a total volume of 10 mL of a standard PBS (pH = 7.4) dispersion of F8BT-PAAC18 nanoparticles (10 ppm F8BT). This solution was filtered using a 0.2 μm filter (Sartorius Stedim Biotech) to give the final PBS dispersion of F8BT-PAAC18 nanoparticles. The identical method was used to prepare all other F8BT-PAAC*n* nanoparticle dispersions in PBS. The absorption spectra of the PBS dispersions of F8BT-PAAC*n* nanoparticles before and after filtration were recorded to measure the yield of nanoparticle preparation, which is defined in eq 2 as

$$\text{yield} = \frac{A_{\text{after filtration}}}{A_{\text{before filtration}}} \times 100\% \tag{2}$$

where $A_{\text{before filtration}}$ and $A_{\text{after filtration}}$ represent the absorbance at 455 nm of the PBS dispersion of F8BT-PAAC*n* nanoparticles before and after filtration through the 0.2 μm filter, respectively. Accordingly, the yield defined here describes the percentage of F8BT-PAAC*n* nanoparticles that passed through the 0.2 μm filter.

Characterization. ^{1}H NMR spectra were recorded using a Varian Inova 500 spectrometer, operating at 500 MHz. Chemical shifts (δ) were recorded in parts per million (ppm) in D_2O with the resonances corresponding to the residual nondeuterated solvent, $\delta = 4.79$ ppm, as the internal reference. UV−vis absorption spectra were recorded on a Cary-Varian 5000 spectrophotometer using matched quartz cuvettes of 1 cm path length. Fluorescence spectra were recorded on a Cary-Varian Eclipse fluorescence spectrophotometer using a quartz cuvette of 1 cm path length.

Fluorescence Quantum Yield Measurements. Fluorescein, with a reported quantum yield of 89%,[27] was used as the reference for fluorescence quantum yield measurements. Five samples of fluorescein in 0.1 M NaOH and F8BT-PAAC*n* nanoparticles in PBS over a range of five concentrations ($A < 0.1$) were prepared. The absorption (at 475 nm) and emission (excitation wavelength of 475

DOI: 10.1021/acs.macromol.6b02002
Macromolecules 2016, 49, 8530−8539

nm) spectra of each sample were recorded. For fluorescein and F8BT-PAAC*n* nanoparticles, the integrated fluorescence intensities were plotted against the corresponding absorbances to give a linear curve with a slope of *m* and an intercept of 0. The fluorescence quantum yield of F8BT-PAAC*n* nanoparticles with reference to fluorescein was calculated according to eq 3:

$$\Phi_{\text{sample}} = \Phi_{\text{fluorescein}} \times \frac{m_{\text{sample}}}{m_{\text{fluorescein}}} \times \frac{\eta_{\text{sample}}^{2}}{\eta_{\text{fluorescein}}^{2}} \times 100\% \tag{3}$$

where Φ represents the fluorescence quantum yield and *η* represents refractive index of the corresponding solvent. The error of the fluorescence quantum yield in this study represents the linear fitting error of the calculation of the slope, *m*.

Morphology, Size, *ζ* Potential, and Surface Charge Density Characterization. Transmission electron microscopy, TEM, was used to characterize the size and morphology of the F8BT-PAAC*n* nanoparticles. For sample preparation, a drop (~50 *μ*L) of F8BT-PAAC*n* nanoparticle dispersion (10 ppm for F8BT) was placed onto a carbon-coated copper grid, and after 2 min the remaining solution was removed using a filter paper. This procedure was repeated three times. A drop (~50 *μ*L) of 2% uranyl acetate solution was then applied onto the grid for staining, and after 2 min the remaining uranyl acetate solution was removed using a filter paper. The samples were observed on a FEI Tecnai G2 Spirit TEM at an operating voltage of 100 kV.

Dynamic light scattering, DLS, was used to measure the apparent hydrodynamic diameters and *ζ* potentials of the F8BT-PAAC*n* nanoparticles. Measurements were performed on a Malvern Zetasizer with a He−Ne laser (633 nm) and a backscattering detector (173°). The hydrodynamic diameter and *ζ* potential were given as the mean value of three independent measurements. The error represents the standard deviation of the mean.

The surface charge densities of bare F8BT nanoparticles and F8BT-PAAC*n* nanoparticles are calculated according to eq 4,[28]

$$\sigma_0 = \frac{\varepsilon\psi_0}{a} \times (1 + \kappa a) \tag{4}$$

where σ_0 is the surface charge density, *ε* is the permittivity of deionized water which has a value of 6.95×10^{-10} C/(V m), ψ_0 is the *ζ* potential of nanoparticles (in V), and *a* is the radius of nanoparticles (in m). The Debye−Hückel parameter, *κ*, is defined as

$$\kappa = 2.32 \times 10^{9} \times \left(\sum_{i} c_i z_i^{2}\right)^{1/2} \tag{5}$$

where c_i and z_i denote the ion concentration (in mol/L) and charge, respectively. The estimated values for *c* are 3.16×10^{-7} mol/L (H^+ ions in water at pH 6.5) for bare F8BT nanoparticles and (3.78−5.31) × 10^{-4} mol/L (for Na^+ or the acrylate ion, see the Supporting Information) for the F8BT-PAAC*n* nanoparticles. The *z* value is one due to the presence of monovalent ions.

Cell Culture. Human embryonic kidney 293 cells, HEK 293, were used for the cytotoxicity and cellular uptake studies. The HEK 293 cells were cultured in DMEM containing 10% FBS, and 100 units of penicillin per mL at 37 °C in a humidified atmosphere of 95% air and 5% CO_2.

In Vitro Cytotoxicity Studies. The cytotoxicity of F8BT-PAAC*n* nanoparticles was evaluated using the MTT assay. The HEK 293 cells were seeded in a 96-well plate at a density of 5.0×10^4 cells mL^{-1} and allowed to adhere for 24 h. After removal of the culture medium, 150 *μ*L of fresh culture medium containing F8BT-PAAC*n* nanoparticles was added and allowed to incubate at 37 °C for 24 h. The five concentrations of F8BT-PAAC*n* nanoparticles tested in the culture medium were 5, 10, 15, and 20 ppm in F8BT. After 24 h incubation, 10 *μ*L of MTT (5.0 mg mL^{-1} in PBS) were added and further incubated for 4 h. The medium was then replaced by 150 *μ*L of DMSO to completely dissolve the formazan crystals. The absorbance at 490 nm was measured using an ELX808 Absorbance Microplate Reader. The cell viability was calculated as a percentage of the culture medium only control.

Cellular Uptake of F8BT-PAAC*n* Nanoparticles. The cellular uptake of F8BT-PAAC*n* nanoparticles was characterized using confocal fluorescence microscopy. The HEK 293 cells were seeded in a 6-well plate loaded with cover-glass slides of 25 mm diameter at a density of 5.0×10^4 cells mL^{-1} and allowed to adhere for 24 h. After removal of the culture medium, the HEK 293 cells were incubated in 150 *μ*L of fresh culture medium containing F8BT-PAAC*n* nanoparticles (5 ppm in F8BT) at 37 °C for 24 h. The culture medium containing the F8BT-PAAC*n* nanoparticles was removed and cells were washed with PBS for three times, and then fixed with 4% formaldehyde. The cell membrane was stained using 100 *μ*L of Alexa Fluor 594 (5.0 *μ*g mL^{-1}) for 10 min at 25 °C. After thorough washing with PBS, the cells were incubated with 200 *μ*L of PBS. The fluorescence images were collected using a Leica TCS SP5 confocal laser-scanning microscope. Fluorescent emission spectra were collected for Alexa Fluor 594 (λ_{ex} = 561 nm) and F8BT-PAAC*n* nanoparticles (λ_{ex} = 458 nm) over the wavelength ranges of 600−700 and 500−600 nm, respectively.

RESULTS AND DISCUSSION

The molecular structures of the linear alkyl group substituted poly(acrylate)s are shown in Figure 1 and Figure S1 in the Supporting Information. In this study, the substituted poly(acrylate)s are abbreviated as PAAC*n*, where C*n* represents the alkyl substituent and *n* denotes the number of carbon atoms in the substituent. The ^1H NMR spectra of the synthesized PAAC*n* and the corresponding substitution percentages are shown in Figures S2−S4 in the Supporting Information.

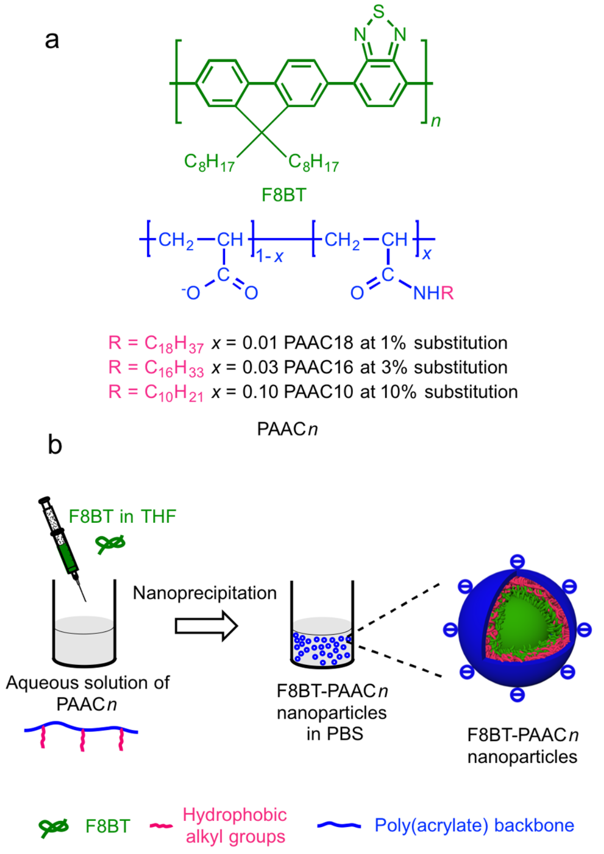

Figure 1. (a) Structures of F8BT and PAAC*n*. (b) Schematic illustration of the preparation of the F8BT-PAAC*n* nanoparticles.

Preparation of F8BT-PAAC*n* Nanoparticles. A wide range of conjugated polymer nanoparticles have been prepared

DOI: 10.1021/acs.macromol.6b02002
Macromolecules 2016, 49, 8530−8539

using nanoprecipitation.[1,4,12,29,30] While such nanoparticles are highly stable in deionized water, they exhibit large-scale aggregation in salt solutions that are ubiquitous in biological systems.[23] Consequently, PAAC*n* is used to stabilize F8BT nanoparticles in PBS, a commonly used buffer with salt concentration similar to physiological conditions. In this study, a modified nanoprecipitation method was employed to prepare stable PBS dispersions of F8BT-PAAC*n* nanoparticles. First, a THF solution of F8BT was injected into an aqueous solution of PAAC*n* under vigorous stirring. After removal of THF, a small quantity of 5 × PBS was then added to the aqueous solution to yield a standard PBS dispersion of F8BT-PAAC*n* nanoparticles. When the solution of F8BT in THF is mixed with an aqueous solution of PAAC*n*, a decrease in F8BT solubility together with hydrophobic interactions within and between F8BT polymer chains cause F8BT aggregation and the formation of hydrophobic F8BT nanoparticles.[31] The hydrophobic alkyl substituents of PAAC*n* subsequently adsorb onto the surface of F8BT nanoparticles, yielding a negatively charged surface. Previously reported strong adsorption of alkyl chain segments of pluronic F-127 and Tween 80 at surface hydrophobic sites of polymer nanoparticles supports the adsorption of the alkyl substituents of PAAC*n* onto surface hydrophobic sites of F8BT nanoparticles.[32] As a consequence of the negatively charged carboxylate groups (Figure 1) on the surface, F8BT-PAAC*n* nanoparticles are stabilized in PBS.

As the potential applications of PAAC*n* in stabilizing F8BT-PAAC*n* nanoparticles are an important consideration, the dependence of the yield of preparing F8BT-PAAC*n* nanoparticles in PBS on the concentration of aqueous solution of either PAAC18 at 1% substitution, PAAC16 at 3% substitution, and PAAC10 at 10% substitution are examined. As shown in Figure 2, all three PAAC*n* are able to adsorb effectively onto the surface of F8BT nanoparticles and stabilize them in PBS, as reflected by the observed high yields at a low PAAC*n* concentration of 50 ppm, while keeping the F8BT concentration at 10 ppm. This concentration is significantly lower than that of SDS (46 000 ppm) used in a recent study to stabilize F8BT nanoparticles.[19] When the concentration of either PAAC18 at 1% substitution or PAAC16 at 3% substitution is increased to 100 ppm, no significant increase in the yields occur, as shown in Figure 2. In contrast, a decreased yield is observed for PAAC10 at 10% substitution upon an increase in concentration. The latter result is attributable to competitive intrachain hydrophobic interactions between decyl substituents, which weaken the hydrophobic interactions between decyl substituent and F8BT nanoparticles, given that a significantly higher number of decyl substituents are present at a concentration of 100 ppm. As a consequence of the results in Figure 2, a PAAC*n* concentration of 50 ppm and F8BT concentration of 10 ppm are used in the subsequent studies.

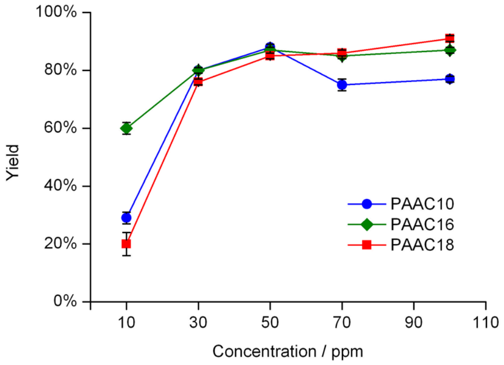

Figure 2. PAAC*n* concentration dependence of yields of F8BT nanoparticles (<200 nm) stabilized with PAAC10 at 10% substitution, PAAC16 at 3% substitution, and PAAC18 at 1% substitution in PBS. The F8BT concentration is 10 ppm.

Optimization of Length and Substitution Percentage of the Alkyl Substituents of PAAC*n*. The length and substitution percentage of the alkyl substituents of PAAC*n* can influence their hydrophobic interactions with the F8BT nanoparticles and thereby influence the adsorption of PAAC*n* onto the F8BT nanoparticle surface. Thus, the length and substitution percentage of the alkyl substituents are optimized according to the yield of F8BT-PAAC*n* nanoparticles in PBS (eq 2), which represents the proportion of F8BT-PAAC*n* nanoparticles with a diameter less than 200 nm. The length of the linear alkyl substituents in PAAC*n* used in the preparation of the F8BT-PAAC*n* nanoparticles has an *n* value of 6, 10, 12, 14, 16, or 18, and the extent of substitution is 1%, 3%, or 10%. Bare F8BT nanoparticles aggregate immediately upon being transferred to PBS, forming aggregates that are larger than 200 nm. The aggregates give a yield of 0, as was also observed by another research group.[23] Similar aggregation of F8BT nanoparticles is also observed in the presence of sodium poly(acrylate), as shown in Figure 3, due to very weak interactions between F8BT and sodium poly(acrylate). However, in the presence of 10% substituted PAAC10, 3% substituted PAAC16 or 1% substituted PAAC18, the yield of F8BT-PAAC*n* nanoparticles in PBS approaches 90%, highlighting the importance of the hydrophobic linear alkyl substituents of PAAC*n* in stabilizing F8BT-PAAC*n* nanoparticles in PBS.

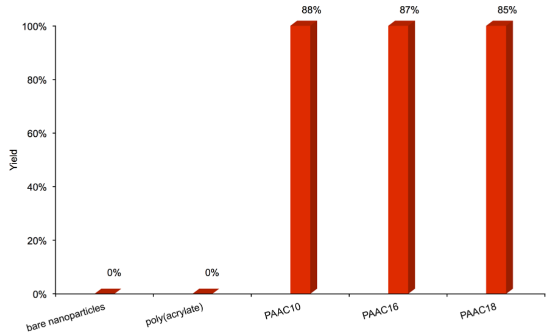

Figure 3. Yields of bare F8BT nanoparticles (<200 nm) and F8BT nanoparticles (<200 nm) stabilized with poly(acrylate), PAAC10 at 10% substitution, PAAC16 at 3% substitution and PAAC18 at 1% substitution in PBS.

The effect of the length of the linear alkyl substituent at a constant 3% substitution for PAAC*n* on the yield of F8BT-PAAC*n* nanoparticles with a diameter of <200 nm is shown in Table 1. The zero yield obtained for PAAC6 indicates that the extent of hydrophobic interaction of the hexyl group with the F8BT nanoparticle surface is insufficient to stabilize the F8BT-PAAC6 nanoparticles. Substitution of the decyl group in PAAC10 results in a 74 ± 1% yield of F8BT-PAAC10 nanoparticles, and further lengthening of the alkyl substituent results in yields of 86 ± 1% and 87 ± 1% for F8BT-PAAC14 and F8BT-PAAC16 nanoparticles, respectively. Additional

Table 1. Yields of F8BT-PAAC*n* Nanoparticles with Diameters <200 nm in PBS.[a]

% substitution	% substituent yield					
	C6	C10	C12	C14	C16	C18
1	–	–	55 ± 1	–	–	85 ± 1
3	0	74 ± 1	83 ± 1	86 ± 1	87 ± 1	83 ± 1
10	80 ± 1	88 ± 1	81 ± 1	–	–	–

[a] The yields are the mean of three independent determinations. The errors represent the standard deviations. A zero yield is obtained in the absence of PAAC*n*.

lengthening of the alkyl substituent results in a decrease in yield to 83 ± 1% for F8BT-PAAC18 nanoparticles, consistent with hydrophobic interactions between the octadecyl groups within PAAC18 competing with hydrophobic interactions between PAAC18 and the F8BT nanoparticle surface. We have previously reported that micelle-like aggregates form in an aqueous solution of 3% substituted PAAC18 at or below a low concentration of 0.3 wt %, or 3000 ppm, through intra-PAAC18 hydrophobic octadecyl substituent interactions.[33] However, a viscous gel-like solution is observed at or above a high concentration of 2 wt % of 3% substituted PAAC18 due to inter-PAAC18 hydrophobic interactions between octadecyl substituents.[34] In the present study, because of the relatively low 50 ppm concentration of PAAC18, it is expected that only intra-PAAC18 chain hydrophobic octadecyl substituent interactions are involved.

The substitution percentage on the backbone of PAAC*n* also has an important role in stabilizing F8BT-PAAC*n* nanoparticles, as seen from Table 1. As the level of substitution increases from 3% to 10% in PAAC6, the yield of F8BT-PAAC6 nanoparticles increases substantially from 0% to 80 ± 1%. The increased substitution strengthens the hydrophobic interactions between the hexyl groups and F8BT nanoparticles as a result of the higher hexyl substituent density compensating for the lower hexyl hydrophobicity than those of longer alkyl groups. Similarly, for PAAC10 the yield increases from 74 ± 1% at 3% substitution to 88 ± 1% at 10% substitution. However, for PAAC12 an increase in substitution of 1%, 3% to 10% coincides with a change in yield of 55 ± 1%, 83 ± 1% to 81 ± 1%, respectively. The similarity between the yields at 3% and 10% substitution implies a weakening of the hydrophobic interactions between the dodecyl substituents and F8BT nanoparticles as a consequence of increasing competitive intersubstituent interactions owing to the increased dodecyl substituent density. A similar effect is seen when the octadecyl substituent substitution increases from 1% to 3% in PAAC18 and the yield changes from 85 ± 1% to 83 ± 1%, respectively. Thus, the overall effect of the length and substitution percentage of the alkyl substituent determines the effectiveness of the PAAC*n*-stabilizing F8BT nanoparticles in PBS.

In summary, PAAC10 at 10% substitution, PAAC16 at 3% substitution, and PAAC18 at 1% substitution show similarly high yields (Figure 3) of 88 ± 1%, 87 ± 1%, and 85 ± 1%, at a low concentration of 50 ppm, and accordingly this concentration is used to prepare F8BT-PAAC*n* nanoparticles for further characterizations. In addition to their stabilizing effect, the PAAC*n* contain a high number of carboxylate groups, which are potential reactive sites for conjugation to functional biomolecules through well-established amide formation reaction. Jin et al. reported the preparation of conjugated polymer nanoparticles adsorbed with polyelectrolytes, which involved employment of two polyelectrolytes, poly(styrenesulfonate) as a stabilizer and poly(sodium methacrylate) to provide carboxylate groups as reactive sites for further bioconjugation.[23] In contrast, PAAC*n* surface functionalization offers the dual functions of offering stabilization and providing bioconjugation sites. Moreover, as the adsorption of PAAC*n* onto F8BT nanoparticles involves only hydrophobic interactions, PAAC*n* can be useful stabilizers for other polymer nanoparticles or aggregates of organic materials.

Surface Charge, Size, and Colloidal Stability of F8BT-PAAC*n* Nanoparticles. The negative surface charge of F8BT nanoparticles in deionized water are evident from their ζ potentials of −26 ± 2, −57 ± 2, −58 ± 2, and −57 ± 4 mV for bare F8BT nanoparticles, F8BT-PAAC10, F8BT-PAAC16, and F8BT-PAAC18 nanoparticles, respectively, in deionized water; the substitution percentages of PAAC10, PAAC16, and PAAC18 are 10%, 3%, and 1%, respectively. For bare conjugated polymer nanoparticles, the negatively charged surface has been attributed to surface chemical defects as a consequence of oxidation of the conjugated polymer in the formation of conjugated polymer nanoparticles.[35] In comparison with bare F8BT nanoparticles, the F8BT-PAAC10, F8BT-PAAC16, and F8BT-PAAC18 nanoparticles have more negatively charged surfaces, as indicated by their more negative ζ potentials (Figure 4a). These results are consistent with a high number of negatively charged carboxylate groups on the surface of the F8BT-PAAC*n* nanoparticles due to the presence of PAAC*n*.

The hydrodynamic diameters of bare F8BT nanoparticles and F8BT-PAAC*n* nanoparticles were measured using dynamic light scattering. Bare F8BT nanoparticles in deionized water have a hydrodynamic diameter of 39 ± 3 nm, while F8BT-PAAC10, F8BT-PAAC16, and F8BT-PAAC18 nanoparticles in PBS have hydrodynamic diameters of 49 ± 5, 57 ± 3, and 70 ± 3 nm, respectively (Figure 4b). The larger hydrodynamic diameters of the F8BT-PAAC*n* nanoparticles in PBS than that of bare F8BT nanoparticles in deionized water are presumably due to the presence of PAAC*n* on the surface. Figure 4c shows the transmission electron microscopy (TEM) images of the nanoparticles by using the negative stain uranyl acetate. The spherical F8BT-PAAC10 nanoparticles appear as bright features surrounded by dark rings as a result of negative staining. Similarly, bare F8BT, F8BT-PAAC16, and F8BT-PAAC18 nanoparticles, all exhibit spherical morphologies, as shown in Figure S5 in the Supporting Information. The size of the F8BT-PAAC*n* nanoparticles in PBS increases slightly in the order: F8BT-PAAC10 < F8BT-PAAC16 < F8BT-PAAC18. This result is consistent with strong binding between F8BT nanoparticles and PAAC10 (at 10% substitution) and a relatively weaker association of F8BT nanoparticles with PAAC18 (at 1% substitution). This trend indicates that the higher alkyl substitution (10%) in PAAC10 enhances the hydrophobic interactions with F8BT nanoparticles and compensates for the weaker interaction between the decyl substituent and the F8BT

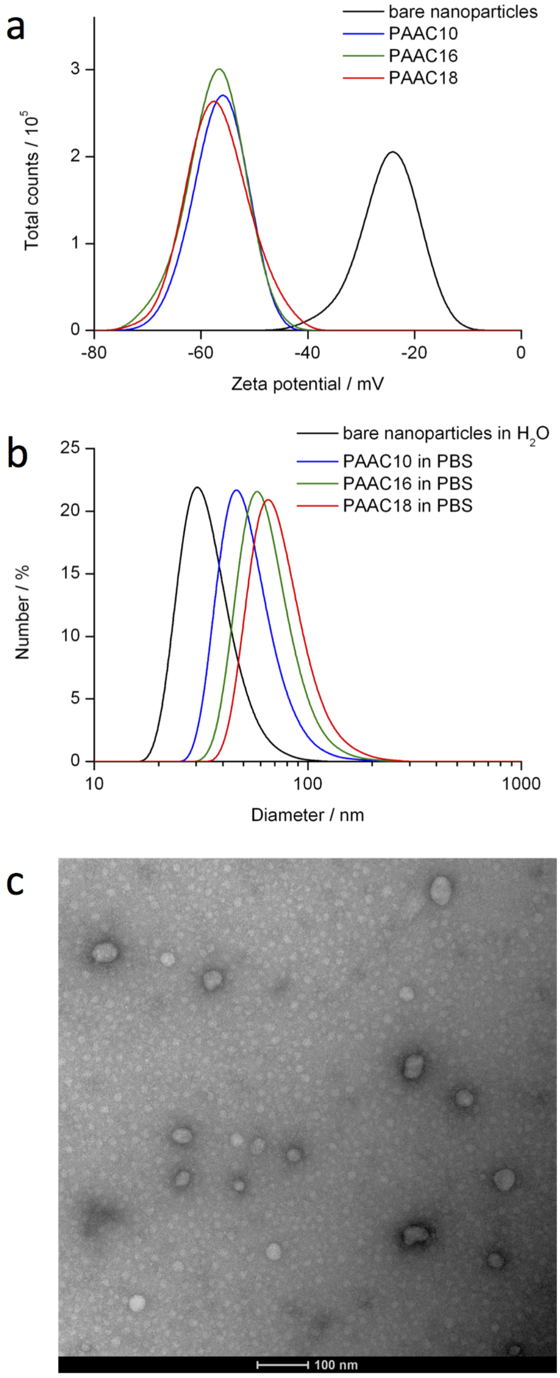

Figure 4. (a) ζ potentials and (b) hydrodynamic diameters of bare F8BT nanoparticles in deionized water and F8BT nanoparticles stabilized with either PAAC10 at 10% substitution, PAAC16 at 3% substitution or PAAC18 at 1% substitution in PBS. (c) TEM images of F8BT nanoparticles stabilized with PAAC10 at 10% substitution.

nanoparticle in comparison with the stronger interaction of the octadecyl substituent of PAAC18 (at 1% substitution).

Given the ζ potentials and hydrodynamic diameters of F8BT and the F8BT-PAAC*n* nanoparticles, the surface charge densities of these nanoparticles can be determined using an established model as shown in eqs 4 and 5.[28] For bare F8BT nanoparticles, F8BT-PAAC10, F8BT-PAAC16, and F8BT-PAAC18 nanoparticles, the surface charge densities are -0.95×10^{-3}, -4.14×10^{-3}, -4.24×10^{-3}, and -4.04×10^{-3} C/m^2, respectively. These results show that the surface charge densities of the F8BT-PAAC*n* nanoparticles are approximately 4.3 times higher than that of bare F8BT nanoparticles, giving rise to the colloidal stability of F8BT-PAAC*n* nanoparticles in PBS.

The small size and long-term dispersion and colloidal stability of F8BT nanoparticles are critical characteristics for their biological imaging application. Figure S6 in the Supporting Information shows the F8BT nanoparticle size variation over a 4-week period. Bare F8BT nanoparticles in deionized water remain stable over 4 weeks without detectable size variations owing to a substantial ζ potential of −26 ± 2 mV. Similar colloidal stability has been reported for other conjugated polymer nanoparticles in deionized water.[1] In contrast, bare F8BT nanoparticles exhibit significant aggregation in PBS yielding aggregates with a diameter greater than 200 nm, which is attributable to the ions in PBS providing a strong shielding effect of the negative surface charge of F8BT nanoparticles. However, when stabilized with PAAC*n* the resultant F8BT-PAAC*n* nanoparticles exhibit remarkable colloidal stability in PBS. As shown in Figure S6 in the Supporting Information, the F8BT-PAAC10, F8BT-PAAC16, and F8BT-PAAC18 nanoparticles are very stable over 4 weeks without any aggregation. These results indicate the adsorption of either PAAC10, PAAC16, or PAAC18 on the F8BT nanoparticle surface, producing a negatively charged surface that greatly enhances their dispersion and colloidal stability. The enhanced colloidal stability also offers the possibility to increase the concentration of the F8BT-PAAC*n* nanoparticles in deionized water to achieve practical applications, which typically require concentrations on the order of millimolar. We have prepared a solution at a concentration of ∼2 mM of F8BT monomers, which is promising for applications including fabrication of water-based nanoparticulate solar cells and potentially organic light emitting diodes.[36,37] Furthermore, regarding colloidal stability, it is anticipated that the molecular weight of F8BT will have an influence on the ability of PAAC*n* to stabilize F8BT nanoparticles. The molecular weight of the conjugated polymer is expected to show a correlation with the alkyl chain length and substitution percentage. This relationship is likely to be explored in a future study. In summary, the small size, high colloidal stability and negative surface charge of the F8BT-PAAC*n* nanoparticles pave the way for the deployment of these nanoparticles in biological imaging applications.

Fluorescence and Cell Imaging Applications. The normalized UV−visible absorption and fluorescence spectra of bare F8BT nanoparticles in deionized water and F8BT-PAAC16 nanoparticles in PBS are shown in Figure 5. The absorption and fluorescence spectra of F8BT-PAAC16 nanoparticles in PBS are similar to those of bare F8BT nanoparticles in deionized water. Similar absorption and fluorescence spectra are also observed for F8BT-PAAC18 and F8BT-PAAC10 nanoparticles in PBS (Figure S8 and S9 in the Supporting Information). In several studies the optical properties of conjugated polymer nanoparticles have been investigated and related to the polymer conformation in the nanoparticle, conjugation length of chromophores, intra- and interpolymer strand aggregation.[38−40] The similar absorption and fluorescence spectra of F8BT nanoparticles with and without PAAC*n* suggest that the nanoparticle has similar polymer chain conformation, packing and folding under both conditions.

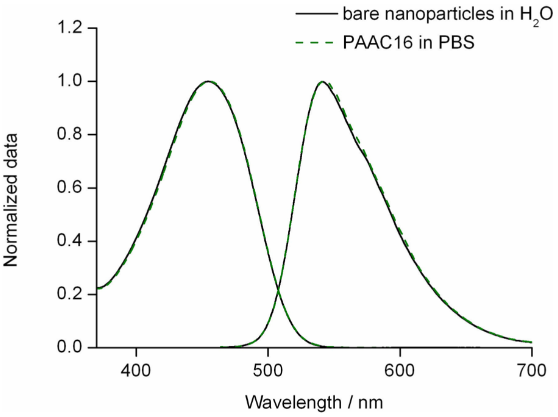

Figure 5. Normalized absorption and fluorescence spectra of bare F8BT nanoparticles (solid) and F8BT nanoparticles stabilized with PAAC16 at 3% substitution (dashed).

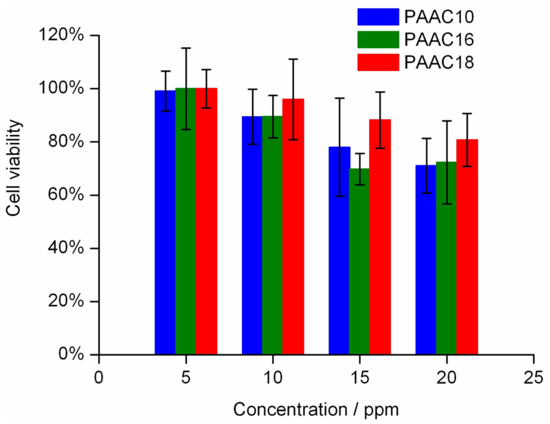

Figure 6. Viability of HEK 293 cells incubated with F8BT nanoparticles stabilized with PAAC18 at 1% substitution, PAAC16 at 3% substitution, and PAAC10 at 10% substitution at concentrations ranging from 0 to 25 ppm, as determined using the MTT assay.

Thus, the presence of PAAC*n* does not interfere the formation of F8BT nanoparticles, indicating that the alkyl substituents are predominantly adsorbed onto the hydrophobic sites on the surface of the F8BT nanoparticle and do not penetrate deeply into the nanoparticle. This phenomenon has implications on the fluorescence quantum yields of bare F8BT nanoparticles in deionized water and F8BT-PAAC*n* nanoparticles in PBS. The fluorescence quantum yields of bare F8BT nanoparticles in deionized water, F8BT-PAAC18 nanoparticles, F8BT-PAAC16, and F8BT-PAAC10 nanoparticles in PBS are 24 ± 1%, 25 ± 1%, 26 ± 1%, and 27 ± 1%, respectively. The fluorescence quantum yield values from this study are comparable with literature values of 28%[22] and 30%.[2,19] The similar fluorescence quantum yields of F8BT nanoparticles in deionized water and F8BT-PAAC*n* nanoparticles in PBS indicate that the emitting chromophores of F8BT-PAAC*n* nanoparticles are located near the core of the nanoparticles such that the influence exerted by the alkyl substituents on the surface of the F8BT-PAAC*n* nanoparticles is negligible. This interpretation is consistent with a recent study showing that the emitting chromophores of a conjugated polymer aggregate are located near the core and away from the surface of the aggregate.[41]

In this study, the biocompatibility of F8BT-PAAC*n* nanoparticles for future biological imaging applications is also reported. The cytotoxicities of F8BT-PAAC*n* nanoparticles toward HEK 293 cells are assessed using the MTT assay. The viability of HEK 293 cells incubated with F8BT-PAAC18, F8BT-PAAC16 and F8BT-PAAC10 nanoparticles at concentrations ranging from 0 to 20 ppm for 24 h is shown in Figure 6. No significant cytotoxicities toward HEK 293 cells are observed for these nanoparticles, although there is a minor decrease in cell viability as a function of concentration. With a concentration of 20 ppm and an incubation period of 24 h, HEK 293 cells exhibit a cell viability value of approximately 70% for F8BT-PAAC16 and F8BT-PAAC10 nanoparticles and approximately 80% for F8BT-PAAC18 nanoparticles. The cell viability results reported herein are consistent with those reported in other studies.[19,42] For instance, Christensen et al. showed that bare F8BT nanoparticles (with a molecular weight of 10000 g mol^{-1}) had no discernible impact on the viability and growth of J774A.1 cells after 18 h incubation at a concentration ranging from 1 to 25 ppm.[42] In their study, a cell viability of approximately 75% was observed for bare F8BT nanoparticles at 25 ppm.[42] In addition, Dailey et al. found that F8BT nanoparticles stabilized with sodium dodecyl sulfate (F8BT-SDS nanoparticles) were highly biocompatible toward J774A.1 cells over the concentration range of 0 to 100 ppm.[19] A cell viability of 80% was observed when J774A.1 cells were incubated with 100 ppm of F8BT-SDS nanoparticles for 24 h. Overall, the results of the present study show that the F8BT-PAAC*n* nanoparticles have low toxicity and are suitable for biological applications.

As F8BT-PAAC*n* nanoparticles are of potential use in intracellular imaging[1] and drug delivery,[15,16] we examine their uptake by HEK 293 cells. Confocal fluorescence microscopy images of HEK 293 cells treated with F8BT-PAAC18, F8BT-PAAC16 and F8BT-PAAC10 nanoparticles, respectively, show a strong green fluorescence in the range 500−600 nm in the cell cytoplasm (Figure 7). Figure S10 in the Supporting Information shows the images from a separate study, in which the cell membranes of HEK 293 cells were stained with Alexa Fluor 594. These images show that the F8BT-PAAC*n* nanoparticles are located on the same focal plane as the membrane, which further support the internalization of F8BT-PAAC*n* nanoparticles by HEK 293 cells. These results strongly suggest the feasibility of using F8BT-PAAC*n* nanoparticles as fluorescence labels for cell imaging.

The mechanism of cellular uptake of bare F8BT nanoparticles (with a molecular weight of 10000 g mol^{-1}) by J774 A.1 cells has been investigated by Christensen et al. These authors showed that F8BT nanoparticles previously treated with a number of pharmacological reagents exhibit inhibition of specific cellular process.[42] They reported a significant inhibition of F8BT nanoparticle uptake for nanoparticles treated with wortmannin, LY294002, and methyl-β-cyclodextrin. This result is consistent with F8BT nanoparticle uptake occurring through a constitutive macropinocytosis mechanism. It is likely that a similar mechanism is involved in the uptake of F8BT-PAAC*n* nanoparticles. It is anticipated that loading of multifunctional materials or therapeutic agents into the F8BT-PAAC*n* nanoparticle may enable its future applications in diagnosis or therapeutics.

■ CONCLUSION

We report the preparation of highly fluorescent and stable F8BT-PAAC*n* nanoparticles with hydrodynamic diameters

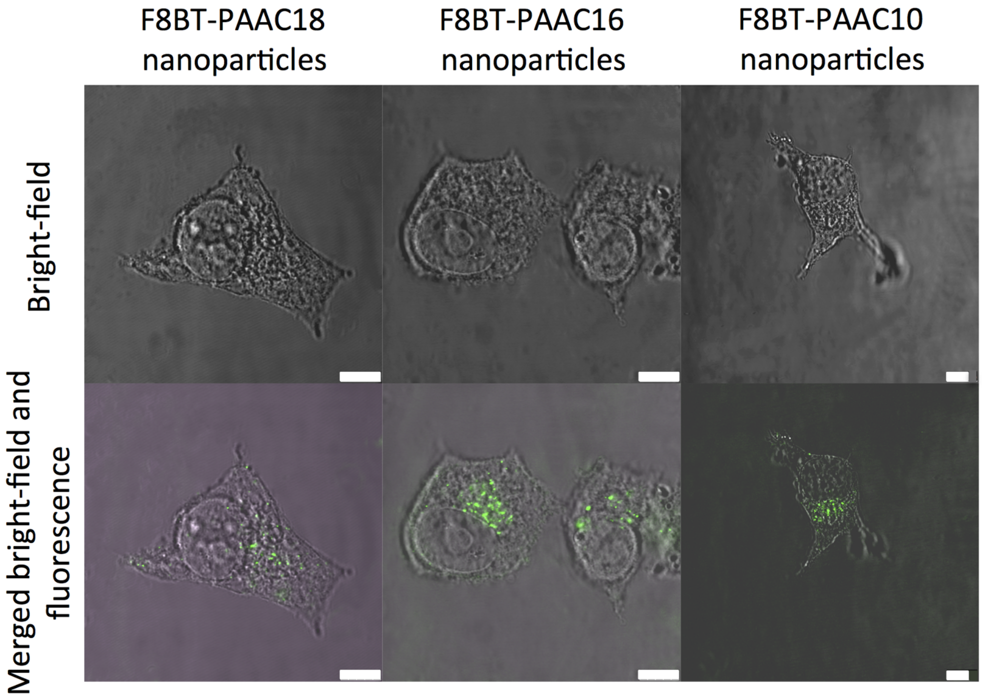

Figure 7. Bright-field images and confocal fluorescence images of HEK 293 cells treated with F8BT nanoparticles stabilized with PAAC18 at 1% substitution, PAAC16 at 3% substitution, and PAAC10 at 10% substitution, respectively. In the merged bright field and fluorescence images, the green emission is derived from F8BT-PAAC*n* nanoparticles. Scale bar: 7.5 μm.

ranging from 49 ± 5 to 70 ± 3 nm. The successful functionalization of PAAC*n* onto the surface of F8BT nanoparticles is based on the association of the alkyl substituents, C*n*, with the hydrophobic sites on the F8BT nanoparticle surface. In contrast to the rapid, large-scale aggregation of bare F8BT nanoparticles in PBS, a high colloidal stability of F8BT-PAAC*n* nanoparticles in PBS is observed, as indicated by a negligible size variation over a 4-week period. This high colloidal stability under the condition of high ionic strength is ascribed to a high surface charge density as a consequence of the PAAC*n* adsorption bearing a large number of carboxylate groups. In addition, F8BT-PAAC*n* nanoparticles show low toxicity to HEK 293 cells and are easily internalized by these cells. Consequently, F8BT-PAAC*n* nanoparticles hold considerable promise for use in cell imaging applications given their high colloidal stability in PBS and high fluorescence quantum yields.

■ ASSOCIATED CONTENT

Ⓢ Supporting Information

The Supporting Information is available free of charge on the ACS Publications website at DOI: 10.1021/acs.macromol.6b02002.

> Molecular structures and NMR spectra of PAAC*n*, TEM images of bare F8BT, F8BT-PAAC16, and F8BT-PAAC18 nanoparticles, size variation of bare F8BT and F8BT-PAAC*n* nanoparticles over 4 weeks, an image of a highly concentrated F8BT nanoparticle solution, absorption and fluorescence spectra of F8BT-PAAC18 and F8BT-PAAC10 nanoparticles, the confocal fluorescence microscopy images in which the green fluorescence from F8BT-PAAC*n* nanoparticles and the red fluorescence from cell membranes stained with Alexa Fluor 594 are merged, and calculations of ion concentrations (PDF)

■ AUTHOR INFORMATION

Corresponding Author

*(T.W.K.) E-mail: tak.kee@adelaide.edu.au.

Present Address

[§]Femtosecond Spectroscopy Unit, Okinawa Institute of Science and Technology Graduate University, Onna, Okinawa 904−0495, Japan

Notes

The authors declare no competing financial interest.

■ ACKNOWLEDGMENTS

This work was supported by research grants from the Australian Research Council (DP0878100). We are grateful to Dr. Qiuhong Hu for her assistance with dynamic light scattering characterization and Ms. Lyn Waterhouse at Adelaide Microscopy at the University of Adelaide for her help in TEM characterization. We also thank Mr. Thomas Fabig for his contributions in preparing nanoparticle samples.

■ REFERENCES

(1) Wu, C.; Bull, B.; Szymanski, C.; Christensen, K.; McNeill, J. Multicolor Conjugated Polymer Dots for Biological Fluorescence Imaging. *ACS Nano* **2008**, *2*, 2415−2423.

(2) Wu, C.; Schneider, T.; Zeigler, M.; Yu, J.; Schiro, P. G.; Burnham, D. R.; McNeill, J. D.; Chiu, D. T. Bioconjugation of Ultrabright Semiconducting Polymer Dots for Specific Cellular Targeting. *J. Am. Chem. Soc.* **2010**, *132*, 15410−15417.

(3) Yu, J.; Wu, C.; Zhang, X.; Ye, F.; Gallina, M. E.; Rong, Y.; Wu, I. C.; Sun, W.; Chan, Y.-H.; Chiu, D. T. Stable Functionalization of Small Semiconducting Polymer Dots via Covalent Cross-Linking and Their

Application for Specific Cellular Imaging. *Adv. Mater.* **2012**, *24*, 3498−3504.

(4) Liu, H.-Y.; Wu, P.-J.; Kuo, S.-Y.; Chen, C.-P.; Chang, E.-H.; Wu, C.-Y.; Chan, Y.-H. Quinoxaline-Based Polymer Dots with Ultrabright Red to Near-Infrared Fluorescence for In Vivo Biological Imaging. *J. Am. Chem. Soc.* **2015**, *137*, 10420−10429.

(5) Chen, C.-P.; Huang, Y.-C.; Liou, S.-Y.; Wu, P.-J.; Kuo, S.-Y.; Chan, Y.-H. Near-Infrared Fluorescent Semiconducting Polymer Dots with High Brightness and Pronounced Effect of Positioning Alkyl Chains on the Comonomers. *ACS Appl. Mater. Interfaces* **2014**, *6*, 21585−21595.

(6) Jin, Y.; Ye, F.; Zeigler, M.; Wu, C.; Chiu, D. T. Near-Infrared Fluorescent Dye-Doped Semiconducting Polymer Dots. *ACS Nano* **2011**, *5*, 1468−1475.

(7) Chan, Y.-H.; Ye, F.; Gallina, M. E.; Zhang, X.; Jin, Y.; Wu, I. C.; Chiu, D. T. Hybrid Semiconducting Polymer Dot−Quantum Dot with Narrow-Band Emission, Near-Infrared Fluorescence, and High Brightness. *J. Am. Chem. Soc.* **2012**, *134*, 7309−7312.

(8) Chan, Y.-H.; Wu, C.; Ye, F.; Jin, Y.; Smith, P. B.; Chiu, D. T. Development of Ultrabright Semiconducting Polymer Dots for Ratiometric pH Sensing. *Anal. Chem.* **2011**, *83*, 1448−1455.

(9) Czaplyski, W. L.; Purnell, G. E.; Roberts, C. A.; Allred, R. M.; Harbron, E. J. Substituent Effects on the Turn-on Kinetics of Rhodamine-Based Fluorescent pH Probes. *Org. Biomol. Chem.* **2014**, *12*, 526−533.

(10) Ye, F.; Wu, C.; Jin, Y.; Chan, Y.-H.; Zhang, X.; Chiu, D. T. Ratiometric Temperature Sensing with Semiconducting Polymer Dots. *J. Am. Chem. Soc.* **2011**, *133*, 8146−8149.

(11) Wu, C.; Bull, B.; Christensen, K.; McNeill, J. Ratiometric Single-Nanoparticle Oxygen Sensors for Biological Imaging. *Angew. Chem., Int. Ed.* **2009**, *48*, 2741−2745.

(12) Dmitriev, R. I.; Borisov, S. M.; Düssmann, H.; Sun, S.; Müller, B. J.; Prehn, J.; Baklaushev, V. P.; Klimant, I.; Papkovsky, D. B. Versatile Conjugated Polymer Nanoparticles for High-Resolution O2 Imaging in Cells and 3D Tissue Models. *ACS Nano* **2015**, *9*, 5275−5288.

(13) Huang, Y.-C.; Chen, C.-P.; Wu, P.-J.; Kuo, S.-Y.; Chan, Y.-H. Coumarin Dye-Embedded Semiconducting Polymer Dots for Ratiometric Sensing of Fluoride Ions in Aqueous Solution and Bio-Imaging in Cells. *J. Mater. Chem. B* **2014**, *2*, 6188−6191.

(14) Childress, E. S.; Roberts, C. A.; Sherwood, D. Y.; LeGuyader, C. L. M.; Harbron, E. J. Ratiometric Fluorescence Detection of Mercury Ions in Water by Conjugated Polymer Nanoparticles. *Anal. Chem.* **2012**, *84*, 1235−1239.

(15) Feng, X.; Lv, F.; Liu, L.; Tang, H.; Xing, C.; Yang, Q.; Wang, S. Conjugated Polymer Nanoparticles for Drug Delivery and Imaging. *ACS Appl. Mater. Interfaces* **2010**, *2*, 2429−2435.

(16) Yuan, Y.; Wang, Z.; Cai, P.; Liu, J.; Liao, L.-D.; Hong, M.; Chen, X.; Thakor, N.; Liu, B. Conjugated Polymer and Drug Co-Encapsulated Nanoparticles for Chemo- and Photo-Thermal Combination Therapy with Two-Photon Regulated Fast Drug Release. *Nanoscale* **2015**, *7*, 3067−3076.

(17) Geng, J.; Sun, C.; Liu, J.; Liao, L.-D.; Yuan, Y.; Thakor, N.; Wang, J.; Liu, B. Biocompatible Conjugated Polymer Nanoparticles for Efficient Photothermal Tumor Therapy. *Small* **2015**, *11*, 1603−1610.

(18) Shen, X.; Li, L.; Wu, H.; Yao, S. Q.; Xu, Q.-H. Photosensitizer-Doped Conjugated Polymer Nanoparticles for Simultaneous Two-Photon Imaging and Two-Photon Photodynamic Therapy in Living Cells. *Nanoscale* **2011**, *3*, 5140−5146.

(19) Ahmad Khanbeigi, R.; Abelha, T. F.; Woods, A.; Rastoin, O.; Harvey, R. D.; Jones, M.-C.; Forbes, B.; Green, M. A.; Collins, H.; Dailey, L. A. Surface Chemistry of Photoluminescent F8BT Conjugated Polymer Nanoparticles Determines Protein Corona Formation and Internalization by Phagocytic Cells. *Biomacromolecules* **2015**, *16*, 733−742.

(20) Pu, K.; Shuhendler, A. J.; Valta, M. P.; Cui, L.; Saar, M.; Peehl, D. M.; Rao, J. Phosphorylcholine-Coated Semiconducting Polymer Nanoparticles as Rapid and Efficient Labeling Agents for In Vivo Cell Tracking. *Adv. Healthcare Mater.* **2014**, *3*, 1292−1298.

(21) Pu, K.; Shuhendler, A. J.; Jokerst, J. V.; Mei, J.; Gambhir, S. S.; Bao, Z.; Rao, J. Semiconducting Polymer Nanoparticles as Photoacoustic Molecular Imaging Probes in Living Mice. *Nat. Nanotechnol.* **2014**, *9*, 233−239.

(22) Wu, C.; Jin, Y.; Schneider, T.; Burnham, D. R.; Smith, P. B.; Chiu, D. T. Ultrabright and Bioorthogonal Labeling of Cellular Targets Using Semiconducting Polymer Dots and Click Chemistry. *Angew. Chem., Int. Ed.* **2010**, *49*, 9436−9440.

(23) Jin, Y.; Ye, F.; Wu, C.; Chan, Y.-H.; Chiu, D. T. Generation of Functionalized and Robust Semiconducting Polymer Dots with Polyelectrolytes. *Chem. Commun.* **2012**, *48*, 3161−3163.

(24) Davis, M. E.; Chen, Z.; Shin, D. M. Nanoparticle Therapeutics: An Emerging Treatment Modality for Cancer. *Nat. Rev. Drug Discovery* **2008**, *7*, 771−782.

(25) Wang, S.; Huang, P.; Chen, X. Stimuli-Responsive Programmed Specific Targeting in Nanomedicine. *ACS Nano* **2016**, *10*, 2991−2994.

(26) Guo, X.; Abdala, A. A.; May, B. L.; Lincoln, S. F.; Khan, S. A.; Prud'Homme, R. K. Novel Associative Polymer Networks Based on Cyclodextrin Inclusion Compounds. *Macromolecules* **2005**, *38*, 3037.

(27) Würth, C.; Grabolle, M.; Pauli, J.; Spieles, M.; Resch-Genger, U. Relative and Absolute Determination of Fluorescence Quantum Yields of Transparent Samples. *Nat. Protoc.* **2013**, *8*, 1535−1550.

(28) Elimelech, M.; Gregory, J.; Jia, X. *Particle Deposition and Aggregation: Measurement, Modelling and Simulation*; Butterworth-Heinemann: Oxford, England, 2013.

(29) Wu, C.; Szymanski, C.; McNeill, J. Preparation and Encapsulation of Highly Fluorescent Conjugated Polymer Nanoparticles. *Langmuir* **2006**, *22*, 2956−2960.

(30) Wu, C.; Szymanski, C.; Cain, Z.; McNeill, J. Conjugated Polymer Dots for Multiphoton Fluorescence Imaging. *J. Am. Chem. Soc.* **2007**, *129*, 12904−12905.

(31) Wu, C.; Chiu, D. T. Highly Fluorescent Semiconducting Polymer Dots for Biology and Medicine. *Angew. Chem., Int. Ed.* **2013**, *52*, 3086−3109.

(32) Reisch, A.; Runser, A.; Arntz, Y.; Mély, Y.; Klymchenko, A. S. Charge-Controlled Nanoprecipitation as a Modular Approach to Ultrasmall Polymer Nanocarriers: Making Bright and Stable Nanoparticles. *ACS Nano* **2015**, *9*, 5104−5116.

(33) Harada, T.; Pham, D.-T.; Lincoln, S. F.; Kee, T. W. The Capture and Stabilization of Curcumin Using Hydrophobically Modified Polyacrylate Aggregates and Hydrogels. *J. Phys. Chem. B* **2014**, *118*, 9515−9523.

(34) Li, L.; Guo, X.; Fu, L.; Prud'homme, R. K.; Lincoln, S. F. Complexation Behavior of α-, β-, and γ-Cyclodextrin in Modulating and Constructing Polymer Networks. *Langmuir* **2008**, *24*, 8290−8296.

(35) Clafton, S. N.; Beattie, D. A.; Mierczynska-Vasilev, A.; Acres, R. G.; Morgan, A. C.; Kee, T. W. Chemical Defects in the Highly Fluorescent Conjugated Polymer Dots. *Langmuir* **2010**, *26*, 17785−17789.

(36) Nicolaidis, N.; Vaughan, B.; Mulligan, C. J.; Bryant, G.; Zillger, T.; Trnovec, B.; Hübler, A. C.; Holmes, N.; Cooling, N. A.; Griffith, M. J.; Bilen, C.; Kumar, P.; Feron, K.; Zhou, X.; Elkington, D.; Belcher, W. J.; Dastoor, P. C. Solution Processable Interface Materials for Nanoparticulate Organic Photovoltaic Devices. *Appl. Phys. Lett.* **2014**, *104*, 043902.

(37) Andersen, T. R.; Larsen-Olsen, T. T.; Andreasen, B.; Böttiger, A. P. L.; Carlé, J. E.; Helgesen, M.; Bundgaard, E.; Norrman, K.; Andreasen, J. W.; Jørgensen, M.; Krebs, F. C. Aqueous Processing of Low-Band-Gap Polymer Solar Cells Using Roll-to-Roll Methods. *ACS Nano* **2011**, *5*, 4188−4196.

(38) Sun, K.; Chen, H.; Wang, L.; Yin, S.; Wang, H.; Xu, G.; Chen, D.; Zhang, X.; Wu, C.; Qin, W. Size-Dependent Property and Cell Labeling of Semiconducting Polymer Dots. *ACS Appl. Mater. Interfaces* **2014**, *6*, 10802−10812.

(39) Nguyen, T.-Q.; Doan, V.; Schwartz, B. J. Conjugated Polymer Aggregates in Solution: Control of Interchain Interactions. *J. Chem. Phys.* **1999**, *110*, 4068−4078.

(40) Nguyen, T.-Q.; Martini, I. B.; Liu, J.; Schwartz, B. J. Controlling Interchain Interactions in Conjugated Polymers: The Effects of Chain

DOI: 10.1021/acs.macromol.6b02002
Macromolecules 2016, 49, 8530−8539

Morphology on Exciton-Exciton Annihilation and Aggregation in MEH-PPV Films. *J. Phys. Chem. B* **2000**, *104*, 237−255.

(41) Tapping, P. C.; Clafton, S. N.; Schwarz, K. N.; Kee, T. W.; Huang, D. M. Molecular-Level Details of Morphology-Dependent Exciton Migration in Poly(3-hexylthiophene) Nanostructures. *J. Phys. Chem. C* **2015**, *119*, 7047−7059.

(42) Fernando, L. P.; Kandel, P. K.; Yu, J.; McNeill, J.; Ackroyd, P. C.; Christensen, K. A. Mechanism of Cellular Uptake of Highly Fluorescent Conjugated Polymer Nanoparticles. *Biomacromolecules* **2010**, *11*, 2675−2682.

Statement of Authorship

Title of Paper	Recent development for multicellular spheroids culture for bioapplications	
Publication Status	☐ Published ☐ Submitted for Publication	☐ Accepted for Publication ☑ Unpublished and Unsubmitted work written in manuscript style
Publication Details		

Principal Author

Name of Principal Author (Candidate)	Xiaolin Cui		
Contribution to the Paper	Write the paper		
Overall percentage (%)	90		
Certification:	This paper reports on original research I conducted during the period of my Higher Degree by Research candidature and is not subject to any obligations or contractual agreements with a third party that would constrain its inclusion in this thesis. I am the primary author of this paper.		
Signature		Date	05/09/2016

Co-Author Contributions

By signing the Statement of Authorship, each author certifies that:

i. the candidate's stated contribution to the publication is accurate (as detailed above);

ii. permission is granted for the candidate in include the publication in the thesis; and

iii. the sum of all co-author contributions is equal to 100% less the candidate's stated contribution.

Name of Co-Author	Dr. Yusak Hartanto		
Contribution to the Paper	Give advice on polymer scaffold		
Signature		Date	05/09/2016

Name of Co-Author	A/Prof. Jingxiu Bi		
Contribution to the Paper	Give advice on searching for reference		
Signature		Date	29/09/2016

Please cut and paste additional co-author panels here as required.

Name of Co-Author	A/Prof. Sheng Dai		
Contribution to the Paper	Give advice on writing		
Signature		Date	29/09/2016

Name of Co-Author	Dr Hu Zhang		
Contribution to the Paper	Help revise paper		
Signature		Date	30/09/2016

Statement of Authorship

Title of Paper	A Mechanistic Study on Tumour Spheroids Formation in the Thermosensitive Hydrogels: Experiments and Mathematical Modelling
Publication Status	☑ Published ☐ Accepted for Publication ☐ Submitted for Publication ☐ Unpublished and Unsubmitted work written in manuscript style
Publication Details	X. Cui, S. Dini, S. Dai, J. Bi, B.J. Binder, J.E.F. Green and H. Zhang, RSC Adv, 2016, 6, 73282–73291 DOI: 10.1039/C6RA11699J

Principal Author

Name of Principal Author (Candidate)	Xiaolin Cui		
Contribution to the Paper	Designed and performed experiments, analysed results and wrote the manuscript.		
Overall percentage (%)	60		
Certification:	This paper reports on original research I conducted during the period of my Higher Degree by Research candidature and is not subject to any obligations or contractual agreements with a third party that would constrain its inclusion in this thesis. I am the primary author of this paper.		
Signature		Date	09/08/2016

Co-Author Contributions

By signing the Statement of Authorship, each author certifies that:

i. the candidate's stated contribution to the publication is accurate (as detailed above);

ii. permission is granted for the candidate in include the publication in the thesis; and

iii. the sum of all co-author contributions is equal to 100% less the candidate's stated contribution.

Name of Co-Author	Saber Dini		
Contribution to the Paper	Design and performed simulation part		
Signature		Date	25/07/2016

Name of Co-Author	Sheng Dai		
Contribution to the Paper	Help with material synthesis part		
Signature		Date	29/09/2016.

Name of Co-Author	Jingxiu Bi		
Contribution to the Paper	Give advice on cell culture part		
Signature		Date	29/09/2016

Name of Co-Author	Benjamin Binder		
Contribution to the Paper	Design simulation part and revise manuscript		
Signature		Date	25/07/2016

Name of Co-Author	Edward Green		
Contribution to the Paper	Design simulation part and revise manuscript		
Signature		Date	25/07/2016

Name of Co-Author	Hu Zhang		
Contribution to the Paper	Design biology part experiment and revise manuscript		
Signature		Date	30/09/2016

Statement of Authorship

Title of Paper	Multicellular spheroids formation and recovery in microfluidics-generated thermoresponsive microgel droplet	
Publication Status	☑ Published ☐ Submitted for Publication	☐ Accepted for Publication ☐ Unpublished and Unsubmitted work written in manuscript style
Publication Details	Colloid and Interface Science Communications, 2016, 14, 4-7. DOI: 10.1016/j.colcom.2016.09.001	

Principal Author

Name of Principal Author (Candidate)	Xiaolin Cui		
Contribution to the Paper	Perform the experiment and writing the paper		
Overall percentage (%)	80		
Certification:	This paper reports on original research I conducted during the period of my Higher Degree by Research candidature and is not subject to any obligations or contractual agreements with a third party that would constrain its inclusion in this thesis. I am the primary author of this paper.		
Signature		Date	23/09/2016

Co-Author Contributions

By signing the Statement of Authorship, each author certifies that:

i. the candidate's stated contribution to the publication is accurate (as detailed above);

ii. permission is granted for the candidate in include the publication in the thesis; and

iii. the sum of all co-author contributions is equal to 100% less the candidate's stated contribution.

Name of Co-Author	Yu Liu		
Contribution to the Paper	Help LBM simulation part		
Signature		Date	23/09/2016

Name of Co-Author	Dr Yusak Hartanto
Contribution to the Paper	Give advice on material synthesis

Signature		Date	23/09/2016

Please cut and paste additional co-author panels here as required.

Name of Co-Author	A/Prof. Jingxiu Bi		
Contribution to the Paper	Give advice on cell culture		
Signature		Date	29/09/2016

Name of Co-Author	A/Prof. Sheng Dai		
Contribution to the Paper	Give advice on material and microchannel design		
Signature		Date	29/09/2016

Name of Co-Author	Dr Hu Zhang		
Contribution to the Paper	Help design experiment and revise manuscript		
Signature		Date	30/09/2016

Statement of Authorship

Title of Paper	Tuning the microenvironment for tumour spheroids formation	
Publication Status	☐ Published ☐ Submitted for Publication	☐ Accepted for Publication ☑ Unpublished and Unsubmitted work written in manuscript style
Publication Details		

Principal Author

Name of Principal Author (Candidate)	Xiaolin Cui		
Contribution to the Paper	Perform the experiment and writing the paper		
Overall percentage (%)	80		
Certification:	This paper reports on original research I conducted during the period of my Higher Degree by Research candidature and is not subject to any obligations or contractual agreements with a third party that would constrain its inclusion in this thesis. I am the primary author of this paper.		
Signature		Date	05/09/2016

Co-Author Contributions

By signing the Statement of Authorship, each author certifies that:

i. the candidate's stated contribution to the publication is accurate (as detailed above);

ii. permission is granted for the candidate in include the publication in the thesis; and

iii. the sum of all co-author contributions is equal to 100% less the candidate's stated contribution.

Name of Co-Author	Dr Yusak Hartanto		
Contribution to the Paper	Give advice on material synthesis		
Signature		Date	05/09/2016

Please cut and paste additional co-author panels here as required.

Name of Co-Author	A/Prof. Jingxiu Bi

Contribution to the Paper	Give advice on cell culture		
Signature		Date	29/09/2016

Name of Co-Author	A/Prof. Sheng Dai		
Contribution to the Paper	Give advice on material and microchannel design		
Signature		Date	29/09/2016

Name of Co-Author	Dr Hu Zhang		
Contribution to the Paper	Help design experiment and revise manuscript		
Signature		Date	30/09/2016

Statement of Authorship

Title of Paper	Exploring thermally reversible hydrogels for heart regeneration
Publication Status	☐ Published ☐ Accepted for Publication ☐ Submitted for Publication ☑ Unpublished and Unsubmitted work written in manuscript style
Publication Details	

Principal Author

Name of Principal Author (Candidate)	Xiaolin Cui		
Contribution to the Paper	Perform the in vitro experiment, material synthesis and writing the paper		
Overall percentage (%)	60		
Certification:	This paper reports on original research I conducted during the period of my Higher Degree by Research candidature and is not subject to any obligations or contractual agreements with a third party that would constrain its inclusion in this thesis. I am the primary author of this paper.		
Signature		Date	05/09/2016

Co-Author Contributions

By signing the Statement of Authorship, each author certifies that:

i. the candidate's stated contribution to the publication is accurate (as detailed above);

ii. permission is granted for the candidate in include the publication in the thesis; and

iii. the sum of all co-author contributions is equal to 100% less the candidate's stated contribution.

Name of Co-Author	Junnan Tang		
Contribution to the Paper	Design and performance the in vivo experiment		
Signature		Date	06/09/2016

Name of Co-Author	Dr Yusak Hartanto		
Contribution to the Paper	Give advice on material synthesis		
Signature		Date	05/09/2016

Please cut and paste additional co-author panels here as required.

Name of Co-Author	A/Prof. Jingxiu Bi		
Contribution to the Paper	Give advice on cell culture		
Signature		Date	29/04/2016

Name of Co-Author	A/Prof. Sheng Dai		
Contribution to the Paper	Give advice on material and microchannel design		
Signature		Date	29/09/2016

Name of Co-Author	A/Prof. Ke Cheng		
Contribution to the Paper	Help design in vivo experiment and revise manuscript		
Signature		Date	05/09/2016

Name of Co-Author	Dr Hu Zhang		
Contribution to the Paper	Help design experiment and revise manuscript		
Signature		Date	30/09/2016